

Annual Report 2007

Indira Gandhi Centre for Atomic Research

reactor technology

safety

fuel cycle

reactor design

fuel clad cross section

chemistry

154 GWd/t burn-up

engineering services

non-destructive evaluation

materials development

civil engineering

materials science

Instrumentation & control



Government of India
Department of Atomic Energy
Indira Gandhi Centre for Atomic Research
Kalpakkam - 603 102

IGC

Annual Report 2007



**Government of India
Department of Atomic Energy
Indira Gandhi Centre for Atomic Research
Kalpakkam - 603 102**



"Actions today mould our tomorrows"

Indira Gandhi



".....we are convinced that if we are to play a meaningful role nationally, and in the community of nations, we must be second to none in the application of advanced technologies to the real problems of man and society."

- Vikram Sarabhai

Editorial Committee

Chairman

Dr. P.R. Vasudeva Rao

Members :

Dr. Amarendra G
Dr. Govindan Kutty K.V
Shri Rajan M
Dr. Sivaprasad P.V
Shri. Somasekharan M
Shri. Srinivasan G
Shri. Subba Rao R.V
Dr. Sundar C.S

Address for Correspondence

Dr. P.R. Vasudeva Rao
Chairman, Editorial Committee,
Director, Chemistry, Metallurgy and
Materials Groups
Indira Gandhi Centre for Atomic Research,
Kalpakam - 603 102
Phone: +91-44-27480229
Fax: +91-44-27480065
Email: vasu@igcar.gov.in

Published by:

Scientific Information & Resources Division
Indira Gandhi Centre for Atomic Research,
Kalpakam - 603 102
Website: www.igcar.gov.in
February 2008

Contents

Foreword

Editorial

I. Fast Breeder Test Reactor	1
II. Prototype Fast Breeder Reactor	11
III. R&D for Fast Breeder Reactors	24
IV. Fuel Cycle	81
V. Enabling Technologies	116
VI. Basic research	144
VII. Infrastructure Facilities	173
VIII. Awards, Publications, News & Events and Organisation	184



- Gamma-ray back scattering scanning facility
- Supercritical Fluid Extraction (SFE) facility in glove box
- Hardfacing of bottom plate of the grid plate by Plasma Transfer Arc (PTA) torch
- Fuel clad cross section of the central fuel pin with 154 GWd/t burn-up
- Sodium cleaning system for FBTR fuel sub assembly
- Machined iron thimbles
- Mixer-settler with rotated helical coils
- Wireless transmission from pulsating sensors

Back Cover Legend

Top : Second batch of Trainee Scientific Officers of Training School with Chief Guest Dr. Anil Kakodkar, Chairman, AEC, Prof. J.B. Joshi, Director, UCIT and other senior dignitaries
Bottom : Students, Faculty Members and Organisers of Six week Summer Training Programme in Physics and Chemistry (STIPAC-07)



FOREWORD

I am happy to release the Annual Report for the year 2007, highlighting various important achievements of the Centre in areas of fast reactor science, engineering and technology development.

The FBTR has been successfully operated over the last one year, thus, realizing its objectives and in the process establishing new benchmarks. The current major mission of FBTR is to irradiate the fuel simulating PFBR fuel composition and towards this, the core has been expanded by adding two fresh Mark-I and eight fresh MOX subassemblies, after discharging one high burn-up (155 GWd/t) Mark-I subassembly for Post Irradiation

Examination. Challenging campaigns have been planned in the areas of testing and evaluation of fuels, materials and components, achieving higher operating temperatures and safety performance.

With regard to our committed mission of contributions to the design and construction of 500 MWe PFBR, we have been on the right path. The PFBR design review has continued, focusing on the issue of regulatory consent for "Erection of major equipment". Detailed analysis of thermal hydraulics and structural mechanics has been carried out for resolving the issues raised by Project Design Safety Committee, Civil Engineering Safety Committee and various specialist groups, constituted by Atomic Energy Regulatory Board. With respect to manufacturing technology, the hard facing of grid plate on two annular tracks has been successfully achieved - a crucial milestone, paving the way for smooth progress of activities related to final manufacturing stage of grid plate for PFBR. The completion of the manufacture of safety vessel, one of the large diameter thin shell components of reactor assembly, conforming to the tolerances higher than international nuclear standards is another significant milestone in our FBR programme. This has demonstrated indigenous manufacture capability and has given confidence towards successful completion of other important large sized vessels of PFBR Reactor Assembly. A sophisticated real time Decision Support System (DSS) comprising the most advanced meteorological forecasting module and a dispersion and dose prediction module was developed and demonstrated for radiological emergency. We are committed to robust synergy with BHAVINI as well as industries to realize the PFBR with the design specifications on time, with a firm commitment to safety and economy.

On materials front, we are working on modified D9I steels with active support from M/S MIDHANI. The base composition is similar to that of D9 SS with respect to all elements, except that titanium, silicon and phosphorous compositions have been optimized. Based on the synergy across various laboratories of our Centre, we are investigating various modified D9I heats with regard to mechanical properties and void-swelling behavior. We are utilizing atomistic experimental techniques to explain the observed trends. A new methodology based on ultrasonic C-scan presentation was identified to image the microstructure evolution during dynamic recrystallization of D9 alloy. Our Centre has also embarked on fabrication of metallic alloy fuel pins for test irradiations. The facility would be commissioned before the end of the year 2008.

Reprocessing is a central and important issue in closing the fuel cycle. The success of fast breeder reactors depends on successful, cost-effective and robust closure of the fuel cycle. Enhanced research and development with large manpower for reprocessing activity is a priority for next few years. We have made significant progress by demonstrating reprocessing the high burn-up carbide fuel and necessary steps are being taken to improve the facilities to take on the reprocessing of the oxide fuels for PFBR. The plant layout for the Fast Reactor Fuel Cycle Facility (FRFCF) is taking good shape.

Indigenous development of compact and reliable sensors has been an important programme of our Centre. It is a matter of pride that the electrochemical hydrogen meter developed in our Centre has been installed in the Phenix reactor in France for detection of steam leak into sodium. Innovations in electronics & instrumentation and sensor development have been the hallmark of our Centre,

widely acclaimed nationally and internationally. The operator information system for Boron Enrichment Plant was installed and commissioned. The entire instrumentation package for oil level sensing, including the actual sensors for deployment in PFBR, were made in-house with remarkable performance. The service groups are doing commendable job in developing valuable infrastructure for the Centre and gearing up to meet the large demands of XI plan targets.

We have been believing and practicing the mantra of synergistic collaborations within the DAE as well as other academic institutes for innovative contributions in fast reactor science & technology. For example, the Kalman filter technique, developed in collaboration with BARC to confirm the dropping of the Diverse Safety Rods into the core of PFBR during a scram, has been tested and results indicate that the technique is suitable for practical implementation. Also, a laser triangulation system has been developed jointly by IGCAR and RRCAT, for planar surface profiling of Titanium dissolver vessel of reprocessing plants of fast reactors.

The successes achieved by our Department are largely due to the development and management of quality manpower. On human resources development front, it is matter of great pride that we have made commendable progress. The Training School of Bhabha Atomic Research Centre (BARC) at IGCAR campus has turned out its first batch officers in September 2007, which is a momentous occasion for the Centre. Further, we have now added two new disciplines for post-graduates in Physics and Chemistry viz., Nuclear Reactor Physics and Nuclear Fuel cycle chemistry. It is also heartening to realize the academic programmes of Homi Bhabha National Institute (HBNI), thus imparting multidisciplinary training courses both for employees and students. We have started University Grants Commission (UGC)-Department of Atomic Energy (DAE) Consortium for Scientific Research (CSR) Node, which will help to strengthen the quality and quantity of research in various Indian Universities in the areas of Physical, Chemical and Engineering Sciences. In its commitment to harness quality manpower for science and technology, the DAE continues to be imaginative and innovative.

Over the last one year, we have shown high commitment to realize goals, strategic sectors, collaboration with academia and research institutes and industries. It has been a 360° progress experience for the Centre. The year 2008 would see milestone achievements in basic science, FBTR campaigns towards valuable contributions to realize PFBR and future FBRs, robust reprocessing of oxide and metallic fuels. I am looking for more passion, higher quality, enhanced commitment to science, technology and mission-mode programmes, innovation and imagination, increased productivity and above all more happiness and fulfillments for you and your families in the year 2008. I would like to quote George Bernard Shaw - "Imagination is the beginning of creation. You imagine what you desire, you will what you imagine, and at last you create what you will...".

Successful realization of the mission of the Centre, namely robust Sodium Cooled Fast Breeder Reactor Science & Technology with Closed Fuel Cycle and the vision of the world leadership in this technology needs a good connecting bridge between the mission and the vision. Moreover, connecting bridge between the mission and the vision has to be short in span of time to reap the benefits. I am inspired by Albert Einstein's quotation - "I never think of the future. It comes soon enough". We would realize the mission and the vision of the Centre soon enough.

IGC Annual Report is a remarkable example of steadily improving the standards in terms of technical content and readability of the significant work being carried out in the Centre. The credit of achieving this excellence is entirely due to Dr. P. R. Vasudeva Rao, Chairman, Editorial Committee and his competent colleagues.



Baldev Raj
Director

EDITORIAL

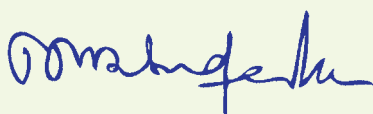
It is with great pleasure that we present you the annual report of the Indira Gandhi Centre for Atomic Research for the year 2007. During the year, the Centre has crossed many important milestones, and recorded many achievements, both with respect to the fast reactor programme and in the basic and applied research programmes. The continued successful operation of FBTR and the progress in construction of PFBR have been a source of inspiration for us and have given us the confidence that we are well on course to achieve the target of a robust and safe commercial fast reactor and associated fuel cycle within the next few years. As we continue to set targets such as higher burn-up and longer life of the fuel cycle plants, new issues in fuel cycle emerge and challenge the scientists. There is also the challenge to further reduce the unit energy cost of the future fast reactors, while simultaneously enhancing safety. Thus, R & D at IGCAR is continuously evolving to meet the challenges and this has kept the research atmosphere dynamic and vibrant. Strategies to meet such challenges expeditiously have to necessarily include commensurate human resource development in terms of training and induction of young minds and enhancement of collaborations with academic and research institutions. Both these aspects have received attention at IGCAR; this year saw the completion of the first year of the BARC training school at Kalpakkam, and introduction of courses on nuclear fuel cycle chemistry and reactor physics and safety for the second batch. The strengthening of the training programme would be an important step that would pay rich dividends for the fast reactor programme in the years to come.

The present annual report amply illustrates the all round progress achieved at the Centre. Besides the mission oriented R & D projects, we also report the impressive achievements in basic research and the attention given to development of infrastructure and facilities, as well as the environment in and around the plant site and township.

The Editorial Committee is grateful to Dr. Baldev Raj, Director for his constant encouragement and guidance in bringing out this report. We would also like to thank the authors for their valuable contributions, reflecting the major research and developments being carried out in the Centre. Overall, bringing this report has been a happy experience for the editorial team; our strength has been further augmented by the support provided by Sri Jayakumar from SIRD and Sri Harikumar from EID. The editorial committee would like to acknowledge Shri M. Somasekharan, Head, Scientific Information Resources Division and Shri M. Ganapathy for rendering necessary assistance in bringing out the report.

We believe that the annual report of IGCAR has continued to maintain the high standards in line with the overall philosophy of the Centre to achieve excellence in every activity. We are at the same time, open to suggestions for further improvement. We have, in fact, received many messages from readers with valuable suggestions and we have tried to implement them in this issue. We have the confidence, therefore, that this issue will be a better reading material than the previous reports both in terms of quality of articles and presentation style, and we need all your inputs to either confirm or negate this conclusion !

Wishing all the readers a Happy and Prosperous New Year 2008,



(P.R.Vasudeva Rao)
Chairman, Editorial Committee
Director, Chemistry, Metallurgy & Materials Group
IGCAR

Chapter -1

FAST BREEDER TEST REACTOR

1.1. Experiments in the 14th Irradiation Campaign

As a part of the programme to conduct a series of experiments in FBTR starting from the 14th irradiation campaign (commenced on February 28, 2007), several important experiments were completed. These are: validation of failed fuel detection system, measurement of flux at the grid plate location, accelerated irradiation of grid plate material as a part of its residual life assessment, and short-term irradiation of a single pin of PFBR fuel for studying the initial restructuring. Concurrently, long-term irradiation of SS 316 and D-9 alloys has also been initiated. The core configuration is shown in Fig. 1.

Experiment to validate failed fuel detection system

This experiment was conducted with a special subassembly having 19 perforated pins (with a total exposure area of 112.8 cm²) of natural uranium loaded successively at five different locations. The main objectives of the experiment were:

- ❖ To calibrate Delayed Neutron Detection (DND) system at different power levels, primary sodium flows and sodium inlet temperatures
- ❖ To establish the feasibility of localization of failed SA using DND system
- ❖ To check the response of Clad Rupture Detection (CRD) in argon system
- ❖ To validate the failed fuel localization setup.

The results were satisfactory and validated the ability of the DND system not only to detect any clad breach, but also to broadly identify the zone of failure from the contrast ratios of the east & west DND signals. Failed fuel localisation system, intended to determine the age of the fuel performed well in detecting the presence of Kr and Xe in cover gas argon.

Residual life assessment of the grid plate

Grid plate, which supports entire core, is one of the important components that limit the life of the reactor. The life limiting factors are residual ductility and swelling. Displacement per atom (DPA) is one of the parameters that is found to have good correlation with the radiation damage to the material. However, DPA cannot be directly measured. Fluxes above 0.1 MeV contribute maximum to the DPA. The fission reactions rates in ²³⁷Np have good correlation with the DPA rate, as the cross-section threshold is around 400 keV. Hence, Neptunium foils were used to measure the grid plate fluence. Standard irradiation experimental subassembly with a capsule was used. The special capsule is made of SS rod containing the foils at the guide sleeve and support plate of the grid plate and core mid plane. As the capsule is longer than the standard irradiation capsules, flow induced vibration test was carried out with a dummy subassembly at FRTG and the vibration found to be negligible. The subassembly was loaded in 4th ring of the core and the reactor operated at 15.6 MWt for about 14 days. The experimental carrier along with the capsule was

discharged and sent to RML hot cell for retrieving the foils from the capsule and counting of fission product activities. Concurrently, test specimens of SS 316 used in the reactor are also being irradiated to simulate the damage. They will be retrieved at the end of the 14th campaign after 70 days of irradiation and measurements of residual ductility and swelling carried out. The results of both these experiments will provide the basis for the residual life assessment of the grid plate.

Irradiation of PFBR test fuel pin for initial gap closure

The peak Linear Heating Rate (LHR) for PFBR fuel is 450 W/cm. From fabrication considerations, the fuel fabricator has asked for relaxation of the tolerances on the pellet diameter. This will result in higher fuel-clad gap, and the fresh fuel will hence have to be operated at lower LHR till the gap closes by cracking and restructuring of the fuel. The duration of operation at low LHR has implications on the economics of power generation. To determine the time required for the gap to close, a single pin of PFBR test fuel was irradiated in FBTR for 14 days. Mixed Oxide with 29% PuO₂ and rest UO₂ enriched with about 53.5% U²³³ is used as fuel for this pin.

Active fuel column length in this fuel pin is 240 mm. The subassembly with the single pin was loaded in the first ring, so that it will operate at a peak linear power of 400 W/cm when the Mark I SA in I ring is generating a peak power of 297 W/cm. The reactor power was maintained at the corresponding value of 15.6 MWt. The pin has been discharged for Post Irradiation Examination (PIE).

Structural material irradiation

To generate baseline irradiation performance data on the indigenously developed D9 alloy at low temperature, two subassemblies with pressurized capsules and tensile and swelling specimens were loaded in the fourth ring at the start of the 14th campaign. Duration of irradiation will depend on the evolution of the core and the temperatures. The maximum damage attained will be about 24 dpa per Effective Full Power Year (EFPY). For the high values of dpa required (>70 dpa), the irradiation hence has to be continued for at least three EFPY.

Testing of PFBR neutron detectors

The PFBR in-core neutron detectors developed by BARC were tested in the detector pits to check their response over the

full range.

Testing of acoustic detector and Kalman reactivity filter

Various methods are being contemplated to confirm the dropping of Divers Safety Rod Drive Mechanism (DSRDM) into the core during a scram. One of these is the Kalman reactivity meter and the other is acoustic technique. The Kalman filter technique was tested in FBTR in the shutdown state, and reactivity changes due to dropping of control rods were studied. The results were found promising. Two acoustic devices have been designed by FRTG and fabricated at CWD for installation in the Experimental canals of FBTR. It will be used

to sense the dropping of control rods during shutdown state of the reactor. The procedures for their handling and disposal have been reviewed by the Pile Handling Procedure Review Committee. Based on the review, modifications are being carried out on the devices.

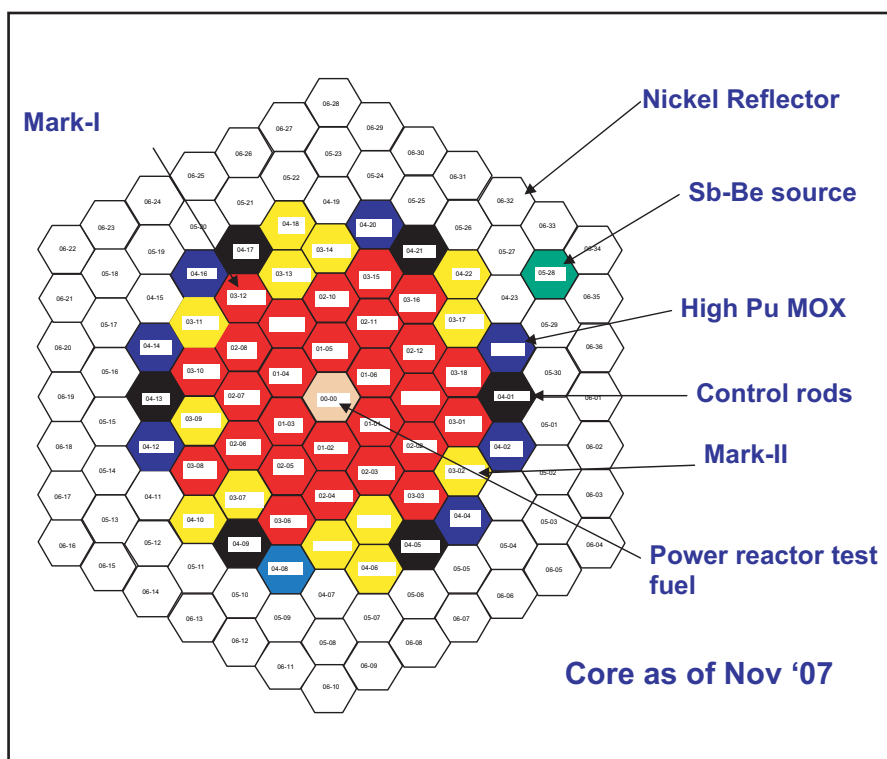


Fig.1 Core configuration for 14th irradiation campaign

I.2. Metallographic Examination of the Mixed Carbide Fuel Pin which has seen 154 GWd/t burn up in FBTR

Remote metallographic examination was carried out on a fuel pin which is proximate to the centre of the core. The fuel pin was cut using diamond wafer wheel to extract specimens from the centre and the end of fuel column. Sequential grinding and polishing of the molded specimens were carried out. Replicas of the polished surface of the specimens were taken and transferred out of the hot cell. They were observed under microscope after decontamination and gold sputter coating.

Photo micrograph of fuel cross section at the centre of the fuel column (see Fig.1) revealed circumferential cracking of fuel and a distinct zone devoid of fuel porosities near the outer diameter. Favorable stress-temperature regime near the outer diameter of the pellet has led to hot compaction of the pellet thereby creating a dense zone. The porosity exhaustion is attributed to the creep of the fuel due to Fuel Clad Mechanical Interaction (FCMI). The micrographs revealed complete closure of

the fuel-clad gap and circumferential cracking both at the centre and end of the fuel column indicating that the entire fuel column has entered the restrained swelling regime. Measurements on the micrographs further revealed that the outer and inner diameter of the clad has increased due to void swelling. The measured values were consistent with the diamteral changes measured using fuel pin profilometer.

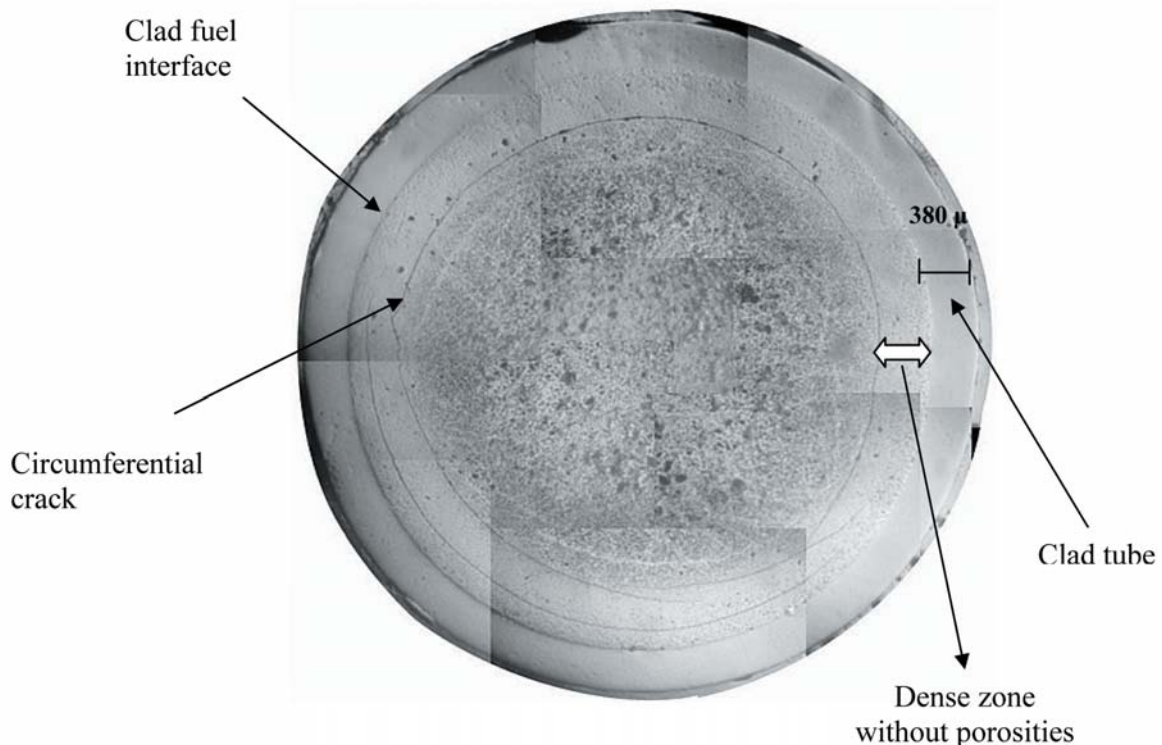


Fig.1 Photomicrograph of the fuel-clad cross section at the centre of the fuel column.

I.3. Seismic Re-evaluation

Seismic re-evaluation of FBTR is taken up as a joint research project with IGCAR and SRI, since the plant has not been seismically qualified at the design stage as per the present norms. In seismic evaluation of an existing plant, current seismic criteria is generally used to qualify a minimum set of Structures, Systems and Components (SSC) required to safely shutdown the reactor, maintain the plant in a safe condition and safely contain /confine radioactive inventory. The systems required to be qualified for achieving these functions should include one main path and one redundant path. The conditions postulated following a seismic event are: simultaneous off-site and plant generated power loss up to 72 hours (other than the seismically qualified emergency

power) and no external supply of make-up water and other media for safety system operation (e.g. diesel oil) for 72 hours. Also, earthquake induced fires and floods and other seismic interactions affecting the safety functions shall be avoided.

The seismic re-evaluation involves ten tasks, viz. Preparation of criteria document, Determination of Review Basis Ground Motion (RBGM), Safety analysis, Collection of as built data, Preparation of seismic SSC list, Plant walk-down, Determination of seismic response of SSCs, Capacity assessment of components, System model analysis and Capacity assessment of plant.

The Criteria document was prepared based on IAEA Safety Report Series 28 (2003), and has been reviewed by AERB review committee.

The RBGM was arrived at by Probabilistic Seismic Hazard Analysis. This was a path-breaking exercise by the Task Force members from CSED/AERB. The geometries and spatial distribution of potential sources of seismic

activity in the region around the plant site were determined from past data (Fig.1). Approximately 100 records of earthquake data for the site from 1807 to 2001 are available. The largest earthquake to have occurred in Peninsular India was the earthquake of February 8, 1900, with a magnitude of 6.0, with epicenter at Coimbatore, at a distance of 400 km from the plant site. From these data, the hazard curve for the site was worked out and RBGM arrived at (Fig.2). The proposed RBGM has been approved by the AERB Review Committee.

For safety analysis, seismically induced initiating events (IE) were identified based on extensive brain-storming sessions. For these IEs, frontline systems were identified. For each of these frontline systems, exhaustive fault trees (FT) were developed up to the component / sensor level based on the as-built drawings and discussion with field personnel. The Seismic Structures, Systems, Components list (SSSCL) was obtained from the minimal cut-sets of the fault trees for the accident sequences. About 400 components are identified in the SSC list. The qualification of

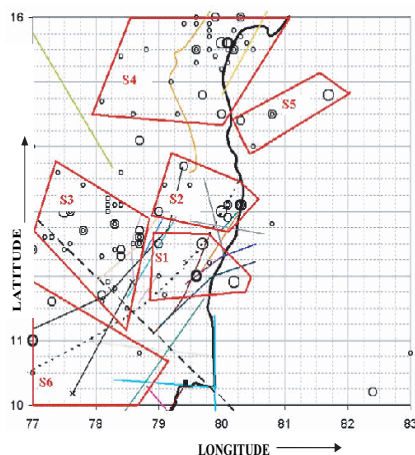


Fig.1 Seismic sources around site

these SSCs has to be done by analysis, testing or from experience data base. The SSC list was further segregated based on qualification methodology. The document on safety analysis has been reviewed by AERB.

The major structures to be analyzed are the Reactor Containment Building (RCB), Steam Generator Building (SGB), Service Building (SB) and Control Building (CB). The major systems to be qualified by analysis are the primary sodium system and secondary sodium system. Consultancy contract was awarded to M/s Engineering Mechanics and Research Company (M/s EMRC), Bangalore, for analysis of RCB, SB & SGB as well as the secondary sodium system. EMRC has completed the modeling and developed floor response spectra for all the buildings for the RBGM. The modeling of secondary sodium

system has also been completed by EMRC, and analysis for the RBGM is in progress. CED, IGCAR carried out a parallel modeling of RCB for checking the EMRC results. The analysis of CB has been carried out by CSED, AERB. The modeling of the primary system has been completed by NEG, IGCAR, and analysis for the RBGM and floor response spectra thereof is in progress. The analysis will include not only structural integrity, but also scammability of the control rods and pump non-seizure. In addition, CED, IGCAR has done the modeling of some support system structures, viz raw water pump house, cooling tower and maintenance building. Analysis of RCB ventilation ducting is being done by ROMG.

Ten components have been identified for qualification by testing on shake-table. For these, the as-built drawings of

the panels have been prepared. Testing will be taken up shortly.

Several components have been identified as getting

qualified from experience data base, subject to proper anchorages. Plant walk-down was carried out by a team of engineers & specialists from NPCIL, AERB & IGCAR. Seismic interactions and anchorages were studied. The findings of the walk-down have been reviewed by the AERB Review Committee. The walk-down revealed several areas where proper anchorages are required, and areas where seismic house-keeping is called for to avoid seismic interaction. Seismic house-keeping has been completed in zero level of RCB.

The results of the analysis of the SSC and of the qualification tests of components in the shake table will be submitted to the Review Committee. Retro-fitting measures, if required, will be taken up based on the recommendations of the Review Committee. The seismic anchorages will be modified wherever required, based on the findings of the plant walk-down and comments of the Review Committee. These are the minimum required for plant relicensing.

Finally, system modeling, capacity assessment of components and seismic margin of the plant will be assessed as a research activity.

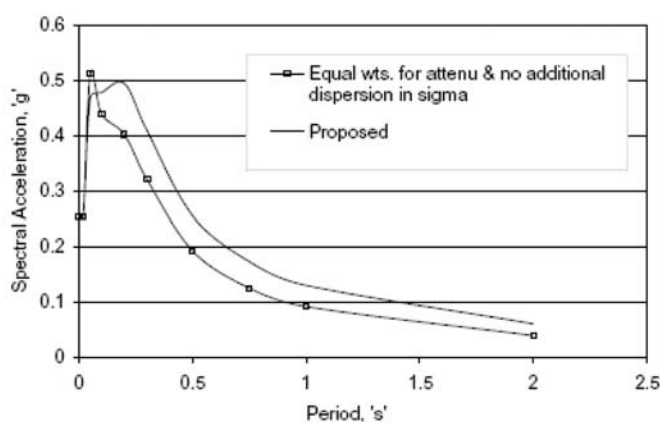


Fig.2 Review basis ground motion

1.4. Validation of Failed Fuel Detection System

An assessment of the sensitivity and localization capabilities of the DND system in FBTR was made by a series of delayed neutron measurements. Simulation of failed fuel pin was by a natural uranium fission product source in the form of a special subassembly consisting of 19 stainless steel clad, natural uranium metal pins, each having a large exposed area in the form of 189 small holes of 2 mm diameter. The exposed area amounted to 112.8 cm², equivalent to 28.2 cm² of regular pin from fission product

release point of view. Before starting measurements with the special subassembly, background measurements in the DND system for the current 49-subassembly core configuration were carried out. Measurements were then taken with the special subassembly loaded in the central location (00/00) and in the locations 02/04, 04/07, 02/10 & 04/19. (The first number gives fuel SA ring number and second number gives the location number within the ring. The locations 02/04 and 04/07 are on the west side and

the locations 02/10 and 04/19 are on the east side- Fig.1). At each location measurements were done at power levels starting from 0.35 MWt and going up to 10 MWt, with the reactor sodium inlet temperature ranging from 453 to 613K.

The delayed neutron signal shows an increase with core inlet temperature in all locations. The typical signal behaviour with temperature is shown in the Fig.2 when the special subassembly is in the central location. The sensitivity of the system is therefore high at higher core inlet sodium temperature.

The observed behaviour of signal as a function of power is shown in Fig. 3, 4 & 5. An actual fuel failure would show a similar behaviour which makes it possible, using the contrast ratios, to localize fuel pin failure to the half sector and the ring in which it is located.

The contrast ratios of the DND signals measured at 10 MW for all the locations are given in Table 1, which shows a strong dependence of the ratio on the location of the special subassembly. These ratios are

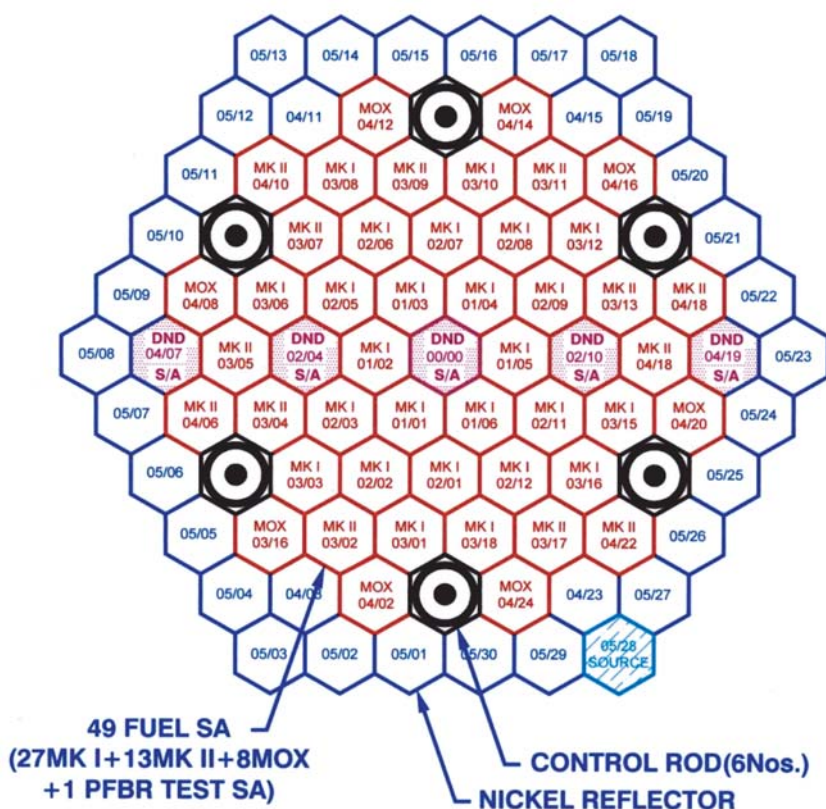


Fig.1 DND subassembly locations

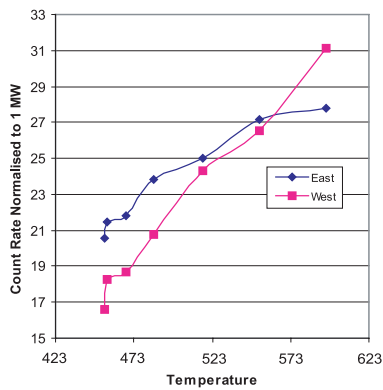


Fig.2 Temperature dependence of DND signals (SA at 00-00)

for signals without background. Hence these values will prove useful in deciphering the location of an actual pin failure.

The expected rise in signal over background per cm² of actual fuel failure is given in

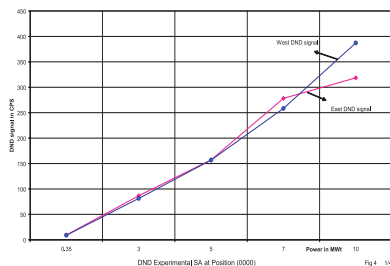


Fig.3 Response of the DND signal as function of power (DND SA in 00/00 location)

Table 2. Considering the counting statistics of the detectors used for display on the console, a measurability criterion of 3σ background value implies a failure if the background counts exceed by 6.7 % on the east and / or 4.8 % on the west under conditions of sodium inlet temperature prevailing more than 573K. The analysis has brought out that the system is capable of detecting even fuel defects to an extent of 0.5 to 1 cm². Using the measurability criteria and the pattern of increase of signal over background, it will be possible to determine the size of the clad opening and localize the defect to the half sector and the ring in which it is located.

The cover gas activity monitors located in the CRD circuit and common cover gas reject circuit also responded very well. Cover gas samples collected at higher powers showed the presence of A_r^{41} ,

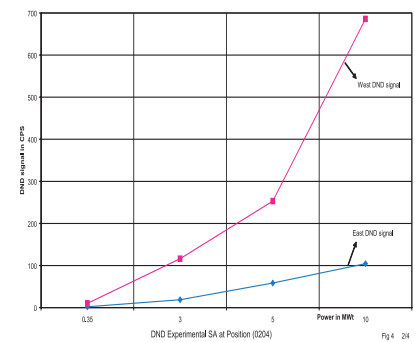


Fig.4 Response of the DND signal as function of power (DND SA in 02/04 location)

K_r^{85m} , K_r^{87} , K_r^{88} , X_e^{135} , C_s^{138} & R_b^{88} . This confirms that cover gas activity will provide the first confirmation of an actual pin failure. General background

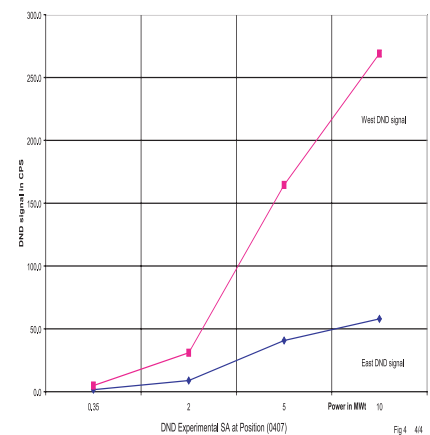


Fig.5 Response of the DND signal as function of power (DND SA in 04/07 location)

Table 1 : Ratios of signals emanating from special SA at 10 MWt

Power at 10 MW	Location of Special SA				
	04/19 (E)	02/10 (E)	00/00 (C)	02/04(W)	04/07 (W)
W/E Ratio	0.06	0.13	1.12	10.03	13.31
E/W Ratio	18.17	7.73	0.89	0.10	0.08

Table 2 : Expected rise in signal (over background) per cm² of actual clad failure at 10 MWt

Power at 10 MW	Location of Special SA									
	04/19 (E)		02/10 (E)		00/00 (C)		02/04(W)		04/07 (W)	
	East	West	East	West	East	West	East	West	East	West
% Rise in Signal per cm ²	15	0.4	50	3	23	13	5	27	1	9

radiation in RCB was 0.3 mR/h, with a maximum of 1.0 mR/h at specific locations. A PVC cocoon was spread over the pile and hoses provided to direct the leaking argon to the exhaust to reduce the activity inside RCB.

During this experiment the

cover gas was also sampled and analyzed using Fail Fuel Localization System (FFLS). The system performed as per the design intent and in actual failure of fuel pin it is expected to give the age of the failed fuel pin. Making use of DND signals, East and West DND signal ratios and the age of the

failed pin obtained from the cover gas analysis, the suspected failed fuel subassemblies can be short listed. Actual failed subassembly can be identified from this list by limited trial and error fuel handling and reactor operations.

1.5. Modification of Trailing Cable System of FBTR to Minimise Failure of Cores of the Cable

Fuel handling operations in FBTR are carried out in the shutdown state of the reactor. Fuel handling is done through a single fuel handling canal which gets aligned over 745 positions of the reactor by relative rotation of two eccentrically mounted rotating plugs, viz. Small Rotating Plug (SRP) and Large Rotating Plug (LRP). Prior to plug rotation, the cables carrying the signals which are required for reactor operation, but not for fuel

handling, are disconnected with the help of disconnectible connectors. However, signals which are essential for fuel handling are routed through a trailing cable system.

The trailing cable system consists of four cables originating from SRP & LRP. During plug rotation, these cables wrap around the LRP and get wound and unwound in cable guide grooves on the LRP. To prevent the cables from slackening and to keep them taut during unwinding, the other ends of the cables are terminated in a cable tower, which houses a set of fixed guide

pulleys at the bottom and a set of mobile pulleys at the top. Counter-weights fixed to the mobile pulleys keep the cables taut. The pulleys in the cable tower are in the east-west plane. Hence, the cables are routed from the LRP through a tortuous path, with two acute turns - one as they come out of the LRP and the other when they turn to the east towards the cable tower (see Fig.1).

Due to the tortuous path with several turns, the cables were getting subjected to tensile and compressive stresses during the winding and unwinding cycles respectively. This cyclic loading was resulting in frequent failure of cores of cables during fuel handling. Most of the failures were taking place when the LRP positioning angle was between

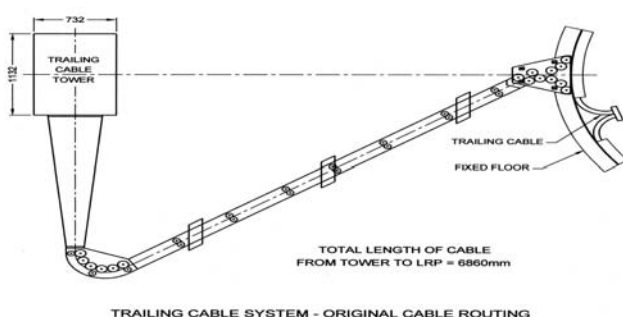


Fig.1 Original cable routing

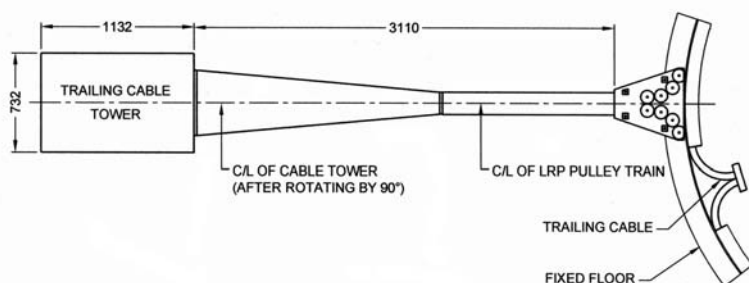


Fig.2 Modified cable routing

160° & 180°. To minimise the failures, the plugs were rotated manually instead of through the motor while crossing this region. Despite this, cable core failures were found to be very frequent and this was hampering fuel handling operations, delaying the plant schedule and warranting replacement of the cable when the spare cores are exhausted.

In order to address the above causes for cable failure, it was decided to modify the layout by rotating the cable tower by 90° so that the pulleys in the cable tower are in the north-south plane, and to route the cables directly from LRP to cable tower eliminating two sharp bends (Fig.2). This required the permanent removal of one of the two Fresh Fuel Transfer Chambers (FFTC), which was approved by the Station Operations Review Committee.

The most difficult part of the modification was rotation of the

six metre tall cable tower which was supported on floor support beams and anchored at two points at top on Reactor Containment Building wall. The tower is not accessible by crane. No vertical lifting of tower was possible due to routing of a massive air conditioning duct over the tower without any clearance. The tower was supported on temporary structures and measures were taken to prevent its tilting during rotation. The tower could be rotated in-situ in a safe way and was anchored by modifying its supports. The cable trays were modified for the new layout Fig.3. With this modification, the total length of the cable got reduced by 7 m and the total number of cable guide pulleys got reduced from 156 to 76. The required pre-tension could be achieved with reduced counterweights of 110 kgf for indigenous cable and 80 kgf for the imported cables as against the earlier values of 162 & 120 kgf respectively.

During plug rotation trials, the cable movement to and from the tower was observed to be very smooth and consistent, without slackening. The reduction in the pre-tension loads and elimination of the two sharp bends in the layout have cumulatively contributed to significant reduction in the cyclic stresses on the cable. Two fuel handling campaigns have been completed without any core failure. It is expected that this modification will significantly reduce cable core failures and minimise the replacement of trailing cables in future. The reactor availability will also get improved considerably.



Fig.3 Trailing cable tower and cable routing after modification

Chapter -2

PROTOTYPE FAST BREEDER REACTOR

II.1. Construction Status of PFBR

The Government of India had accorded administrative approval and financial sanction for construction of the 500 MWe Prototype Fast Breeder Reactor (PFBR) at Kalpakkam in September 2003. Bharatiya Nabhikiya Vidyut Nigam (BHAVINI) Limited a public sector company under DAE, is responsible for construction and operation of PFBR. IGCAR is responsible for design, associated R&D and manufacturing technology, and getting consent from regulatory bodies for construction of reactor. The formation of task force with members drawn from IGCAR and BHAVINI has greatly helped in resolving the technical issues in manufacturing in a timely manner.

The construction of PFBR has progressed very well (Fig.1-3). The manufacturing of safety vessel with thermal insulation, large diameter main sodium and argon tanks, and thermal baffles has been completed. Manufacturing of long delivery mechanical components of Nuclear Steam Supply System (NSSS), viz grid plate, shutdown mechanisms, core support structure, top shields, IHX, sodium pumps, steam generators, inclined fuel

transfer machine and decay heat removal heat exchangers are in different stages of progress in Indian industries. Manufacturing of main vessel and inner vessel is in advanced stage at site assembly shop.

Construction of 8 numbers of Nuclear Island Connected Buildings, diesel generator buildings, service building, service water pump house and ventilation stack is in progress at various elevations. The



Fig.1 Overall view of the reactor site



Fig.2 Reactor vessel



Fig.3 Safety vessel

contracts for construction of turbine building, sea-water intake structure and sea-water outfall channel have been awarded.

Purchase orders have been placed for main plant turbo generator package, instrumentation and control package, 6.6 kV switchgear, diesel generators, switchyard and main cranes. Overall, the project is on schedule and the reactor is expected to be commissioned by September 2010.

II.2. Design and Development of Thermal Insulation for Safety Vessel

In PFBR, which is a 500 MWe sodium cooled pool type reactor, all reactor internals including core and primary coolant (sodium) are contained in a single vessel called main vessel surrounded by safety vessel, which serves the purpose of containing sodium

and ensuring minimum sodium level to facilitate core cooling in the unlikely event of leak in main vessel. The load from these vessels is transferred to concrete structure known as reactor vault. To limit the heat flux to reactor vault concrete and thereby ensuring the

integrity of the same, stainless steel plate type thermal insulation which can withstand high gamma radiation is provided on outer surface of the safety vessel.

Design

Thermal insulation on safety

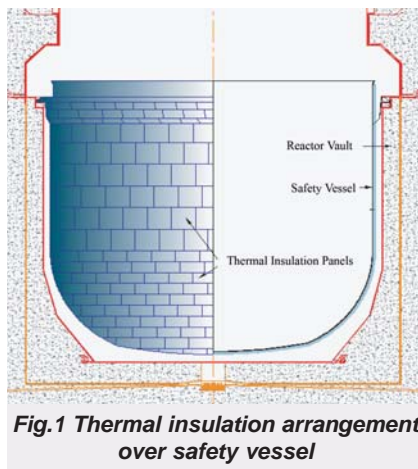


Fig.1 Thermal insulation arrangement over safety vessel

vessel limits the heat transfer from safety vessel to the reactor vault concrete (Fig.1) in order to maintain the temperature of the concrete within the permissible design limit of 338 K under normal operation.

The SS plate type insulation is designed in the form of panels, each measuring $\sim 1\text{m} \times 1\text{m}$ (Fig.2). Each panel consists of two slabs and interconnected through studs. In each slab, 17 plates of 0.1mm thick mirror polished sheets are encased in a box of 1mm thick whose surfaces are also mirror polished. As the heat transferred through radiation

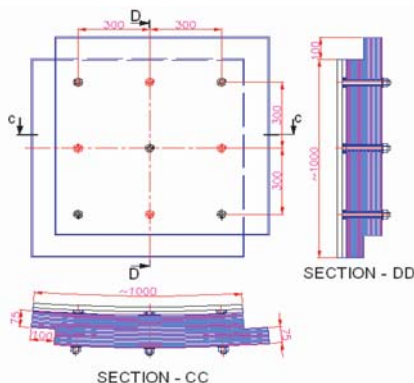


Fig.2 Schematic view of a panel of SS plate type insulation

mode depends on the surface emissivity (Fig.3), mirror polish has been specified for these sheets which give a surface emissivity of as low as 0.05. Multiple panels are secured all over the outer surface of safety vessel through studs welded on outer surface of safety vessel.

The thickness of insulation panels and the number of insulation sheets in each panel are based on optimisation study carried out towards restricting the heat flux to reactor vault concrete. Based on the study with respect to the number of sheets, emissivity of sheets and thickness of panel, the number of sheets is selected to be 34 with total thickness of panel to be 150mm.

Development lessons

As the polished sheets are very thin and flimsy, maintaining the spacing between them was a crucial task. A gap of 4.26 mm was specified in the design and dimples were provided to achieve the required spacing. As the initial trials with 100 mm dimple spacing did not yield desired results, the same was optimised to 50 mm with which the desired results were obtained.

During the course of trials, another major challenge was

faced in the forming of dimples. Initial dimpling trials with the imported material of higher hardness was giving good finish but tearing occurred at dimples. To overcome this problem, the dimple radius and fillet radius between the dimple and the sheet was increased. Further trials with these changes improved the dimple forming and problem of dimple cracking was resolved.

The other challenge was with respect to stacking of the sheets one over the other. Due to self weight as well weight of sheets supported over it, total height of the stack was not achieved. Towards this, a novel spacing arrangement with multiple spacers was designed and incorporated (Fig.4).

Validation

As direct correlation between surface roughness and the emissivity could not be found in literature, experiments were

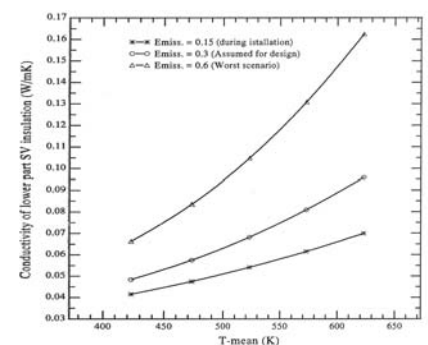


Fig.3 Thermal conductivity of insulation panel as a function of temperature and emissivity of the sheets



Fig.4 One typical panel with sheet spacing arrangement

carried out to evaluate the emissivity of the plates polished and the same has indicated that the mean emissivity to be 0.047 against the design value of 0.05 (Fig.5).

Further, experiments were carried out in an experimental set-up, at IGCAR, to assess the heat transferred through the

insulation panels and the results have reinforced the theoretically calculated values enhancing the confidence in design.

Fixing of panels over safety vessel was under taken and the same has been successfully carried out (Fig.6).

The safety vessel thermal insulation panels have been fabricated as per the technical

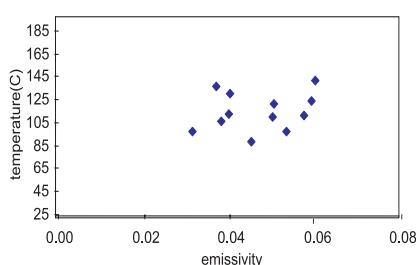


Fig.5 Results of emissivity measurements for the polished sheets



Fig.6 View of safety vessel with thermal insulation

specification meeting all the design intents. Experiments conducted to measure emissivity and heat transfer have reinforced the design calculations. Fixing of panels over safety vessel has been successfully carried out concluding the successful design, development and manufacture of thermal insulation panels for FBR for the first time within the country.

II.3. Thermal Hydraulic Design of PFBR Reactor Vault Cooling System

In PFBR, the main vessel houses the entire primary circuit including primary sodium and core. It is supported over a huge cylindrical concrete Reactor Vault (RV) as shown in Fig. 1. The safety vessel surrounding the main vessel is also supported on RV. During normal operation, the temperature of main and safety vessels is $\sim 693\text{K}$. During

decay heat removal (DHR) conditions, this temperature increases to $\sim 848\text{K}$. Due to these high operating temperatures of the vessels, RV gets heated. From design considerations, the temperature of RV has to be less than 338K during normal operation and less than 363K during DHR condition. To achieve these temperature limits, RV is cooled

by DM water by a dedicated cooling system. Square section cooling pipes are chosen for this purpose, which are welded to the RV liner. The cooling tubes are segregated into two loops with alternate pipes connected to one loop. This ensures that in case of leakage in any one of the loops, the other loop is available. At the design stage, it was assumed

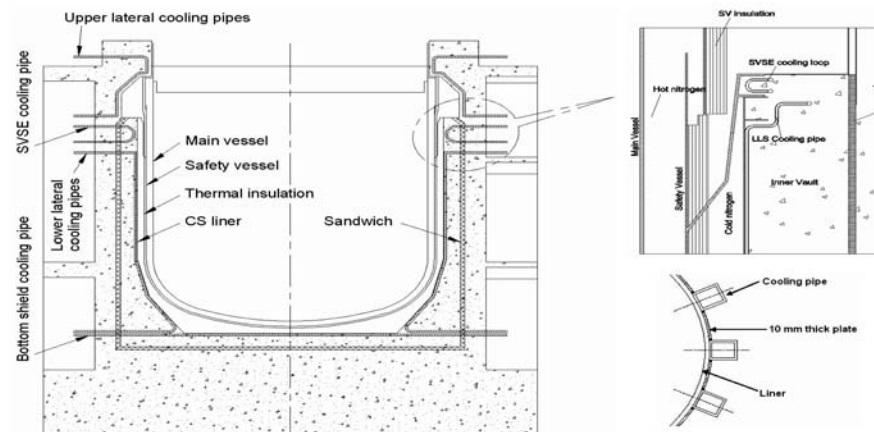


Fig.1 Schematic of the RV cooling system

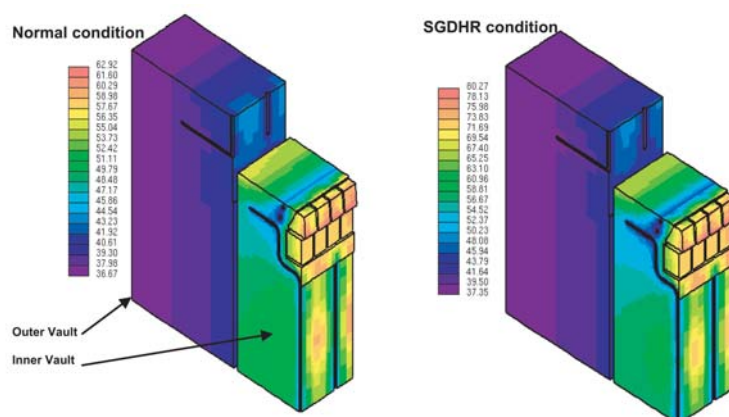


Fig.2 Temperature distribution in reactor vault around SVSE embedment during normal and SGDHR conditions

that the cooling pipes are welded to the liner (through out) the length. But, near the safety vessel support embedment, the cooling pipes cannot penetrate the support flanges. Hence, a part of concrete trapped inside the flanges remains un-cooled. Further, from the point of view of avoiding use of sharp bends in the pipes, the cooling pipes have to be re-routed during construction. The effects of these changes on the concrete temperature around the safety vessel support embedment

(SVSE) have been assessed by a comprehensive Computational Fluid Dynamic (CFD) analysis and suitable design provisions have been identified and implemented at the construction site.

As a part of the analysis, many parametric studies (12 configurations) have been carried out and the need of additional cooling loop in the SVSE zone is identified. Also, it is seen that there is a local hotspot in RV where the conical support of the safety vessel

emerges out of the insulation. To mitigate this hot spot, it was essential to increase the circumferential conductance in the RV liner. This is achieved by interconnecting the cooling pipes by 10 mm thick carbon steel plates for a height of 1.2 m, as shown in Fig. 1. Also, the water flow rate has to be doubled for the lower lateral shield region of RV. The number of cooling tubes and the water flow rate in the additional cooling loop of SVSE have been determined to be 288 and 60 m³/h respectively. The temperature distribution in RV with these modifications is depicted in Fig. 2.

From limitations in space around SVSE, the number of headers that can be connected to the SVSE cooling loop and the size of headers are to be as minimum as possible. However, from heat removal considerations, the flow rate that is required to be sent through each and every cooling pipe should be more than a

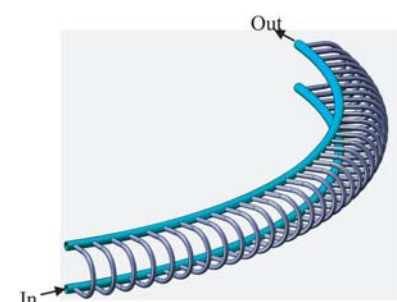


Fig.3 Header with "end-in & end-out" configuration for SVSE cooling

minimum value. Detailed 3-D hydraulic investigations have been carried out to arrive at a compact layout for the supply and discharge headers of the SVSE cooling circuit satisfying the design and layout requirements. With the acceptable number of headers (4) and header size (40 NB), there are 36 tubes connected to each header. The flow distribution was highly non-

uniform in the "end-in & end-out" configuration. In the "central-in & central-out" configuration, with orifices in the tubes and 20 % extra flow in the circuit, the required flow could be achieved with minimum pressure drop in the system. The "end-in & end-out" header configuration and the flow distribution in the modified configuration are depicted in Fig. 3 and 4 respectively.

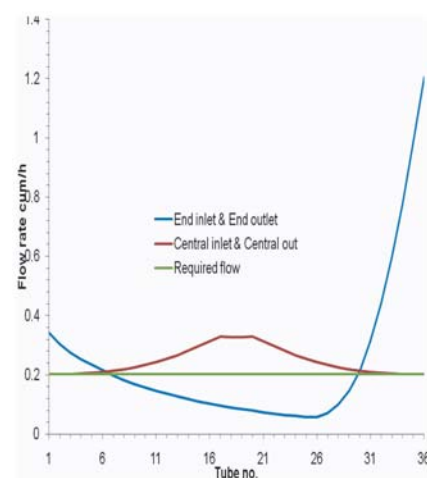


Fig. 4 Flow distribution in the SVSE cooling loop

II.4. Structural Integrity of Grid Plate under Accidental Fall of Subassembly with Transfer Arm

PFBR core consists of 1758 subassemblies (SAs) including 181 fuel subassemblies (FSA), 120 blanket subassemblies (BSA), 9 control subassemblies (CSA), 156 storage subassemblies (SSA) and the remaining shielding subassemblies. Each SA has a circular foot at the bottom, that is inserted in to the respective sleeve and thus the core SAs are free standing on the grid plate, behaving like a cantilever beam. Grid plate (GP), apart from supporting the SAs, acts as a plenum to distribute the required amount of sodium coolant to the SAs. Thus, the grid plate does the important safety function in the reactor and hence, it is designed respecting the RCC-MR class 1

component rules. As per the design criteria, the structural integrity is ensured under all the operating conditions including postulated accident scenarios. Analysis had been carried out to demonstrate the structural integrity of grid plate under impact force developed due to the free fall of a single SA along with gripper of transfer arm (TA), during the handling operation.

Impact scenario

Within the reactor assembly, the SAs are handled by transfer arm (TA) for the three major operations: (1) introduction of fresh SA in to the respective location in grid plate after removing from the transfer pot (TP), (2) transfer of spent fuel

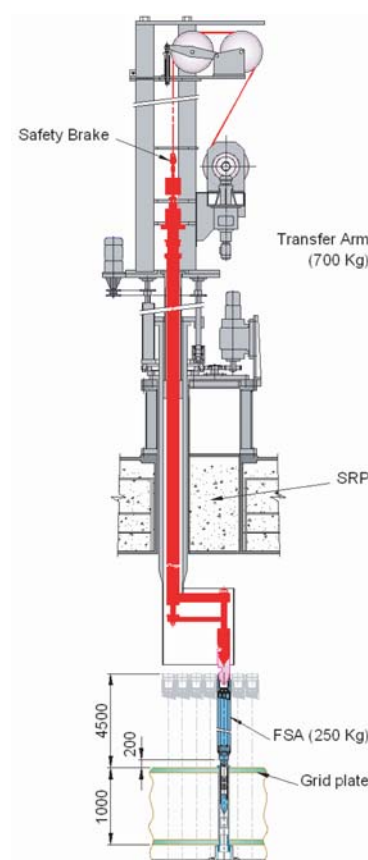


Fig.1 Schematic of gripper assembly and SA

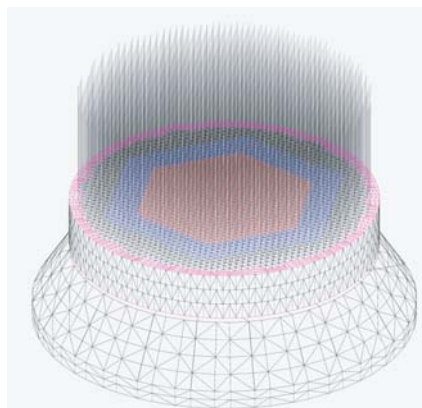


Fig.2 Finite element mesh of structure

SA to the respective storage locations in the grid plate and (3) transfer the spent fuel SA from the storage locations to the TP. For carrying out these operations, the guide tube of TA is lowered by 4.5 m within which the gripper assembly is guided vertically either during lifting the SA or during introduction of the SA. In each operation, the gripper assembly is translated to the maximum distance of about 4.5 m in the vertical direction to cover the entire SA, during the withdrawal of say, spent fuel SA from the

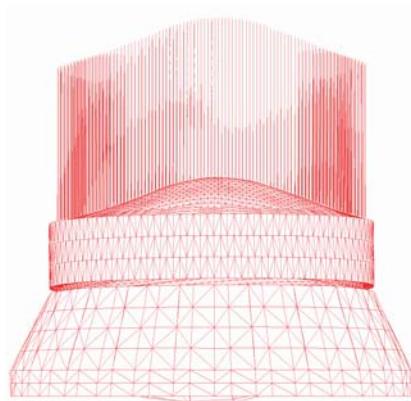
GP. In the subsequent operation to introduce the same in to the respective storage location in the grid plate, the gripper assembly along with the SA, is lowered. The raising / lowering operations of gripper assembly is executed carefully through double wire rope system with safety brakes, to rule out any possibility of a high impact of gripper assembly along with the SA on the grid plate. With the presence of safety brakes at very 200 mm distance, a maximum free fall of 200 mm is only possible, in case of failure of wire ropes. Fig.1 shows the schematic sketch of the gripper assembly and SA during a typical handling operation.

The impact scenario is defined as: 'the free fall of gripper assembly along with SA on the grid plate over the distance of 200 mm during the last stage of accidental drop due to the

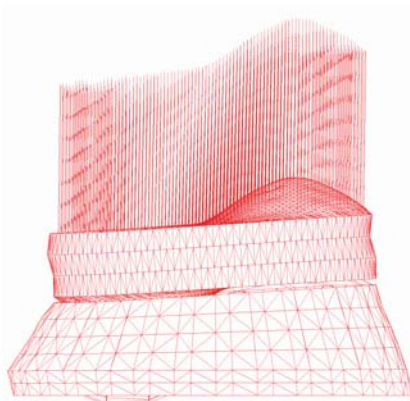
failure of wire rope'. The total mass of the gripper assembly (700 kg) and SA (250 kg) is 950 kg. Thus the kinetic energy that is transmitted to GP at the respective sleeve location is $950 \times g (10\text{m/s}^2) \times 0.2 = 1900 \text{ J}$. The maximum damage to the GP is expected when the impact occurs at the central sleeve location. Accordingly, an impact with the energy potential of 1900 J is postulated at the central location of grid plate and analysed for checking the structural integrity of grid plate.

Finite element modelling

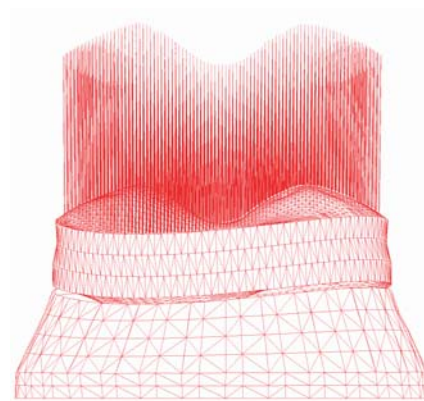
The core is supported on the GP and GP is supported on the Core Support Structure (CSS). The CSS is attached with the main vessel bottom at the triple point. Accordingly, the finite models are generated for core SAs, GP and CSS. SAs and sleeves in the GP are modeled with beam elements and plates



Symmetrical bending of top plate - 20 Hz



Asymmetrical bending of top plate - 26 Hz



Bending of top plate Higher mode- 34 Hz

Fig.3 A few typical vibration modes, relevant to impact analysis of GP

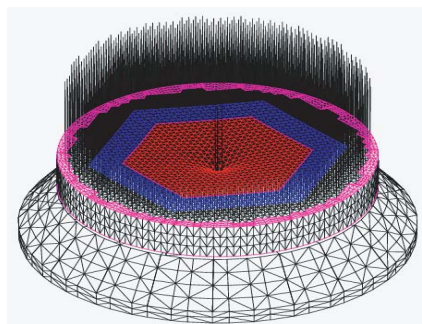


Fig.4 Peak deformations of grid plate

and stiffeners, top and bottom plates and intermediate shells of GP and CSS are modeled with plate / shell elements. The finite element mesh generated with CAST3M code, issued by CEA France is shown in Fig.2.

Free vibration analysis

Natural frequencies and mode shapes should be known to simulate the deformations correctly in the subsequent impact analysis, which are

determined by free vibration analysis. For this CAST3m, is used. A few important mode shapes are depicted in Fig.3. Since, upon impact, the nature of deformation is bending of top plate, the mode depicting the bowing of top plate that occurs at 20 Hz, is the critical mode as far as impact is concerned.

Impact analysis

With the understanding of natural vibration behaviour and energy balance, the duration of impact and subsequently, peak force are defined as a triangular pulse in a classical way as follows:

$$\begin{aligned} \text{Velocity at time of impact} \\ v_{\max} &= \sqrt{2 \cdot g \cdot h} \end{aligned}$$

$$= 2 \text{ m/s}$$

$$\text{Impulse at time of impact (mv)} = 1900 \text{ N-s}$$

$$\text{The duration of impulse (t)} = 0.025 \text{ s}$$

$$\text{Peak force (Fmax)} = 76 \text{ k N}$$

Dynamic analysis of grid plate along with core and core support structure was carried out using CAST3M code and peak deformations and stresses are extracted. Fig.4 shows the deformation patterns at a critical instant and peak value is found to be ~ 0.1 mm and the associated Von Mises stress is found to be 20 MPa, which is local in nature. These values are found to be insignificant from the structural integrity considerations.

II.5. Hardfacing of Bottom Plate of Grid Plate Assembly

Grid plate of PFBR is a massive structure consisting of a two plates (top and bottom of ~ 6.5 m in diameter and large number of sleeves in which foot of the sub assemblies rest. This support structure also acts as boundary between cold and hot sodium in the reactors. Both the grid plate assembly and the core support structure are made of 316LN stainless steel and immersed in flowing

sodium. Hence, there should not be any self welding between these components at their contact location. Hardfacing using Ni base hardfacing alloy (AWS Ni-Cr-B alloy) is proposed on two annular grooves machined on the bottom plate of the grid plate. These grooves are located towards the periphery of the grid plate and hence, diameters of these grooves are close to

that of the grid plate itself and total length (circumference) of single harfaced deposit was close to 21 m. The component is designed in such a way that area of contact between grid plate and the core support structure is confined to these hardfaced grooves in the bottom plate.

As the Ni base hardfacing alloys are highly prone to



Fig.1 Grid plate mounted on the furnace

cracking, hardfacing such a massive component was not very easy. The process chosen for deposition is plasma transferred arc welding (PTAW) which uses hardfacing alloy powder as the consumable. During technology development of the grid plate (using plates of the similar dimensions as that of the actual PFBR grid plate), extensive cracking of the deposit was observed when deposition was carried out as per the procedure finalized initially based on trials carried out on 80 mm thick 1000 mm diameter plate. Subsequently a detailed review of the design of the groove, welding process, procedure, heat treatment etc. was taken up in which designers, materials engineers, hardfacing agency and manufacturer of the grid plate participated. The groove width was reduced from 45 to 20 mm and the groove angle increased from 30 to 60°. This enabled to carry out hardfacing in single layer and single pass of deposition. Preheat

temperature for deposition increased from 773 to 923 K and furnace for preheating and stress relieving heat treatment was modified to ensure that the temperature variation across the component during heating or cooling is reduced considerably. Insulation was improved to reduce the heat losses. It was also decided to carry out hardfacing continuously using four PTAW machines position on a circular track which is placed concentric to the bottom plate. Machine controls were suitably modified to have smooth deposition between starting and ending location of the deposits, which are found to be more prone to cracking than the other location so the deposit. New trials were taken up during technology development for hardfacing of the grid plate and cracking of the deposits reduced considerably in these attempts. The process was further refined and it was demonstrated on the grid plate for technology development that crack free deposits that meet all the design requirement could be made using this improved procedure.

After successfully demonstrating the procedure on the technology development grid plate, hardfacing of PFBR grid plate was taken up.

Because of prior experience, it was possible to achieve much better control over temperature during heating and the heat treatment stages. Deposition was carried out simultaneously using four PTAW machines mounted on the track at 90° apart. After bottom plate reached preheat temperature the entire operation of hardfacing two grooves of ~6.5 m dia took only a few hours. Fig. 1 shows the grid plate mounted on the furnace with hardfacing operation in progress. Fig. 2 shows a close up of the deposit and the torch. Neither cracks, nor debonding nor surface porosities were observed on the deposits. There was no need to carry out any repair though a procedure for repair had been finalized. The deposits made on the PFBR grid plate are certainly better than deposits made during technology development. This was possible only because of the dedicated efforts of designer, engineers, hardfacing agency and the manufacturer of the components.



Fig.2 Close-up a PTA torch and hardfaced deposit as hardfacing is in progress

II.6. Acceptable End Plug Weld Repairs for PFBR Fuel Pins

In PFBR, heat is generated mainly in 181 fuel subassemblies. Each fuel subassembly has 217 fuel pins which contain MOX fuel. The manufacturing of fuel pins is the most challenging activity, in particular, the welding of end plug after inserting the fuel pellets and other structural elements within the clad. Some repair welds are unavoidable. Strategy of rejection of pins with repaired welds should be adopted carefully to maximize recovery during manufacture. The fuel pin is made of 20% cold worked D9 material (15 % Cr-15 % Ni - Ti alloy) and end plug is made of SS 316 LN. A schematic of a typical weld configuration is shown in Fig.1 along with dimensions. The temperature in the region of the end plug is decided by the core outlet temperature (833 K) under steady state operation and the maximum fission gas pressure accumulated at the end of 100 GWd/t burnup can be 6 MPa. Under this environment, the thermal creep damage is the main governing failure mode for this weld. Since, there is no established analysis tools available to qualify the repair welds,

experimental route is followed to recommend the acceptable number of weld repairs for the end plug.

Experimental methodology

Fuel pin end plug welds for PFBR are carried out at Advance Fuel Fabrication Facility (AFFF), Tarapur. A few numbers of welds with no repair, 3 repairs and 4 repairs were selected from the production samples for the test purpose. A dedicated test setup has been made at Structural Mechanics Laboratory in which a set of 6 tubes can be tested simultaneously. The fuel pins with end plug welds were tested at 973 K to accelerate the damage under an internal pressure of 20 MPa to account for possible higher burnup targets as well as uncertainties in the fission gas release phenomenon. The test setup is shown in Fig.2. The application of correct pressure is ensured, by measuring the hoop and longitudinal strains in the vicinity of end plug welds for a few typical pins. Fig.3 shows the measured strain for various pressures. The pins are subjected to simulated pressure and temperature conditions in

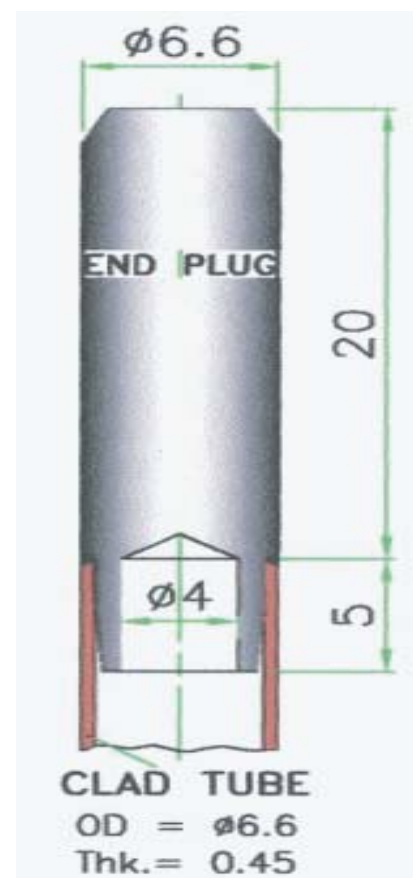


Fig.1 Geometrical details of end plug weld



Fig.2 Test setup for simulating creep damage in FBR fuel pins

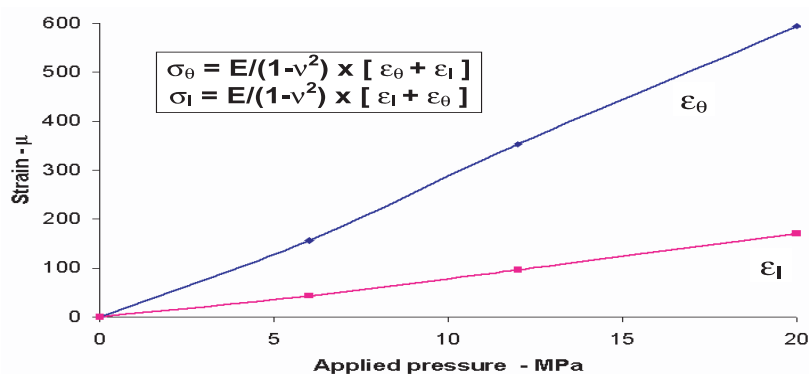


Fig.3 Measured strains vs fission gas pressure



Fig.4 Bulging of pins at the time of development of cracks

the furnace, and the leak is monitored continuously. A leak in the pin is the indication of failure, that is detected by a fall in the steady state pressure in the chamber. Fig.4 depicts a set of six typical leaked pins showing bulging at the time of crack detection. Totally 12 pins were tested: 2 pins without repair, 5 pins with 3 repairs and 5 pins with 4 repair. The observed cracks were investigated thoroughly by image processing analysis. Fig.5 shows that the crack is longitudinal in nature, than can be caused by the hoop stress and is observed just below the weld joint.

Basis of accelerated tests

The life of fuel pin in the reactor is 2 y. The permissible cumulative creep damage under maximum fission gas pressure (12 MPa) at a temperature of 833 K is 0.25. Under actual environment with the presence of fuel and fission gas, it is reported that creep damage is accelerated, which is accounted by a factor called 'fuel adjacency factor'. The pessimistic value reported for this effect is 10. This implies that allowable creep damage without considering the fuel adjacency effect (W) should be limited to 0.025. Minimum rupture life required for the

weld is derived from the definition of creep damage by time fraction rule: $W = t / t_r$; where t is actual duration of operation (2 y) and t_r is the minimum time to rupture under the imposed stress and temperature. Accordingly, t_r , the minimum rupture life to be ensured and demonstrated by tests under similar conditions is $2 / 0.025$, equal to 80 y.

To accelerate the creep damage, a higher temperature of 973 K is chosen as an optimum parameter to complete the tests within a reasonable shorter time, without affecting the creep damage mechanism to be simulated. Under this higher temperature, the minimum rupture time to be ensured is calculated by the application of Larson-Miller Parameter (LMP), defined as: $T \times (20 + \log t_r)$, which is considered to be constant under same stress. For the required life of pins 80 y which gives the value of $t_r = 80 \times 365 \times 24 = 700800$ h and $T = 833$, the LMP is $833 \times (20 + \log 700800) = 21.529$. For the accelerated temperature of 973 K, the minimum rupture life should be $21.529 / (973 \times (20 + \log t_r))$, which is equal to 134 h (~5.6 d). The minimum rupture time to be ensured is 5.6 d. With this target, tests are conducted.

Table 1 : Measured rupture lives of end plug welds with and without weld repairs (days)

Case	Specimen-1	Specimen-2	Specimen-3	Specimen-4	Specimen-5
No repair	42	41.5	-	-	-
3 repairs	18.5	20	21	22	25.5
4 repairs	9.5	11	10.5	12	13

Test results

The rupture lives measured for the various test cases are given in Table-1 and same have been depicted in Fig.6, which indicated that, the minimum rupture time required (5.6 d) are ensured even for the welds with 4 repairs.

In view of a limited number of tests that have been completed, it is recommended to restrict the weld repair to 2 at this stage of manufacturing. However, tests are being continued to get more confidence in accepting 3 or 4 repair welds.

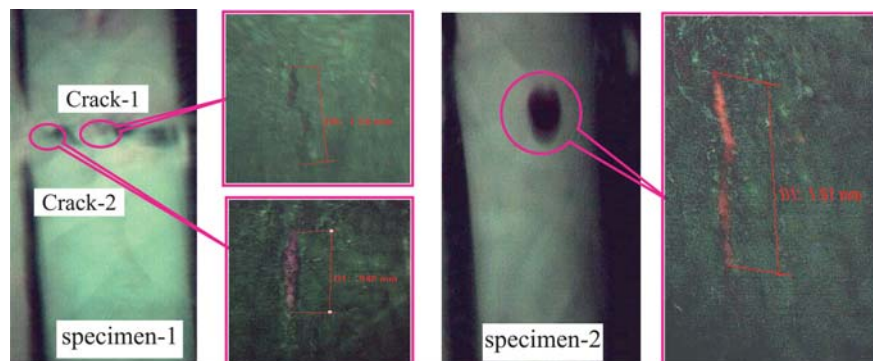


Fig.5 Longitudinal cracks seen in the fuel pins at the welding zone

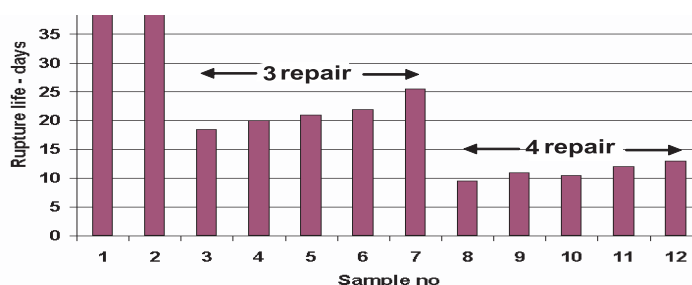


Fig.6 Measured rupture lives of pins tested

II.7. Qualification of Back up Seals

To seal the annular gap between rotating and stationary parts of the rotatable plug support arrangement, elastomeric seals are provided. This comprises of two numbers of inflatable seals and one back-up seal. During reactor operation, the annular gap is sealed by one of the inflatable seals along with a back-up seal. Before starting plug rotation, the second inflatable seal is inflated and the back-up seal is disengaged and kept in raised condition.

The back-up seal is a static seal with sealing achieved by the compression of the seal. A trapezoidal shape seal has been selected and to reduce the compression load required to seal the surfaces, special geometrical features are included. The seal is fixed to a seal holder and to apply required compression load uniformly over the seal surface, load applying arrangement is provided. The seal bridges two annular surfaces at the top, one rotating and the other stationary.

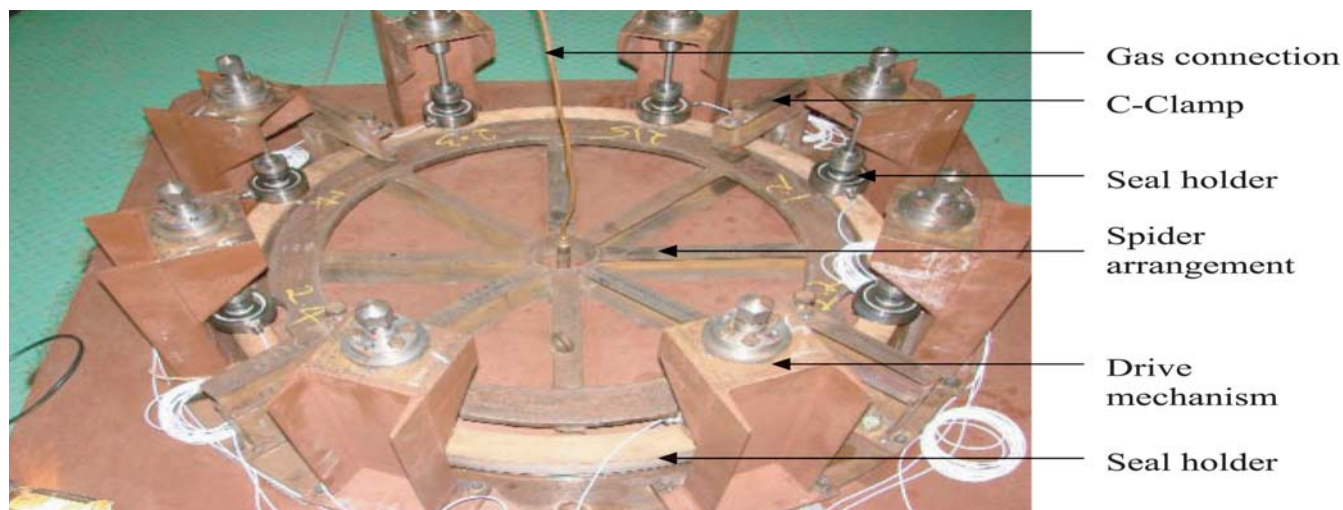


Fig.1 Details of backup seal test facility

As the diameter of the sealing surfaces is very large, mismatch in the elevation of the two sealing surfaces is expected and also there can be wide variation in the flatness of the two surfaces. This mismatch between the elevation of

surfaces has been considered in the design. To validate the design, it was decided to test a sample prototype seal.

Fig.1 gives the details of the seal test rig and Fig.2 gives the details of the seal geometry. The rig consists of two test plates 1 & 2, machined with outer and inner sealing surfaces, respectively. Eight number of support brackets are bolted in a uniform spacing along the circumference of the sealing surfaces to mount the clamping mechanisms. It consists of a trapezoidal threaded loading shaft, thrust bearing to reduce the torque while applying required load, and compression type load cell to measure the load applied, Belleville washers to avoid sudden relaxation of the load under small displacement of the mechanism due to vibrations. Fig.3 gives photographic

illustration of the seal holder with seal. Test sample of one meter diameter with 1:1 cross section as per reactor seal has been chosen for the testing. Considering symmetric loading and a clamping pitch nearer to actual condition, eight numbers of clamping points are selected.

The effectiveness of sealing (allowed leakrate ≤ 0.001 cc/s) per meter length of seal was checked for clamping loads of 500N, 1000N and 1400N per each clamping point. Leak rate measurements done for an inter seal pressure of 250mbar with level differences upto 2 mm showed the leak-tightness of the seal to be less than 10^{-3} stdcc/s. Hence the performance of the seal has been demonstrated successfully.

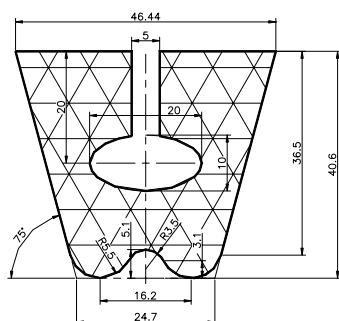


Fig.2 Details of the seal geometry



Fig.3 Seal holder with seal

Chapter -3

R&D FOR FBRs

III.A. Modeling and Simulation Experiments

III.A.1. Effects of Interconnection of Reactor Vault with Nuclear Island Connected Buildings on Seismic Behaviour of an FBR

In a pool type sodium cooled fast breeder reactor, the entire radioactive primary circuit is housed in a single vessel called main vessel, which is the most critical component of the reactor assembly system. The main vessel transmits about 2500 t to the top shield, contributed by core mass, self weights of main vessel and reactor internals and 1150 t of primary sodium. The weight of top shield along with the components supported by it is about 1200 t. With all these, the reactor assembly weighing about 3700 t is supported at the top. The dynamic forces that are developed by a seismic event cause a great concern to structural integrity of thin shell structures, core subassemblies, etc.

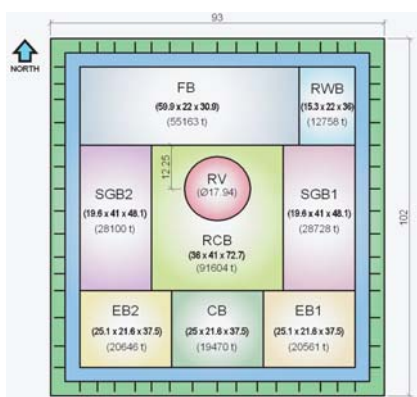


Fig.1 PFBR plant layout of NICB

The magnitudes of displacements and stresses developed in the structural systems depend strongly on the seismic support excitations, more precisely the floor response spectra at the support points (FRS). The dynamic characteristics of primary systems, mainly civil structures, decide the FRS. Adopting the concept of connected buildings is one of the means of mitigating seismic amplifications. Accordingly, the main buildings of nuclear island viz. reactor containment building (RCB), steam generator buildings, fuel

building, control building, electrical buildings and radwaste building are connected carefully giving due considerations to safety, economy, operation and maintenance aspects. RCB houses the reactor vault which supports the reactor assembly and this apart, it contains many cells at various levels. In the connected building layout concept, the connection of reactor vault with the adjacent buildings has to be seen critically. By way of connecting the reactor vault with the adjacent cells within RCB, the reactor vault along with the reactor assembly gets connected automatically to the entire nuclear island connected buildings (NICB). NICB layout is shown in Fig.1. With this connection, the adjacent cells get support from reactor vault without calling for additional structures which helps in achieving further economy. However, the adjacent

buildings can influence the seismic responses of reactor assembly components significantly.

In this article, the seismic responses of reactor assembly components are quantified under the two assumptions: (1) the reactor vault is connected to the adjacent buildings of NICB through floor slabs at three levels as in PFBR (Fig.2a) and (2) the reactor vault along with reactor assembly is an isolated structural system constructed from base raft without any connection with the adjacent buildings within NICB (Fig.2b). The analysis was carried out using CAST3M, a computer code issued by CEA France.

Effects on connected and isolated reactor vault

The floor response spectra (FRS) generated at the reactor assembly support with and without connection are

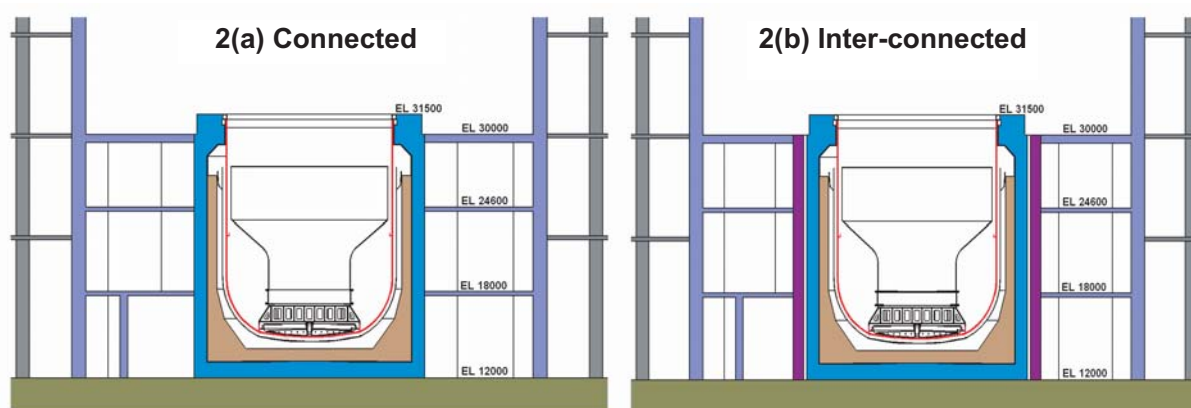


Fig.2 Reactor assembly mounted on connected and inter-connected reactor vault

depicted in Fig.3. The FRS for isolated reactor vault shows only two dominant peaks representing the swaying mode of main vessel (5.1 Hz) and reactor vault (14.2 Hz). Once the reactor vault is connected with the NICB, reactor vault is mastered by various buildings in the NICB, due to which the vault has many coupled vibration modes. This imposes many constraints to ensure that the natural frequencies of reactor internal are not lying in the resonance ranges. The significant effect is the influence of fundamental frequency of about 3 Hz which corresponds to the swaying mode of the buildings as seen in Fig.3. In view of the natural frequencies of core & control subassemblies and absorber rod drive mechanisms lying around 3 Hz, the dynamic

Table 1 : Displacements of absorber rods and control plug

Sl. No	Parameters	Isolated vault (mm)			Connected vault (mm)		
		X	Y	Z	X	Y	Z
1	Displacement of core top	30.7	40.1	6.4	48.4	48.0	7.6
2	Displacement - control plug bottom	9.1	9.1	3.9	10.6	8.8	4.6

Table 2 : Primary stress intensities

Sl.no	Component	Isolated reactor vault						Connected reactor vault					
		P _m (Mpa)			P _m +P _b (Mpa)			P _m (Mpa)			P _m +P _b (Mpa)		
		X	Y	Z	X	Y	Z	X	Y	Z	X	Y	Z
1	Main vessel	130	130	27	206	206	122	140	140	31	222	222	144
2	Inner vessel	103	103	14	123	123	87	126	126	18	156	157	103

Table 3 : Strain energy generated in the vessels

Sl.no	Component	Isolated reactor vault						Connected reactor vault					
		P _m (Mpa)			P _m +P _b (Mpa)			P _m (Mpa)			P _m +P _b (Mpa)		
		X	Y	Z	X	Y	Z	X	Y	Z	X	Y	Z
1	Main vessel	130	130	27	206	206	122	140	140	31	222	222	144
2	Inner vessel	103	103	14	123	123	87	126	126	18	156	157	103

amplifications become significant and critical from reactor shutdown point of view. Further, while the FRS are nearly the same in the X and Y excitations in the case of isolated reactor vault, they are quite different in the X and Y directions in the case of connected vault. This increases

number of analysis / tests required for the seismic qualification studies.

Apart from FRS, other important effects are presented in Table 1, Table 2 and Table-3, from which it is clear that there are increases of: (1) radial and axial displacements

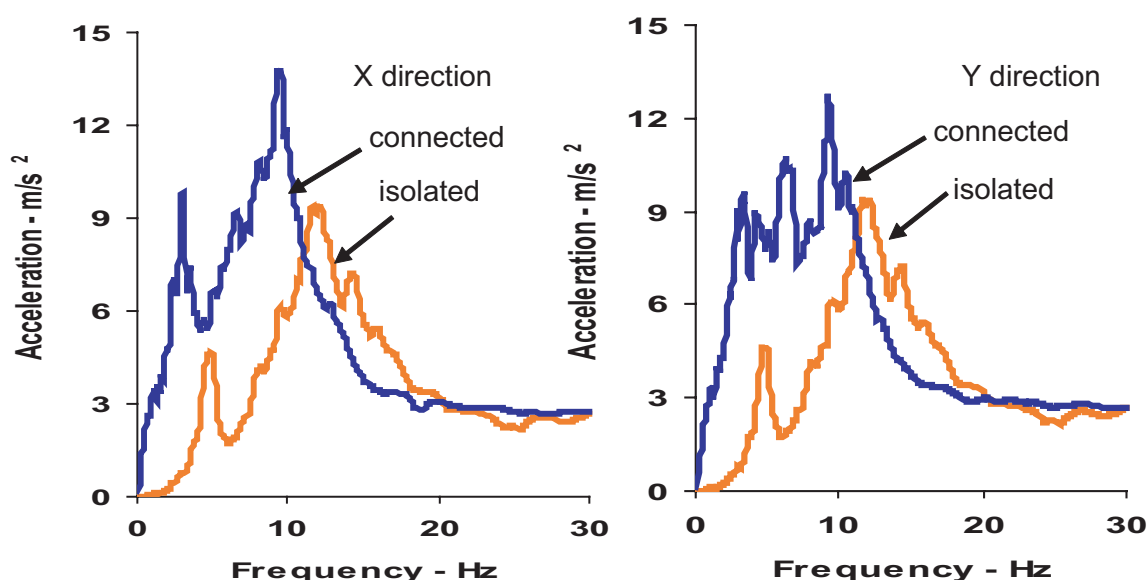


Fig.3 Floor response spectra at reactor assembly support for safe shutdown earthquake

of core top and absorber rods and vertical accelerations of core subassemblies which are of concern to reactor safety (Table 1), (2) primary membrane stress intensities for the main vessel and inner vessel (Table 2) and (3) generation of high strain energies at the critical portions which can enhance the buckling risks of main

vessel and inner vessel (Table 3).

In view of increased displacements, stresses and strain energies at critical locations when the reactor vault is connected with the remaining structures of NICB, it is preferable to isolate the reactor vault, by directly constructing it from the base

raft without inter-connecting it with the adjacent buildings of NICB, from the seismic loading considerations. This also provides some flexibility to design and analyse the reactor assembly components independently without linking to the finalisation of design of rest of the civil structures. This can be adopted for future FBRs.

III.A.2. Modal Analysis of PFBR Fuel Subassembly

PFBR Fuel subassembly (FSA) consists of 217 fuel pins held vertically in the form of a bundle within a hexagonal wrapper tube. Flow induced vibrations (FIV) in FSA is a potential cause for fatigue, wear and vibration induced fretting in the subassembly parts which can lead to reactivity noise and premature failure of fuel pins and other SA parts. The coolant flow in SA is in highly turbulent regime and it can cause flow-induced vibration of fuel pins and FSA as a whole. The overall subassembly vibration will be in its cantilever mode. The SA vibration will also depends upon the sodium exit velocity, restraints at the supports in the grid plate and the buttons and the interaction of the discharge coolant jets with control plug

parts positioned above the subassembly as well as with surrounding subassembly jets.

As part of the FIV experimental program on FSA, modal measurements were carried out on SA in water to estimate the modal parameters. Theoretical modelling of FSA was also done using ANSYS FEM software to extract the natural frequencies and mode

shapes. Beam element was assigned to discretize the model and the full SA is divided in into six sections. In the analytical modelling, two cases were taken as support boundary conditions for FSA.

Case 1. Hinged support at the location where FSA rests on the sleeve top and simply supported at the discriminator location.

Table 1 : Modal frequencies in water

Mode	Case-1 (Hz)	Case-2 (Hz)
1	3.7	3.9
2	22.2	24.0
3	64.6	66.2
4	126.0	128.1
5	147.9	149.0

Case 2. Hinged support at the location where FSA rests on the sleeve top and fixed support at the discriminator location.

Natural frequencies in water obtained from analytical prediction are given in Table 1. It is observed that almost similar values for natural frequencies are obtained in both SA support conditions.

The SA was erected in the sleeve fixed in the Grid Box assembly, which in turn was supported on a vibration isolated test structure. Experimental modal analysis

was carried out by exciting the SA laterally using a 50N force electro-dynamic exciter suspended from a top support structure. Fig.1 shows the experimental setup.

Sine-Random signal generator is used to give input to the power amplifier through which the exciter is actuated. The response of the SA is measured using accelerometers installed at various locations along the length of the subassembly. Output of the force transducer and response accelerometers are recorded in FFT analyzer to estimate Frequency Response Function (FRF) up to 100 Hz. Modal frequencies above 100 Hz do not have much influence on the overall SA response due to FIV mechanisms. Hence modal measurement and analysis for the present study was carried out in the frequency range upto 100 Hz. The FRF at various

measurement locations are transferred to modal analysis software to find out the modal parameters using polynomial curve fit method. Experiment was repeated by changing the excitation point. Fig. 2 shows a typical FRF measured in water and the first three natural frequencies are 3.5, 21.3 and 56.5 Hz.

Hence it is confirmed that the experimental values are matching with analytical prediction. To confirm the natural frequencies obtained from the random test, SA was excited with sinusoidal excitation at 3.5 Hz. It was observed that subassembly was vibrating with more than 10 mm displacement at the top end. Results from this investigation will be employed for interpreting vibration signatures obtained from FIV studies on subassemblies.

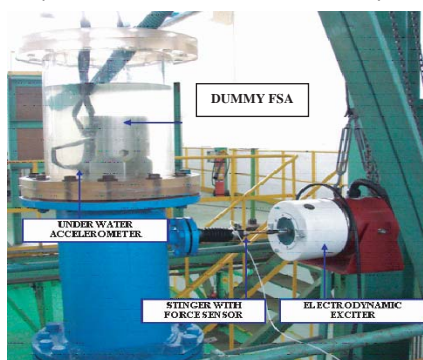


Fig.1 Experimental setup for vibration measurement in water

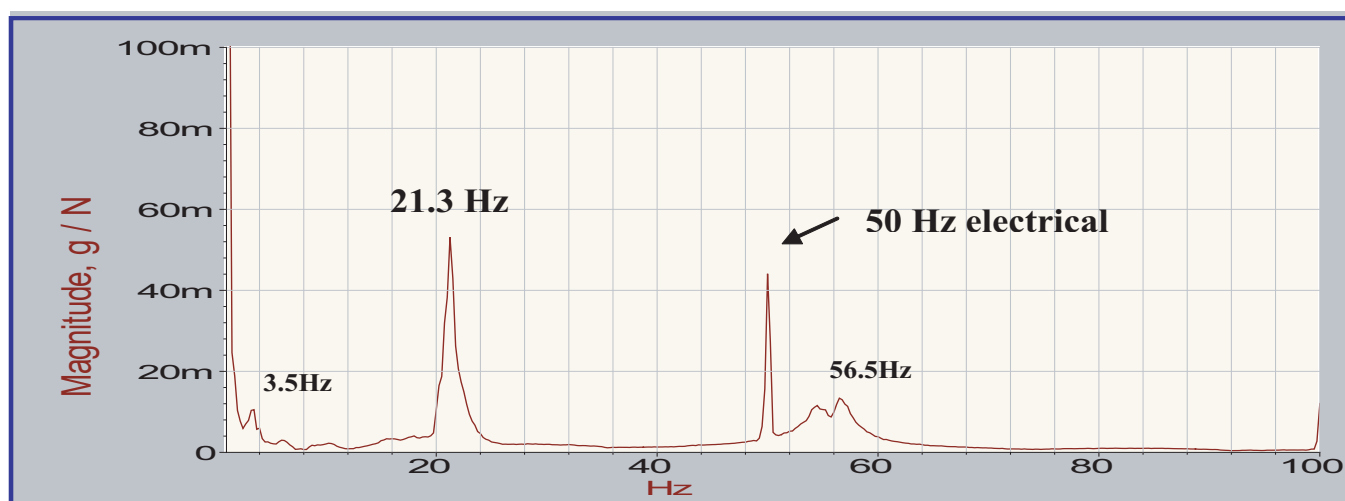


Fig.2 Frequency response function [Accelerometer 2730 mm from top of SA]

III.A.3. Investigation of Devices for Gas Entrainment Mitigation in Hot Sodium Pool

In Fast Breeder Reactor pools, the sodium free surfaces are blanketed by inert argon cover gas. The free surfaces of sodium pools are not static and are associated with significant vertical and horizontal velocities. These velocities lead to free level fluctuations and formation of vortices, which are potential sources for gas entrainment in the sodium pools. Various mechanisms of gas entrainment, transportation of gas to grid plate through heat exchangers (IHX) and pumps, agglomeration of gas inside the grid plate and its final passage through the core (Fig. 1) need to be understood well. This is an important safety problem as passage of argon gas through core leads to positive reactivity. To understand the various mechanisms responsible for gas entrainment, experiments had been carried out at IIT-Madras. This problem has been studied through multi-dimensional Computational Fluid Dynamic (CFD) analysis. The CFD results have been validated against experiments on 1/4th scale water model. Design solutions to mitigate gas entrainment have been proposed.

The core flow enters the hot pool as a horizontal jet (also called core jet) in between the control plug skirt and subassembly top. It induces a large anti-clockwise circulation zone, which occupies almost the entire hot pool (Fig. 2a). The maximum horizontal velocity with which the jet enters the hot pool is 3 m/s and as a result of this, the maximum horizontal velocity on the free surface is seen to be 1.0 m/s (Fig. 2b). The reason for this high free surface velocity is the presence of skirt. By keeping the free surface velocity low, sodium free level

can be made quiescent and possibility of gas entrainment can be avoided. To avoid gas entrainment, the free surface velocity of sodium has to be less than 0.5 m/s. Reduction of free surface velocity is possible by altering the hot pool flow pattern such that the influence of core jet is minimized near the free surface.

Detailed 3-D thermal hydraulic studies were carried out to see the efficacy of using baffles fitted to inner vessel upper shell, redan and control plug in reducing free level velocity. The effect of

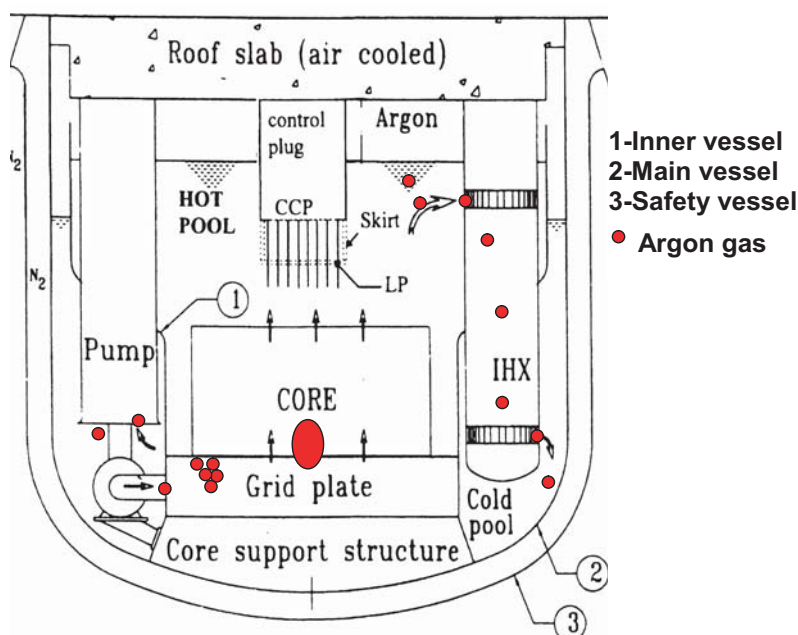


Fig.1 Transport path of entrained argon gas in FBR

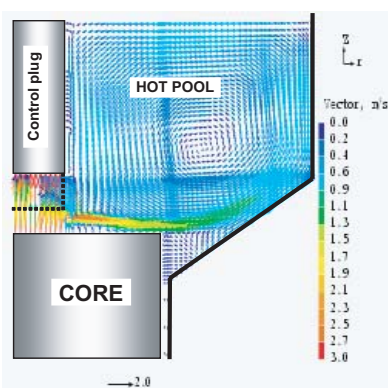


Fig.2a Flow distribution in a vertical plane (reference design)

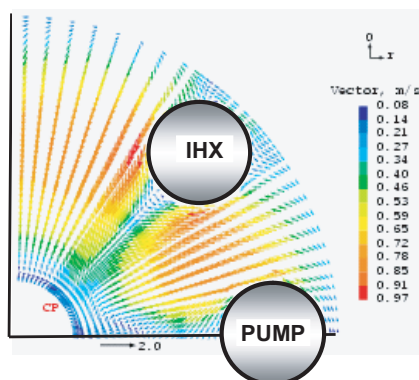


Fig.2b Velocity distribution at free surface of sodium (reference design)

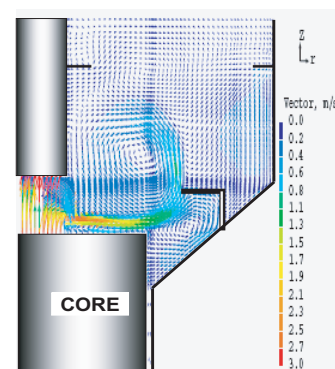


Fig.3 Flow distribution with 3 baffles (option-a)

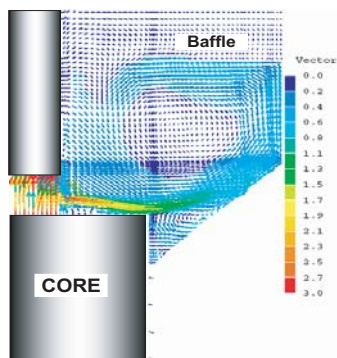


Fig.4 Flow distribution with 2 m width baffle (option-b)

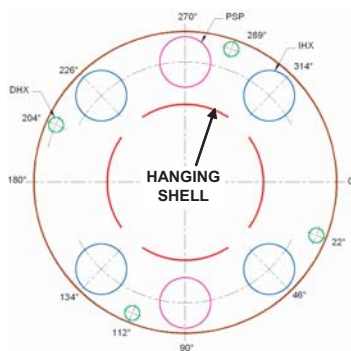


Fig.5a Details of hanging shell with cut-outs (option-c)

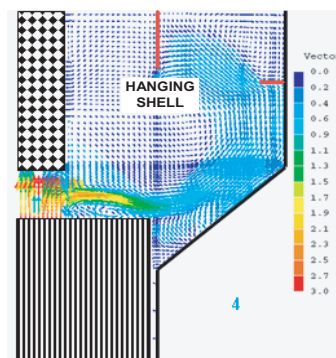


Fig.5b Flow distribution with hanging shell and baffle (option-c)

modifications in the control plug skirt, in the form of providing circumferential slots either in the top or in the middle of the skirt was also studied. These studies were carried out with the objective of finding the lowest possible free level velocity.

The following are the conclusions of the study:

(a) Inverted L baffle on redan along with horizontal baffles on control plug and upper shell of inner vessel, was seen to be

very effective in mitigating free surface velocity to 0.18 m/s (Fig. 3).

(b) By using a single annular plate of 2 m width above IHX inlet, the velocities on the free surface can be kept within 0.25 m/s (Fig. 4).

These devices are judged to be un-practical considering the advanced stage of manufacture of inner vessel and control plug.

(c) By having a horizontal baffle of 0.5 m width attached to the upper shell of inner vessel and lowering the roof slab inner shell upto IHX inlet, the free surface velocity could be reduced to 0.40 m/s (Fig. 5a and 5b).

Considering the ease of construction, option (c) has been selected.

III.A.4. Flow Induced Vibration Studies on FBTR Special Subassembly

An experiment is planned in FBTR to measure the fast flux using special foils in the grid plate area under power operation to assess its integrity. The foils are fixed on carrier capsules and are loaded in reactor core (4th ring) using a special subassembly (SA). Flow Induced Vibration (FIV) of this special subassembly has been studied in water, before loading it into the reactor core.

The SA has 15.5 mm hole throughout the length. The



Fig.1 Strain gauges

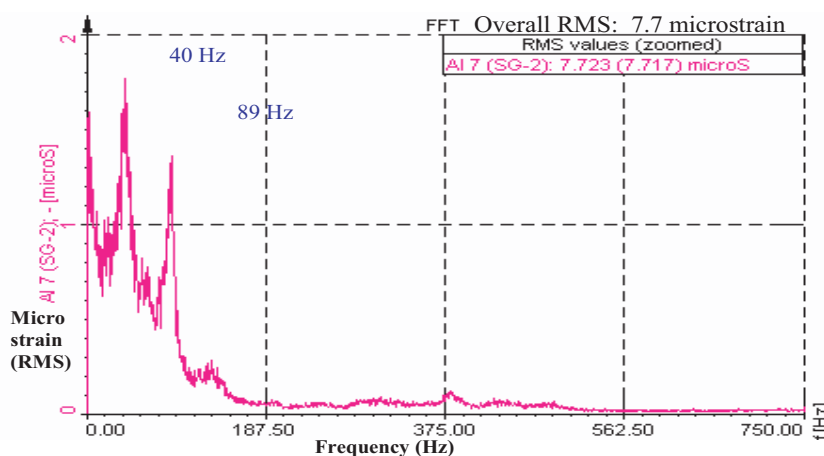


Fig.2 Vibration spectra of carrier capsule at nominal flow

capsule carrier is made of 12 mm dia SS rod and its over all length is 1661.5 mm. The test section was erected on a vibration isolated foundation in Hall-II. The subassembly was held vertically in the grid box and the support conditions and flow path to the subassembly was simulated as in the reactor.

Two foil type strain gages were installed at 900 on the carrier capsule. Under- water accelerometers and strain gauges (~100 mm from grid plate support) were also installed on hexcan (Fig.1). The water flow through the SA was arrived at based on Burgreen correlation. The loop flow rate was measured using volume collection method.

The vibration spectra were

recorded using Dewetron data acquisition system. At nominal flow (4.83 m³/h), measured vibration level of carrier capsule is ~7.7 micro-strain (which corresponds to a stress level of 1.3 MPa). Fig.2 shows the vibration spectra of carrier capsule for nominal flow. The measured vibration level on subassembly hexcan is ~1.84 micro-strain (which corresponds to a stress level of 0.28 MPa).

Vibration stress levels measured on both carrier capsule and on the hexcan are well below the permissible alternating stress limit of 16.1 MPa at operating temperature. Hence the special subassembly was found to be safe against FIV phenomenon.

III.A.5. Investigation of Thermal Striping at the Bottom of the Control Plug

When non-isothermal fluid streams mix adjacent to a structure, the surface of the structure experiences temperature fluctuations and can develop cracks due to thermal fatigue. This phenomenon is called thermal striping. In fast breeder reactors, the coolant coming out from the fuel subassemblies is hotter than the coolant coming out of the blanket and absorber rod subassemblies. The improper mixing of the jets issuing out from these subassemblies results in temperature fluctuations in the fluid. This may lead to the structural damage of control plug components like shroud tubes, lattice plate, skirt etc.

An experiment has been carried out in SAMRAT model to understand the mixing behaviour and to determine the extent of thermal striping in the above core area of PFBR. SAMRAT is a 1/4 scale model of PFBR primary circuit. De-mineralized water is used as simulant in this model.

It has been established by the earlier researchers that air or water can be used to simulate

thermal striping phenomenon in sodium if Reynolds (Re) number and Peclet (Pe) number are sufficiently large ($Re > 20,000$ and $Pe > 600$) both in prototype and model. The fluid thermal fluctuations as measured using the simulant fluid, can be transposed to the prototype condition if temperature is measured outside the thermal boundary layer. The attenuation of temperature fluctuations within the boundary layer can be determined accurately using sodium experiments.

In the present work mixing in the fuel-blanket interface region was studied. Hot water at 343 K was sent through the fuel zone and cold water at 308 K was sent through blanket zone. To measure the fluid thermal fluctuations, fast response thermocouples (time constant better than 15 ms) were used.

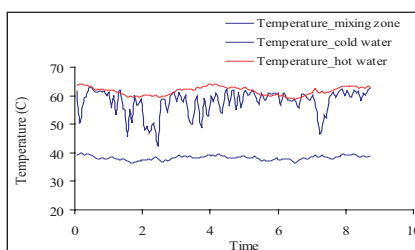


Fig.1 Time series plot of temperature at mixing region

Fig.1 shows a typical time series plot of the temperature as measured in the mixing zone. From the statistical analysis of data the mean temperature as seen by each thermocouple was estimated. These temperature data are presented in a

$$T_{mean}^* = \left(\frac{T - T_c}{T_h - T_c} \right)_{mean}$$

and

$$\Delta T_{rms}^* = \frac{\Delta T_{rms}}{(T_h - T_c)_{mean}}$$

normalized form to transpose the result into reactor case by substituting the prototype parameters. The normalization is done in the following manner.

where,

T = Mean temperature of the fluid as measured by the thermocouple mounted in CP

T_h = Mean temperature of the hot inlet fluid (Thermocouple mounted at the SA exit)

T_c = Mean temperature of the cold inlet fluid (Thermocouple mounted at the SA exit)

ΔT_{rms} = Root mean square of temperature fluctuations.

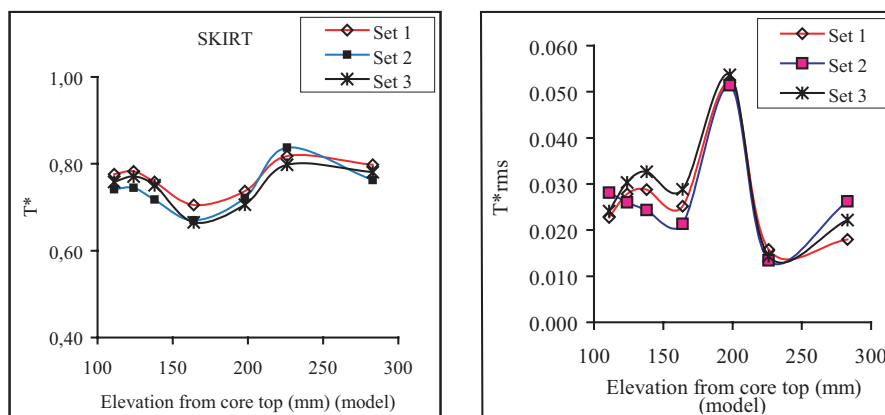


Fig.2 Characteristics of thermal fluctuation along the skirt height

The normalized mean temperature (T^*_{mean}) and the fluctuations ΔT^*_{rms} are plotted against the elevation of the skirt above core top for various experimental conditions. The result is presented Fig.2. The ratio of Re between fuel and blanket zone was kept same as that of prototype. Different

experimental conditions represent different Re of the fuel zone. It can be seen from the above figure that normalized mean temperature is initially decreasing along the elevation of the skirt due to the mixing by blanket flow but again it sees the hot water temperature at higher elevation. This is

because of the fact that the blanket flow is covered by the fuel zone flow due to the flowering and bending of the jets. The maximum non-dimensional temperature fluctuation $(\Delta T^*_{rms})_{max}$ as estimated from the experimental measurement is 0.054. This value is useful to estimate the maximum fluid temperature fluctuation in the vicinity of the skirt at prototype condition. The maximum temperature fluctuation is estimated for the above mentioned component at prototype condition is ± 16.2 K (with 95% confidence level) which is well below the acceptable thermal striping limit (± 30 K in fluid).

III.A.6. Investigations of Flow Reversal in the U-Tubes of Decay Heat Exchanger

Unlike fossil fuel power plants, a nuclear reactor generates heat even after it is shut down. This decay heat is to be removed successfully to keep system temperatures within acceptable limits. To accomplish this task, natural convection driven Safety Grade Decay Heat Removal System (SGDHRS) has been provided, which has redundant and independent circuit as shown in Fig. 1. Each circuit of SGDHR

consists of a sodium to sodium heat exchanger (DHX) and a sodium to air heat exchanger (AHX) linked by an intermediate sodium loop.

One design of DHX, has 'U' tubes with two-passes. There are 90 tubes which are arranged to have 5 inner rows and 2 outer rows and are supported by anti-vibration plates along the length. Intermediate sodium enters the

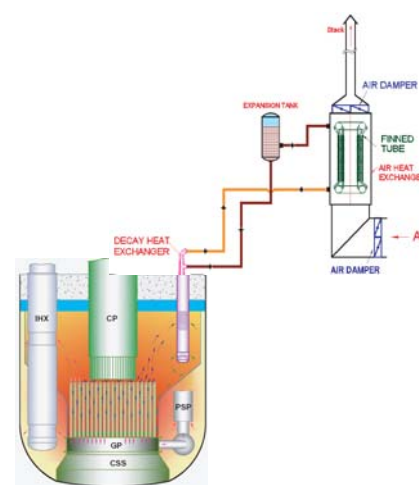


Fig.1 Safety grade decay heat removal circuit

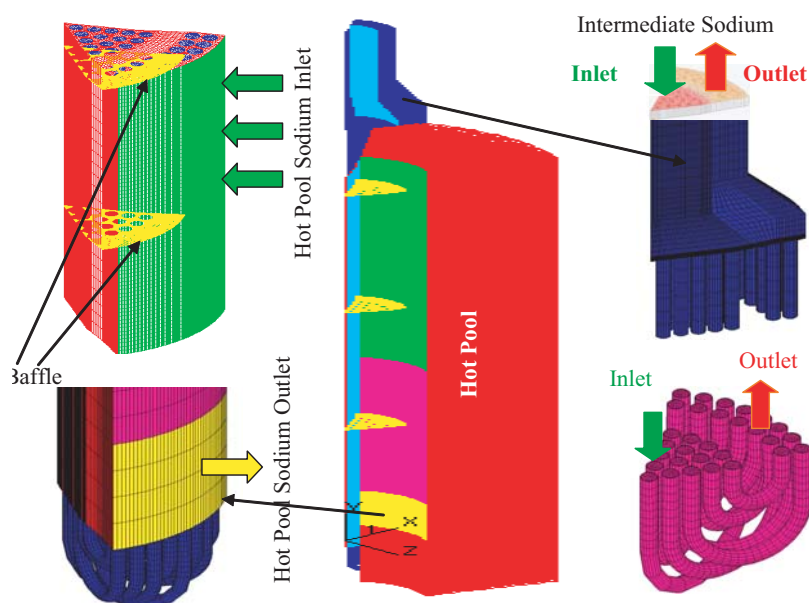


Fig.2 Computational model

inner rows of tubes from the top, picks up heat from the primary sodium and leaves from the outer rows at the top. Primary sodium in the hot pool enters the DHX in radial direction through a perforated outer shell, exchanges heat with the intermediate sodium, gets cooled and leaves back to the pool through the bottom window. To enable connectivity between the 5 inner rows and 2 outer rows through U bends, the lengths of U-tubes are made unequal. Also, the tubes see varying primary sodium temperature. Due to these reasons, there is a risk of flow reversal in some tubes. The flow reversal adversely affects the heat removal capacity of the SGDHRS and hence, it is essential to investigate the possibility of flow reversal in the tubes, which is the objective of

the present study.

In the present investigations, a 3-D 60° sector model of DHX comprising of 15 tubes and hot pool has been considered (Fig. 2). The intermediate sodium flow rate (32 kg/s) and its inlet temperature (539 K) to DHX have been estimated from a coupled 1-D model of the entire circuit. The resistances offered by fine scale structures viz. the porous shell, anti-vibration plates etc. are accounted by additional sources added to the momentum equations. High Reynolds number $k-\epsilon$ turbulence model has been used for modeling turbulence. About 4 lakhs structured hexahedral mesh have been used for the computational fluid dynamic (CFD) simulation. The flow and temperature

distributions of intermediate sodium in the tubes and primary sodium on the shell side have been solved as a conjugate problem, using the CFD code STAR-CD.

The temperature of primary and intermediate sodium in the DHX at various elevations is depicted in Fig. 3. The anti-vibration plates cover the inner leg of U-tubes and hence it divert the primary sodium from the inner leg to the outer leg, thereby increasing the heat transfer in the outer leg. The intermediate sodium temperature distribution along the length of the tube centerline for all the 15 tubes is shown in the Fig. 4. The mean temperature of the intermediate sodium at the outlet is 723 K. In the co-current direction (i.e., inner leg), the heat absorbed is the least by the inner-most row (i.e. Tube-1) and it increases as one moves outwards. It is the maximum in Row-5 (Tubes 11-15). At the bottom end, the maximum temperature difference is 71 K. This large difference in temperature is compensated in the counter-current direction (outer leg), leading to a marginal temperature difference of 17 K at intermediate sodium outlet. This is due to the favorable (larger) driving temperature gradient between the

intermediate and primary sodium for the outer row. Fig. 5 shows the mass flow rate of intermediate sodium from inlet

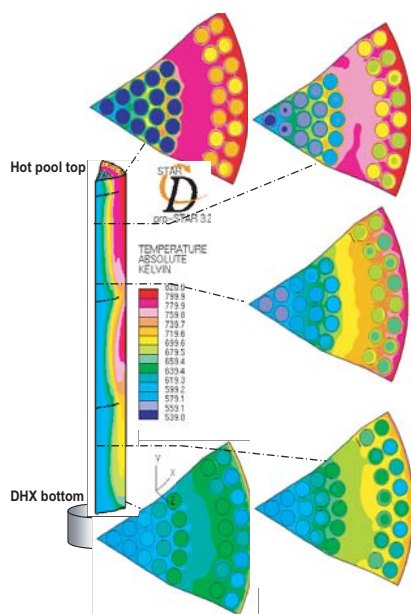


Fig. 3 Temperature distribution of sodium at various elevations

plenum to the U-tubes. The average flow rate of sodium is 0.36 kg/s/tube. However, due to flow non-uniformity it can be seen that the minimum flow rate is 0.31 kg/s and the maximum flow rate is 0.38 kg/s. In general, the flow rate is higher in the outermost row which is connected to three inner rows. That is, the flow rate is more in the tubes where the heat transfer is more in the upward leg. The differences in the flow rates among the tubes are only marginal (-13 % to + 5 %) and there is no flow reversal in any of the tubes. Thus, through this CFD study, it has been established that there is no risk for flow reversal in the SGDHRs of PFBR.

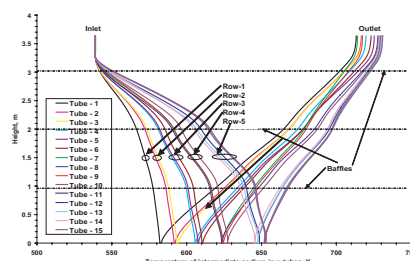


Fig. 4 Central line temperature of intermediate sodium inside U-tubes along the length

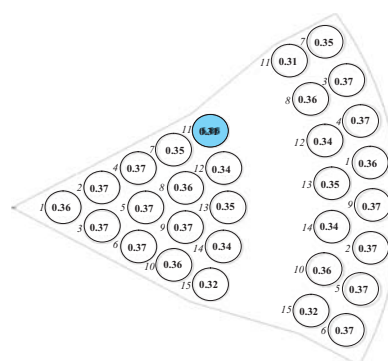


Fig. 5 Mass flow rates (in kg/s) of intermediate sodium through the tubes

III.A.7. Gas Entrainment - Effect of Ring Baffle Geometry

There is a large sodium free surface in the hot pool of PFBR. Argon, which is an inert gas, is provided above the free surface of hot pool to accommodate volumetric expansion of sodium and to prevent any contact between sodium and atmosphere. Presence of high free surface velocity and immersed components produces surface vortices which in turn entrain the cover gas into the hot pool. This entrainment of cover gas can attract unfavourable

Table 1 : Numerical results for free surface velocities for different baffle plate configurations

Case	Description of Baffle Plate	Maximum free surface velocity
Case 1	Without any baffle plate	0.50 m/s
Case 2	Ring type baffle plate (no porosity)	0.30 m/s
Case 3	Ring type baffle plate (10 % porosity)	0.29 m/s
Case 4	L – shaped baffle plate (vertical leg height is 0.5 times the horizontal leg and no porosity)	0.283 m/s
Case 5	L – shaped baffle plate (vertical leg height = length of horizontal leg and no porosity)	0.351 m/s
Case 6	Same as case 5 but 10% porosity in the vertical leg	0.277 m/s
Case 7	Same as case 5 but 20% porosity in the vertical leg	0.276 m/s

operational problems of the reactor.

Hence, it is important to mitigate the gas entrainment at the free surface of the hot pool. Making free surface quiescent is one of the means to mitigate gas entrainment from free surface. The numerical and experimental studies carried out in a large scale model showed that inclusion of ring type baffle plate below the free surface was very effective to reduce the free surface velocity. With the employment of such simple baffle plate the free surface velocity was reduced to half of its original value. No surface vortices were also seen at the free surface. However, it was found from the experiment that approximately a margin of 100 mm on the nominal free level height is available in PFBR at nominal flow rate before the onset of vortex activated gas entrainment from free surface. With the objective to improve this margin, improvements on the baffle plate design are necessary so that free surface velocity can be reduced further. In the present work, the effect of various baffle plate geometry on the hydraulics of the SAMRAT model hot pool was investigated numerically using PHOENICS code.

A 90° sector model of hot pool in cylindrical coordinate system

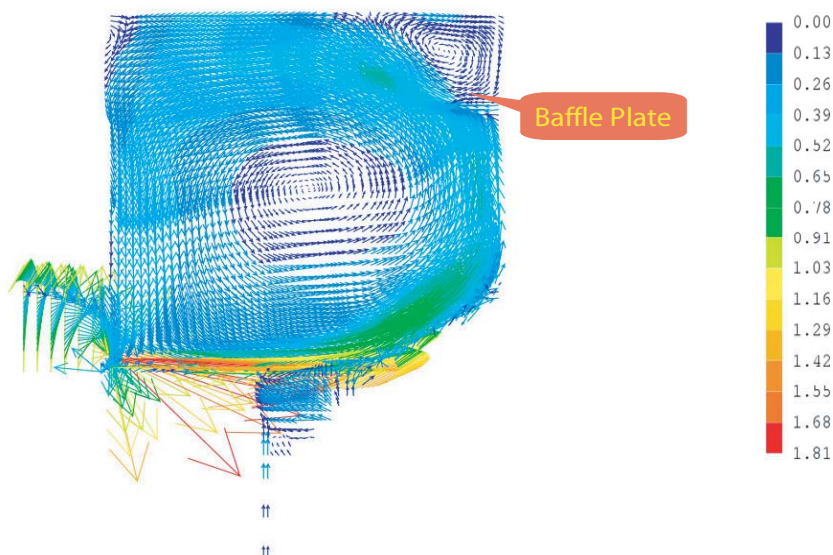


Fig.1 Flow pattern in hot pool with simple ring type baffle plate

with one IHX and half pump was considered for analysis to reduce the computational time. The computational domain is subdivided with a grid structure of 69 X 77 X 74 (total 3, 93,162) cells to achieve fairly accurate results independent of grid. Fixed mass flow rate is provided as the inlet boundary condition at Fuel, Blanket, Storage and Cavity zone. The skirt is modelled as porous plate. Flow through Control Plug based on experimental measurement is modelled by specifying mass sink at the bottom of the CP and flow is considered to enter the hot pool uniformly at different levels of the CP. All the structural components in hot pool are modelled by blocking the cells at corresponding locations. The conical portion of the inner vessel is modelled

as steps. The IHX is modelled as hollow cylinder.

Experiment was carried out with simple ring type baffle plate geometry. The numerical results were compared with these experimental results and a fair agreement was observed. Fig.1 shows the flow pattern in hot pool with ring type baffle plate geometry (without any porosity). The numerical results for different baffle plate configurations analysed are presented in Table 1. The results show that there is little incentive in adopting a complex geometry of baffle plate as the reduction in free surface velocity is minimal. This may be due to the fact that the minor variations in the baffle plate geometry do not have dominant influence on the global flow patterns.

III.A.8. Assessment of Dynamic Instability in Once Through Steam Generator

Hydrodynamic flow instability in Once Through Steam Generators (OTSG) is one of the important problems in the design and operation of Liquid Metal Fast Breeder Reactors. Under certain operating conditions, water flow in OTSG is susceptible to instability due to the close coupling between the thermal and hydraulic processes. Sustained flow oscillations due to instability are undesirable since they result in flow mal-distribution among the tubes or in SG modules resulting in thermal stress, mechanical vibrations and system control problems.

Many types of dynamic instabilities can occur in SG, but the cause of the main type of instability important for the

design of SGs is the propagation of density waves. This type of low frequency instability is referred to as density wave oscillations. This occurs because of the phase mismatch between the primary perturbation (water flow) and the response to this perturbation (pressure drop). As many tubes are operating under essentially constant pressure heads, this mismatch can lead to sustained/diverging oscillations. For example, when water flow is reduced, or sodium flow is increased, vapour generation rate and pressure drop change. Time delays between these processes can, under certain operating conditions, cause sustained oscillations, leading to the onset of dynamic instability.

Water flow oscillation in tubes manifests as oscillations in the steam temperature at the tube outlet/pressure fluctuations. However it is difficult to instrument individual tubes in SG for such measurement in an operating plant. If the flow oscillation in the tube manifests itself in the overall module flow, then fluctuation in the overall flow/flow noise could be

utilized for on-line stability measurements. Towards this experiments were conducted in the sodium heated once through steam generator in SGTF (Fig.1). To confirm the extent of oscillation in the steam temperature and in inlet water flow, 3 tubes out of 19, were monitored besides overall module flow.

Main objective of the present study was to assess the occurrence of dynamic instability in SG through module inlet flow perturbations, confirmed by ΔP measurements across the orifice at entry to the tubes and steam temperature fluctuation measurement at the outlet of tubes. Flow Instability measurement was carried out at 20% power level (1.1 MWt). By decreasing the SG outlet pressure, instability regime was approached. Fluctuations in the steam outlet temperature and in the inlet flow were monitored continuously to detect the onset of instability phenomenon.

During the operation in the unstable region, the mean outlet temperature in all the tubes was found to be decreased and very large

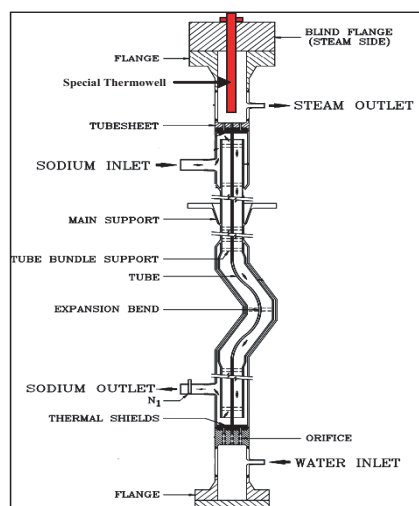


Fig.1 SGTF steam generator

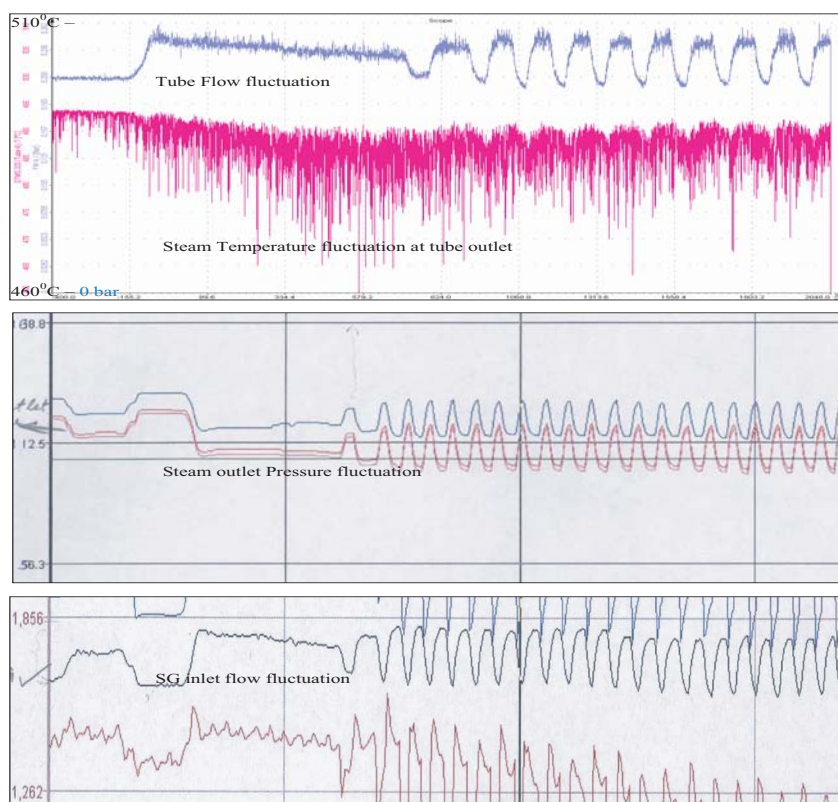


Fig.2 Instability build-up

fluctuations (10-20 K) in temperature readings are observed (Fig.2). Fluctuations, periodic in nature were

observed at the output of the differential pressure transmitters connected across the orifices during the instability

phenomenon.

Fig.2 also shows the variation of both the thermocouple output and the differential pressure transmitter output for a tube. Similar pattern of oscillation is observed in other tubes also. Oscillations observed in flow, in tubes were found to be in the same phase. A similar trend is also observed in the module feed water inlet flow to SG during instability. The above has indicated the feasibility of an instrumentation scheme for on-line measurement of dynamic instability in once through Steam Generator in an operating plant through flow fluctuation in overall module flow.

III.B. Sodium Technology

III.B.1. Sodium Cleaning of FBTR Dummy Subassembly by Steam-Nitrogen Process Using In-house Developed Hydrogen Sensor (PEMHS)

Sodium cleaning method based on steam-nitrogen is a simple and effective process. Residual sodium sticking to the fuel sub assemblies (FSA) received at Head End Facility (HEF) from FBTR and its reaction products with air are likely to interfere with chopping process. Hence

the residual sodium has to be removed. Sodium cleaning is carried out in HEF by steam/nitrogen process. To gain experience in sodium cleaning of FSA by steam/nitrogen process and to optimize the process parameters, the mock-up

sodium cleaning experiment was carried out in an in-house developed system.

The sodium cleaning process involves following steps.

1. Steam cleaning: Removal of adhering sodium by reaction with steam carried by nitrogen.

2. Water wash: Washing FSA with demineralised water.

During the reaction of sodium with steam, sodium hydroxide and hydrogen are produced. Hydrogen forms an explosive mixture with air beyond its threshold limit of 4% (v/v) when released to the atmosphere. For safe operation of the cleaning process, hydrogen concentration is required to be monitored online and preferably maintained below safe limit of 2% (v/v) of hydrogen. Nitrogen is used as the carrier gas for steam and also to keep the hydrogen concentration low at the safe level. After completion of the sodium cleaning by steam nitrogen process, the adherent sodium hydroxide is washed with dematerialized water. Hydrogen release occurs during water washing also and has to



FIG.1 Sodium cleaning system for FBTR SA

be monitored. The completion of the steam cleaning and water wash of sodium is indicated by the hydrogen

concentration reducing to near background value.

Proton exchange membrane based hydrogen sensor (PEMHS) was used for online monitoring of hydrogen evolved during sodium cleaning of FBTR mock subassembly. The sensor is an amperometric device based on NAFION which is a Proton Exchange Membrane (PEM). Platinum is used as both anode and cathode. The amount of sodium removed during the cleaning process can also be estimated from the total hydrogen released. Prior to its application for sodium cleaning, mock experiments were carried out at the site of sodium cleaning.

Schematic of the set-up used for sodium cleaning is shown in Fig.1. It consists of an inner chamber and an outer chamber. the inner chamber is for positioning of FSA and the outer chamber is for preheating of the FSA. Testpot-1 of SILVERINA loop at engineering Hall-1 was used for sodium wetting of mock-up FSA. The same was loaded into the leak tight stainless steel cleaning chamber under nitrogen atmosphere using the crane.

Steam cleaning

FSA was lowered, positioned in the cleaning chamber and

once-through circulation of nitrogen was maintained in the chamber with a flow rate of 10 Lpm. Nitrogen gas from the chamber was tapped at a flow rate of 200 Std. CC/min and let into the proton exchange membrane based hydrogen sensor (PEMHS). Hydrogen concentration was monitored online via data acquisition system.

Hydrogen concentration value was also displayed prominently. Steam from the electrical boiler, at 403 K and 1.1kg/cm², was admitted to the cleaning chamber. Increase in hydrogen concentration was reduced by enhancing the nitrogen flow rate and reducing the steam supply to maintain the hydrogen concentration below 2%. Reduced amount of steam slows the sodium water reaction and hence hydrogen generation. Higher nitrogen flow-rate (20 Lpm) diluted the hydrogen present in the chamber and hence reduces the concentration of hydrogen. Any increase in pressure in the cleaning chamber beyond 1.5kg/cm² could be released using the safety valve. The steam condensate was collected in drain cooler during the cleaning process. Once the hydrogen release reduced to near back ground value, steam cleaning was stopped and the steam condensate collected.

The variation in concentration of Hydrogen in nitrogen during steam wash is shown in Fig.2. Before the introduction of steam, hydrogen was observed in the concentration range of 0.05% in the nitrogen stream (region A of Fig.2.). This can be attributed to the reaction between sodium and residual moisture in the nitrogen gas. Abrupt increase in hydrogen concentration was observed at region C and steam supply was cut off to reduce further reaction. Nitrogen flow rate was increased to reduce the hydrogen concentration to safe limit of 2%. This sharp increase of hydrogen concentration may be due to condensation of steam in the chamber and may be prevented by preheating of the system. Once the hydrogen concentration reached less than 1%, steam was let in (region D). The steam supply should be regulated with respect to the hydrogen concentration

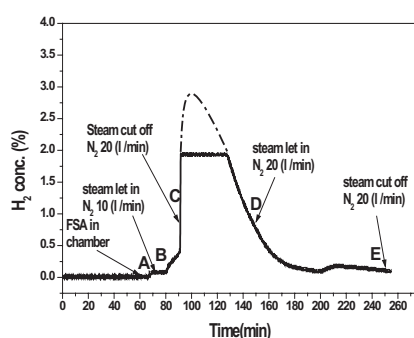


Fig.2 Hydrogen released during steam cleaning of FBTR FSA by steam-nitrogen process

monitored with the sensor, and the nitrogen flow rate has to be adjusted to control the concentration of steam and hydrogen. In addition to hydrogen concentration, the rate of rise of hydrogen signal has to be considered while regulating the nitrogen flow rate and steam supply. It is recommended to have an automated system which receives the hydrogen concentration signal from the sensor and adjust the flow rate of nitrogen and supply of steam to the chamber.

Water-wash

In order to remove any un-reacted sodium and sodium hydroxide sticking on the subassembly, water washing was carried out by filling and circulating DM water from a reservoir using a pump. Water level in the chamber was raised slowly by letting in water from the bottom. Hydrogen was continuously monitored and whenever it exceeds 2%, water was dumped immediately from the cleaning chamber to prevent hydrogen build-up. The process was continued by maintaining the hydrogen concentration within safe limit till the whole of FSA was submerged in water. Once the hydrogen concentration reached near background value, it was presumed that the



Fig.3 View of FSA after cleaning

cleaning operation was completed. The water in the chamber was circulated to ensure the complete removal of sodium hydroxide. The wash water was quantitatively collected for sodium estimation. The FSA was lifted using EOT crane, visually examined, dried and stored. The FSA after the cleaning process is shown in Fig. 3.

The entire operation has given enough confidence over the design and operation of the cleaning system and the hydrogen sensor developed at chemical group. The campaign also demonstrated the technical feasibility of safe transfer of sodium wetted FSA to the cleaning chamber in ambient atmosphere. The parameters critical in the cleaning process were identified.

III.B.2. Studies on Thermochemical Aspects of Sodium-Alcohol Reaction and Characteristics of the Product

In sodium cooled fast reactors, a thin layer of sodium gets deposited on the surface of steel components that are in physical contact with liquid sodium. Some of these components need to be taken out for periodic maintenance or replacement. Exposure of these components to ambient air poses fire hazard and possible hydrogen explosion due to vigorous reaction of sodium with moisture present in air. To avoid this, sodium needs to be removed from the component surface prior to maintenance work. Alcohols are generally employed world wide for cleaning sodium from small and delicate components. Ethyl carbitol used for cleaning sodium storage tanks which contains a few kilogram of sodium has been reported to cause run-away reactions leading to accidents in France and Germany. For clear understanding of the chemistry of sodium-alcohol reactions, data on thermochemical properties like enthalpies of reaction, enthalpies of solution, enthalpies of formation and heat capacity of the constituents and reaction products in sodium-alcohol

system are essential. Owing to limited or non-availability of such data, studies have been taken up in this system.

Enthalpies of solution, reaction and formation

Molar enthalpies of solution of sodium in methanol, ethanol and n-propanol and of sodium alkoxides in their corresponding alcohols were measured at 298.15 K using an isoperibol solution calorimeter. The measured molar enthalpies of solution of sodium in the above alcohols are $\Delta_{\text{sol}}H^0_{\text{m}(\text{Na}/\text{ROH})} = -204.0 \pm 1.1$, -190.4 ± 1.3 and -180.9 ± 0.8 kJ mol⁻¹, respectively. The measured molar enthalpies of solution of sodium alkoxides in its corresponding alcohols are $\Delta_{\text{sol}}H^0_{\text{m}(\text{RONa}/\text{ROH})} = -76.8 \pm 0.3$, -54.8 ± 0.4 and -41.9 ± 0.7 kJ mol⁻¹, respectively. The molar enthalpies of reaction of sodium with methanol, ethanol and n propanol were measured and found to be $\Delta_{\text{r}}H^0_{\text{m}(\text{Na}/\text{ROH})} = 127.11 \pm 1.34$, -135.59 ± 1.40 and -138.97 ± 1.07 kJ mol⁻¹, respectively. From these results and other data, the standard molar enthalpies of formation, $\Delta_{\text{f}}H^0_{\text{m}(\text{RONa})}$ of sodium

methoxide, sodium ethoxide and sodium n propoxide were calculated and found to be 366.3 ± 1.3 , 413.3 ± 1.4 and 441.6 ± 1.2 kJ mol⁻¹, respectively. Fig. 1 shows the variation of $\Delta_{\text{f}}H^0_{\text{m}(\text{NaOR})}$ vs $\Delta_{\text{f}}H^0_{\text{m}(\text{ROH})}$ measured in the present study and compared with literature data (Leal and NBS). A linear correlation has been found between $\Delta_{\text{f}}H^0_{\text{m}(\text{NaOR})}$ and $\Delta_{\text{f}}H^0_{\text{m}(\text{ROH})}$ as given in Eqn. (1), which is useful to predict the enthalpies of formation of higher sodium alkoxides.

$$\Delta_{\text{f}}H^0_{\text{m}(\text{RONa}, \text{cr})} = (1.19 \pm 0.02) \Delta_{\text{f}}H^0_{\text{m}(\text{ROH}, \text{l})} - (82.10 \pm 6.15) \quad (1)$$

In a similar fashion, enthalpies of solution of sodium and sodium alkoxides in respective alcohols were plotted against enthalpies of formation of corresponding alcohols and shown in Fig. 2. The linear correlations obtained from Fig. 2 are given in Eqns. (2) and (3), respectively. These correlations may be used to estimate the enthalpy of solutions of higher n-alkyl derivatives of sodium alkoxides.

Compound	$C_{p,m}$ (250–550 K) ($\text{J K}^{-1}\text{mol}^{-1}$)	Std. error ($\text{J K}^{-1}\text{mol}^{-1}$)	
Sodium methoxide	$37.52 + 1.0002 \times 10^{-1}T - 2.0311 \times 10^5 T^{-2}$	0.52	(4)
Sodium ethoxide	$61.42 + 1.2247 \times 10^{-1}T - 6.2744 \times 10^5 T^{-2}$	0.59	(5)
Sodium n-propoxide	$60.04 + 1.9738 \times 10^{-1}T - 4.7697 \times 10^5 T^{-2}$	0.76	(6)
Sodium iso-propoxide	$48.69 + 2.4420 \times 10^{-1}T - 2.6535 \times 10^4 T^{-2}$	0.83	(7)

$$\Delta H_{\text{sol}}^{\circ}(\text{Na}/\text{ROH}) =$$

$$-(0.362 \pm 0.01) \Delta H_{\text{f}}^{\circ}(\text{ROH}, \text{l}) - (290.70 \pm 2.68)$$

(2)

$$\Delta H_{\text{sol}}^{\circ}(\text{RONa}/\text{ROH}) =$$

$$-(0.551 \pm 0.01) \Delta H_{\text{f}}^{\circ}(\text{ROH}) - (208.60 \pm 3.47)$$

(3)

Heat capacity

Heat capacity of sodium methoxide, sodium ethoxide, sodium n-propoxide and

sodium iso-propoxide were measured using DSC technique in the temperature range 240–550 K. Fig.3 shows the variation of heat capacity values of sodium alkoxides as a function of temperature. The values were fitted to a polynomial by least-squares method and the expressions obtained are given above.

Using these values, other thermodynamic functions such as enthalpy increments, entropies and Gibbs energy functions were derived.

The variation in $\Delta C_{p,m}$ as a function of temperature for addition of one $-\text{CH}_2-$ group from sodium methoxide to sodium ethoxide and ethoxide to n-propoxide was computed. It can be inferred that $C_{p,m}$ for addition of one $-\text{CH}_2-$ group can be considered to be same for both the alkoxides. It is thus established in this study that the heat capacity values of higher alkoxides such as sodium n-butoxide, sodium n-pentoxide can be estimated from data on that of the lower alkoxides.

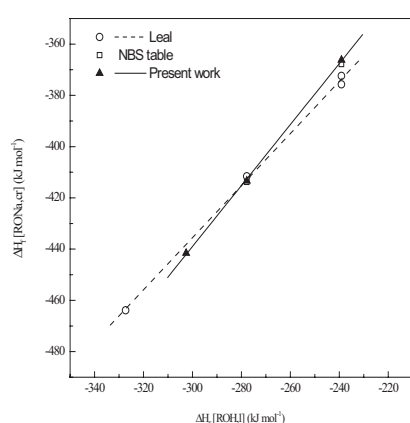


Fig.1 Variation of enthalpy of sodium alkoxides versus enthalpy of formation of the corresponding alcohol

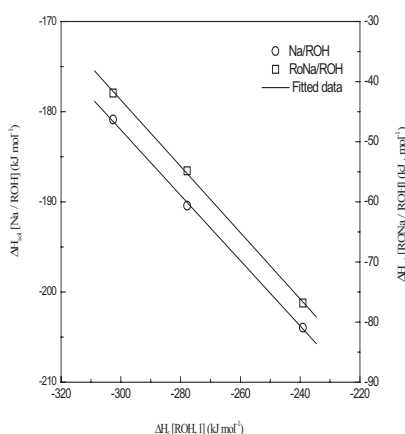


Fig.2 Variation of enthalpy of solution of Na/ROH and RONa/ROH versus enthalpy of the corresponding alcohol

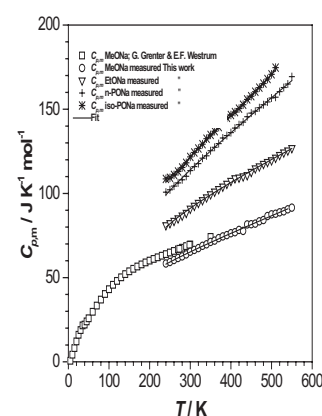


Fig.3 Variation of heat capacity as a function of temperature of sodium alkoxides

III.B.3. Electron Microscopy Investigation on a Failed Bellow Sealed Valve in Sodium Circuits in Large Component Test Rig

The Bellows sealed valves are used in the sodium circuits to achieve leak tightness. The outer surface is in contact with molten liquid sodium and the inner surface with air or oxygen. The valve in service for nearly 40,000 hours in the temperature range of 150-550°C at the Large Component Test Rig (LCTR) failed during an operation at 300-350°C. The failure manifested as perforations at highly stressed regions on the outer ply. Further, wall thinning and dissolution of the material was observed on the inner ply. A detailed metallurgical investigation was carried out to identify the cause of failure. Examination of the material showed that it is Ti modified 316 austenitic stainless steel. The outer and inner ply showed fine pits on the surface. The grain boundaries of the outer ply showed signatures of sensitization as seen in Fig.1.

Detailed electron microscopy investigations showed the presence of large number of fine deformation twins (Fig.2). The observation of fine twins is a signature of deformation at

high strain rates, since it is well known that f.c.c metals undergo deformation twinning only under high strain rates. This could have been introduced during the forming and fabrication processes or thermal cycling during service.

X-ray diffraction analysis showed the presence of α -Fe along with γ -Fe. The specimen was also magnetic. A high value of hardness (360VHN) was observed. These observations suggest the presence of a martensite phase. TEM observations also showed the presence of martensite laths in matrix. No reversion of martensite was observed, which can be understood since martensite reversion temperatures in 304 and 316SS are reported to be higher than 773 K. The service temperature of 573-623 K, precludes formation of martensite. This confirms that the martensite observed in the bellows is strain induced martensite, formed during fabrication. This can be understood since after fabrication the bellows are not stress relieved to impart better

fatigue resistance. The presence of strain induced martensite is reported to cause low temperature sensitization at long durations. This explains the cause of sensitized microstructure in the present case.

Based on the observations it is inferred that prolonged exposure of a sensitized microstructure with pinholes to flowing sodium has led to caustic corrosion resulting in wall thinning and dissolution of the material causing failure of the bellows. Hence, it is recommended that the bellows should be stress relieved prior to service to avoid strain induced martensite which causes low temperature sensitization.

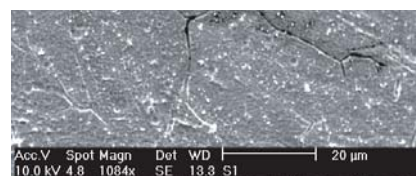


Fig. 1 Sensitized microstructure in the outer ply



Fig. 2 Microstructure with fine deformation twins in the inner ply

III.C. Core and Structural Materials

III.C.1. Effect of Titanium on Creep Properties of 14Cr-15Ni -Ti Stabilised Austenitic Stainless Steel

For the initial core of PFBR, the structural material chosen for clad and wrapper tubes is a 20% cold worked 14Cr-15Ni-Ti stabilised austenitic stainless steel (SS). The target burn-up of fuel is 100,000 MWd/t. For future cores of PFBR, it is envisaged to use a material of lower swelling so that fuel burn-up of about 150,000 MWd/t can be achieved. Towards this, a modified composition of 14Cr-15Ni-Ti stabilised SS (designated as D9I) is being developed by adjusting the amounts of the minor elements such as titanium, silicon and phosphorous. These elements have a strong influence on void swelling of austenitic SS. Since void swelling and thermal creep are the most important considerations for core structural materials for FBRs, the influence of these elements on the thermal creep properties has been systematically studied by varying titanium in the range of 0.16 to 0.30 wt%, silicon in the range 0.75 and 0.95 wt % and phosphorous in the range of 0.025 to 0.04 wt%. The amount of carbon in these heats was kept unchanged at a level of about 0.04 wt% and

this corresponded to Ti/C ratio in the range of 3.8 to 8.6 for the whole range of titanium content. Fifteen laboratory heats of D9I SS were prepared by vacuum induction melting of high purity electrolytic grade raw materials, followed by vacuum arc remelting (VAR) process. The VAR ingots were hot forged and then hot rolled into plates of 12 mm thickness,

curves of the four heats with various titanium contents. Maximum rupture life was obtained for titanium content in the range of 0.22 to 0.24 wt%; rupture life decreased by increasing or decreasing the amount of titanium from 0.23 wt%. The peak in rupture life was more pronounced at lower creep stresses as shown in Fig.2. The silicon content was

Table 1: Chemical composition and titanium to carbon ratio (Ti/C) of D9I SS heats.

	P	Si	Ti	Ni	Cr	Mn	Mo	C	N	B	S	Ti/C
Heat 1	0.026	0.76	0.18	15.53	14.38	1.71	2.36	0.047	0.0084	0.0053	0.0041	3.8
Heat 2	0.025	0.75	0.23	15.49	14.39	1.64	2.35	0.039	0.0086	0.005	0.0043	5.9
Heat 3	0.026	0.77	0.25	15.48	14.37	1.51	2.33	0.04	0.0087	0.005	0.0039	6.3
Heat 4	0.025	0.73	0.36	15.43	14.29	1.63	2.35	0.042	0.008	0.0056	0.0044	8.6
D9 SS	0.02 max	0.5-0.75	5C-7.5C	14.5-15.5	13.5-14.5	1.65-2.35	2-2.5	0.035-0.05	0.005 max.	10-20 ppm	0.01 max.	5-7.5

subsequently solution annealed in the temperature range of 1323-1423 K, pickled and passivated. The average grain size of the material was 40 ± 7 microns. The chemical composition of the four heats and the specifications for D9I SS is given in Table 1.

Creep properties

The influence of titanium content on creep properties has been studied at 973 K at different stress levels in the range of 150 to 250 MPa. Fig. 1 is a comparison of the creep

0.75 wt% and phosphorous content was 0.025 wt% in all these heats. The element titanium is a strong carbide former (TiC). Since carbide precipitate has a strong influence on creep properties,

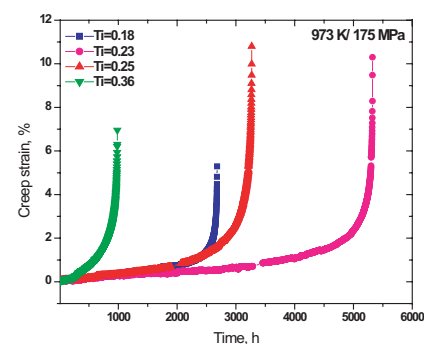


Fig.1 Influence of titanium on creep curves of D9I SS.

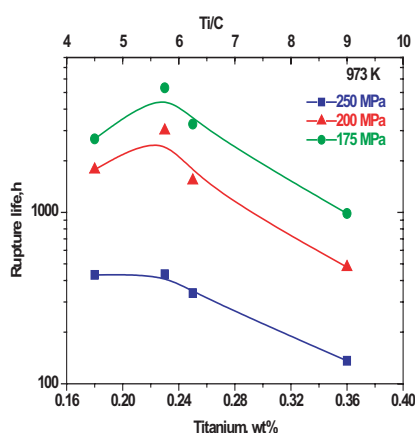
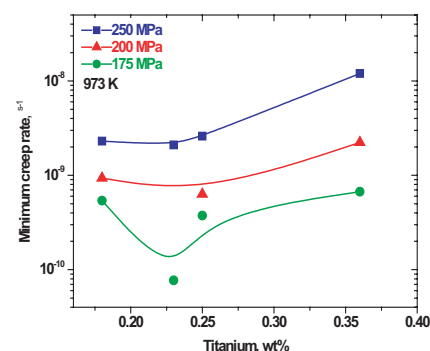


Fig.2 Influence of titanium on creep rupture life of D9I SS (phosphorous = 0.025 wt%, silicon = 0.75 wt% and carbon = 0.04 wt %).

Ti/C ratio is considered an important parameter to assess the influence of titanium. From Fig. 2, it is seen that Ti/C ratio of 5.5 to 6 provides maximum creep strength in D9I SS containing 0.025 wt% phosphorous and 0.75 wt% silicon. The variation of minimum creep rate with titanium content also showed a minimum value corresponding to 0.22 to 0.24 wt% titanium (Fig. 3). Creep rupture ductility

generally decreased with increase in titanium content.



(b) Fig.3 Influence of titanium on minimum creep rate of D9I SS (phosphorous = 0.025 wt%, silicon = 0.75 wt% and carbon = 0.04 wt %).

III.C.2. Effect of Titanium on the Void Swelling Behavior in (15Ni-14Cr)-Ti Modified Austenitic Steels Studied by Ion Beam Simulation - Step Height and Positron Lifetime Studies

One of the important property changes caused by irradiation in the fast reactor structural materials is void swelling. The dimensional changes introduced by void swelling limits the lifetime of structural components used in a reactor. Therefore, resistance to void swelling is a major consideration in the choice of materials for the core components. The titanium modified steels exhibit greatly improved swelling resistance under breeder reactor conditions and consequently, have become a prime

candidates for structural applications. Titanium modified (15Ni, 14Cr) steel and its improved versions with phosphorous additions (designated as D9 and D9I) are envisaged for use as fuel cladding and wrapper materials in Indian fast breeder reactor (FBR) programme. Accelerated heavy ions which have the inherent advantage of producing high displacement rates have been used for evaluating the effect of minor alloying elements.

The void swelling behavior of

two steels: (A) (15Ni-14Cr)-0.25Ti and (B) (15Ni-14Cr)-0.15Ti were studied using heavy ion irradiation for understanding the influence of titanium in the void swelling resistance of the alloys. The cold worked samples were pre-implanted with a uniform helium concentration of 30 appm. This was followed by a 5 MeV nickel ion irradiation to create a peak damage of ~ 100 dpa at damage rate of 7×10^{-3} dpa/s at various irradiation temperatures between 700 and 970 K. The gross swelling in the specimen

was determined by step height measurements. Figure 1 shows the void swelling in the two alloys as a function of the irradiation temperature. It is found that the peak swelling temperatures and the magnitude of swelling for the two alloys are different. Whereas the alloy with 0.15% Ti displayed a swelling of $\sim 15\%$ at the peak swelling temperature of 923 K, the alloy with 0.25% Ti has a swelling maximum of $\sim 4\%$ at 823 K. With similar thermo-mechanical treatment effected on both the alloys the difference in void swelling behavior is solely due to the effect of chemical composition.

In order understand the drastically different behaviour of the two alloys with regard to void swelling, the TiC

precipitate formation in these two alloys was studied by positron lifetime measurements. The un-irradiated alloys were subjected to isochronal annealing and the positron life time was measured after each annealing. These alloys show different TiC precipitate formation behavior (Fig.2). The observed variation of lifetime τ displays distinct stages viz., a monotonic decrease in τ from the initial cold worked state upto ~ 900 K in alloy B and ~ 800 K in alloy A. This is followed by a stage where there is an increase in lifetime to saturation, followed by a decrease in lifetime. The first stage corresponds to point defect recovery arising out of the migration of vacancies to sinks such as dislocations. The subsequent stage where there is an increase in lifetime τ is the

result of positron trapping by the TiC precipitate which forms during the heat treatment. The increase in average lifetime of positrons in this stage for alloy A in comparison to alloy B is due to the higher number density of TiC precipitates in the former. The observed lower void swelling in alloy A can be attributed to the higher number density of TiC precipitates. It is further seen (Fig.2) that there is a difference in the onset of TiC precipitation by 100K between the two alloys. The Shift in the peaking swelling temperature can be attributed to the difference in the onset temperature for TiC precipitation for the two alloys. Thus, positron lifetime measurements helps to rationalize the different swelling behavior in alloys with different Ti concentrations.

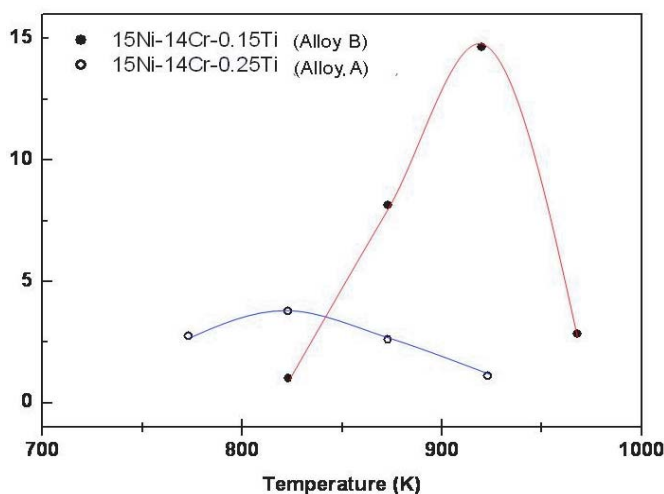


Fig.1 Temperature dependence of void swelling measured by surface profilometry for the D9 alloys with different titanium concentration

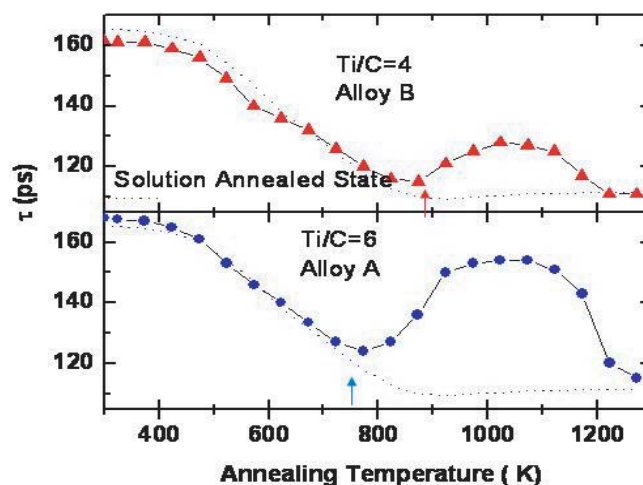


Fig.2 Variation of positron life time with annealing temperature for the cold-worked D9 alloys with different titanium concentration, alloy A (Ti / C = 6) and alloy B (Ti / C = 4)

III.C.3. Improvement of Mechanical Properties of Modified 9Cr-1Mo Steel by Heat Treatment

Modified 9Cr-1Mo steel is ferritic steel, used extensively in the standard normalized and tempered condition (20-30 μ m grain size) in fossil power plants, steam generator of PFBR, petrochemical industries and many other heat transport systems due to its good mechanical properties up to 823 K and physical properties. However, the weldments of these steels are susceptible to Type IV cracking during service due to its low creep strength of the inter-critical heat affected zone (ICHAZ). Improvement of Type IV cracking resistance of these steels by alloying additions has been suggested by many authors. In the present work, it has been shown that increase in prior austenite grain size of the modified 9Cr-1Mo steel by heat treatment increases the room temperature and higher temperature yield strength (Fig. 1) by ~25% without significantly effecting the tensile ductility. Increase in heat treatment temperature results in increase in grain size of the material and super-saturated solid solution of carbon and alloying elements. This could be the reason for increase in strength of the

material in the higher normalization temperature and tempering condition. It is interesting to observe that yield strength of the weld joints made with these large prior austenite grain size materials also increases (Fig. 2) in same magnitude at room temperature and high temperature.

The increase in yield and tensile strength of the weld joints can be correlated with increase in hardness of the ICHAZs in the higher grain size material. It can be mentioned here that hardness of the ICHAZ in weld joint, which was made with 120 μ m grain size base metal is increased by 20 VHN_{200g}. The microstructure observation shows that presence of martensite in this zone could be the reason for increase in hardness of this zone. This is further reflected in the tensile tested weld joints. The radial profile of tensile tested specimen shows two necking (Fig. 3) when the weld joint was made with 20-30 μ m grain size material, which was absent when it was made with 120 μ m grain size material. This clearly showed that larger grain

sizes can affect the deformation behavior of cross weld tensile specimen. The hardness profile taken from one side of the tensile tested specimen to the other side of the specimen shows that hardness increases in the broken side of the specimen when weld joint was made with 120 μ m grain size material but it decreases when it was made with 20-30 μ m grain size material (Fig.4), clearly indicating former

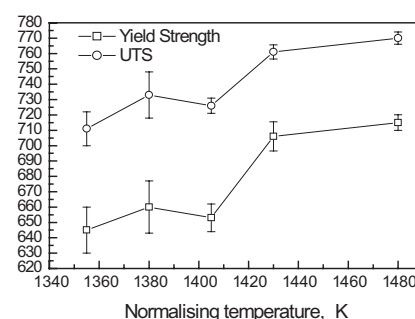


Fig.1 Change of tensile strength of base metal with normalizing temperature in the 1033K/3h tempered condition (UTS: ultimate tensile strength)

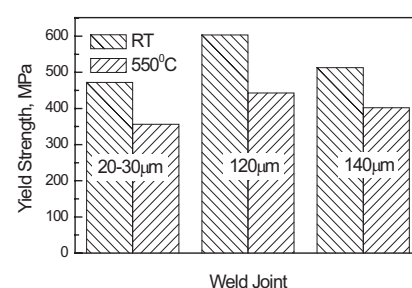


Fig.2 Change of tensile strength of weld joints with normalizing temperature in the 1033K/3h tempered condition

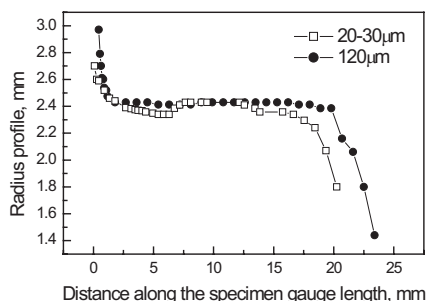


Fig.3 Radial profile from the un-broken side of tensile tested specimen to un-broken side

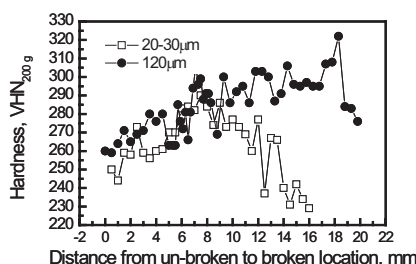


Fig.4 Hardness profile from un-broken to broken side of tensile tested specimen

material is undergoing hardening and latter material is undergoing softening with microstructure modification.

The present result clearly shows that increase in prior austenite grain size has significant effect on mechanical properties of the material and its weld joints.

III.C.4. Verification of the Applicability of the Invariant Shape Master Curve Hypothesis under Dynamic Loading Condition at the Ductile-Brittle Transition Temperature Regime of 9Cr-1Mo Steel

The fracture toughness of ferritic steels in the ductile-brittle transition temperature (DBTT) regime is subjected to inherent scatter as the associated cleavage fracture initiation is predominated by randomly distributed brittle precipitates, inclusions, weak lath boundaries etc., generally referred to as 'weakest links', in the region of highest stress buildup. A schematic of this mechanism is shown in Fig. 1.

To take into account this scatter in predicting a DBTT of engineering sense, a 3-parameter Weibull distribution model, as given in Eqn.1, is used in ASTM E 1921 to define a term called 'Reference

Temperature (T_0)' at which the median fracture toughness (median: cumulative probability $P_f = 0.5$) is $100 \text{ MPa.m}^{0.5}$ for a specimen of one inch equivalent thickness.

$$P_f = 1 - \exp\left\{-\left[\frac{(K_{JC} - K_{min})}{(K_0 - K_{min})}\right]^b\right\} \quad \dots\dots\dots(1)$$

T_0 is a material specific parameter and used in indexing the Master Curve, claiming to follow an invariant shape in describing the fracture toughness variation of all the BCC metals in their DBTT regime. The Master Curve equation, as given in ASTM E 1921 is shown in Eqn. 2. $K_{JC}(\text{median}) = 30 + 70 \exp(0.019 (T - T_0)) \quad \dots\dots\dots(2)$

The invariant shape Master Curve hypothesis has been found to hold good for quasi static condition of loading. However under dynamic loading condition, along with the extra inertial component towards crack initiation, the rate-sensitive material flow properties elevate the crack front stresses, suppress

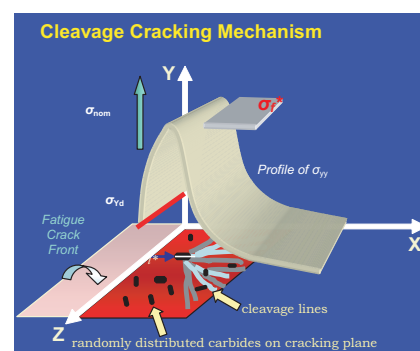


Fig.1 Schematic representation of the mechanism of cleavage cracking in DBTT regime

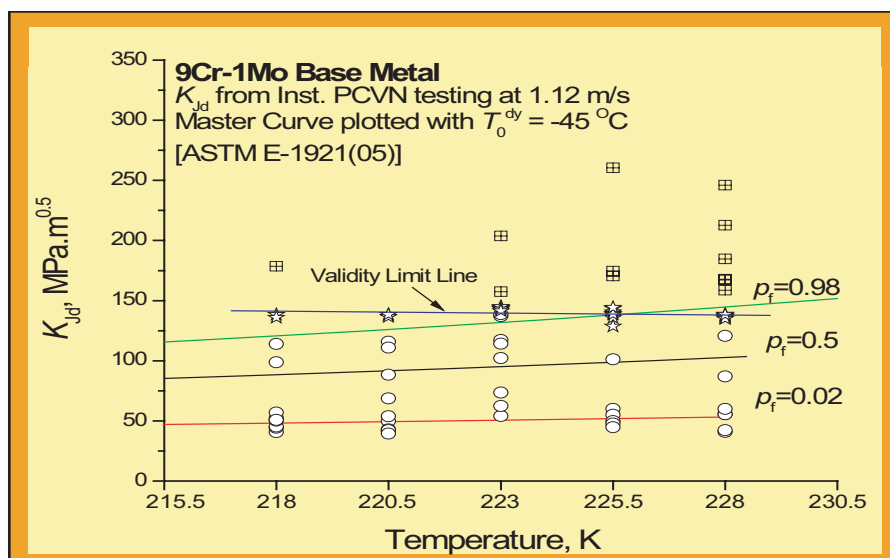


Fig.2 Dynamic fracture toughness results of 9Cr-1Mo steel with respect to the ASTM E 1921 master curve

plasticity, increase constraint and thus reduce fracture toughness. This combined effect has raised speculation regarding the adoption of the quasi static Master Curve shape even in dynamic situation and it needs to be experimentally resolved. Experimental verification of this aspect has been carried out with plain 9Cr-1Mo steel. It may be noted that the 9Cr-1Mo steel is one of the candidate materials for wrapper in future Fast Breeder Reactors aiming a burn up >200,000 MWD/t. To this end, predicting dynamic fracture toughness based reference temperature (T_0^{dy}) is important for ensuring the integrity of critical component under accidental/dynamic loading scenario.

Dynamic fracture toughness (K_{Jd}) of plain 9Cr-1Mo steel has

been determined from instrumented impact testing with pre-crackled Charpy specimens. The dynamic loading gives rise to inertial oscillations in the specimen originating from interactions of forward and reflected stress waves. Towards getting a load signal with minimum oscillation effects, testing has been conducted at a reduced loading rate (~ 1.12 m/s). The calculated stress intensity factor has been $\sim 10^6$ Mpa.m^{0.5}/s, which is well regarded as a dynamic situation. It has been noticed that increase in loading rate up to 5.12 m/s, the maximum capacity of the available Charpy machine, affects the stress intensity factor rate only marginally.

At temperatures of 213, 218, 220.5, 223, 225.5, 228 and -233 K, T_0^{dy} have been

determined to be 225.85, 227.25, 210.91, 208.87 and 209.53 K respectively. If the same invariance of the Master Curve holds good even in this high loading rate then theoretically, the T_0^{dy} results obtained from all the test temperatures within the DBTT regime would show the same values. Apparently, the T_0^{dy} values show differences in the present campaign. However, taking into account the experimental uncertainties involved in a dynamic fracture toughness evaluation procedure, it is reasonable to say that the T_0^{dy} remains practically unchanged (± 10 K) within the DBTT regime. The lower T_0^{dy} values at the higher test temperatures can be attributed to the loss of constraints at the crack tip. Thus, it is proposed that the same invariant shape of the Master Curve describing the fracture toughness variation under quasi-static condition also can be applied in the high strain rate loading. The T_0^{dy} of the 9Cr-1Mo steel is conservatively predicted as of -228 K and the same has been chosen to index the Master Curve, as shown in Fig. 2. Except a few, the individual dynamic fracture toughness data has been seen to lie well within the 98% and 2% confidence limit.

III.C.5. Low Cycle Fatigue Behaviour of 316 SS Weld Metal and Modified 9Cr-1Mo Weld Joints

The effect of thermal ageing (823 K / 10000h and 873 K / 10000h) on strain controlled fatigue behaviour of 316 SS weldmetal was investigated at 823 and 873 K. The aged weld metal showed lower fatigue life compared to unaged weld

metal in the temperature range 823-873 K, Fig. 1.

The use of liquid sodium as a heat transfer medium in fast breeder reactors necessitates the assessment of the creep, low cycle fatigue and creep-fatigue interaction properties of structural materials in flowing sodium. The fatigue life of indigenous modified 9Cr-1Mo steel weld joints tested in flowing sodium were compared with that in air at 823 and 873 K. Fig. 2 shows the fatigue life of Mod.9Cr-1Mo steel weld joint in high purity sodium (less than 2 ppm of oxygen) compared with that in air at 823 K. Fatigue life in sodium environment was significantly higher compared to that

obtained in air at both the temperatures. The lack of oxidation in sodium environment is considered to be responsible for delayed fatigue crack initiation and propagation with associated increase in fatigue life.

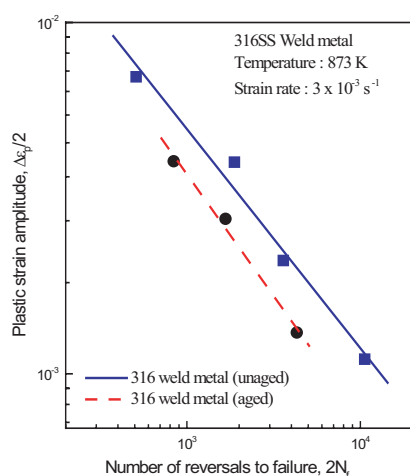


Fig.1 Comparison of fatigue life of aged and unaged 316 weld metal, 873 K.

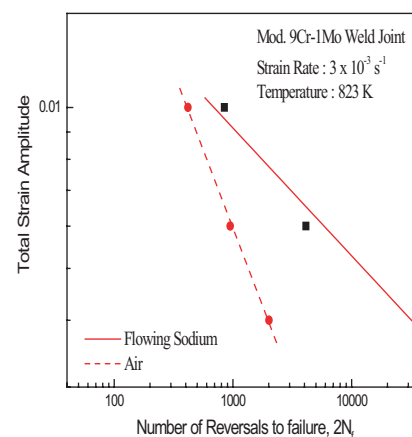


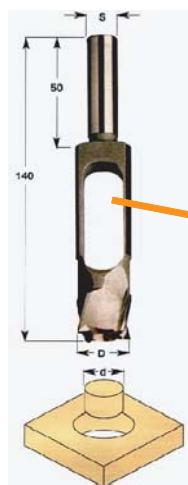
Fig.2 Strain-life plots at 823 K for Modified 9Cr-1Mo weld joint in air and flowing sodium

III.C.6. Mechanical Properties and Microstructural Studies on Irradiated SS316 Wrapper

The irradiation experience worldwide has proved that the main factor affecting high fuel burn-up in fast reactors is related to the irradiation damage of the structural materials. To understand the irradiation performance of the

Stainless Steel SS316 in FBTR at various levels of displacement damage (dpa- displacement per atom), mechanical testing and TEM (Transmission Electron Microscopy) studies have been carried out.

The mechanical properties of irradiated SS 316 cladding are evaluated by conventional tensile testing carried out remotely in the hot cells of Radio Metallurgy Laboratory (RML). For evaluating the mechanical property changes in



**Hollow
end mill tool**

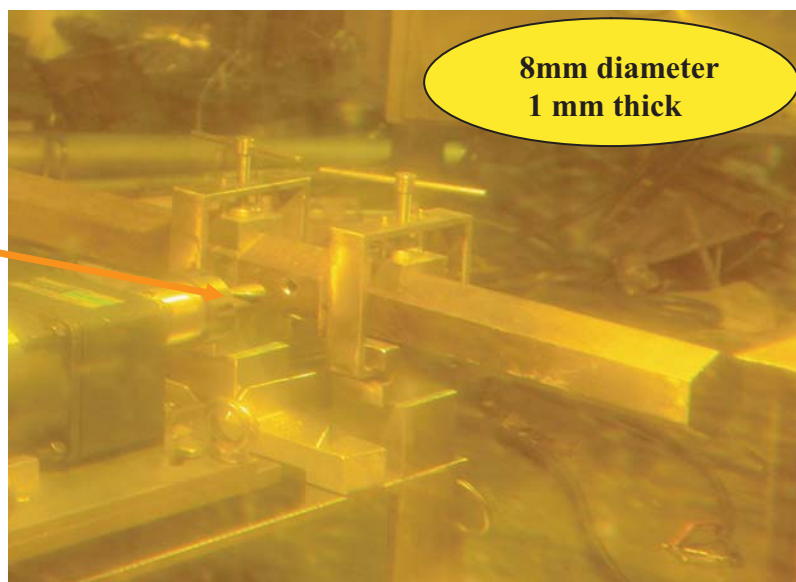


Fig.1 Specimen Extraction Inside hot cells

irradiated wrapper, small specimen test techniques have been evolved. The small specimen test techniques enable the characterization of mechanical behaviour using extremely small volume of the material. By using small specimens for testing irradiated materials, the radiation dose levels drastically decrease in proportion to its volume and it becomes possible to take them out of the hot cells and conduct mechanical testing in comparatively simple shielded enclosures with reduced radiological hazards.

The Shear punch (ShP) testing is a small specimen testing technique, in which a cylindrical punch with a flat end is forced to punch a hole in a clamped small disk specimen of 1 mm thick and 8 mm

diameter. The load-displacement curve obtained during the ShP test is similar to that of the conventional tensile test and is analyzed to evaluate the uniaxial tensile properties like yield strength (YS), Ultimate Tensile Strength (UTS) and % elongation. The shear punch tests were standardized for SS316 wrapper material using different cold rolled microstructures (30%, 35%, 40 %, 50% & 60% cold worked) and a solution annealed microstructure of the virgin material. By carrying out both tensile and shear punch on generated microstructural conditions, tensile-shear punch correlation equations for strength and ductility parameters have been determined.

For estimating the tensile

properties of the irradiated SS316 wrapper, small specimens of 8 mm diameter and 1 mm thick were extracted using a specially designed hollow end mill tool at different locations along the length of the irradiated wrapper corresponding to dpa (displacement per atom) varying from 2 to 56 (Fig.1). Shear punch test was carried out on these highly irradiated small specimens in mechanical test machines outside the hot cells with local lead shielding surrounding them and the conventional tensile properties were estimated using the derived correlations (Fig. 2).

Disc specimens of 3 mm diameter obtained after shear punch testing were used for preparing TEM specimens for structure-property correlation

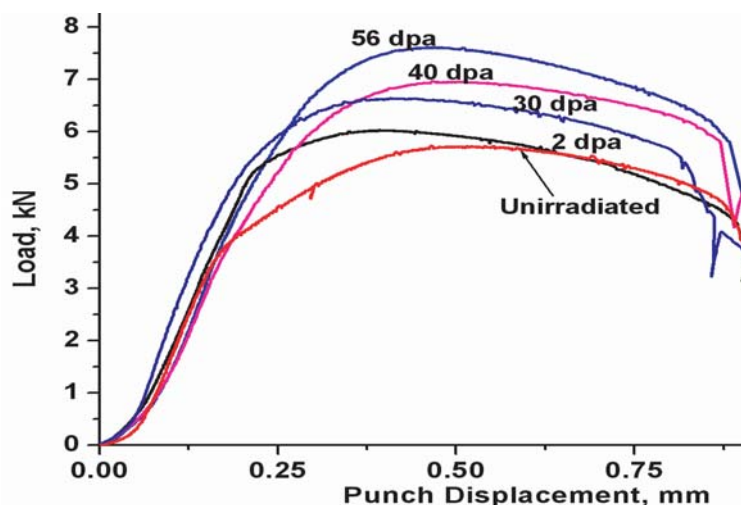


Fig.2 Shear punch testing of irradiated SS316 specimens (a) test setup (b) load-displacement plots showing increase in the maximum load with increasing dpa

studies. Prior to preparation of irradiated specimens, extensive trials were carried out with unirradiated specimens to optimize the pre-thinning and electrolytic thinning parameters. TEM specimens were prepared using special fixtures developed for handling irradiated specimens. Irradiated specimens which had

undergone displacement damage from 2 dpa to 56 dpa have been examined using 200 keV Analytical TEM.

A considerable increase in the strength and decrease in the ductility of the wrapper with increasing displacement per atom (dpa) have been observed from the small specimen

mechanical tests. The transmission electron microscopic studies revealed the presence of voids and precipitates in the matrix (Fig 3). Precipitates were identified to be of M₂₃C₆ type and precipitation of second phases corroborates the hardening observed on the wrapper.

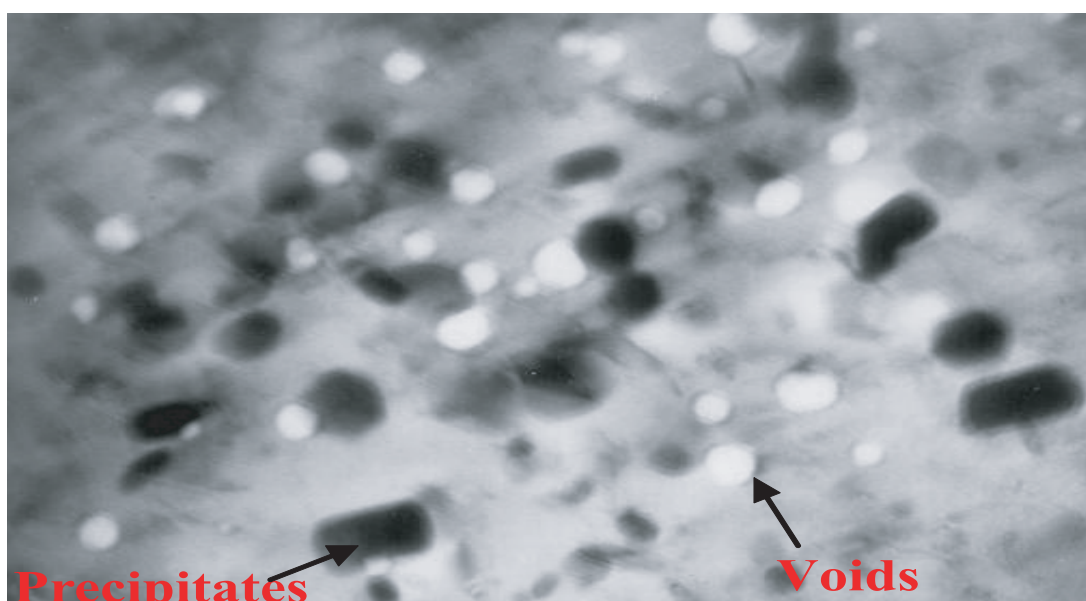


Fig.3 TEM image of the irradiated SS316 at a displacement damage of 40 dpa

III.C.7. High Temperature Fretting Wear Studies on Stainless Steel Type AISI 316LN

In Fast Breeder Reactor, stainless steel tubes supported on stainless steel rollers are being used in the primary heat exchanger for transferring heat from radioactive sodium to sodium in the secondary circuit. Because of the flow induced vibration as a result of the flow of sodium the tubes and roller joints undergo fretting wear, which is a serious concern because of the presence of radioactive sodium in the heat exchanger. The role of environment especially that of temperature and the frequency of fretting wear of stainless steel is not well understood in the literature. Hence an in-depth study was taken up to characterise the fretting wear behaviour of stainless steel and stainless steel pairs. The fretting wear studies of stainless steel type AISI 316LN against Stainless steel type AISI 316LN

were conducted under various operating conditions such as load (10 N and 50N), frequency (25 Hz, 75 Hz and 125 Hz) and temperature (623, 783 and 823 K). Temperature was the main variable input parameter while coefficient of friction (μ) and wear were the output parameters. It was observed that μ did not depend appreciably on load, frequency or temperature while wear rate showed high dependency on these parameters. Influence of temperature on wear depended on the frequency selected. For higher frequency of oscillation (125 Hz and 75 Hz), wear rate reduced with increase in temperature from 623 to 823 K. For 25 Hz, however, it increased with temperature possibly because of fretting fatigue. The wear rate was observed to be maximum at 75Hz. On other hand, wear

rate decreased as load increased.

Further, microstructural examinations were conducted on the worn samples to analyze the wear behaviour and to understand the wear mechanisms. The microstructural examinations at SEM level revealed that the failure (i.e., the cracking and thus removal of material) on stainless steel 316LN is due to fatigue at lower frequencies. The interesting new observation is that adiabatic shear deformation (Fig. 1) and crushing are responsible for the failure at higher loads and higher frequencies.

A typical microstructure is given in Fig. 2(a) and the crack propagates perpendicular to the shear bands and the material fractures. Fig. 2(b) shows the fractured grain in which the fracture is perpendicular to the shear bands. These shear bands are observed to be perpendicular to the motion of the pin. The above observations revealed that at low 623 K and at 25 Hz the material failure is due to fatigue. The microstructure of the sample tested at 25 Hz and 350 Hz under a load of 100N

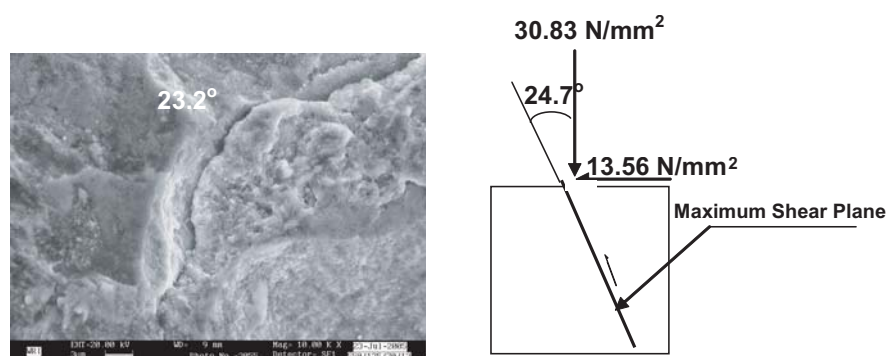


Fig.1 Microstructure of the sample tested at 823 K, 125 Hz and 70 N load shows the evidence of crack because of shear deformation

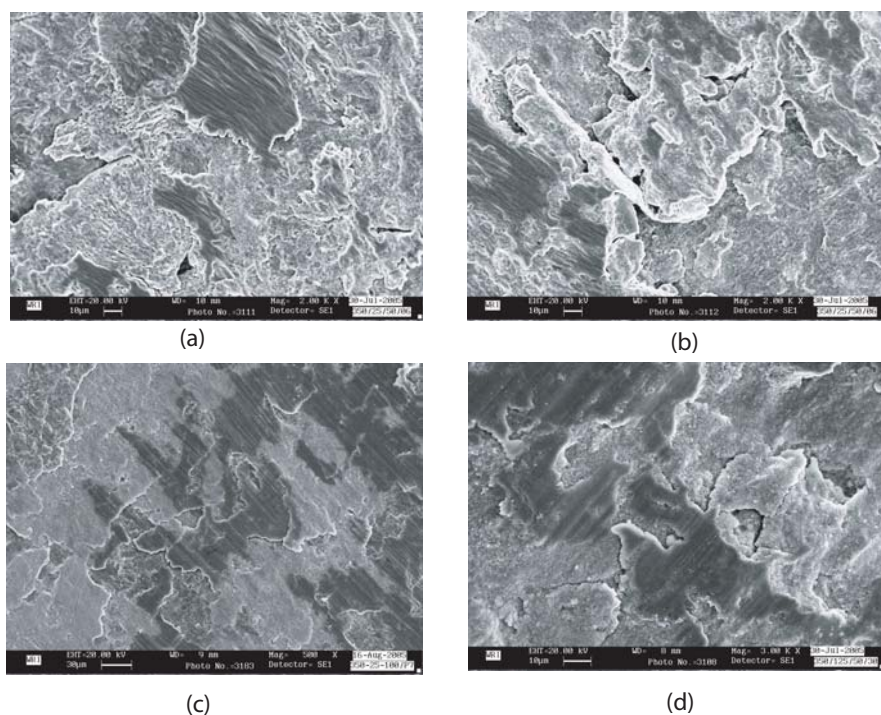


Fig.2 Microstructure of the sample tested at 623 K (a) and (b) at 25 Hz and 50N load showing the presence of fatigue cracks. (a) Initiation of fracture in a grain containing the shear bands. (b) Fractured grain in which the fracture has occurred perpendicular to the shear bands. (c) At 25 Hz and at 100L and (d) (d) 623 K, 125 Hz and 50N

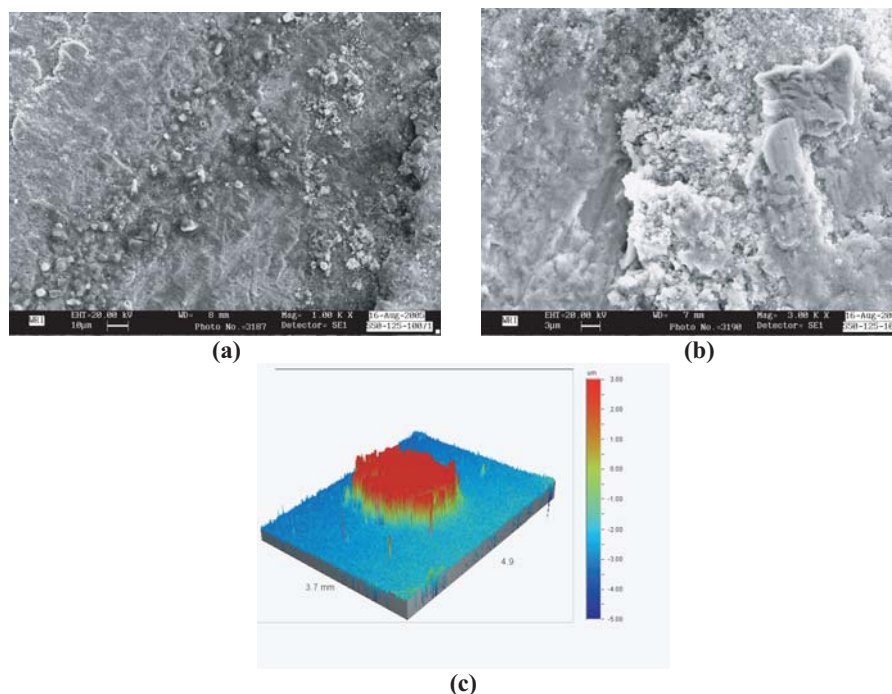


Fig.3 (a) and (b) Microstructures of the sample tested at 823 K, 125 Hz and 100 N load showing the presence of oxide particles in the scar and (c) Topography of the scar measured using 3-D profilometer showing a layer of material of about 2 mm thickness on the scar

is given in Fig. 2 (c), which indicates shear bands and cracks perpendicular to shear bands. Hence at temperature 623 K and at 25 Hz the failure of the material is by fatigue. Fig.2(d) presents the microstructure of the scar of the sample tested at 623 K, 125 Hz at 50N. The above figure indicates presence of oxide particle and glazed surface and absence of fatigue cracks. The particles and cracks in Fig. 2(d) could be due to the crushing failure of oxide particles.

Another interesting observation is that the wear rate at 823 K is higher at 75 Hz than at 25 Hz and 125 Hz. During deformation the work hardening tendency is high for 316LN material and it undergoes dynamic recovery at temperatures above 973 K at strain rates lower than 0.1 s^{-1} . At 25 Hz the micrograph exhibits severe plastic deformation. The lower speed of deformation ($\sim 5 \text{ s}^{-1}$) helps the material to recover, which reduces the degree of strengthening due to work hardening and results in softer material that accommodates plastic deformation. Since the material is ductile and plastically deform without fracture at 25 Hz the wear rate is observed to be low. As the deformation speed is higher

($\sim 15 \text{ s}^{-1}$) than at 25 Hz, the deformation leads to work hardening and reduces the tendency for recovery process. This situation makes the material less ductile and leads to fracturing of the material. The harder material at the surface results in surface cracks and material removal. In view of the above, the wear is high at 75 Hz. At 125 Hz, the higher deformation speed ($\sim 25 \text{ s}^{-1}$) results in higher temperature at the tip of the pin. The calculated rise in the temperature is above

1223 K. This increase in temperature induces the oxidation of the surface. The oxide layer thus formed on the sliding surfaces forms a glazing layer. Moreover, the oxide layer is stronger than that of the base material. Because of the presence of glazed layer the wear rate is low at 125Hz. Fig. 3(a-b) reveals the presence of oxide particles in the microstructure of the wear scar. The Topography of the scar was examined using 3D surface profilometer and it is presented in Fig. 3(c). Fig. 3(c) shows that

the scar was covered with a layer of material of about 2 mm thickness. This layer could be oxide layer. Tests were also performed at a load of 100 N at 125 Hz and at 823 K to confirm the influence of heat generated during fretting on the formation of oxide layers.

The above observations reveal that the wear rate is higher at 125 Hz. In the steam generator of PFBR, the level of oxygen is 2 ppm hence, it is essential to carry out in-sodium tests at 125 Hz.

III.C.8. Effect of Flowing Sodium on Corrosion and Tensile Properties of AISI Type 316LN Stainless Steel at 823 K

Austenitic stainless steels (SS) of different grades are used as structural materials in primary circuit, IHX and piping in secondary loop of fast breeder reactors owing to their good compatibility with sodium in addition to their desirable properties of adequate high temperature mechanical properties and resistance to neutron irradiation. Sodium is used as coolant in liquid metal fast breeder reactors due to its multifaceted properties of high thermal conductivity, low vapour pressure, high boiling

point, large heat capacity and low cost.

Long term exposure of austenitic SS to high temperature sodium leads to mass transfer and corrosion. This corrosion is predominantly governed by the impurities present in the sodium, especially carbon and oxygen. Presence of oxygen in sodium significantly influences the corrosion processes because leaching is usually preceded by the formation of ternary compounds of the steel

constituents with oxygen and sodium. The most commonly encountered corrosion product in sodium containing less than 10 ppm oxygen is NaCrO_2 . The transfer of elements from structural materials by liquid sodium is reported to influence

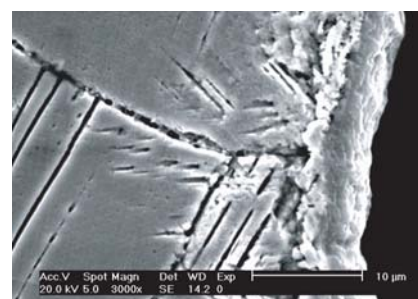


Fig.1 Microstructure showing 316modified layer

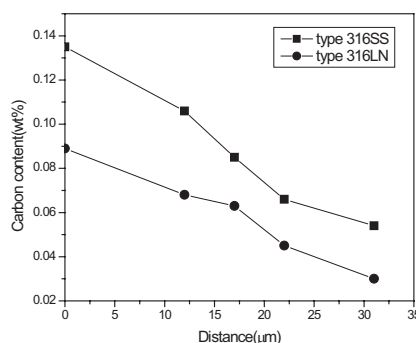


Fig.2 Measured carbon profile for types 316SS and 316LN stainless steel exposed for 16000 hours obtained by SIMS analysis

the corrosion and mechanical properties.

Here we report the results of the changes in microstructure, tensile and corrosion properties of AISI type 316LN SS on exposure to high temperature liquid sodium at 823 K for 16000 hours and compare them with the corresponding changes in type 316 SS exposed for the same duration in high temperature liquid sodium.

In both the steels, thermal ageing at 823 K caused carbide precipitation at the grain boundaries. Due to leaching of elements, there was a surface modified layer of ferrite up to around 10 μm (Fig.1) in type 316LN SS while the modified layer was up to about 15 μm in type 316 SS. The average microhardness of mill-annealed type 316LN SS was 174 VHN. Thermally aged type 316LN SS showed an average hardness of 236 VHN.

An increase of nearly 50 VHN was observed nearer the surface in sodium-exposed material vis-à-vis thermally aged material. The hardness values decreased and reached the matrix value at around 100 μm. This increase in hardness indicated surface carburization of the material due to sodium exposure.

The concentration profile of carbon determined by SIMS showed that, in type 316LN SS, the peak concentration of carbon was attained at 10 μm, immediately after the end of the degraded layer, while the bulk concentration was attained at a distance of 38 μm. In type 316 SS, carbon concentration had attained a maximum of 0.135 wt% at a depth of 43 μm and equaled the bulk concentration at a distance of 74 μm from the surface. The carbon content was less than the bulk concentration up to a depth where a degraded layer which contained ferrite was formed on the surface. The reduction in carbon content in the degraded layer was because the solubility of carbon in ferrite is lower resulting in carbon being rejected from the degraded layer. Comparative carbon profiles of type 316 and 316LN SS, for the period of exposure of 16000 hours, measured by SIMS analysis is shown in Fig.2.

Based on the measured carbon profiles by SIMS, the probable carbon profile after 40 years (Fig.3) was predicted by calculating and using an effective diffusion coefficient. The expected carburization depth was around 260 μm for type 316LN SS.

Tensile test results showed an increase of 22% in yield strength (YS) and a reduction in total elongation by 33% on sodium exposure of annealed material. Thermal exposure of the annealed material at 823 K for 16000 hours, without exposure to sodium, caused an increase in YS by 8% and a decrease of 13% in total elongation. The increased changes on sodium exposure vis-a vis thermally aged condition was attributed to carburization. Similar changes in mechanical properties were observed for type 316 stainless steel.

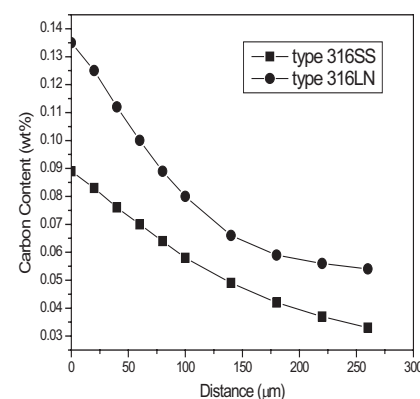


Fig.3 Calculated carbon profile of types 316 and 316LN stainless steel after 40 years

III.C.9. Effect of Metallurgical Variables on the Stress Corrosion Cracking Behaviour of AISI Type 316LN Stainless Steel

High-nitrogen stainless steels (SS) are an important class of engineering materials with their better property combinations such as strength, toughness, creep resistance, non-ferromagnetic behaviour, corrosion resistance and stress corrosion cracking (SCC) resistance. Sensitisation is a common problem encountered with normal grades of austenitic SS. The problem of sensitisation can be overcome by using low carbon austenitic SS. To overcome the loss of strength due to carbon reduction, nitrogen is added to these SS. For PFBR, nitrogen content is limited to 0.08 wt. % in view of improved weldability, code data availability and to minimise scatter in mechanical properties.

The response of nitrogen additions to SCC is varied. Addition of nitrogen to austenitic SS could influence its SCC resistance by influencing two opposing and competing factors viz. decrease in stacking fault energy, which causes an increase in slip planarity and thus deteriorates SCC resistance, and improved

passive film stability which improves SCC resistance. In the present study, AISI type 316LN SS from two different sources, henceforth referred to as SS-1 and SS-2, were tested for SCC crack growth behaviour in boiling aqueous solution of 5M NaCl + 0.15M Na₂SO₄ + 2.5 ml/l HCl (b.p = 381.5 K; pH = 1.3) at various values of K_I (stress intensity factor). SS-2 had a slightly higher Cr, Ni and Mo contents than SS-1, while the nitrogen contents were similar (0.086wt. %). SS-1 was tested for its SCC crack growth behaviour in the mill-annealed condition while SS-2 was tested in the mill-annealed, 15% cold rolled and thermally aged (973 K/800 hours) conditions. The present results were compared with those of AISI types 316 and 304N SS carried out in our laboratory earlier.

The comparison between the SCC behaviour of SS-1 and SS-2 is shown in Fig.1. SS-2 possessed higher K_{ISCC} (threshold stress intensity factor for stress corrosion cracking) and J_{ISCC} (integral threshold stress intensity factor for stress corrosion cracking) and lower

plateau crack growth rate (PCGR) than SS-1, despite the contents of major alloying elements and carbon and nitrogen being nearly the same. Initially, the lower average grain size ($\approx 55 \mu\text{m}$) of SS-2, vis-à-vis that of SS-1 ($\approx 70 \mu\text{m}$) was thought to be the cause for this significant difference in the crack growth rate. However, the difference in the grain sizes was very small to cause the large differences observed. Based on orientation microscopic studies, it was found that the effective grain boundary energy, which is a function of energies of different low angle grain boundaries and grain size, was very low for SS-2. The presence of these special grain boundaries resulted from the processing history of the material. This difference in the nature of the grain boundary characteristics were correlated to a higher resistance to SCC in SS-2.

Fig.2 shows that (i) on cold working, the values of K_{ISCC} and PCGR of mill-annealed SS-2 reduced, (ii) high temperature aging caused a decrease in the value of K_{ISCC} and an increase

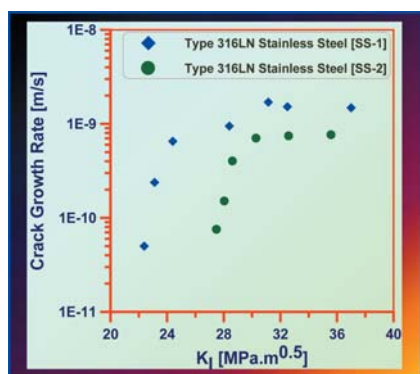


Fig.1 Comparison of two type 316LN thermal SS from different sources

in PCGR of mill-annealed material, and (iii) type 316N SS weld metal possessed lower value of K_{ISCC} and higher PCGR than annealed SS-1. Cold work increases the number of active sites, such as vacancies, dislocation cores and stacking faults where the passive film will not be very adhering and protective, and dissolution can occur easily for SCC to initiate. Hence, lower K_{ISCC} for cold worked material vis-à-vis annealed material. The lower PCGR for the cold worked material could be assigned to any or both of the following reasons: (i) restricted liquid mass transport to the crack tip due to less load line displacement because of higher strength of cold worked material, and (ii) a more lateral dissolution occurring at the crack tip of the cold worked material due to the high strain energy and high defect density there. The lateral dissolution would cause blunting of the crack tip and hence more time

Table 1: Comparison of SCC crack growth data for types 316LN (SS-1 and SS-2), type 304N and type 316 stainless steels

Parameters	304N SS	316 SS	316 LN SS-1	316 LN SS-2
K_{ISCC} (MPa.m ^{0.5})	17.0	13.0	22.38	27.5
J_{ISCC} (kPa.m)	0.9	1.0	2.601	4.47
da/dt (m/s)	1.3E-8	4.0E-9	1.75E-9	7.33E-10

would be required for the crack to resharpen and propagate, thus slowing down crack growth.

The weakly adherent passive film on thermally aged SS-2 requires lower values of K_I to break and expose the bare material to the environment. Hence, the aged material possessed lower K_{ISCC} vis-à-vis annealed material. Since the dissolution rate of the Cr-depleted regions is faster the necessary environmental conditions would be attained more rapidly in the thermally aged material leading to a higher PCGR. Also, the Cr-depleted regions provide easy pre-existing active paths for SCC propagation leading to higher PCGR.

Table 1 shows the comparison of K_{ISCC} and PCGR of type 316LN SS (SS-1) from the present study alongwith the corresponding values for type 316 and 304N SS. Comparison of the crack growth behaviour between types 316LN and 316 SS, showed that type 316LN SS had higher K_{ISCC} and lower PCGR than type 316 SS. This

was because of lower carbon and higher nitrogen contents in the former. Higher values of K_{ISCC} , which would mean increase in resistance to SCC initiation, was explained based on improved passive film stability, which also aids in decreasing the plateau crack growth rate of type 316LN SS vis-à-vis type 316 SS. Type 304N SS had lower values of K_{ISCC} and higher PCGR than type 316 LN SS. This indicated the role of Mo in resisting SCC initiation and growth.

Comparison of crack growth data of types 316 and 304N SS gives an insight to the effects of Mo and N on the SCC behaviour of austenitic SS. The Ni content was higher by 2%, Cr content was lower by 2% and carbon content was higher

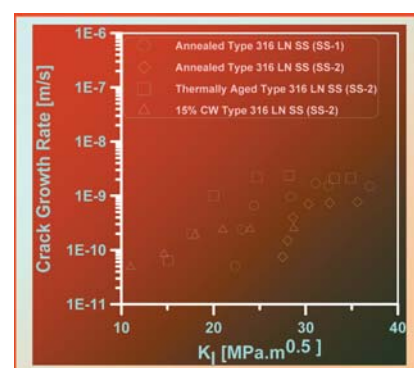


Fig.2 Effect of cold work and aging on SCC crack growth behaviour of annealed SS-2

by 0.01% in type 316 SS. Presence of higher Ni and lower Cr would nearly neutralise any beneficial or detrimental effects of these additions on the SCC properties of SS. Type 316 SS showed lower PCGR and lower K_{ISCC} than type 304N SS. This suggested that nitrogen

imparted better resistance to SCC initiation, as compared to Mo, due to a more adherent passive film that it helped to form. However, Mo imparted better resistance to crack growth for the SS. This was because of the effect of nitrogen in lowering the stacking fault energy, which, in

turn, would promote planar slip. Planar slip accelerates SCC crack growth. However, the presence of both these elements synergistically improves the SCC resistance of austenitic SS as evidenced by better SCC properties for type 316 LN SS as compared to the other two SS.

III.C.10. Creep Strength Reduction Factors for 316L (N) SS Welded Joints

Long term creep properties of indigenously developed 316L(N) SS plates and 316N SS electrodes have been characterized at 973 and 923 K. Creep properties of 316L(N) SS plates, 316N SS weld metal and 316L(N)/316N SS weld joints have been studied at stresses ranging from 120 to 300 MPa and rupture lives as long as 3 years. The specified chemical composition of 316L(N) SS plates and 316(N) SS welding electrodes, and the actual composition of the plates and the weld metal used in this study, are given in Table 1. For the creep design of welded components for fast reactor applications, RCC-MR has specified reduction factors for the strength of welded joints, which is defined as weld strength reduction factor (WSRF). WSRF is defined as the ratio of the creep strength of

the weld joint to that of the base metal at the same temperature and creep rupture time. It is essentially an additional factor of safety since creep strength of weld metal and weld joints are generally lower than that of the plate material. WSRF is a function of creep temperature and time. The creep properties of 316L(N) SS plates and welding electrodes have been developed indigenously and

their creep properties have been evaluated. Fig. 1(a) and 1(b) show the variation of WSRF values with rupture life, at 873 and 923 K respectively as recommended by RCC-MR code. WSRF decreases with increase in rupture time. For a given creep rupture time, the strength reduction factor is lower at higher temperature. Typically, at 923 K, WSRF=1 at short rupture life, and its value decreases to about 0.65

Table 1 : Specified and actual chemical compositions of 316(L)N SS plate, 316(N) SS electrode, 316L(N) SS plate and 316(N) SS weld metal.

Element	PFBR specification		Actual composition	
	316(L)N SS base metal	316(N) SS electrode	316(L)N SS plate	316(N) SS weld metal
C	0.024-0.03	0.045-0.055	0.022	0.06
Ni	12.0-12.5	11.0-12.0	12.5	11.1
Cr	17.0-18.0	18.0-19.0	17.56	18.8
Mo	2.3-2.7	1.9-2.2	2.35	1.8
Mn	1.6-2.0	1.2-1.8	1.68	1.3
Si	0.5 max.	0.4-0.7	0.35	0.53
S	.01 max.	0.02 max.	0.016	0.014
P	0.03 max.	0.025 max.	0.026	0.043
Cu	1.0 max.	0.5 max.	0.07	0.22
B	0.002 max.	0.002 max.	.0012	--
N	0.06-0.08	0.06-0.10	0.077	0.10

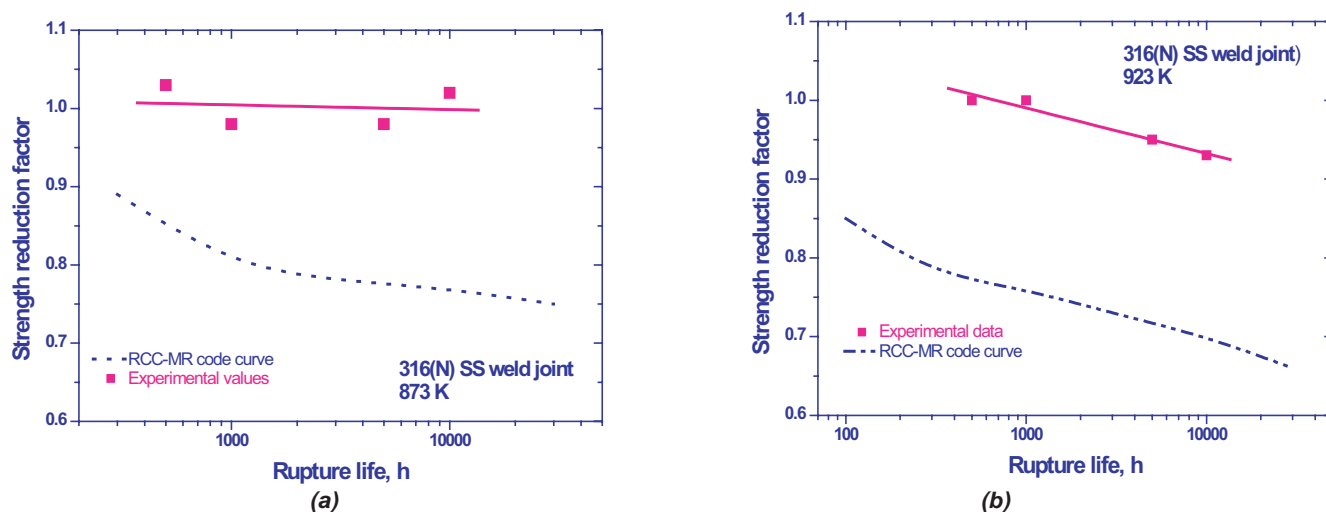


Fig.1 Variation of WSRF values with rupture life, at (a) 873 and (b) 923 K

corresponding to a rupture life of about 25000 hours. The strength reduction factors for the 316N SS weld joints in the present investigation were

found to be higher than the RCC-MR code values; WSRF values at 873 K were found to be close to 1 and was found to be above 0.85 at 923 K. This

implies that the creep strength of the weld joint is close to that of the plates and are significantly higher than the values specified in the codes.

III.C.11. Cross Section TEM Studies on the Effect of Plasma Nitriding of Cr Plated Type 316L Stainless Steel

Hardfacing of stainless steel (SS) components is commonly used to improve the chemical and mechanical properties. Amongst many alternatives,

chromium nitride (CrN or Cr_2N) can attain hardness up to 2400 HV, is thermally stable up to ~ 1273 K and is preferable to Stellite and Colmonoy coatings

in radioactive environments. Plasma nitriding is a diffusion driven process and is able to partially nitride the electroplated (EP) Cr, such that

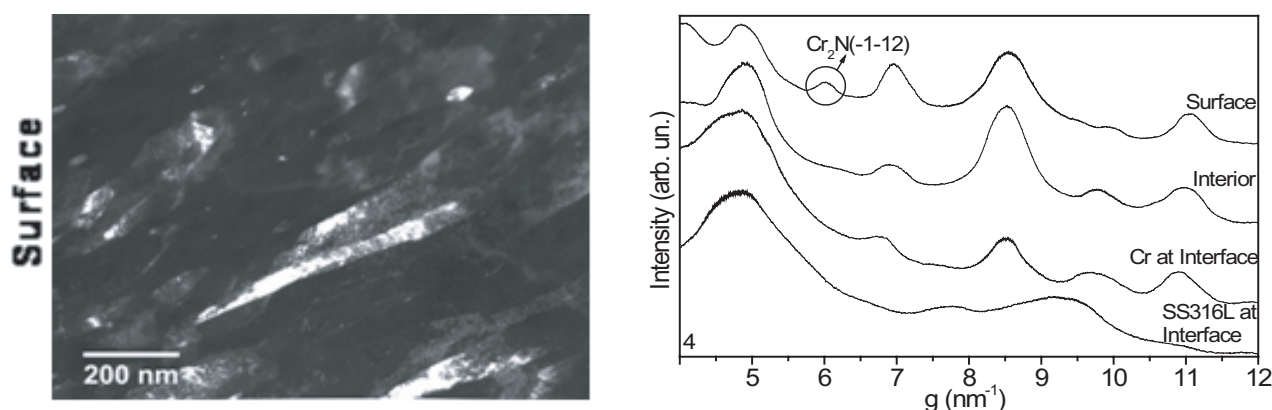


Fig.1 XTEM results on a plasma nitrided Cr sample: (a) DF TEM image near the surface, (b) Intensity plots derived from SAD patterns at various depths from surface.

the nitrided layer is confined to the surface. Cross-section TEM (XTEM) has been undertaken to characterize the nitride phase. Fig. 1 represents the results on a specimen that was nitrided at 773K for 24hrs, (a) TEM micrograph taken close to

surface, and (b) SADP intensity plots against the reciprocal lattice vector, $1/g$, taken from various depths from the surface. Fig. 1(a) shows that the EP-Cr is columnar in nature. Fig. 1(b) shows that a Cr_2N phase is

found only on the surface while all other peaks are from Cr. The results show that nitride forms only on the surface as a mixture of Cr and Cr_2N , under the given conditions of plasma nitriding.

III.C.12. In - house Development of Test Facilities to Study Hydrogen Assisted Cracking in Steel Weldments

Hydrogen Assisted Cracking (HAC) is one of the major forms of cracking that occur in steel welds. Four different tests, namely UT-Modified Hydrogen Sensitivity Test (UT-modified HST), Implant test, Gap Bead-on-Plate (G-BOP) test and Y-groove test, were set up indigenously to study this form of cracking in steel weld joints. Susceptibility of modified 9Cr-1Mo steel and its weld metal produced from indigenously developed welding electrodes

has been studied using these tests. Results from various tests (except from Y-groove tests) indicated that a preheat of the order of 473-523 K is necessary to prevent HAC in these steel welds. In the case of Y-groove test, restraint was low because of the lower thickness of the plate used for testing (12 mm and 30 mm) and it was found that with increase in plate thickness, the preheat temperature to prevent cracking increased. Fig.1 and 2 show the

various of preheat temperature with volume % hydrogen in the shielding gas for UT-modified HST and with lower critical stress for implant test respectively. No cracking was observed at higher temperatures for the given testing parameters.

Results from different tests indicated that both weld metal and base metal are susceptible to HAC with weld metal more susceptible than the base

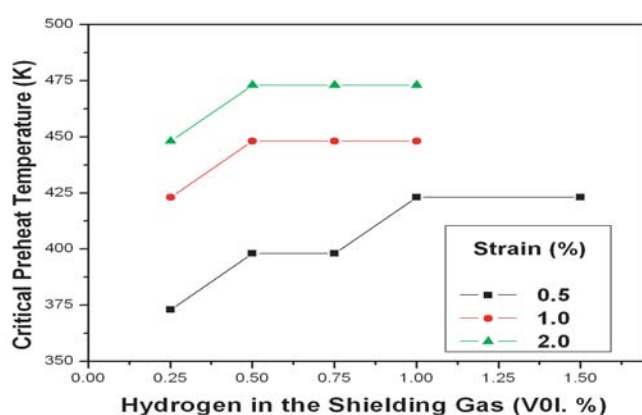


Fig.1 Variation in critical preheat temperature as function of hydrogen in the shielding gas and strain applied on the specimen in UT-modified HST

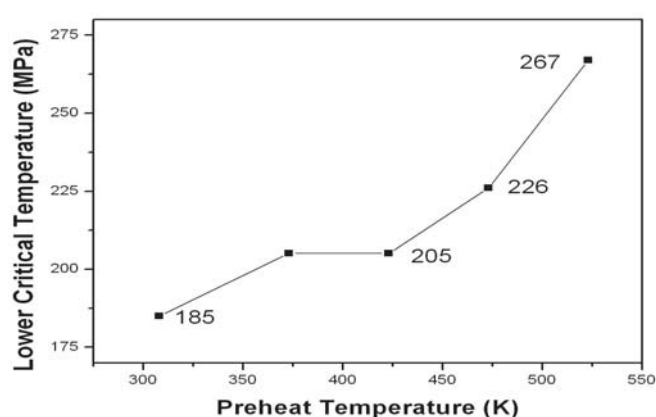


Fig.2 Variation of lower critical stress above which the specimens cracked as a function of preheat temperature. No cracking was observed in specimens prepared at preheat temperature >573 K.

metal. In UT Modified HST cracking apparently initiated in the weld metal and extended up to fine grained HAZ in the base metal. In the implant test, cracking was predominantly in the weld metal at high stress levels and in HAZ at low stress

levels. In Y-groove tests, cracking was confined to weld metal both for straight Y-groove (designed to facilitate weld metal cracking) and in inclined Y-groove (designed to facilitate HAZ cracking) confirming higher susceptibility of weld metal to

cracking than the base metal. G-BOP test is specially designed to evaluate susceptibility of the weld metal to HAC and critical preheat temperature determined from this test is comparable to that determined from UT-modified HST and implant test.

III.C.13A. Fabrication of Non-instrumented Irradiation Capsules for Measurement of In-pile Creep and Mechanical Properties of D-9 Material Using Pre-pressurized Capsules and Tensile Specimens in FBTR

Irradiation induced swelling and creep are important phenomena that affect the design, operation and performance of core structural materials of Fast Breeder Reactors. Alloy D9 is selected for FBR fuel cladding and wrapper tube in view of its enhanced swelling resistance to neutron irradiation and irradiation creep compared to than those of type 316 stainless steel. The Alloy D9 which is a modified type 316 stainless steel with controlled additions of titanium and silicon has been developed indigenously in collaboration with MIDHANI. The irradiation creep behaviour of the indigenously developed D9 alloy has to be evaluated in order characterise and qualify the material for use in FBR.

Pressurised capsules technique is used for evaluating the irradiation creep behaviour of Alloy D9 because this method does not require any instrumentation during irradiation testing in nuclear reactors. Two numbers of non-instrumented irradiation capsules for irradiation of pressurised capsules and tensile specimens of D9 in FBTR have been fabricated to generate baseline irradiation performance data on this

material at low temperature and low fluence irradiation conditions.

Pressurised capsules were fabricated from indigenously developed D9 clad tube of outer diameter 6.6 mm and 0.45 mm wall thickness. The tube is closed by welding at one end and fitted with special end plug at the other end, which enables filling of gas at the desired pressure into the tube using a pressurising



Fig.1 View of irradiation capsule with D9 pressurised capsules and D9 disk specimens (before assembly and welding)

system. A gas mixture of 97% argon and 3% helium was used for the pressurisation. After pressurising, the gas entry path is sealed with a soft gasket and welding is carried out to close the special end plug with a cap. The diameter of the special end plug has been designed to accommodate all features within the diameter of 6.6 mm. The length of the pressurised capsule is about 74 mm. The pressure of gas in the pressurised capsule was determined using the pressure gauge connected in the pressurising system and by using gas laws. These pressurised capsules were fabricated using the specially developed pressurising set up. All the components required for this work were machined in house. The final end caps were welded using laser welding to avoid over-heating of the sealing portion. The finished

capsules (Fig. 1) were helium leak tested and found to be acceptable.

Fifteen numbers of such D9 pressurised capsules have been fabricated and arranged in five partitions in an irradiation capsule along with D9 disk specimens. Out of these 15 pressurised capsules, 5 numbers each were filled with pressures of 2.1 MPa, 4.2 MPa and 6.3 MPa at room temperature respectively. The corresponding pressures at the irradiation temperature of about 623 K are 4.4, 8.8 and 13.2 MPa and the hoop stresses that are developed in the pressurised capsules at the irradiation temperature are 30, 60 and 90 MPa respectively. The second irradiation capsule contains D9 tubular tensile specimens, small size flat tensile specimens and disk specimens of D9. A few

specimens of type 316 stainless steel (FBTR Quality) are also included in this irradiation capsule. Holes have been drilled on the wall of irradiation capsules to allow the reactor sodium to enter and surround the pressurised capsules / specimens during irradiation. The irradiation temperature of pressurised capsules / specimens is same as temperature of sodium (619 to 623 K). The irradiation capsules are assembled in two special steel subassemblies and have been loaded presently in the 4th ring of FBTR for irradiation (Fig. 1). The desired duration of irradiation is one year or above. After irradiation, the capsules will be discharged from the reactor and taken to Radiometallurgy Laboratory and post irradiation examination will be conducted on the pressurised capsules and other specimens.

III.C.13B. Development of Fly Ash Concrete for Nuclear Power Plant Structures

To conserve precious natural resources, and to use industrial waste materials gainfully in nuclear projects, use of fly ash in project sites at Kalpakkam was explored, by consolidating knowledge gained in various units of DAE.

Positive effects of using fly ash in concrete are as below:

- Better quality of concrete; better rheology, higher strength, enhanced durability.
- Eco-friendly, minimizing greenhouse gas emissions

associated with the manufacturing of Ordinary Portland Cement (OPC), environment friendly disposal of millions of tones of fly ash.

- Preservation of resources, saving in energy requirements

in the production of OPC, preservation of limestone and coal reserve.

For deploying fly ash in plants construction, development of different mixes of Traditionally Placed Concrete (TPC) and Self Compacting Concrete (SCC)

using fly ash, suitable for NPP structures is undertaken in collaboration with AERB, NPCIL and BHAVINI. Main results of the work under taken are summerised in this article.

Concrete ingredients which are in use for the construction

of PFBR were used in this study. Fly ash from Ennore thermal power station was used. All the concrete ingredients were tested as per the relevant specification. Table 1 gives the mix proportions.

The graphs in Fig.1 are representative of the trends in fly ash concrete. Interpretations drawn are summarized below.

Fly ash concrete mixes have better slump retention property, more cohesiveness, lesser bleeding, comparable air content, slightly lower density and slightly delayed setting time as compared to control mixes (ie. mix with no flyash). All the three mixes meet the strength requirement of grade M50, M35, M20 respectively at 56 days. For all the three grades of concrete the Rapid Chloride Penetration Test (RCPT) values at 28 days as well as at 56 days is much lower for fly ash concrete mixes as compared to respective control mix. The reduction in RCPT values is due to improvement of pore structure with the addition of fly ash in the concrete mix.

Based on the results, fly ash concrete mixes were identified and recommended for the construction of Power Island structures of PFBR.

Table 1 : Concrete mix proportions

Grade	Binder			Aggregates, kg			W/b	Admixture %
	Total (kg)	Cement (kg)	Fly Ash %replacement	Coarse	Fine			
					Crush Sand	River Sand		
50	585	292.5	50	1038	170	427	0.28	1.6
50	525	315	40	1083	191	485	0.291	1.6
50	410	410	0	1083	246	548	0.37	1.3
35	420	210	50	1140	219	510	0.35	1.6
35	375	225	40	1130	235	549	0.38	1.8
35	320	320	0	1172	265	590	0.45	0.9
20	385	115.5	70	1113	371	353	0.4	1.2
20	335	134	60	1143	397	378	0.45	1.4
20	295	147.5	50	1163	421	401	0.5	1.6
20	250	250	0	1194	489	466	0.5	1.0

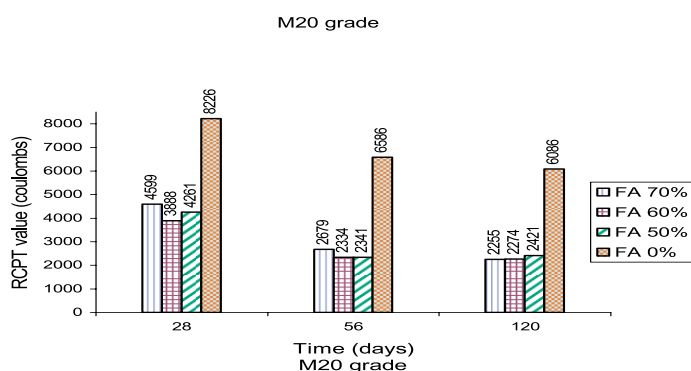
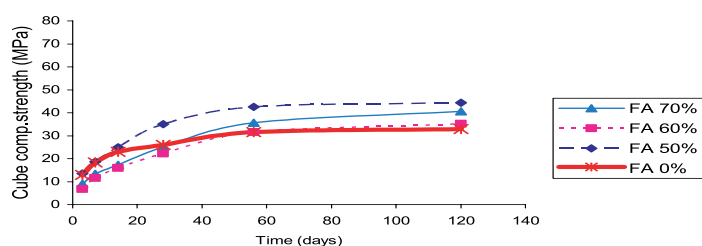


Fig.1 Properties of fly ash concrete

III.D. Control Rod Materials

III.D.1. Augmentation of Boron Enrichment Plant

Because of the higher cross-section of ^{10}B for the reaction $^{10}\text{B}(n,\alpha)^7\text{Li}$, boron compounds enriched in the ^{10}B isotope are generally used for control rods of Fast Breeder Reactors (FBRs), neutron counter and neutron capture therapy of malignant tissues. Natural boron has 18.8 at% of ^{10}B and 81.2 at% of ^{11}B . For efficient control of fast reactors, it is required to use highly enriched boron in ^{10}B isotope.

Ion exchange chromatography is one of processes that are used for the separation of natural isotopes of boron. In this process, a strong base anion exchange resin in hydroxyl form is exchanged with boric acid solution. After loading boric acid to the required band length, it is displaced with an acid to achieve the desired enrichment. The technology for enrichment of isotopes of boron to 65% in ^{10}B required for PFBR has been demonstrated at the centre. Using ion exchange resin with 0.3mm to 1.2 mm particle size (termed as normal resin), it has taken almost 4 years to achieve 65% enrichment. Mathematical calculations indicated that

using ion exchange resin with 0.3mm to 1.2 mm particle size, it would not be possible to achieve enrichment in ^{10}B to 91%. Studies were undertaken to improve upon the equilibration time required to achieve the enrichment. Investigations revealed that the use of fine particle size resin could result in reduction in equilibration time for enrichment as the value of Height Equivalent to a Theoretical Plate (HETP) which is an important parameter in column performances in ion exchange chromatography can be reduced significantly by using smaller particle size resin.

Laboratory and pilot scale experiments were carried out using resin with particle size of 0.075 mm to 0.15 mm, (termed as fine resin) for evaluation of the resin for enrichment performance. The results of experiments carried out with normal resin and with fine resin under identical conditions are shown in Fig.1. From this figure, it could be seen that enrichment to 40% in ^{10}B could be reached using fine resin whereas for normal resin enrichment to only 26% in

^{10}B could be reached in the same time.

A computer code 'CASCADE' was developed for predicting the enrichment profiles for boron enrichment based on Fujine's model (developed for Lithium isotope enrichment). In this model, the band is divided into theoretical stages. The governing equations are derived from the material balance of the isotope in the resin phase and solution phase in a theoretical stage at any given time. The enrichment profiles are calculated by using band length, band velocity and total time of operation as inputs using assumed values of HETP. The calculated profiles are then compared with experimental enrichment profile, and the value of HETP that closely matches calculated profile, is taken as the value of HETP of the column. Once HETP is estimated, the same model is

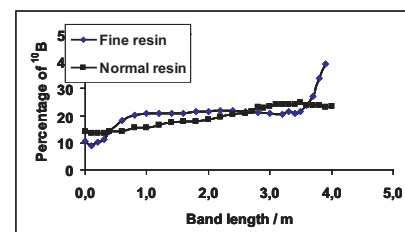


Fig.1 Enrichment profiles after 36 m of borate band movement

used for predicting the enrichments that could be achieved later in the columns. The accuracy of the mathematical model is assessed by comparing isotopic enrichment profiles obtained during operation with theoretical values obtained using mathematical model.

The calculations carried out for the data obtained during operation of pilot plant using fine resin are listed in Table 1. The samples for isotopic profile were taken after 18m and 36m of band movement. It can be seen from the results that the projected enrichments are within $\pm 10\%$ error. Hence, the mathematical model gives confidence in simulation of boron enrichment process.



Fig.2 A view of augmented boron enrichment plant.

Table 1 : Analysis of data for pilot plant using fine resin

Experiment No	Band velocity (cm/h)	Estimated HETP (mm)	Migration length m	Enrichment %		% Error in prediction
				Theoretically predicted	Experimentally attained	
1	5	7	18	32.15	32.66	1.6
			36	38.0	40.1	5.2
2	10	7	18	29.95	31.60	5.2
			36	32.1	37.0	13.2
3	10	7	18	32.15	31.4	-2.3
			36	37.9	38.9	2.6
4	10	7	18	32.1	33.8	5.0
			36	38.0	41.0	7.3
5	10	5	54	42.6	47.0	9.4
			36	41.8	41.0	-1.9
			54	47.4	47.0	-0.85
			72	52.1	52.9	1.5
			90	56.3	55.9	-0.36
			108	59.9	54.6	-9.7

Based on the results of these experiments, the Augmented Boron Enrichment Plant (ABEP) was designed for the production of boron enriched in ^{10}B . Fig.2 shows a photograph of the plant. The plant consists of two streams of ion exchange columns each having 5 process ion exchange columns interconnected in series. One external

regeneration column is provided for each stream. The fine resin was charged to process ion exchange columns and pretreated for 5 cycles of OH - Cl exchange by using 1.25N NaOH and 1.0 N HCl followed by intermittent washing with DM water. In the final cycle of pretreatment, the resin was retained in hydroxyl form and thoroughly washed with DM water. Boric acid

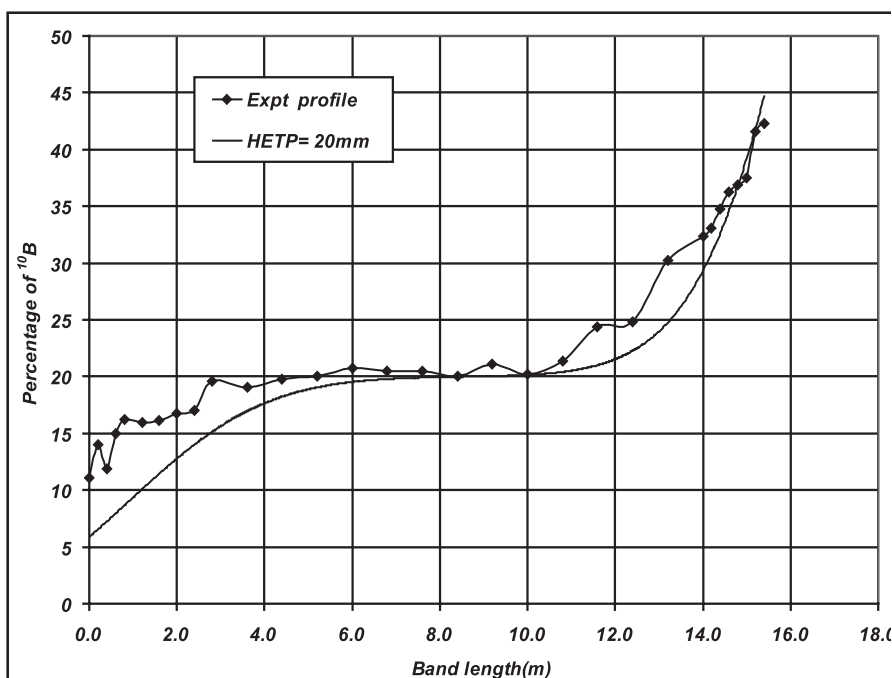


Fig.3 Enrichment profile obtained after operation of ABEP for 2 months

solution in the concentration range of 0.30-0.35M was charged to three ion exchange columns interconnected in series to develop the required length of borate band.

After commissioning the plant, the displacement of borate band in ABEP was started. Once the column was exhausted (ensured by the absence of boric acid in the sample drawn from the outlet of the column), the resin was hydraulically transferred to a Regeneration Vessel (RV) for

regeneration. After regeneration and rinsing the resin in RV, it was transferred back to the same process ion exchange column. The pressure drop observed per column was in the range of 1.5 to 2 bar initially and later it stabilized to 1.2 bar per column. After completion of 4 cycles of band displacement, samples were drawn from the rear end of the borated band and sent for isotopic analysis. As shown in Fig. 3, the enrichment in ^{10}B to 40% was achieved in 2 months of operation using fine resin

whereas with normal resin it took 11 months to reach the same level of enrichment in ^{10}B .

The operation of the plant has given confidence in using fine resin with manageable pressure drop in columns, external regeneration of the fine resin after hydraulic transfer, and all the more that enrichment could be attained reach faster compared to ion exchange columns using normal resin.

III.D.2. Removal of Fluoride from the Effluent Generated during Elemental Boron Production

Boron carbide containing 65% enriched ^{10}B will be used as the control rod material in FBRs. R&D programme is being pursued for enrichment of isotopes of boron using ion exchange chromatography, production of elemental boron from potassium fluoroborate through molten salt electrowining process. During the production of elemental boron from potassium fluoroborate, effluents rich in fluoride are generated. These effluents cannot be disposed off into water bodies due to the disposal limit of less than 2 mg/litre of fluoride. Hence, a

method for effluent treatment was developed to effectively treat these fluoride effluents in two stages. In the first stage, the concentration is reduced to less than 20 mg/litre using chemical methods. This effluent is further treated using membrane filtration to reduce the fluoride levels to <2 mg/litre before disposal.

1000 litres of the fluoride effluent was taken up for treatment. This effluent was first analyzed for fluoride concentration using fluoride ion selective electrode. The concentration of fluoride ions

in the effluent was found to be 180 mg/litre. The effluent was transferred to a storage tank and calcium ion (as calcium chloride) equivalent to 25% excess over stoichiometric value of quantity of fluoride ions was added. The pH of the reagent was adjusted by adding sodium hydroxide. The contents of the vessel were mixed thoroughly. The precipitates were allowed to settle down in the reaction vessel. A sample was taken from the sampling port of the vessel and analyzed for fluoride. In this way, the fluoride concentration was brought down to 20 mg/litre.

R&D experiments were carried out to reduce the fluoride levels from 20 mg/litre to <2 mg/litre using nanofiltration from simulated fluoride solutions. Initially, experiments were carried out using membrane having pore size of 50nm. It was observed that fluoride concentration in the permeate was same as in the feed solution. Further experiments were carried out using

membrane having pore size of 0.1nm. It was observed that when fluoride solution with concentration of 20 mg/litre was passed through the membrane, the fluoride concentration in the permeate was approx 14 mg/litre indicating a slight reduction in fluoride ion concentration. When 100 mg/litre of calcium was added to the feed solution and passed through the

membrane, the permeate had a fluoride concentration of 2.4 mg/litre. In another experiment, when 10 mg/litre of aluminium and 100 mg/litre of calcium were added and passed through the above membrane, the fluoride level of the effluent was less than 1 mg/litre which is below the disposal limit of 2 mg/litre. Thus, a scheme for reduction of fluoride levels in solutions has been evolved.

III.E. Safety Studies

III.E.1. Experimental Demonstration of Stability of PFBR Core Subassemblies under Seismic Excitations

PFBR core consists of a central fuel region enveloped by blanket region, which in turn, are surrounded by neutron reflectors. Physically the core is made up of different types of subassemblies (SA), 1757 in total, supported on the Grid plate (GP) and one typical SA mounted on the GP is shown in Fig. 1. The heat generated in the subassemblies is removed by the coolant sodium flowing axially through them. In order to provide the required flow, the pressure of sodium in the GP is maintained at about 0.7 MPa, which develops an upward lift on each of the core SA. A maximum hydraulic lifting force, equal to 24 % of weight

of SA is possible, in case of pump running at 110 % of design flow rate. During normal operating condition of the reactor, the net gravitational acceleration acting on each SA (even though it is less than 1 g) is always downward and hence there is no fear of any uplift. However, there exists a concern during seismic events, in particular, under vertical excitation component. The seismic analysis of reactor assembly indicates that the peak vertical acceleration of GP can be as high as 0.88 g under SSE (Fig.1). The safety criterion to be respected is that under combined effect of self weight, upward fluid force and seismic

excitations, no SA should get lifted off. This critical safety issue has been resolved by experimental investigations.

Experimental simulations

One free-standing fuel subassembly is considered for the investigation. This implies

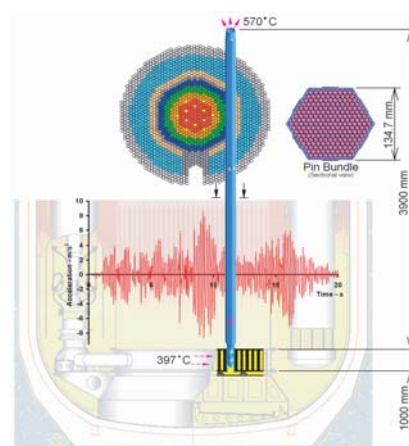


Fig.1 Essential input data (one SA mounted on GP)

that the effects of mechanical interaction with neighbouring subassemblies are ignored to yield conservative results. The mass of the test mock-up subassembly is 245 kg equal to that of the PFBR subassembly. Further, the test mock-up is geometrically similar to reactor conditions. The upward fluid force is simulated by pumping water under pressure using the setup shown in Fig. 2. The SA is made to freely hang through a load cell so that it can measure the weight of the SA accurately. The measured weight by the load cell is plotted as a function of applied pressure at the bottom in Fig. 2. A pressure of 0.7 MPa is applied at the

bottom of SA to generate the targeted upward lift force equal to 30% of weight of SA.

Seismic excitations

Test has been done by using tri-axial shake table of 10 t capacity existing at the Centre. Experimental setup is shown in Fig.3. A dedicated data acquisition system with 64 channels is used for capturing the structural response under seismic excitation. Three LVDTs are used for measuring the relative displacement of the SA with respect to GP top. The set up is subjected to vertical excitations with the peak accelerations to ensure the realistic transmission of seismic

excitations to the SA.

Excitations corresponding to peak acceleration of 0.5 g and 1.0 g are applied and the accelerations are measured at the GP top portion. The applied accelerations and the average relative displacements with respect to GP top surface, measured by LVDTs are shown in Fig.4. The random variation of displacements for the peak acceleration of 0.5 g (Fig.4a)

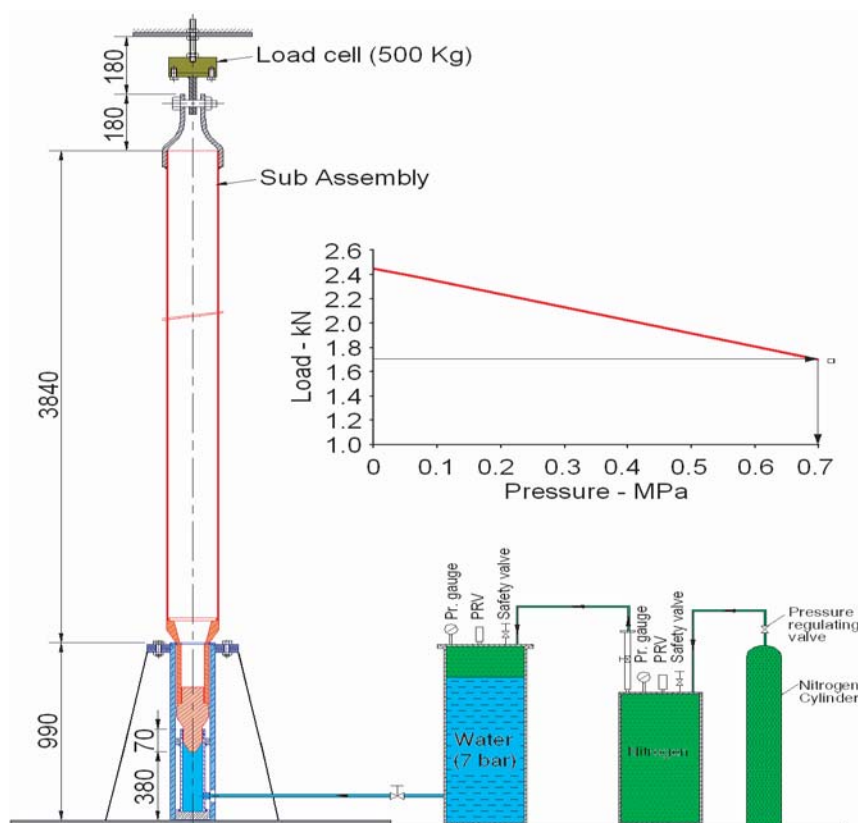


Fig.2 Simulation of upward force



Fig.3 SA mounted on shake table



Fig.4a: SA Displacement for 0.5 g (vertical)

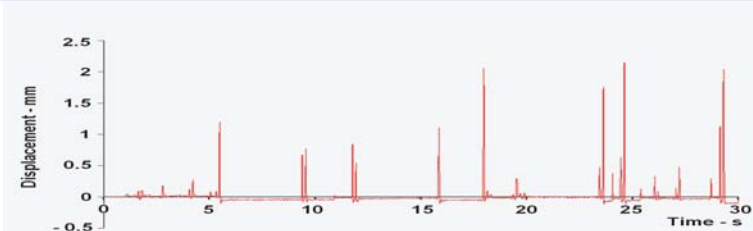


Fig.4b SA Displacement for 1.0 g (vertical)

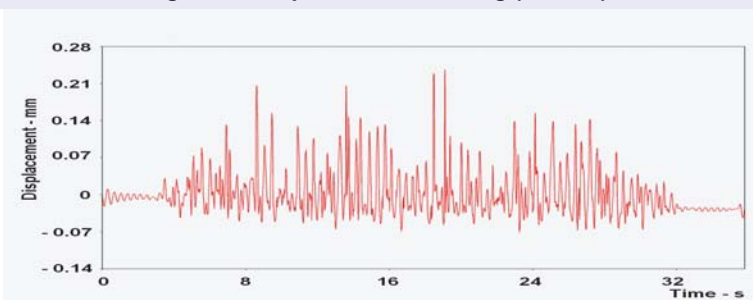


Fig.4c SA Displacement for 1 g (multi-axial)

indicates that there is no impact and hence SA always gets attached with grid plate. Further, the discrete displacement peaks observed for 1.0 g (Fig.4b), imply that there are impacts from which it is inferred that the SA gets lifted off. However, the magnitude of lift off is insignificant (< 2 mm).

In order to investigate the effects of horizontal excitations, tests are repeated for 1.0 g peak acceleration, by way of applying seismic excitations in all the three X, Y and Z direction using the input time history corresponding to the GP location. The random variation of displacement response with peak value < 0.3 mm, indicates that there is no lift off of SA (Fig. 4c). This further demonstrates that there is no risk of instability or lift off of subassemblies under seismic loading.

III.E.2. Real Time Decision Support System for Radiological Emergency as a New Feature during the Off-site Emergency Exercise - 2007

The real time Decision Support System (DSS) developed at the centre for radiological emergency was demonstrated for the first time during the off-site emergency exercise on August 24, 2007. This biennial exercise is conducted by the Kalpakkam Emergency Committee to train and activate the emergency response administration and the systems for keeping it in live

condition to cope with a real case of an extremely unlikely emergency. It contains the most advanced meteorological forecasting module and involves integration of the same with a dispersion and dose prediction module, commissioning of a real time meteorological data acquisition & archival system from 50 m meteorological towers installed around Kalpakkam and

creation of a realistic geographical data base used as the surface boundary condition in the model.

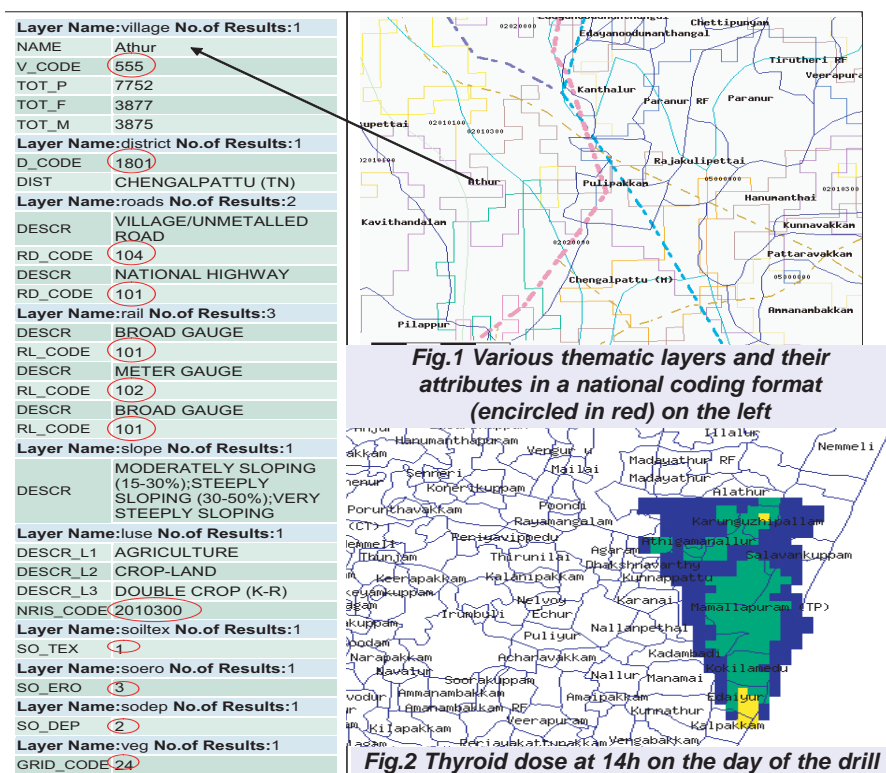
At the front end, the DSS has a web based on-line Geographic Information System (GIS) display and query module developed in collaboration with Regional Remote Sensing Service Centre (RRSSC-ISRO), Nagpur. This module is a

software package indigenously developed by RRSSC following the system requirement specification laid down by RSD, IGCAR. The expertise of RRSSC in remote sensing data analysis and geo-projection of the local data base in a high resolution imagery was a specific contribution to the DSS. The DSS has three options namely to show the dose projection assuming an emergency under loss of coolant accident in MAPS, dose projection under an unit release of activity and dose projection for known release rate that can be entered by any client on his machine. These options are provided because the actual release rate is unknown in case of an accident. During simulation of the Off-site Emergency, on the day of the emergency drill, the DSS could show the forecast of the radioactive plume in a 100 km radius, and now cast the radioactivity and dose spread in a local range of 10 km radius. The meteorological data was displayed on-line in order to know the wind speed and direction towards which the radioactive plume would travel. The data showed that since morning hours the direction was from west and it changed to south east in the afternoon due to sea breeze onset.

The villages Kadampady and

Ambur were preplanned for evacuation drill. However the DSS showed many other villages falling under the footprint of high dose values requiring evacuation in case of a real release. The GIS query module helped as a ready reckoner to list out details about the villages likely to be affected. For example, the spatial query module 'SQ' could show on-line, the plume trajectory prediction at any given time of the day, the present plume position based on real time data, the villages, population dose and severity of the emergency such as whether evacuation is required etc. Similarly, the radius query could list out the villages having shelters and hospitals within a specified radius. Village

information database of the DSS is designed in a manner similar to the format of VRC (Village Resource Centre), an informatics kiosk being set up by ISRO throughout the country. Fig 1 shows the thematic layers and the coding followed in the national format. The predicted plume during sea breeze in agreement with actual data is shown in Fig. 2. The Kalpakkam Management Committee and members of the National Disaster Management Authority were shown the DSS and its various functionalities. They suggested that the model may be implemented in other sites of nuclear power plants. Also it was pointed out that such a system is required for large chemical plants.



III.E.3. State of the Art Automatic Multilevel Meteorological Tower System

Meteorological towers are the platforms providing continuous in-situ information within the lower atmospheric layer called the Atmospheric Boundary Layer (ABL). Though there is a number of meteorological towers ranging in height from 30 to 60 m in the country, many of them do not have multilevel sensors installed for all the basic atmospheric parameters like wind speed & direction, temperature, relative humidity and pressure. Our effort has been to operationalise a simple, reliable and easy to maintain system of multilevel meteorological tower based on a generic type of data acquisition system.

Fifty meter tall meteorological lattice type guyed tower was designed in collaboration with Structural Engineering Research

Centre, Chennai, and erected at Kalpakkam. As compared to the free-standing fixed base tower, the above design can be implemented at a comparatively lower cost. At Kalpakkam, one of the towers is located on the coast and the other two are located perpendicular to the coast at distances of 7 km and 15 km from the coast. Other features of the tower developed in-house are signal conditioners, remote data acquisition system (RDAS) with a more generic input data base covering various sensor models, user friendly software and on-line data communication links through ethernet, e-mail and RF transreceivers.

System electronics and hardware

The towers are instrumented at multi levels with conventional sensors for various parameters and fast response sonic anemometer for turbulence measurement. Fig. 1 shows the distributed network modules and the signal conditioners. A rugged, user-friendly data acquisition system was designed around an industrial embedded computer platform

with RS 485 based embedded distributed network modules located near the tower base as an interface with the sensors. Since the nodes are connected in parallel, they can be disconnected from the host without affecting the performance of the remaining nodes. The biggest advantage of using such a configuration is that the main data acquisition system i.e. an industrial PC can be housed in a weather proof shelter box fixed on the tower so that no separate room or cabin is required. It can also be kept in a laboratory away as far as 600 m from the tower, the connecting cable being a two core cable for RS 485 signal from the RDAS to the tower.

The universal network controller used for RDAS is a system that has an application ready platform and supports several standard networking interfaces, such as Ethernet, wireless Ethernet, RS-232, RS-485 and on board I/O interfaces. It has an open architecture and is extremely reliable in the field as it has a fan-less, cable-less architecture. The system was found to be extremely rugged



Fig.1 Distributed network modules and signal conditioners at the base of the tower

and robust and suitable for use in harsh and critical environments such as the one we have at Kalpakkam tower location, a coastal site. The system has a strong mechanical design, and has excellent anti-shock and anti-vibration properties.

Software, data structure and online data links

The application software has been designed around DASYLab. The system installed at the tower has all the user friendly menus for configuring the parameters and also has real time graphical and tabular displays of real time data and recent data (values and trends) on the monitor. The screen, in addition to showing the status of the DAS, has links to a number of other data display screens. Most of the ready

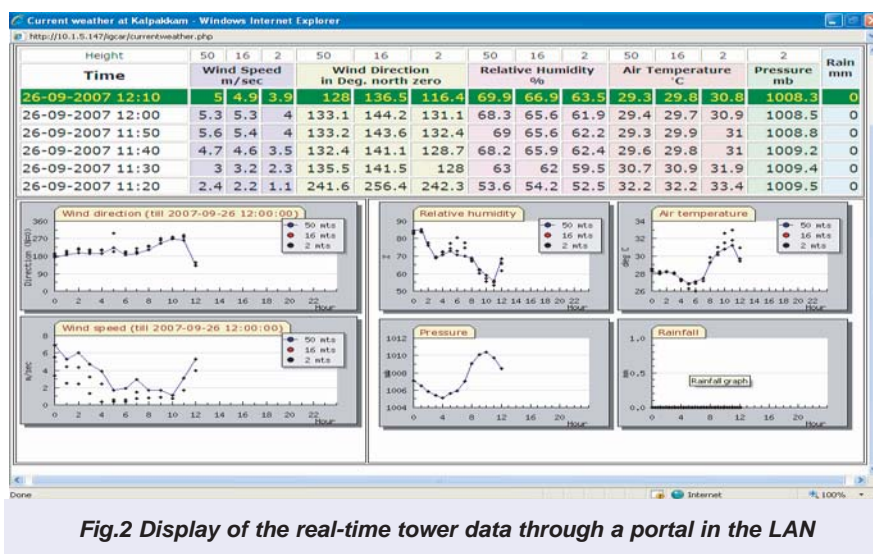


Fig.2 Display of the real-time tower data through a portal in the LAN

made field - installed RDAS do not have the real time graphical output facility. The salient feature of the software developed for this system is that all the above features and the various screens are available in real time and on-line without interrupting the data acquisition during the actual logging of data in the field.

The system is operational in

the field and has been providing input data to the real-time dispersion model of a decision support system for radiological emergency. In the present installation, the 10 min. averaged tower data is received by a server located about 8 km away from the tower and real time data is displayed through a web portal in the local LAN of IGCAR. A typical display of data is shown in Fig.2.

III.E.4. Devices to Minimize Gas Entrainment in PFBR Surge Tank

Gas entrainment is an undesirable phenomenon and it is to be avoided from considerations of cavitation in the secondary sodium pumps and heat transfer in the secondary circuit. In the secondary circuit of Fast Breeder Reactors the potential source of entrainment of argon

cover gas into liquid sodium is in the surge tank located upstream of the Steam generator. It is therefore essential to mitigate the entrainment of the argon gas into liquid sodium in the surge tank itself. The phenomenon of gas entrainment was modeled in a 5/8 scale model of the

surge tank of PFBR. The choice of the scale size was based on the similitude criteria derived from non dimensional analysis of the dominant forces which initiate the phenomenon of entrainment. The geometrical and flow parameters that strongly influence the mechanism of entrainment were

investigated in these studies. The need for devices to mitigate entrainment was established from these studies.

Efforts to finalize an optimum configuration of the device that would serve to eliminate entrainment was carried forward through a series of flow visualization tests in the model using water as the simulant. The selection of the devices employed for testing was, governed by the philosophy to reduce the height of the liquid column above the outlet nozzle for the onset of entrainment.



Fig.1 Pepper pot assembly in model



Fig.2 Ring plate cylindrical perforated shell

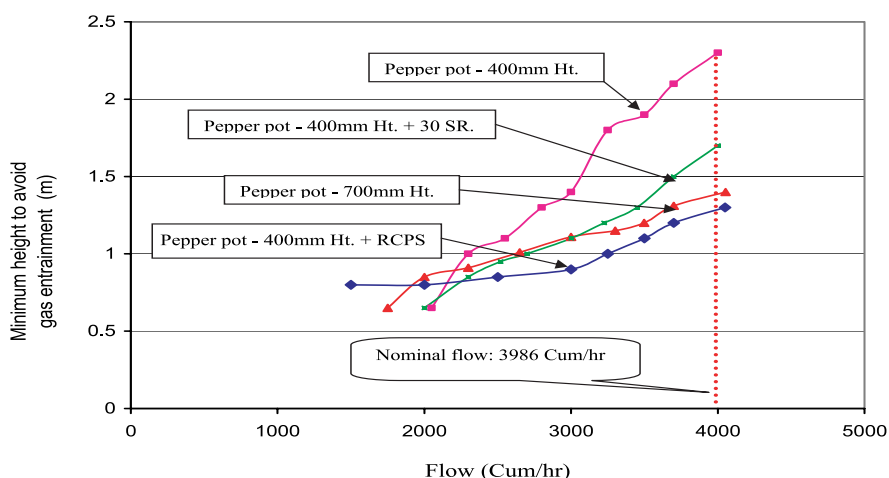


Fig.3 Minimum height required to avoid gas entrainment for different conditions

The efficacy of devices was proven with simple stiffener rings and porous plates, wherein the height of liquid column at which initiation of entrainment occurs had dropped considerably compared to the case without any device. However the reference height of the liquid column based on the operational requirements was even lower. It was necessary to test a combination of devices like the stiffener ring in conjunction with porous plates to reduce this liquid column height. A series of test with 22 different configurations were conducted to reduce this height. The pepper pot configuration (Fig.1) was one device which, when tested produced very encouraging results. But to reduce the liquid column height further to the required levels the variations in the geometry of the pepper pot alone was not sufficient. Hence,

this device was used in combination with a Ring plate Cylindrical Perforated Shell (RCPS) (Fig. 2). This combination was found to be very effective and the minimum possible height of liquid column without entrainment for nominal flow was 1320 mm from the outlet nozzle corresponding to 2050 mm in prototype. The tests have confirmed the adequacy of the configuration and the same is recommended for deployment in the reactor. Fig. 3. shows the minimum height required to avoid gas entrainment for different combinations in model. The effect of devices is not considerable at low Froude No. (upto 2.5) whereas for higher Froude No. the configuration of devices plays an important role in minimizing the gas entrainment phenomenon at lower heights of liquid column.

III.E.5. Simulated Sodium Test Results of Eddy Current Position Sensor

Eddy Current Position Sensor (ECPS) has been conceptualized to detect whether the DSR has reached its bottom most deposited position or not and to find out free fall time of DSR using ECPS signal. In the earlier version of ECPS, primary coils housed in DSR electromagnet side and secondary coils housed in sheath side were kept axially aligned. Detailed analysis for reactor conditions indicated that in reactor primary coil and secondary coils will get axially misaligned up to a maximum of 45mm due to thermal expansion and irradiation induced dimensional changes. Therefore a new configuration of ECPS which can take care of axial misalignment of 45mm was conceptualized and tested in laboratory scale. Air test was carried out in a 1:1 model where the presence of sodium was simulated by an equivalent thickness of aluminum sheet between primary side and secondary side coils.

In ECPS (Version-3), where axial misalignment of 45mm is taken care of, secondary coil occupies whole 65mm axial length on DSR sheath side. This secondary coil also works as

signal transfer coil. In primary side totally three coils (one primary & two pick-up coils) are housed in 105mm axial length. Schematic of ECPS-3 is shown in Fig.1. While conceptualizing the ECPS-3 schematic, constraints of space availability of 65mm only on DSR sheath side is taken into account and advantage is taken of the fact that axial misalignment of maximum 45mm is only in one direction i.e. DSR electromagnet moving 45mm below compared to secondary sheath side coil.

The primary is excited by a constant current source and produces an alternating magnetic field which induces a voltage in the secondary coil on the sheath side. An alternating current starts flowing due to induced secondary voltage since the secondary side circuit is closed. The magnitude of this secondary current depends on the impedance of the secondary circuit. The impedance of the sensor coil (on secondary side) is a function of the permeability of the material in the sensor coil region. Since the piston of the DSR is made of modified 9Cr-

1Mo, which is magnetic material, the dropping of DSR causes a change in the impedance of the sensor coil resulting in a change in secondary side current. This change in secondary current causes a change in the net magnetic flux and hence in the pick-up voltages.

Initially, the bottom pick-up will be aligned with the secondary coil, as the axial misalignment takes place the bottom pick-up will move downwards and the top pick-up (which is identical to the bottom

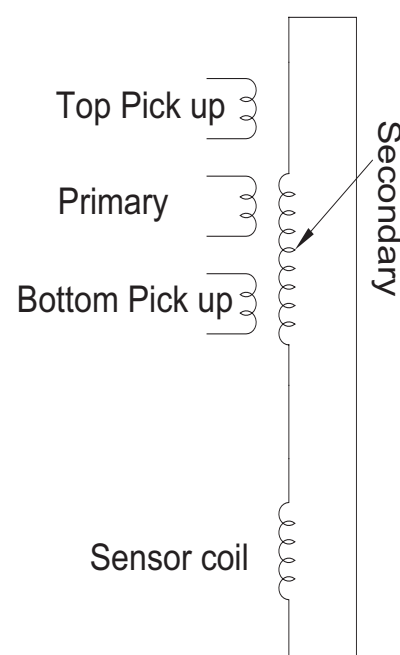


Fig.1 Schematic of ECPS to take care of axial misalignment

one) will align with secondary coil. At any time atleast one pick-up coil will be aligned with secondary coil. The change in voltage in pick up coil due to change in position of DSR will be the indication of DSR reaching bottom most position. Further, in order to avoid the ambiguity as to which pick-up voltage to be sensed, the sum of the pick-up outputs is taken and analyzed to detect DSR position.

In order to validate the proposed configuration a 1:1 model was fabricated. Presence of sodium within the annular space between the primary and the secondary side coils is simulated by 1mm thick

aluminum sheet. The set-up was tested at various frequencies from 100Hz to 1000Hz at constant current of 100mA, 200mA and 300mA. From the test results it is seen that at 300mA current the change in pick-up output is varying from 10-16mV for various misaligned positions.

Fig. 2 shows the simulated laboratory test result for change in pick-up voltage with and without target when the axial misalignment is 45mm between primary and secondary side. The maximum change for 45mm comes out to be 13mV which can indicate the position of DSR.

Thus, from the experimental

results of the simulated sodium testing, it can be observed that the proposed configuration is able to give a measurable change in pick-up output (10-16mV) for different misaligned positions and hence, can be applied for position detection of DSR in the fast reactors.

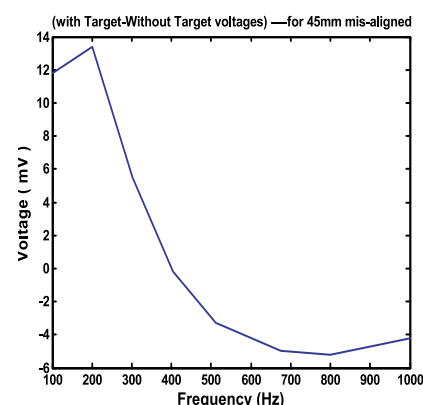


Fig.2 Pick-up output voltage variation with frequency with 45mm axial misalignment

III.E.6. Techniques for Assessing Concrete Damage

In the secondary circuits of Fast Breeder Reactors, if a sodium spillage occurs on concrete, sodium - concrete reaction takes place and the concrete gets weakened. To assess the damage, Differential Thermal Analysis (DTA) and Fourier Transform Infrared Spectroscopy (FTIR) techniques have been adopted. The status of the sodium interacted concrete has been evaluated by studying the change in Ca(OH)_2 content through DTA and O-H stretching frequencies

through FTIR techniques. To study these techniques, blocks of specially cast limestone concrete with a square cavity were exposed to burning liquid sodium at initial temperature of 873 K for 30 minutes in open

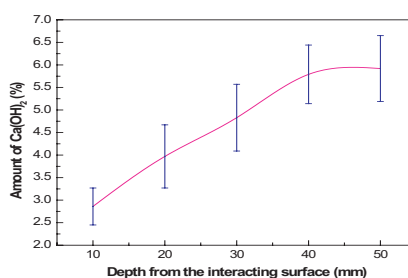


Fig.1 Variation of Ca(OH)_2 content as a function of depth

air. Samples were collected from 5 locations of the cavity floor of the sodium interacted blocks. From each location 5 samples were taken for every 1 cm depth.

Differential thermal analysis (DTA) technique

Ca(OH)_2 is one of the hydration products of Portland Cement and is in the range of 6 to 7 % in concrete. It decomposes in the temperature range 753 to 773 K endothermically. DTA is a

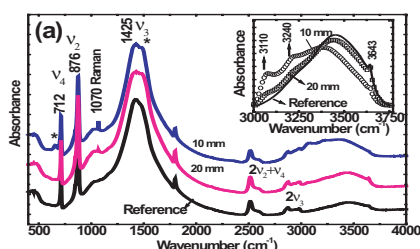


Fig.2a Room temperature infrared spectra of reference sample along with sodium exposed samples removed from 10 and 20 mm from the affected surface of concrete

convenient method to estimate the Ca(OH)_2 content through its characteristic decomposition. The content of Ca(OH)_2 as obtained from the peak area at 753 K from DTA, is plotted as a function of depth for the samples from one of the blocks in Fig.1. From the figure it is clear that the concentration is increasing linearly up to about 40 mm depth of interacted concrete. Thus it is clear that DTA is a sensitive means to obtain the Ca(OH)_2 content, which in turn is an indicator of the concrete damage.

Fourier transform infrared (FTIR) studies

Alternatively, the quality of concrete can also be determined from their characteristic stretching frequencies from the mid infrared region absorption spectrum. Control runs have also been carried out to delineate the thermal effects of sodium fire from that of the chemical interaction effects. Definite signatures of

thermochemical degradation indicating dehydration and structural modification of the limestone concrete have been obtained for the first time using this technique.

Fig.2a shows the room temperature mid infrared spectrum of the limestone aggregate reference concrete along with the spectra of sodium exposed samples as a function of depth. The spectrum revealed the broad absorption feature centered around 3500 cm^{-1} attributed to stretching mode of bound water in concrete. In particular the sharp feature at 3643 cm^{-1} riding on the broad water background is said to arise due to the O-H stretching of Ca(OH)_2 - the major hydration product of Portland Cement. Estimating the area under this peak at 3643 cm^{-1} could follow the extent of degradation of concrete. It is clearly evident from the figure that the spectrum of the sodium exposed sample removed from 10 mm from the affected surface shows appreciable changes as compared to that of the reference sample. The stretching modes of water in the affected sample reveals a significant softening associated with a dramatic increase in the intensity of the low frequency components as compared to

that of the reference sample (inset in Fig. 2a). The intensity of the 3643 cm^{-1} peak is also seen to significantly decrease. These changes indicate the loss of both free and bound water from the concrete on account of sodium exposure, thus degrading the concrete. The appearance of a new mode at 1070 cm^{-1} and the splitting of the doubly degenerate ν_3 and ν_4 modes indicate a structural transformation of the limestone aggregates.

Fig.2b shows the changes in the vibrational frequencies of the stretching modes of water as a function of depth from the affected surface. It is evident from the figure that the conversion of bound water into free water is confined to depths of 30 mm from affected surface. Thus infrared spectroscopy helps to provide an insight into the changes occurring at the molecular level.

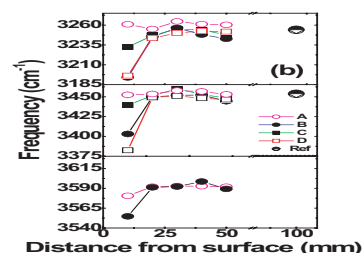


Fig.2b Variation of stretching frequencies of water as a function of depth from the affected surface of concrete. Half shaded circles correspond to the unexposed reference samples. A, B, C and D correspond to various location on the sodium interacted surface

III.E.7. Characteristics of Debris Bed Formed by Woods Metal Melt Stream - Water Thermal Interaction

Under a postulated, very low probability core meltdown scenario of a Fast Reactor, the physical status of debris generated during the molten fuel interaction with the coolant, plays a crucial role for the post accidental decay heat removal. Towards this, simulant thermal interaction experiments with woods metal melt-water system under gravity driven stream mode are being carried out. The physical properties (such as density, surface tension and kinematic viscosity) of liquid woods metal (a fusible bismuth based low melting point alloy with 50 % Bi, 25 % Pb, 12.5 % Sn, and 12.5 % Cd with melting point at 345 K) and liquid uranium dioxide are similar. The low



Fig.1 Melt release system



Fig.2 Jet breakup

melting point of woods metal facilitates experimentation on both hydrodynamic and thermal fragmentation phenomena. The experimental melt release system is shown in Fig.1. Molten woods metal heated to a temperature 373 K in an alumina crucible, is released through a nozzle of 8 mm diameter into a water column of

70 cm height at a rate of ~ 600 g/s. The melt release rate has been assessed from the readings from the online electronic mass balance. Stream break up length is assessed to be 110 mm from the processed high speed melt stream images taken at 100 fps (Fig.2), which agree closely with the theoretical value predicted from Raleigh-Taylor instability consideration. The debris heap formed is shown in Fig.3. The bed profile measurements are processed in MATLAB to get its volume and hence the average bed porosity. Solidified debris constituted the heap, and the observed average bed height (for 20 kg run), bed porosity and heap repose angle are 15 cm, ~ 0.61 and 42° respectively. No significant changes in the heap porosity and debris size spectrum are observed with variation in initial inventory. Experiments are repeated at elevated melt



Fig.3 Heap formation

temperatures of 433 K and 493 K with a melt inventory of 20 kg. The debris size distribution obtained with different melt temperatures are shown in Fig. 4. For a melt temperature of 493 K the bed porosity decreased to 0.466. This information on debris bed characteristics are being further processed to address the reality in a sodium cooled fast reactor and the results can still be used as first approximation to assess recriticality and bed coolability of relocated molten core material.

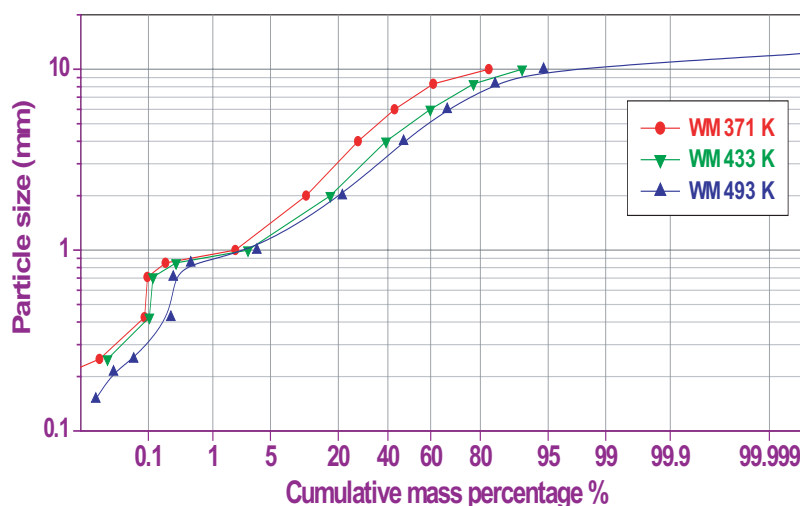


Fig.4 Size distributions at different melt temperatures

III.E.8. Variations in Biofouling Settlement Pattern in the Coastal Waters of Kalpakkam

Coastal power plants, which use seawater for cooling the condenser and other auxiliary systems, face great monetary losses due to the settlement of marine sedentary organisms. These organisms are identified as "Biofouling organisms" or "Biofoulers" and the process is

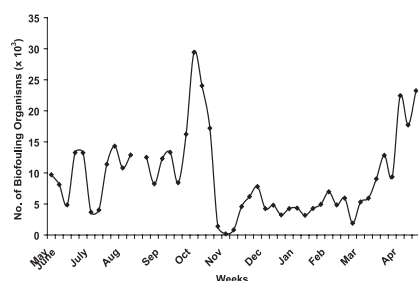


Fig.1 Variations in settlement pattern of biofouling organisms on weekly panels during the period May 2006 - April 2007.

known as "Biofouling", which creates major operational problems such as condenser tube blockages, reduction in heat transfer, increased pressure drop and pump vibration etc. PFBR is going to use about 30 m³/s of seawater for cooling. In order to devise an effective biofouling control measure for PFBR cooling water system, it is essential that the present biofouling potential (qualitative, quantitative and their variations) at Kalpakkam coastal water is studied. In view of this, a study was carried out with the objectives, to find out a) the present settlement



Fig.2 A view of a teak wood panel exposed to coastal water at Kalpakkam for 7 days

pattern of biofoulers and b) seasonal succession of macrofoulants. Teak wood panels (size 12 x 9 x 0.3 cm) were suspended at 1 m depth below the lowest low water mark approximately 400 m away from the shoreline on epoxy coated mild steel frames

from the jetty of Madras Atomic Power Station. Three series of observations (weekly, monthly and cumulative at 30 d intervals) were made. Different evaluating parameters viz. composition of organisms, number of organisms settled on the panels, both % of number and % of area coverage and biomass (g/100 cm²) have been used to study the fouling pattern.

A substantial temporal variation in fouling pattern was observed with respect to all the parameters evaluated. A wide

variation was observed in the number of settled organisms on weekly panels (Fig. 1). Major fouling organisms observed during the study were barnacles, hydroids, ascidians, oysters, sea anemones and green mussels. In addition to these sedentary organisms, epizoic animals like errant polychaetes, flat worms, amphipods, crabs were also observed. A wide variation in the settlement pattern of the weekly panels was observed with the range of 1-136 numbers per sq.cm, however, in the monthly panels the number

of organisms per sq. cm ranged from 11-69 due to increase in the size of foulers. Result showed that the fouling intensity was significantly different between the successive weeks. .

The percentage of area coverage of weekly panels showed a well-marked variation, ranged between 0.08 and 100%, whereas, in case of monthly and cumulative panels, it was found to be 89 - 100% and 100% respectively. Barnacles and mussels were found to be the major macrofoulants in this coastal water. A substantial increase in biomass was noticed with time (Fig. 2, 3, 4). For example, biomass observed on 7 d, 28 d, 56 d, 112 d and 150 d is 11, 77, 97, 185 and 648 g/100 cm² respectively. Pronounced variations were also observed in case of the species diversity, species richness and evenness values. The unique feature of this study is that the photographs of each series were taken and available in digital form. Fouling pattern at an interval of 7 d was observed for the first time in this coast. Result of this study could be used for arriving at more effective biofouling control regime in cooling water system of PFBR.



Fig.3 A view of a teal wood panel exposed to coastal water at Kalpakkam for 30 days



Fig.4 A view of 112 d old panel, covered with green mussels (*Perna viridis*)

Chapter -4

FUEL CYCLE

IV.A. Fuel Properties and Performance

IV.A.1. Recovery of Plutonium and Americium from Waste Matrices by Supercritical Fluid Extraction

Handling of plutonium in a radioactive laboratory involves the usage of tissue paper and recovery of plutonium from the same assumes significance from the point of view of accounting of special nuclear material (SNM) as well as radioactive waste management. Supercritical Fluid Extraction (SFE) technique, which produces relatively less or no secondary waste, is very much preferable for such applications. Supercritical fluids possess the properties of gas-like diffusivity and viscosity, liquid-like density and low surface tension, which help them to easily penetrate through the pores of the sample matrix and extract the components of interest more efficiently. Supercritical fluids provide faster, cleaner and efficient extractions,

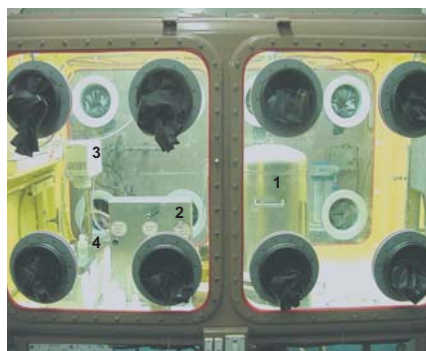


Fig.1 SFE facility in glove box. Components such as pumping systems of CO₂ and modifier were kept outside glove box. (not shown in picture). 1. Secondary vessel accommodates in it primary extraction vessel with its constant temperature heating system 2. Panel incorporating various SS lines, check valves and needle valves 3. Backpressure regulator and 4. Plutonium collection.

and they become gas at the end of extraction and escape leaving the dissolved solute. Thus SFE technique provides an excellent alternative to recover the actinides with minimum generation of secondary liquid waste.

SFE based procedures were earlier developed in our laboratory for the recovery of uranium from tissue paper waste, removal of silicone oil from urania microspheres, separation of uranium from thorium etc.

An SFE system (Fig.1) was set-up in a glove box for studies involving plutonium. The glove box facility was modified suitably for safely handling radioactive materials under high pressure conditions. The primary extraction vessel was

accommodated in a secondary vessel in order to contain any accidental release of gaseous carbon dioxide from it, which may otherwise damage the negative pressure environment of the glove box. The two pumps used for pumping liquid carbon dioxide and the modifier containing extractants in methanol were placed outside the glove box. However the backpressure regulator and heating oven, which accommodated the extraction vessel were housed inside the glove box. The collection

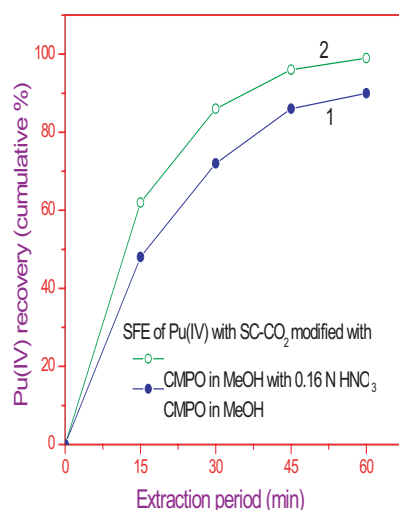


Fig.2 Extraction profile for Pu(IV) from simulated waste. Sample: Pu(IV) (5 g) loaded on to a tissue paper. Experimental conditions: CO₂ flow rate: 2.5 mL/min; Modifiers: (1). 2 wt % CMPO in methanol and (2). 2 wt % CMPO in methanol with 0.16 N HNO₃, flow rate: 0.25 mL/min. Pressure: 300 bar, and Temperature: 308 K.

system was also arranged inside the glove box, from which the extracted sample was taken out for assay.

Studies on the extraction behaviour of plutonium loaded onto a tissue paper were carried out using supercritical carbon dioxide (Sc-CO₂) modified with various ligands. Complete extraction of Pu(IV) in its nitrate form from tissue paper matrix was achieved for the first time using Sc-CO₂ modified with n-octyl(phenyl)-N, N - diisobutyl carbamoylmethyl phosphine oxide (CMPO) in methanol containing 0.16 N HNO₃ (Fig.2). Pu (IV) was also completely removed from other matrices such as teflon, stainless steel and glass. Complete recovery of Pu(IV) was demonstrated for tissue paper matrix containing 5, 25 and 50 g plutonium. Complete extraction was also obtained for Pu (III) and Am(III) under similar experimental conditions. Besides the simulated waste, recovery of Pu (IV) from actual tissue paper waste generated in the laboratory was also demonstrated satisfactorily.

Future endeavor envisages the development of procedures to recover plutonium present in powder form in various waste matrices. The development of a large scale facility for the actinide decontamination of various matrices is the ultimate objective of these efforts.

IV.A.2. Radiation Stable Resins for the Recovery of Actinides and Palladium

The purification and concentration of plutonium from dilute process solutions are major steps in nuclear spent fuel reprocessing in current PUREX plants. Due to its simplicity, ion exchange processes have advantages over the other separation methods for the concentration and purification of plutonium. Anion exchange process is being commonly used by most of the nuclear plants and laboratories for plutonium processing and purifications. The inability of several elements to form the anionic complexes in nitric acid solution makes it possible to get a better decontamination factor. The conventional anion exchange resins have a styrene-DVB based copolymers matrix.

In India, the purification and concentration of plutonium is carried out by conventional anion exchange. The two major problems which have been encountered during plutonium purification using the anion-exchange process are

- i) very slow sorption and desorption kinetics,
- ii) radiation degradation of

the anion-exchange resin in intense radiation field.

The use of resin beads with high porosity and lower bead size is preferred to overcome the slow kinetics. The combination of hostile conditions such as high radiation and concentrated nitric acid can degrade the resins and various accidents had been reported during the anion-exchange process of plutonium purification. Thus, anion-exchange resins, which possess high radiation and chemical stability, are preferred for the purification of plutonium. From the literature it is found that pyridine-based ion exchangers have the highest order of radiation stability. This is because vinylpyridine resins are less susceptible to electrophilic attack than the styrene-based resins. At the centre, a programme has been initiated to synthesise and develop gel-type 4-vinylpyridine (PVP) resins for plutonium processing and precious metal recovery. The PVP resins were synthesized by suspension polymerization technique and after that resin was methylated with iodomethane. Three different

cross-linked (4, 8, and 12%) gel-type 4-vinylpyridine resins were characterized, and evaluated for processing and purification of plutonium and palladium from nitric acid medium. For palladium recovery PVP resin was used as it is and for plutonium methylated resin was used. The results were compared with those obtained with the conventional anion-exchange resin namely, Dowex 1X4, which has been studied extensively.

Variation of $D_{Pu(IV)}$ as a function of acidity

From Fig.1 it is seen that $D_{Pu(IV)}$ value of 4% cross-linked PVP resin is lowest at all acidities and for 8% the $D_{Pu(IV)}$ is highest. In Dowex 1x4, the maximum $D_{Pu(IV)}$ value is attained at 7 - 8 M, whereas for PVP resins, the maximum shifts towards 8 - 10 M nitric acid. The $D_{Pu(IV)}$ for 8% and 12% crosslinked resins is high as compared to Dowex 1X4.

Elution studies

The column performance of PVP resins was compared with that of Dowex 1X4 under similar conditions. Pu(IV) was loaded from 8 M nitric acid and

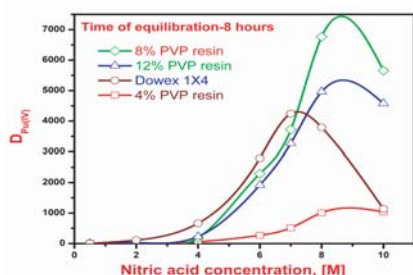


Fig.1 Variation of $D_{Pu(IV)}$ with nitric acid concentration.

after washing the column, it was eluted with 0.5 M nitric acid. It is seen from Fig.2 that for 4% PVP resin, about 99.8% of the loaded plutonium could be eluted within 3 bed volumes, whereas for 8% PVP about 93% of plutonium could be eluted. The 12% resin shows a poor and incomplete elution pattern; only 86% of plutonium could be eluted within 5 bed volumes. Under similar conditions Dowex 1X4 also exhibits poor and incomplete elution pattern. Even after 6 bed volumes only about 66% of the loaded Pu could be eluted.

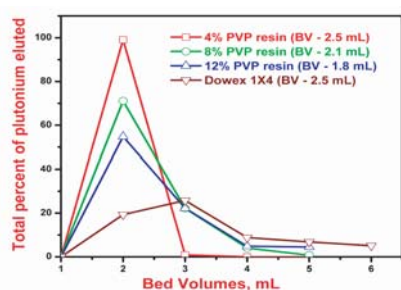


Fig.2 Elution profile of PVP resins and Dowex 1X4.

Radiation degradation

The resins were irradiated in a Co-60 gamma chamber in presence of 8 M nitric acid, after which the resins were analysed for capacity, moisture

content and Pu distribution ratios. All the resins were irradiated up to 200 MRad of total absorbed dose. As expected, for all the resins the $D_{Pu(IV)}$ decreased with the increase in dose. The value of $D_{Pu(IV)}$ of 200 MRad irradiated 8% PVP resin was nearly identical to that of 100 MRad irradiated Dowex 1X4. At 200 MRad of total cumulative dose, PVP resin shows little damage in the form of dimples over bead surface (Fig.3) but it takes up plutonium over a range of nitric acid concentration, whereas Dowex 1X4 was completely degraded. As the total absorbed dose increases, the strong-base capacity of the resin decreases, indicating the deterioration of functional group (i.e. methyl group) upon irradiation. The deterioration of the polymer matrix upon irradiation is also manifested in the increase in moisture content of the irradiated resin and increase in volume of resin.

Palladium recovery

Palladium is a precious metal with good catalytic, corrosion and oxidation resistant properties, which have resulted in its widespread use in different industries. The natural abundance of palladium is very low and thus, there is an incentive in recovering palladium from the high level

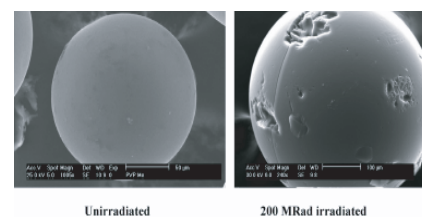


Fig.3 SEM images of unirradiated and 200 MRad irradiated 8% PVP resin.

waste generated in Fast Reactor Fuel Reprocessing. At IGCAR, we have developed a method for the recovery of palladium from nitric acid medium. We have used 8% PVP resin for the recovery of palladium from 2 M and 4 M nitric acid medium. In a small column of 7.2 ml about 1000 ml of solution containing 210 ppm of palladium was passed and it was observed that even the last 200 ml of effluent contains less than 2 ppm of palladium. Similar results were obtained when 400 ml of solution containing 800 ppm of palladium was passed. Palladium was eluted with 0.5M thiourea in 0.1M HNO₃ and 95% of loaded palladium was eluted in four-bed volume of column. When the solution containing palladium, ruthenium and rhodium were passed through the column only palladium was loaded.

The above studies indicate that 4-vinylpyridine resins can be used for recovery and purification of plutonium as well as for the recovery of palladium from radioactive waste solutions.

IV.A.3. Matrix Effect on Laser Desorption/Ionization of Uranyl Nitrate Solution in Laser Mass Spectrometry

Development of simple and direct methods for measurement of burn-up of fast reactor fuels is an important area. The direct determination of burn-up based on the method based on measurement of intensity ratio (i.e. ratio of ion intensity corresponding to a burn-up monitor element to that corresponding to U) requires the determination of U in uranyl nitrate solution. If only one of the ionic species UO_2^+ , UO^+ , U^+ were to be present in the laser-vaporized plume, the burn-up measurement could be subject to error, since the single species signal may get saturated. (For 10 at % fission, the number of atoms of heavy elements present in a spent fuel would be a few hundred times more than that of ^{143}Nd atoms produced). However, if the U bearing species U^+ , UO^+ and UO_2^+ are all present, then the saturation problem may not exist. Furthermore, if the ion intensity of one of the above species were to become comparable to that of ^{143}Nd bearing species, then determination of the ratio of Nd/U will be easier and more reliable. With these aspects in mind, a study of the effect of

different matrices such as Tri-butyl phosphate (TBP), Nicotinic acid and Polyethylene oxide (PEO) of molecular weight 2000, on the laser desorption and ionization of uranyl nitrate solution was taken up. The experiments were carried out using a laser mass spectrometry system comprising of an in-house developed reflectron time-of-flight mass spectrometer. A schematic of the experimental facility is shown in Fig.1. Methanol was used as the medium for PEO and TBP matrices and water was used for nicotinic acid matrix. The matrix to sample ratio was maintained about 100:1. About $10\mu\text{L}$ of the sample and the matrix mixture

dissolved in 1 ml of the medium was loaded on the Al sample holder (see Fig.1), dried under IR lamp and transferred to the sample chamber. The samples contained typically about 10^{19} atoms of U. Under low intensity laser beam, the spread in kinetic energy of the ions produced will be low, and thus resolution in the mass spectrum will also be better. Only UO_2^+ and UO^+ were observed on laser desorption/ionization of uranyl nitrate solution without any matrix (Fig. 2a). On addition of a matrix, keeping all other experimental conditions same, the signal intensity increased in all the three cases. With nicotinic acid as the matrix, UO^+ was the

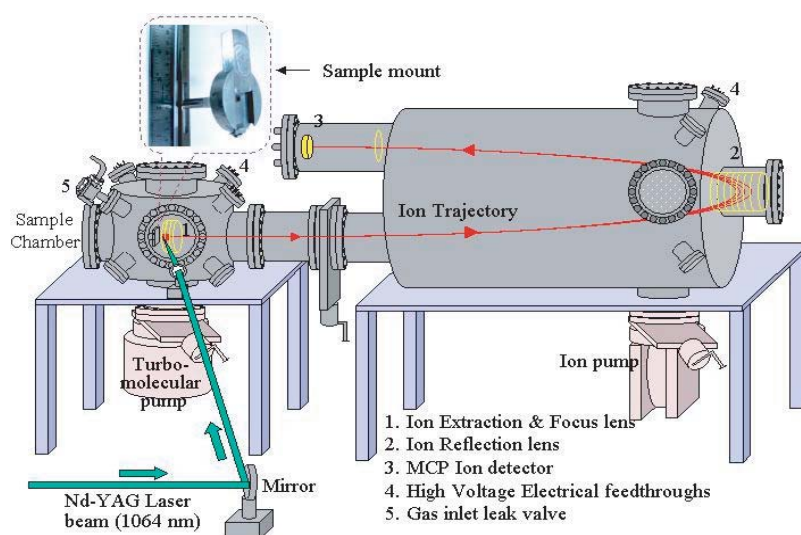


Fig.1 Laser TOF-MASS Spectrometry - Schematic

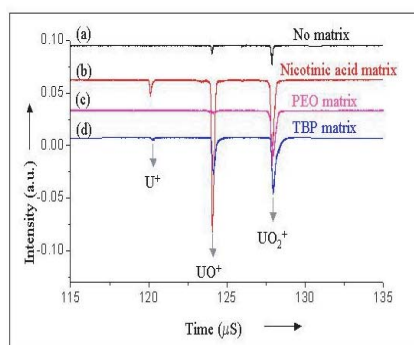


Fig.2 Effect of matrix on the signal intensity in the laser desorption/ionization mass spectrum of $UO_2(NO_3)_2$ solution

most intense signal, followed by UO_2^+ and U^+ (Fig. 2b); with PEO as the matrix, only UO_2^+ was observed (Fig. 2c); and with TBP as the matrix UO^+ and UO_2^+ were the major species with very small amount of U^+ (Fig. 2d). The nicotinic acid matrix seems to score over others, since the total U gets divided into all the three forms (UO^+ , UO_2^+ , U^+), and the

peaks are also sharper (better mass resolution). Compared to the no-matrix condition, improvement in signal intensities was observed most with nicotinic acid as matrix (10 times), implying that use of this matrix will involve considerable reduction in the quantity of sample required for the analysis.

IV.A.4. Thermophysical Property Measurements on Urania-Thoria and Urania-Gadolinia Solid Solutions, and U-Zr Alloys

Uranium-thorium mixed oxides are being considered as the fuels for the thermal reactors such as Advanced Heavy Water Reactors and high temperature gas cooled reactors. Gadolinium is one of the major fission products and its oxide forms solid solutions

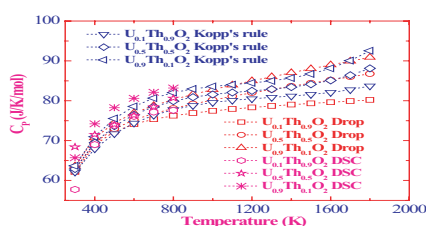


Fig.1 Heat capacity of $(U,Th)O_2$ Solid solutions

with uranium oxide in the oxide fuel. Hence the thermophysical properties of the solid solutions of urania with thoria and gadolinia are important. Heat capacity data are available for

thoria rich (≤ 20 mol % urania) mixed oxides only and that too over a limited temperature range. Enthalpy increments of $(U_{0.1}Th_{0.9})O_2$, $(U_{0.5}Th_{0.5})O_2$ and $(U_{0.9}Th_{0.1})O_2$ were measured by inverse drop calorimetric method using a high temperature differential drop calorimeter in the temperature range 430-1805 K. Heat capacity data were computed from the measured enthalpy increments.

Direct measurements of the heat capacity of these mixed oxides were also carried out in the temperature range 300-800 K using a heat flux differential scanning calorimeter. It can be seen from Fig.1 that the heat capacity data of all the three mixed oxides obtained by two

different calorimetric methods are in very good agreement with each other within 3% in the overlapping regions and that they are also in agreement with the values computed using Neumann-Kopp's rule.

There exists discrepancy in the literature data for the heat capacity and no data exist for high temperature thermal expansion of urania-gadolinia solid solutions. Hence, heat capacity measurements on $(U_{0.9}Gd_{0.1})O_{2.125}$, $(U_{0.8}Gd_{0.2})O_{2.187}$ and $(U_{0.5}Gd_{0.5})O_{1.984}$ were carried out using a heat flux differential scanning calorimeter in the temperature range 298-800 K and the thermal expansion measurements were performed

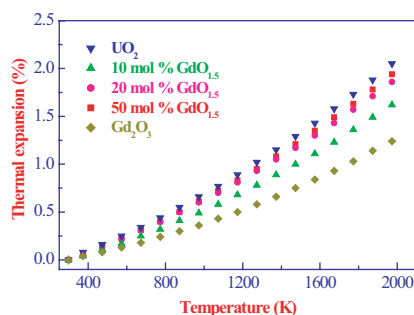


Fig.2 Thermal expansion (%) as a function of temperature for $\text{UO}_2\text{-GdO}_{1.5}$ solid solutions

on these solid solutions 298-1973 K using high temperature X-ray diffraction. The thermal expansion of these solid solutions are shown in Fig.2.

U-Zr metal alloys will be used as the blanket material in fast breeder reactors. Hence heat capacity data of U-Zr alloys is important. Heat capacity data of U-Zr alloys are available only for alloys with >13 at.% Zr. Heat capacity measurements were carried out on U-Zr alloy with 2, 5 and 10 wt.% Zr using heat flux differential calorimeter in the temperature range 298-800 K to generate the first experimental data which are shown in Fig.3. The measured heat capacity of pure U along

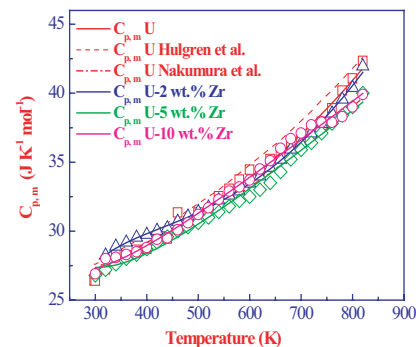


Fig.3 Heat capacity of U and U-Zr alloys

with other literature values is also shown in Fig. 3 along with the literature values.

IV.A.5. An Automated Facility for Charging of Fuel Micro Spheres into the Sintering Furnace

Fuel preparation in the form of micro spheres generated by the SOLGEL process is an attractive alternative to the powder route of preparation. An automated fabrication facility on the SOLGEL route has been set up in the Radiochemistry Laboratory. The fuel materials in the form of micro spheres produced by the gelation process are first dried and are then to be loaded in a charge carrier and placed remotely into a high temperature furnace for sintering. This operation is to be mechanized and performed remotely. Towards this, an automated gripping device

positionable along three co-ordinates, for positioning and subsequent lowering of the charge carrier into the furnace, has been developed. The device consists of an electrically actuated x-y platform which is mounted above the furnace as shown in Fig.1. The platform which can be positioned in the horizontal plane, is holding an electrically operated telescopic arm fitted with a pneumatically actuated two jaw gripper. The Z axis position indicator mounted on the platform indicates the depth to which the gripper has been lowered. A reed sensor fixed on the end effectors is used for

sensing the gripping operation. The system has been commissioned with an overall positioning accuracy of 0.5 mm. With no direct vision, the lowering of the charge into the furnace is assisted by a PAN-TILT camera, as shown in the inset in Fig.1.



Fig.1 Automated gripping devices for the introduction of charge carrier into the sintering furnace

IV.A.6. Dismantling and Metrology of FBTR FSA and Fuel Pins after 155 GWd/t Burn-up

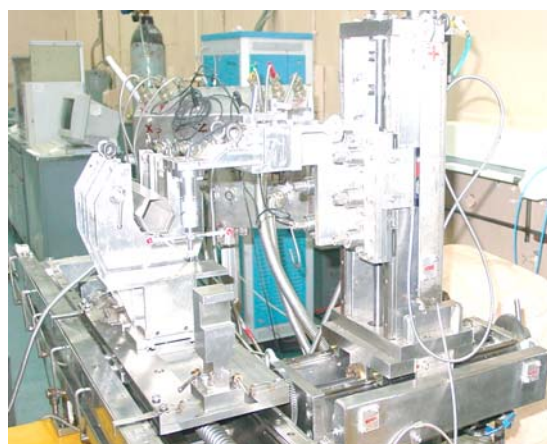
A new computer controlled Dimensional-Measurements-cum-Laser-Dismantling (DMLD) machine was developed and installed inside the hot cells to carry out remote metrology and laser based dismantling of high burn-up FBTR fuel subassemblies (FSA). The machine consists of a mechanical system located within the hot cell, and the associated motion control system and laser system located outside the hot cell. Fig.1 shows photographs of the four axis mechanical system of the machine.

High level of gamma radiation, deformed nature of the FSA and the requirement of high level of measurement accuracy provided immense challenges in developing this

machine especially for remote operation and maintenance. Laser-based cutting was adopted due to its favorable features such as fast and non-contact nature of cutting, absence of moving parts, ease of remote operation, minimum remote repair/replacement of parts, absence of coolant and minimum generation of waste such as dust, chips etc. However challenges were involved in delivering the required laser power precisely at the cutting location with optimized parameters and avoiding welding between the outer and inner hexagonal sheaths of FSA during cutting.

Precise dimensional measurement of the FSA is required to assess whether the incremental deformations due

to irradiation is likely to pose any constraints in the fuel handling operations, and thereby limit the burn-up of the fuel. The DMLD machine make use of an induction type touch trigger sensor mounted on the YZ- stage and a custom- made motion control software for dimensional measurements of the FSA. The machine automatically acquires the coordinates of large number of surface points at various cross sections along the length of the FSA through automatic scanning as defined by the user. These cross-sections of the FSA are reconstructed by plotting this data in the 2D drafting environment of CAD software. The width-across-flat and corner-to-corner distance of various cross sections are



(a) Outside hot cell



(b) Inside hot cell

Fig.1 Photographs of the mechanical system of the DMLD machine

Table 2 : Results of dimensional measurements on FSA and fuel pins after 154GWD/t burn-up

On the hexagonal wrapper of FSA		On the fuel pins	
Maximum % increase in width-across-flat	1.4 % (0.7 mm)	Diametric Strain on Cladding (maximum)	5 % (0.27mm)
Maximum % Increase in corner-to-corner distance (max)	1.2 % (0.68 mm)	Increase in length (maximum)	0.8 % (4.28 mm)
Head- to-foot misalignment	7.5 mm		

measured from the reconstructed cross sections. By assembling various cross-sections in the 3D-modelling environment of CAM software, the 3D wire frame model of the FSA is reconstructed. The magnitude and direction of the head-to-foot misalignment, angular twist etc., are measured from this model.

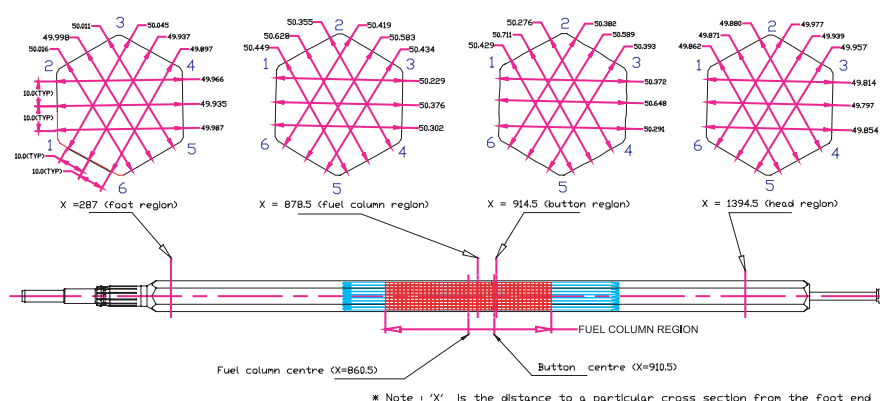
The machine was used to carry out metrology and dismantling of the FBTR FSA that was discharged after a burn-up of 155 GWd/t. The reconstructed cross sections of the FSA at some typical axial locations are shown in Fig.2. Dimensional accuracy of these figures lies within $\pm 0.015\text{mm}$. The variation of flat-to-flat distance along the length of the FSA is shown in Fig.3. The maximum increase in flat-to-flat distance and corner-to-corner distance observed are respectively 0.7mm and 0.68mm, and they occur at the region corresponding to the centre of the fuel column. Fig.4 shows the reconstructed

wire-frame model of the FSA. The head-to-foot misalignment of the FSA was found to be 7.5mm and no twist was observed.

Fig. 5 shows the Nd-YAG laser system developed by RRCAT, Indore, for laser cutting. The power and signal cables and the fibre optic cable which delivers the laser power at the cutting torch pass through specially designed leak-tight penetrations in the cell wall. The DMLD machine has additional provision for cutting the FSA with a motorized diamond wheel. The fuel pin bundle was disengaged from

the FSA after cutting the inner and outer hexagonal sheaths transversely using laser at the location 605mm from the foot end of the FSA.

13 selected fuel pins extracted from the FSA were subjected to length and diameter measurements. Length was measured using a measuring bench fitted with dial gauges and working on comparison principle with an accuracy of $\pm 0.02\text{mm}$. The increase in lengths of fuel pins measured was found to vary from 1.89mm to 4.28mm. A fuel pin profilometer with two linearly variable differential

**Fig.2 The reconstructed cross sections of high burn-up FSA.**

transducers (LVDT) fixed on a motorized carriage was used for scanning the fuel pins along the length for diameter measurements. The

measurement accuracy of this device is $\pm 0.005\text{mm}$. A plot of the diameter variation along the length of a fuel pin in two perpendicular orientations is

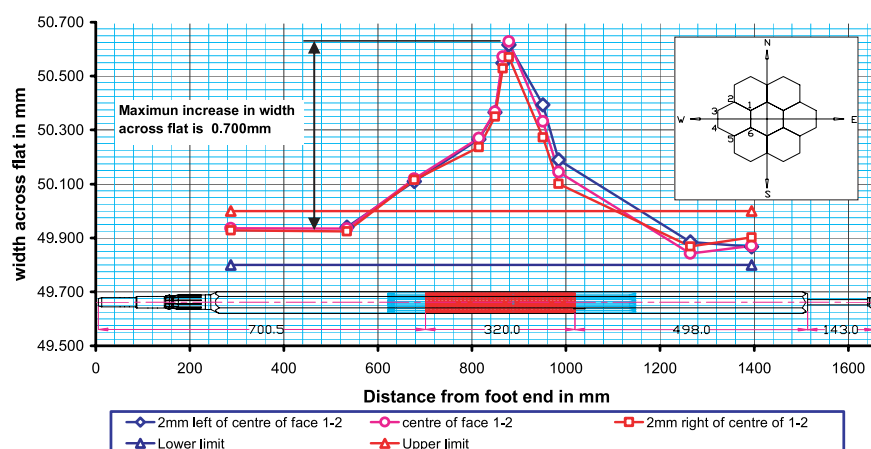
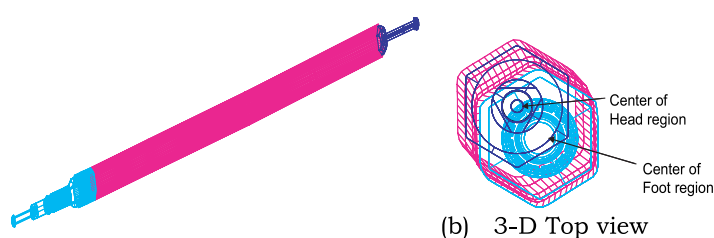


Fig. 3 Variation of flat-to-flat distance along the length of the FSA



(a) 3-D image of 154 GWd/t FSA

Fig. 4 Reconstructed wire-frame model of the FSA



Fig. 5 Nd-YAG Laser system developed by RRCAT

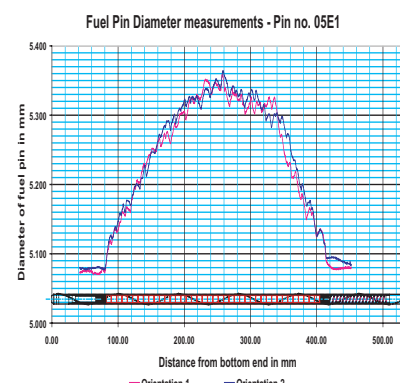


Fig. 6 Variation in diameter along the length of a fuel pin

shown in Fig.6. It can be seen that fuel pin clad has undergone increase in diameter in the fuel column region. The maximum increase in diameter in various fuel pins vary from 0.17mm to 0.27mm at the centre of fuel column. The results of dimensional measurements on FSA and fuel pins are summarized in Table.1. It indicates that there is significant increase in dimensions after 155 GWd/ t burn-up.

Along with other PIE results, the results of dimensional measurements of the FSA and fuel pins will help in determining the residual life of the FSAs. The experience gained during the development of the above machine will be utilized to develop a production-scale system for the inspection and dismantling of PFBR FSAs prior to reprocessing.

IV.A.7. Development of Remote Inspection Devices

Poolside Spent Sub-assembly Inspection Bench for PFBR

A prototype special purpose remote inspection bench has been developed to carry out the dimensional measurement / profilometry and visual examination of spent sub-assemblies (SA) of PFBR at the spent fuel storage pool. The main purpose of dimensional measurement/profilometry of spent SA is to evaluate the extent of irradiation-induced deformation like bow, bulge across the faces and elongation of hexagonal SA wrapper and to give a quick feedback on the

performance of the SA to the plant operators. The inspection bench is designed in such a way that all moving components excepting the measuring probes, are kept above the storage pool eliminating the need for expensive underwater compatible components. Two LVDTs have been used as induction type touch trigger probes to enable acquisition of coordinates on the SA surfaces by respective encoders on the principal translational axes.

The inspection bench has been installed and commissioned at Engineering Hall No.2. Preliminary testing of the inspection bench has been carried out on dummy PFBR sub-assembly kept in air. With the acquired surface coordinates, profiles of the cross sections along the length of the SA have been generated and integrated using standard modeling software to get a 3D wire frame model of the SA. Special VB-based software has been developed for aiding the standard modeling software in making the 3D wire frame model by proper test data structuring and archival. From the wire frame model, extent of deformations such as bulge across the faces & corners, bow & elongation of the SA could be visualized and determined. From the test results with SA in air and subsequent optimization of trigger parameters and speed of the scan axes, overall measurement accuracy is found to be ± 0.2 mm and repeatability is ± 0.1 mm.

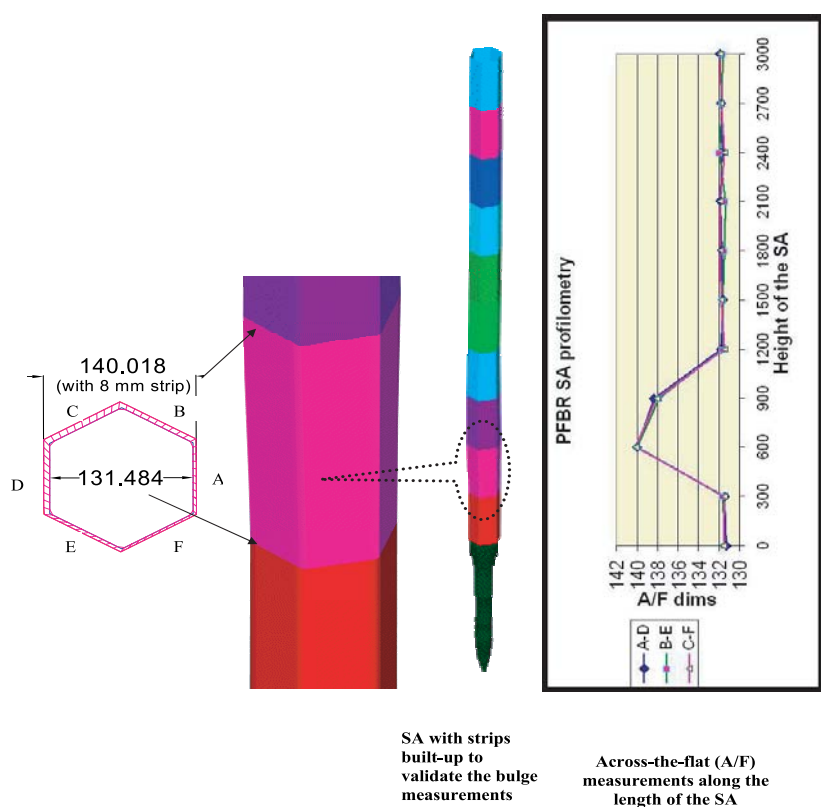


Fig.1 Test results on dummy SA conducted in air

In order to validate the system to evaluate bulges across the hexagonal wrapper faces and



Fig.2 In-situ fabricated water tank around the sub-assembly

slewing of the SA, small strips of known thickness across opposite faces of the SA at various locations along the length were introduced. Results of the test have satisfactorily revealed the areas of bulges and the slope of the SA with respect to the axis of the SA base. The results of the tests on

the SA conducted in air are shown in Fig1.

Following the testing of the SA in air, testing and validation of the SA was carried out under water by enveloping the SA with an in-situ-fabricated tank (Fig.2). Sequence of operations had to be necessarily optimised

for testing of SA in water to take into account the effects of water turbulence arising due to the movements of the measurement axes. The entire SA was inspected and measurements were carried out. The performance of the inspection has been found to be satisfactory and motions of all four axes have been smooth. The results of under water testing of the SA were compared with the results obtained during air testing and the results have been satisfactory. Exact simulation of the storage pool could not be done and the minor deviation observed during the underwater testing from the air testing could be attributed to the small diameter of the water tank.

2-Axis Scanner for Wall Thickness Measurements of CORAL Dissolver Vessel

As part of the in-service inspection (ISI) of CORAL, it is required to inspect the dissolver vessel for assessing the loss of wall thickness due to corrosion. The dissolver consists of two cylindrical limbs, namely dissolver vessel and electrolyser. The inner diameter of the vessel is 100 mm and depth is 560 mm upto sparger which is at the bottom of the vessel. In order to inspect the dissolver vessel for evaluating the loss of wall thickness, a

prototype remote inspection device was conceptualized and developed. The device is essentially, a two axis scanner having rotation (θ) and vertical telescopic (Z) motions. The θ - axis has 360° and Z - axis has about 450 mm travel ranges. Each telescopic stage is connected by two wire ropes with each one assigned for one direction of motion. A lead screw and nut mechanism is adopted for the telescopic motion. Fig. 1 shows the

device being tested in the mock-up dissolver vessel. The inspection technique is by immersion ultrasonic testing with water as the coupling medium. Stepper motors are chosen for precisely positioning the ultrasonic probe around the internal surface of the vessel and identifying the inspection locations without feedback elements. All materials of the construction for the device are made of corrosion resistant steel AISI 304L. Overall size of

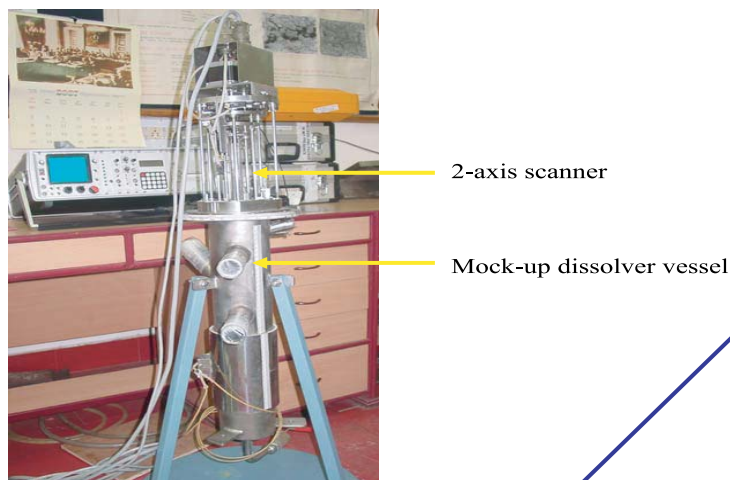


Fig. 1. 2-Axis Scanner in the mock-up dissolver vessel

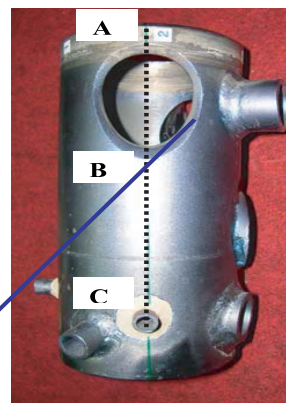


Fig. 2. Titanium Mock-up dissolver vessel

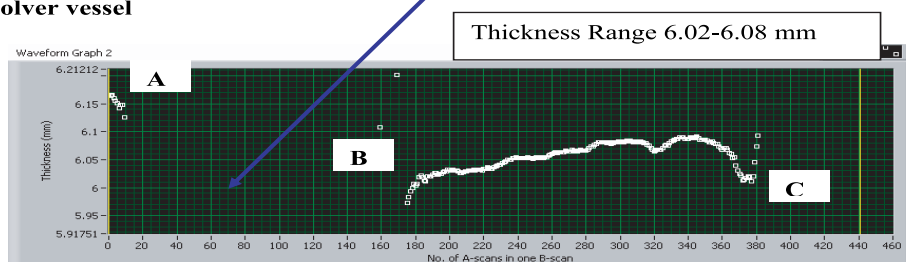


Fig. 3 (a) Thickness profile of the vessel along the markings ABC shown in Fig. 2

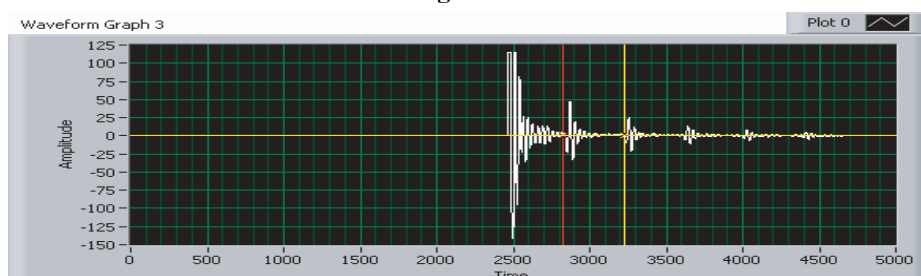


Fig. 3 (b) Typical ultrasonic A-scan signal (from a good region) used for the thickness measurements by cross correlation technique

the device is 220 mm long (in retracted condition) x \varnothing 195 mm enabling it to be deployed through the glove port and blister box on to the vessel to be inspected.

Improvements have been made in the design of the telescopic module for precise movement and the device has

been made in two modules to facilitate deployment into the containment box. The device has been tested in a mock-up vessel under non-active environment and validated for its performance and reliability. The performance of the device has been found to be satisfactory as seen in the test results. Fig.2 shows the

Titanium mock-up dissolver vessel and figs 3 (a) & (b) show the ultrasonic test results on the mock-up vessel. It is planned to introduce a degree-of-freedom in the end-effector whereby it would be possible to manipulate the ultrasonic probe so as to enable inspection of the critical nozzle welds in the vessel.

IV.A.8. Development of Gamma Ray Backscattering Facility for Application to Concrete, Corrosion & Composites

The need for advanced techniques for detection and evaluation of embedded corrosion and a class of sub-surface defects that requires access only to the one side of any material or structure to be inspected has drawn attention to X-ray or gamma backscatter as a desirable choice. Among the techniques using X-ray or gamma radiation, the transmission modality is usually employed. However, transmission measurements may not always be possible due to surrounding space constraints and for if the object is too bulky to produce sufficient radiation penetration. Transmission provides line-integrated information along the path of radiation from the source to the detector, which masks the position of an anomaly present along the transmission line. The



Fig.1 Gamma-ray backscattering scanning facility

scattering modality provides alternative and in this method point-wise information can be obtained by focusing the field of view of the source and detector so that they interact around a point. Since both the source and detector are located on one side of the object, examination of extended structures becomes possible. The gamma scattering method is a viable tool for inspecting material since it is an interaction which is strongly dependent on the electron density of the scattering medium, and in turn, its mass density. Therefore the information obtained by this technique is strongly related to the material density, thus allowing changes in the material uniformity to be monitored.

An indigenous gamma-ray backscattering scanning facility has been designed, built and commissioned. The scanning system (Fig. 1) consists of four main modules: the first module is the source container, second module houses the detector, the third is an independent 4-axis job positioning system and the

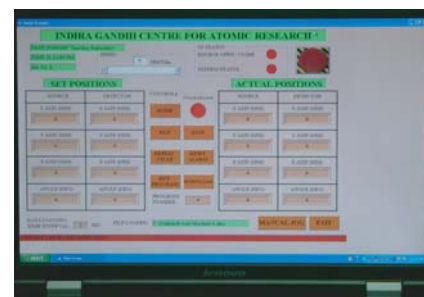


Fig. 2 The screen display for easy operation of complete system through PC

fourth is the control panel and PC (Fig. 2). The source and detector modules are mounted on a fabricated mild steel frame and driven by AC servomotors, linear motion (LM) guides and ball screws. The axial travel is 500 mm and the vertical travel is 400 mm with an accuracy of ± 0.05 mm. Computer Numerical Control (CNC) rotary tables of size 170 mm each are mounted over the Z-axes of the source and detector modules and the source and detector units are housed over these CNC rotary tables. Provision is available in the system to use either horizontal or streamlined side looking dipstick HPGe detectors. The source and detector modules are designed to support 450 kg load. The movement of source and detector units are programmed



Fig.3 The PC display of a typical scattered PHS

and controlled by 8-axes Galil servo controller through PC. The 4-axes job positioning system is an independent unit. Test samples weighing up to 10 kg can be fixed on the table. It consists of X, Y, Z, θ stages run by AC servomotors programmed and controlled by Galil servo controller through PC. The travel lengths available in this system are 450, 150 and 250mm respectively in X, Y and Z directions and in addition to a 360-degree job rotation provision. The positioning accuracies of the system are within ± 10 microns. Two limit switches and one reference switch are provided for each axis. Many interlocks are provided in the system for the safe operation. The source and detector unit are mounted on caster wheel with jack. All electrical controls are mounted on transportable control panel. A pointing laser is mounted on the source and detector housing for easy alignment of the source and detector. An operator friendly VB program

was written for easy operation of complete system through PC. Two lead casks were designed and fabricated to house the γ -source and the detector and the lead melting and pouring was carried out in-house.

A ^{137}Cs radioactive source of strength 155.4 GBq with a lead shielding and a collimated and shielded 50% efficiency coaxial HPGe detector providing high resolution energy dispersive analysis of the scattered spectrum are mounted separately on the source and detector sub assemblies of 6-axis system. The performance of the system was benchmarked by studying two Mild Steel (MS) plates of the same dimensions, one normal as a standard reference and another corroded one for corrosion detection and quantification. Scanning of the specimen mounted on 4-axis system was achieved by its lateral movement across the source and detector collimators by computer commands. The scattered intensity from the specified volume element (voxel) of the MS plate is detected using the HPGe detector and the pulse height spectrum (PHS) was accumulated and displayed using an 8K-channel analyzer which was interfaced with a PC for data storage and analysis.

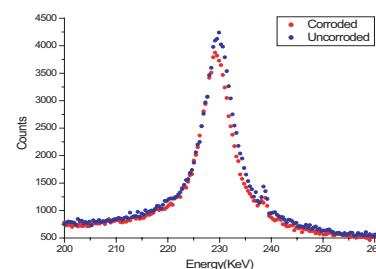


Fig.4 The photo peak part of scattered spectra from normal and corroded MS plates

The display of a typical scattered PHS recorded with the number of channels nearly equal to 2000 with each channel width of 0.374 keV is shown in Fig. 3 and the photo peak parts of the scattered spectra from normal and corroded MS plates are shown in Fig.4. The photo peak intensity of scattered spectra plotted for normal and corroded MS plate regions is shown in Fig. 5. It can be seen clearly from this figure that the scattered intensity decreases as one move from normal to the corroded MS plate.

To provide a sound theoretical proof for the

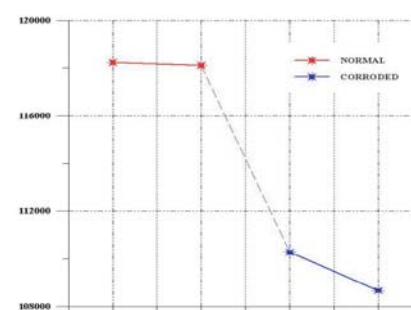


Fig.5 The photo peak intensity of normal and for corroded regions of MS plates

experimental analysis of detection and quantification of corrosion in mild steel by gamma ray scattering the Monte Carlo simulations have been done by using the Monte Carlo N- Particle (MCNP) code, which takes into account the detailed characteristics of the source, detector and the scatterer in calculating the gamma scattered intensity from the MS plates. The result of MCNP PHS simulations and their comparison with the experimental ones are shown in Fig. 6 for the normal MS plate and in Fig. 7 for the corroded one. A good agreement in the shape of the PHS is seen between the experimental spectra and MC simulated ones.

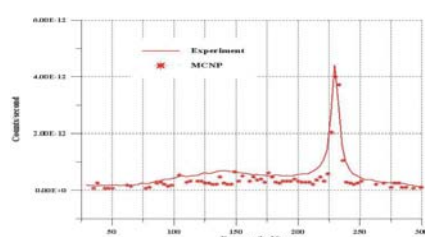


Fig.6 The scattered PHS and its comparison with MCNP simulated one for normal MS plate

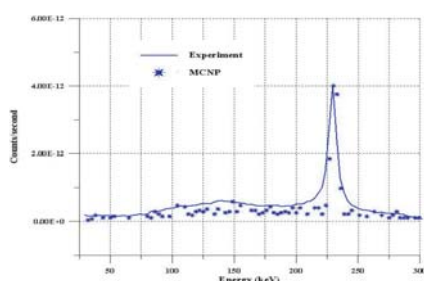


Fig.7 The scattered PHS and its comparison with MCNP simulated one for corroded MS plate

Table1. Density of MS corroded plate (kg/ m³) reconstructed from the experimental and MCNP simulated gamma scattered intensities and the average density value obtained by weight and volume measurements

	Density (kg/ m ³)
Experiment	$6.607 \times 10^3 \pm 0.661 \times 10^3$
MCNP	$6.937 \times 10^3 \pm 0.732 \times 10^3$
From weight and volume measurements	7.526×10^3

A methodology to reconstruct the densities of the corroded regions of the MS plate directly from the scattered intensities is developed and implemented. In this method the density, ρ of the specimen need not be known and only the knowledge of the target material's mass attenuation coefficients, μ/ρ and μ'/ρ is sufficient to correct for absorption of incident and scattered radiation. These mass attenuation coefficients are independent of the physical state of the matter (independent of density) and the knowledge of composition of the material is sufficient for reconstruction. The experimental and MCNP reconstructed densities from a typical voxel of the corroded MS plate are given in Table 1 along with the average density value obtained by weighing the MS plate in a weighing balance and estimating its volume by fluid displacement method. From the Table 1 it can be seen that a good agreement is seen

between the experimental values, MCNP calculations and average density value within estimated errors.

The measured gamma scattered photo peak intensity from corroded MS plate decreases up to 6.46% compared to a normal MS plate and this corresponds to an average density loss of $0.416 \times 10^3 \text{ kg/ m}^3$ (5.24%) due to corrosion in a MS plate of size $235 \times 155 \times 10 \text{ mm}$. This amount of metal loss due to corrosion has been detected and quantified in the present study. The experimental and MC results show that the scattering method is highly sensitive to changes in electronic and physical densities of the voxel under study and the magnitude of corrosion can be clearly identified and quantified by monitoring single scattered events.

IV.B. Reprocessing and Waste Management

IV.B.1. Reprocessing of Spent FBTR fuel in CORAL

The reprocessing of all the pins from FBTR with the burnup upto 100 GWd/t have been reprocessed successfully in CORAL which has provided immense opportunity for studying various solvent extraction flowsheet conditions on the performance. The performance of the solvent extraction process with high plutonium feed concentration was studied. With an aqueous plutonium feed as high as 30 gms per liter(gpl), the organic could be loaded to as high as 25 gpl. The strip product from the first cycle with a Pu concentration of as high as 20 gpl could be obtained. As the required decontamination factor was obtained in the first cycle itself, the product was

qualified for reconversion. This is a very encouraging result, considering the fact that during a codecontamination cycle, we have been able to establish the conditions for high decontamination factor as well high strip product concentration which will be fit for direct reconversion. This high Pu concentration has improved the precipitation characteristics in the Pu reconversion also. Most of the campaigns could be completed in a single extraction cycle itself, though in a very few cases, to get the required Ru decontamination, the second cycle was required.

The inspection of chopper and chopper-dissolver

interconnecting chute was carried out using a fibroscope during the course of the campaign. Some chopped pellets were seen to have accumulated in the chopper-dissolver chute and were cleared mechanically. Dissolver was inspected with a camera using a telescopic arm. No undissolved solids or corrosion of vessel was observed in the dissolver.

In the spent solvent treatment facility, various washing reagents such as ammonium carbonate and sodium carbonate were used. Pu retained in the lean organic could be quantitatively recovered. Fig.1(a) and (b) show the setup for spent solvent



Fig.1(a) Solvent treatment facility: Mixer settler in operation inside the glove box



Fig.1 (b) Closer view of the Mixer settler

treatment. The lean solvent could be reused in the plant. The operational experience is being analysed to evolve a viable flowsheet for DFRP.

As the gamma back ground is very high in the CORAL facility, it was not possible to monitor Pu in the hulls by gamma assaying. A separate facility is being constructed to accomplish this measurement

using HPG or Lithium Bromide detector can be used.

Some of the centrifugal extractor motors required replacement. HEPA filters in the vessel off gas system and glove box off gas system were changed since the pressure drop across the filters were more than 75mm. These filters did not have any significant α contamination which is

indicative of the effective first stage filtration in the respective circuits.

The facility is gearing up for taking the next important milestone of reprocessing 155 GWd/t burnup FBTR fuel. After review of the operation of this facility during the earlier campaigns, AERB has cleared the proposal for taking up this campaign.

IV.B.2. Thermodynamic Measurements on Aqueous Solutions of Uranyl Nitrate Hexahydrate at 298.15 K and 0.1 MPa

Uranyl nitrate hexahydrate (UNH) is an important key solute in the nuclear solvent extraction processes like PUREX, UREX and UREX+. Information on the thermodynamic parameters for aqueous solutions of uranyl nitrate is severely limited. Recently at Reprocessing

Group, thermodynamic parameters of UNH in aqueous solutions viz. activity coefficients, osmotic coefficients, excess Gibbs energy and vapour pressures were measured. Selected results of these investigations are highlighted here.

ASTM Grade-1 water as per ASTM D-1193-99 with a resistivity of 18.2 M Ω cm at 298.15 K and TOC <15ppb was used in the experiments for reagent/solution preparation and as water standard. Solutes were weighed in a precision balance (0.01mg resolution). When not in use, the solutions were kept in air-tight closed condition in a shaker-bath at

298.15 K. Shaker-bath was coupled to a chiller for cooling. To ensure the ripple-free power supply to all the equipments, AC supply was regulated with an uninterrupted power supply set at high sensitivity. The ambient conditions during the experiment were monitored with a digital hygrometer (0.1%) consisting of thermometer (0.1 K) and pressure sensor (0.1 kPa). Density was measured by a vibrating-tube densitometer with a resolution of 1×10^{-6} g/mL with a built-in thermoelectric peltier element module for maintaining temperature of sample in a thermostatted U tube. Water activity was measured by a thermodynamic water activity meter with a built-

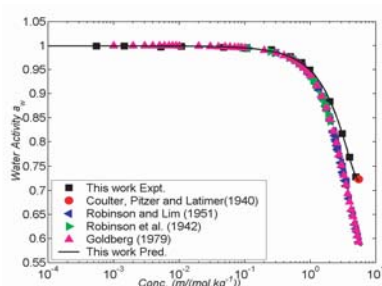


Fig.1 Experimental determination of water activity of aqueous uranyl nitrate hexahydrate solutions at 298.15 K and 0.1 MPa. The present experimental and calculated data are compared with those reported in the literature.

in thermoelectric peltier element module for maintaining temperature of sample. Samples were loaded in polystyrene cups and placed into the activity meter. The activity meter was standardized using a two-step procedure. In the first step, purified and degassed ASTM-Grade-1 water was used as a standard in addition to the four aqueous electrolyte solutions supplied in sealed ampules as standards. These solutions were 0.5 m KCl ($a_w = 0.984 \pm 0.003$), 6.0 m NaCl ($a_w = 0.760 \pm 0.003$), 8.57 m LiCl ($a_w = 0.500 \pm 0.003$) and 13.3 m LiCl ($a_w = 0.250 \pm 0.003$). In the second step, 19 aqueous solutions of AR grade urea (1×10^{-4} to 13 m approx.) were made and their water activities were determined experimentally.

Experimentally determined water activity values for urea-water system were compared with two sets of literature data and an excellent agreement was observed. 14 solutions of uranyl nitrate were made ($\sim 5 \times 10^{-4}$ to 5 m). The water activity values for the uranyl nitrate solutions were determined and plotted in Fig.1 along with the values reported in the literature

The osmotic coefficient was derived from water-activity values and based on that activity coefficient of uranyl nitrate in aqueous solution was estimated. From water activity values, vapour pressure of aqueous solutions of uranyl nitrate was also estimated and is shown in Fig.2 along with the literature data. Both match

well. Based on similar methodology, activity coefficients of various other key and non-key solutes of interest to reprocessing are being evaluated. Incorporation of these activity coefficients in the mathematical models for nuclear solvent extractions would reduce the margin of error in the predictions from the computer simulations.

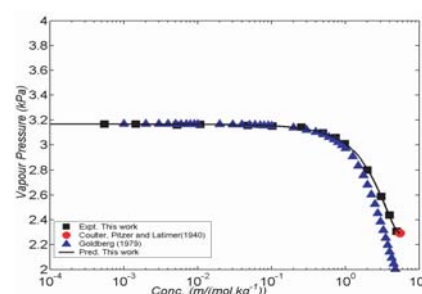


Fig.2 Variation of vapour pressure of aqueous solution of uranyl nitrate hexahydrate with concentration at 298.15 K and 0.1 MPa. The present experimental and calculated data are compared with those reported in the literature.

IV.B.3 Study of TBP-Nitric Acid Runaway Reaction and Synthesis of Red-Oil

TBP nitric acid runaway reaction was studied in a high temperature-high pressure autoclave (shown in Fig.1) and red-oil was synthesized. It was established that presence of metallic nitrates was not essential for red-oil formation as thought earlier. Various single-phase as well as two-phase experiments have been completed.

From Fig.2 it is observed that temperature profile had a threshold of about 403K. This



Fig.1 A view of the experimental setup for study of runaway chemical reactions of interest to reprocessing

threshold temperature is initiation temperature. From Fig.3, it can be seen that the amount of pressure generated per mL of TBP exceeds even 500 psi /mL of TBP. It underlines the absolute necessity of removal of entrained as well as dissolved organics from the aqueous salt solutions before they are concentrated by means of

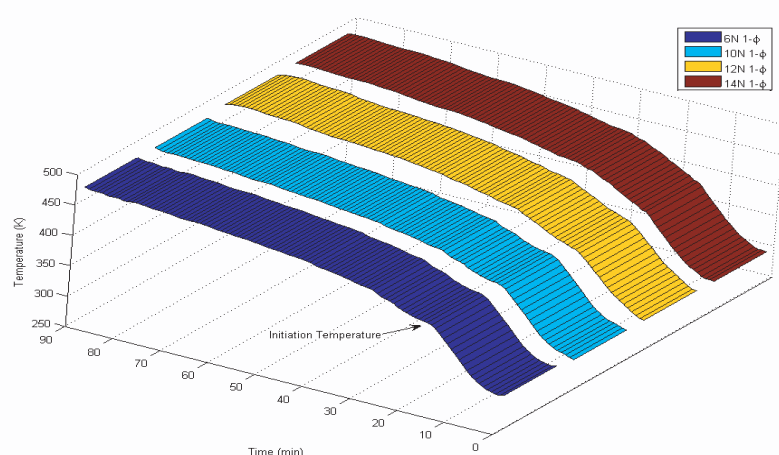


Fig.2 Comparison of single-phase experiments for temporal temperature profiles.

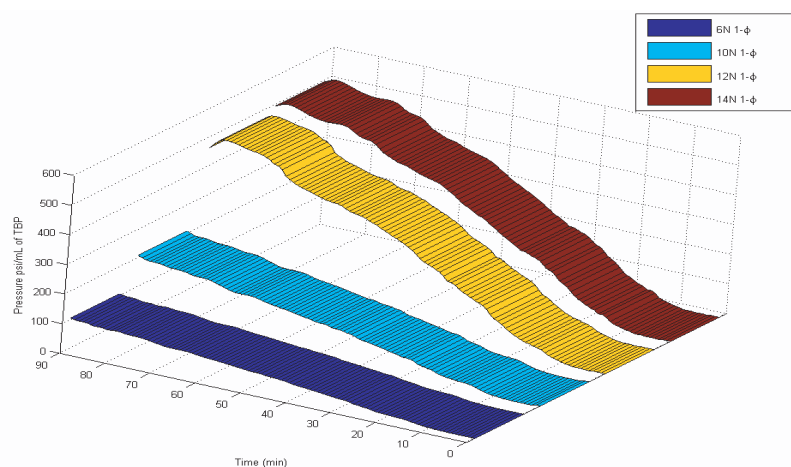


Fig.3 Comparison of single-phase experiments for temporal pressure profiles on the basis of psi/mL of TBP fed

evaporation. Even very low quantities of organic would be enough for an explosion in the case of a red-oil event as the energy involved is very high.

The main results from the red-oil related work done at Reprocessing Group are as follows-

1. TBP-Nitric acid runaway reaction starts only at the

temperatures at or greater than 403.15 K. This was found valid for all the runs either single or two phase system. For control of this situation, operating temperature has to be kept below 393K.

2. Once the runaway reaction starts, the heating rate increases due to auto catalytic reactions involved and pressure starts to shoot up. This feature can be used to detect onset of

runaway reactions and for setting of process interlocks to prevent energetic reaction to happen. As the rate of pressure-rise approaches a pre-decided limit, related logic can provide opening up of larger and safe vent area as well as additional cooling to quench the reaction by bringing temperature below 393-383K.

3. The pressure generated per g or per mL of the Feed TBP is a function of several variables like acidity of the equilibration, amount of acid present in the system during reaction and the temperatures prevailing during reactions.

4. The most important finding is that for prevention of red-oil formation, 10 M limit as earlier proposed in the literature is strictly not valid as found from the recent experiments carried at RR&DD. Red-oil event was observed in the experiments with nitric acid of as low as 2 M concentrations. Thus the prevalent safety guidelines for limiting concentrations need a relook. Pressure generated is quite high even in the experiments with lower acidity. Thus possibility of runaway reaction at the lower acidity needs to be investigated. Further studies are in progress to identify the safe operating regimes during evaporation.

IV.B.4. Recovery of Valuables from Waste Using Room Temperature Ionic Liquids

Room temperature ionic liquids (RTIL) have recently gained recognition in the area of nuclear fuel cycle. They are compounds comprised entirely of ions and are molten at temperatures lower than 373 K. Substitution of unsymmetrical organic cations, for e.g. 1 butyl-3-methylimidazolium cation (bmim) in place of sodium ion in sodium chloride (MP 1074 K) results in the formation of room temperature ionic liquid, bmimCl having melting point of 340 K. As these compounds possess several amazing physical and chemical properties congenial for nuclear reprocessing and waste treatment, they have acquired popularity for their role as solvent/medium for a wide variety of applications. These studies examine the feasibility and merits of

employing RTILs in liquid-liquid solvent extraction process and as electrolytic medium for non-aqueous reprocessing. Furthermore, RTILs are excellent candidates for solubilizing cellulose, starch and wood. Tissue paper is one of the cellulose based materials generated in significant volumes at nuclear fuel cycle facilities. Therefore, studies using RTILs are focused on the recovery of valuable fission platinoids present in the spent nuclear fuel and the development of methods for the treatment of tissue paper waste followed by the recovery of valuables present in the tissue matrix.

Significant quantities of PGMs (Palladium, rhodium and ruthenium) are present in the high burn-up fuel discharged from fast reactors. We have attempted an electrochemical method for the recovery of PGMs using RTIL as electrolytic medium. The study revealed that PGMs in bmimCl are speciated as chlorocomplexes, for e.g. rhodium (III) in bmimCl is present as $[\text{RhCl}_6]^{3-}$ and other chlorocomplexes. Palladium and rhodium chlorocomplexes

are reduced to their metallic form by an irreversible single step two or three electron transfer, respectively, at the glassy carbon electrode. The mass transfer of rhodium (III) was slower compared to palladium (II) under similar conditions. Electrowinning of rhodium from bmimCl medium results in the deposition of metallic rhodium (see Fig.1a). Electrodeposition of fission palladium from co-existing fission rhodium resulted in a separation factor of 10 (Pd/Rh), when the deposition was conducted at palladium deposition potential. The separation factor decreased with increase of applied negative potential (towards rhodium deposition potential). The study indicated that co-deposition of fission rhodium (~10%) is inevitable during electroseparation of fission palladium from a solution of rhodium(III) and palladium (II) present in bmimCl, due to proximity of palladium and rhodium reduction onset potentials.

Significant volumes of tissue paper waste containing special nuclear materials are generated

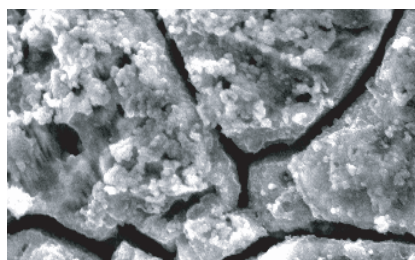


Fig.1a SEM image of rhodium deposits obtained by the electrolysis of 20 mM rhodium chloride in bmimCl for 2 hours on SS plate (3 cm x 4 cm) at -1.7 V (vs. Pd quasi-reference) at 373 K.

during nuclear fuel cycle operations. A new method has been developed for treating these tissue paper wastes using RTIL and electrochemical recovery of the valuables present in it. The procedure involves the dissolution of tissue paper waste in 1 butyl 3-methylimidazolium chloride. The study indicated that dissolution of 5 - 7 wt. % tissue paper in bmimCl was complete within 60 minutes at 373 K. The time required for dissolution increased with increase of loading. The limiting solubility of tissue paper was 15 -17 wt.% at 373 K. Contaminants such as uranium (VI) and Pd (II) present as chloride/nitrate salts also dissolve in bmimCl along with tissue paper. However they can

be recovered by electrodeposition. Electrolysis of a solution of uranium (VI) and palladium(II) loaded tissue paper in bmimCl resulted in deposition of uranium oxide (UO_2) and metallic palladium (see Fig.1b), respectively, which were characterized by X-ray diffraction and scanning electron microscopy. The study established the possibility of dissolving tissue paper and other cellulose based materials containing soluble uranium (VI) and Pd(II) compounds in bmimCl, and their recovery from the resultant solution. Cellulose pulp was regenerated by adding surplus water after the recovery of valuables and the ionic liquid, bmimCl, was also regenerated for further use by vacuum distillation of water.

These experiments confirmed the attractive possibility of developing processes for recovering valuable elements from tissue paper waste without generating significant quantities of secondary waste

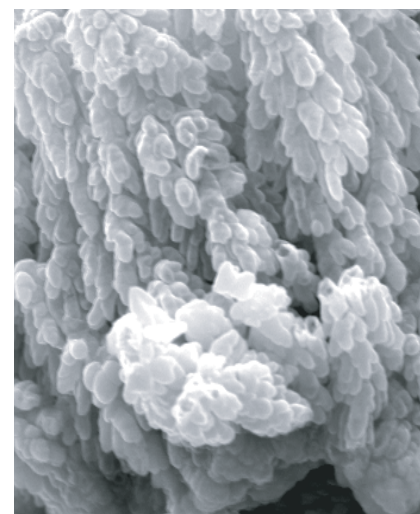


Fig.1b SEM image of palladium deposit obtained by electrolysis of palladium chloride (100 mM) in 5 wt.% tissue paper-bmimCl-DMSO solution for 2 hours on SS plate at -1.0 V (vs. Pd quasi reference) at 298 K.

IV.B.5. Development of a Novel Mixer-Settler with Rotated Helical Coils as Mixer for Nuclear Solvent Extraction

For current designs of radiochemical plants, solvent extraction (SX) contactors with no periodic maintenance are the first choice. In addition, as costs of specialty solvents for nuclear extraction are quite high, there is a demand of SX operation at extreme flow ratios of the two phases (aqueous and organic). Recently a novel mixer-settler was visualized and



Fig.1 A view of the experimental setup

developed for this kind of service. The mixer of the novel SX contactor is based on rotated helical tubes and does not involve any mechanical moving part. This mixer-settler was realized in a glass version at present and tested for hydrodynamics in non-mass transfer region as well as mass transfer region. A view of the experimental setup is shown in Fig.1. Non-mass transfer runs were carried out with pre-equilibrated 30% TBP/kerosene/0.01N acid/water biphasic system. Drop population sizes were measured with a laser drop-size analyzer (Fig.2). Mass transfer runs were carried out with

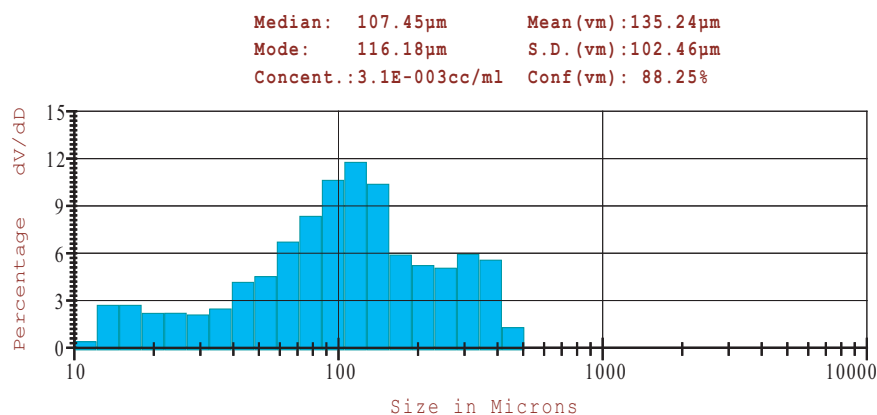


Fig.2 Experimental determination of drop population sizes using laser based drop-size analyzer. Result of water -30% TBP/NPH System at O/A = 6 and 1% SDS concentration.

aqueous nitric acid feed of 4N concentration for extraction runs at different aqueous / organic ratios ranging from 0.04 to 200. In addition, with the loaded organic product from the extraction, back-

extraction runs were also carried. Nearly 100% mass transfer efficiency was observed in all the cases. Therefore prototype was validated and design of a multi stage unit is in the progress.

IV.B.6. Current Status of Demonstration Fast Reactor Fuel Reprocessing Plant

With the successful completion of the several campaigns of spent FBTR fuel reprocessing in CORAL, many modifications have been incorporated in the process flowsheet of Demonstration fast reactor fuel reprocessing plant (DFRP). Also the design of critical equipment such as chopper, dissolver and centrifugal extractors have been updated. These equipment are in advanced stage of fabrication at vendors' works. A view of the chopper-

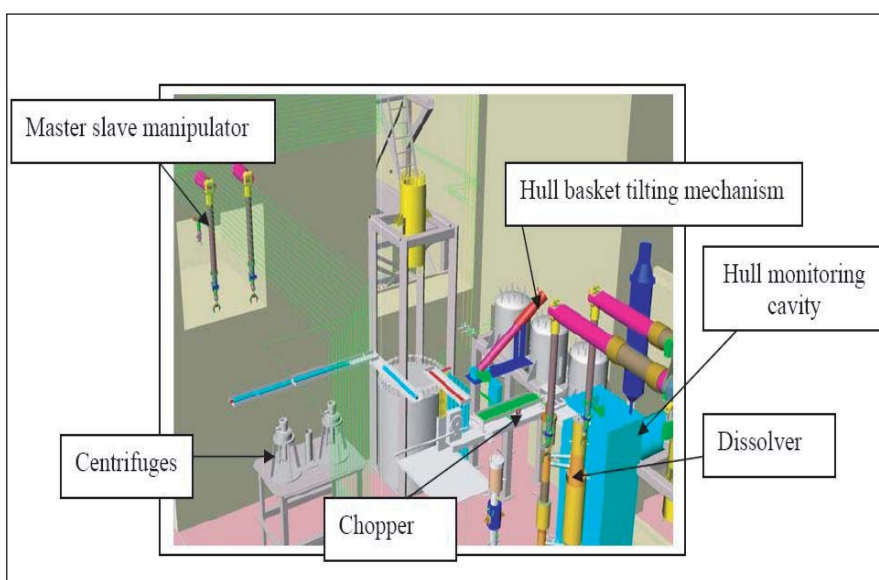


Fig.1 Perspective view of the FBTR chopper-dissolver cell in DFRP with partial piping

dissolver cell is given in Fig.1.

The piping engineering of all the cells have been completed except the dissolver cell. 3D drawings of these have helped in visualizing effectively the erection and maintenance problems. Most of the

packages for piping have been tendered out. The erection of equipment and piping will be completed and the plant will be ready for commissioning by 2009.

The construction of the head end facility, in which FBTR and

PFBR spent fuel will be dismantled, is in progress. The detailed design of this facility has been completed by the consultants. This facility will be integrated with the rest of the plant by 2010.

IV.C. Materials for Fuel Cycle

IV.C.1. Athermal Decomposition Modes of Phase in a Ti-5%Ta-1.8%Nb Alloy

Titanium alloys are chosen for a variety of industrial applications due to their high strength/weight ratio and excellent corrosion resistance, which can be achieved by tailoring the microstructure. The origin of a myriad of microstructures is due to a variety of phase transformations of the high temperature BCC β phase, which is unstable at room

temperature. However, the stability of β phase at room temperature can be influenced by addition of β stabilizing elements and cooling rate. Lean β as well as solute rich alloys undergo a diffusionless martensitic transformation. In the former alloys, β quenching results in a hexagonal martensite while in the latter an orthorhombic martensite forms. Another class of transformation

namely the displacive omega transformation is also reported to occur in group IV metals Ti, Zr, Hf etc. The presence of both martensite and omega phase in a Ti-5Ta-1.8Nb alloy subjected to isothermal treatments in different phase fields has been investigated.

Transmission Electron Microscopy studies established that the $\alpha + \beta$ Ti-5Ta-1.8Nb

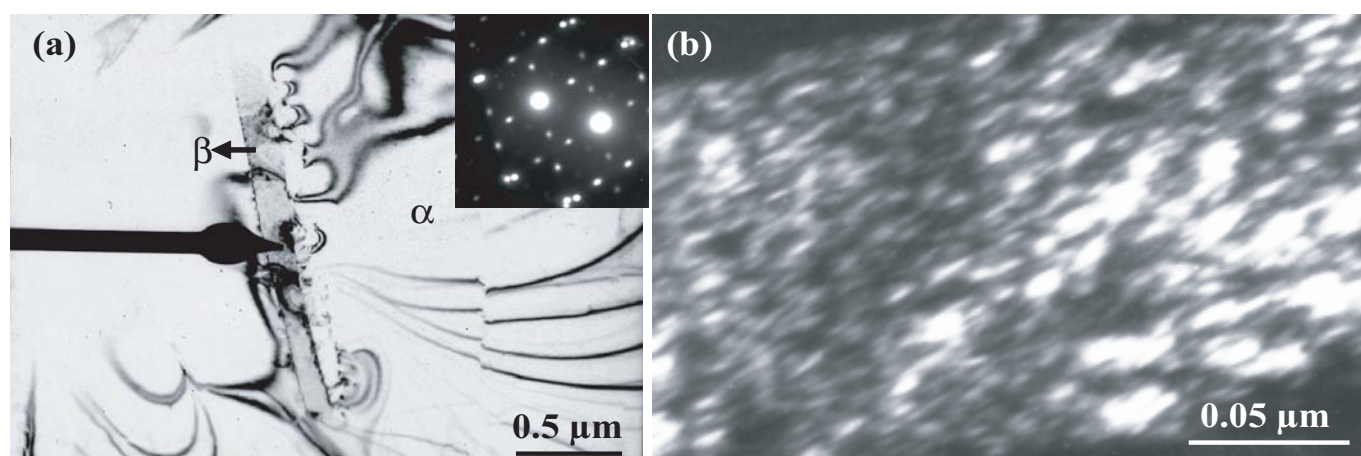


Fig.1 (a) Transformed β microstructure on isothermal treatment in $\alpha + \beta$ phase field below M_s temperature; inset is the diffraction pattern showing the presence of α, β and ω phases (b) Darkfield micrograph showing fine ellipsoidal particles of ω phase in retained β

alloy undergoes a martensitic transformation when quenched from the α phase field (1143K) forming a hexagonal martensite. However, β phase if sufficiently enriched with stabilizers results a transformed β microstructure (Fig. 1(a)) on water quenching, when isothermally treated in the $\alpha+\beta$ phase field at 973K, which is below martensite start (M_s) temperature. Analysis of SAD patterns (inset of Fig. 1(a)) from retained β showed the presence of β phase. The orientation

relationship between α and β , ω and β phases were found to be obeyed, as reported for Ti and its alloys. Dark-field microscopy of ω reflections, showed a dense distribution of fine, ellipsoidal particles of sizes ranging from 4 to 10 nm (Fig. 1(b)). The ellipsoidal morphology of the particles is attributed to the low misfit between α and β phases, since it can be ellipsoidal or cuboidal depending on the degree of misfit. The lower misfit in this alloy is attributed to the similar

atomic size of Ti, Ta and Nb. The hardness of the β annealed alloy, the structure prior to the isothermal treatment showed no significant increase after isothermal treatments, which is also attributed to the poor solid solution strengthening effect of Ta and Nb. It was also observed that aging this alloy under similar conditions showed no evidence for decomposition of β phase. These observations therefore confirm that athermal phase forms in this alloy.

IV.C.2. Effect of Deformation Mode on Texture Development in Ti-5Ta-2Nb Alloy

Ti-5Ta-2Nb alloy has been developed as a structural material for fuel reprocessing applications due to its excellent oxidation and corrosion resistance. The alloy undergoes a variety of phase transformations depending on the temperature and cooling rate. The products show distinct microstructural features and texture. Further, the texture is influenced by the prior deformation.

This alloy has α (hcp) phase as the predominant phase at room temperature, while β (bcc) phase gets stabilized at higher temperatures. The alloy

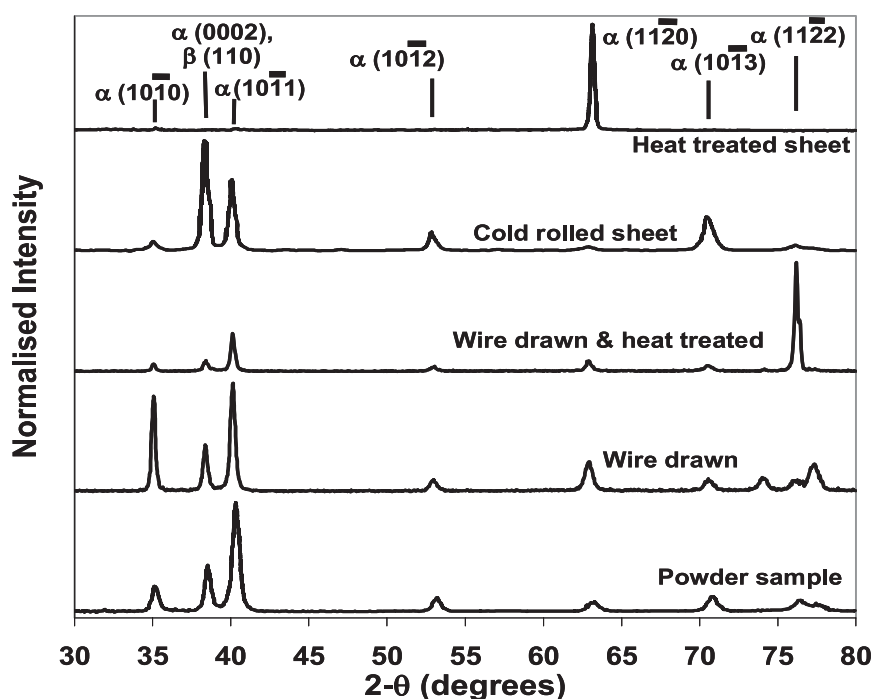


Fig.1 XRD of wire and sheet sample before and after heat treatment, compared with powder sample. Surface of sheet and wire cross-section have been studied.



Fig.2 Crystal orientation map of phase for heat treated wire sample. Inverse pole figure contour shows primary concentration near to (1 1 -2 2)

was deformed by two modes (namely wire drawing and cold rolling), followed by β solution annealing at 1273 K/1 hour and slow cooling to room temperature, resulting in $\alpha + \beta \rightarrow \beta \rightarrow \alpha + \beta$ phase transformations. The evolution of crystallographic texture in the transformed product has been characterized using X-ray Diffraction (XRD) and SEM-EBSD (Scanning Electron

Microscopy-Electron Back Scattered Diffraction) techniques. Fig. 1 shows the XRD intensity of the various (h k i l)_α crystallographic planes, for the wire/sheet samples before and after heat treatment, compared with the powder sample. An increased relative intensity of certain plane suggests preferential crystallographic alignment or 'texture'. Before heat treatment, a 'deformation texture' of [1 0 -1 0]_α//AD (Axial direction) for the wire sample, and a (0 0 0 2)_α//ND (Normal direction) texture for the sheet sample was observed. Heat treatment resulted in a different and more pronounced 'transformation texture' of [1 1 -2 2]_α//AD for the wire, and (1 1 -2 0)_α//ND for the sheet sample. SEM-EBSD analysis was used to study microscopic detail of texture. Fig. 2 and 3 show the 'Crystal Orientation Map' for the heat treated wire, sheet samples respectively, depicting the type of crystallographic planes (color indexed) which are aligned with the sample surface. The EBSD result is in concordance with XRD. The comparison of crystallographic orientation of α lamellae and its neighboring β lamellae showed 'Burgers Orientation Relation' (BOR) to be obeyed. Thus, the alloy is seen to acquire a 'deformation texture' dictated by

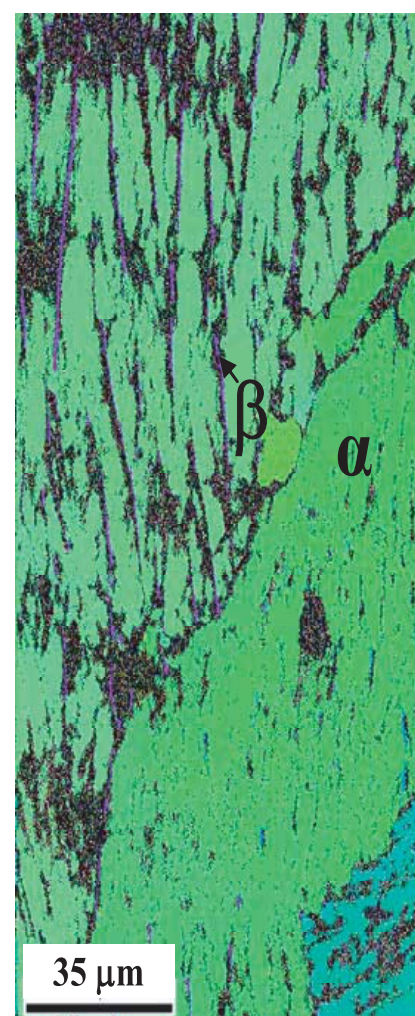


Fig.3 Crystal orientation map of α and β lamellas for heat treated sheet sample. grains are oriented with (1 1 -2 0) alignment.

the deformation mode. Heat treatment leads to high temperature β -texture and a distinct 'transformation texture' of α , as dictated by the orientation relationship during β to α transformation.

IV.C.3. Application of Zircaloy-4 for Highly Corrosive Nitric Acid Environments in Reprocessing Plants

Reprocessing of spent nuclear fuel used in FBRs involves use of nitric acid of high concentrations and temperatures for dissolvers and evaporators which are highly corrosive. The materials chosen for the fabrication of such reprocessing plant equipment should possess excellent corrosion resistance, ease of fabricability and reliability. Conventional austenitic stainless steels are not preferable in such highly oxidizing conditions as they undergo severe intergranular corrosion. Studies carried out earlier indicated good corrosion resistance of Commercially Pure Titanium (CP-Ti) and Ti-5%Ta as

compared to AISI type 304L SS in highly oxidizing nitric acid. Thus, titanium was chosen for fabricating electrolytic dissolver of CORAL plant, with a dissimilar joint by explosive joining process for linking to type 304L SS equipment in the plant, for reprocessing of spent fuel from FBTR. For future reprocessing plants, based on research and international experience, developmental efforts have been made for the fabrication of dissolvers by using Ti-5%Ta-1.8Nb alloy.

The excellent corrosion resistance of zirconium in nitric acid has been known for over 50 years. Zirconium is highly resistant to nitric acid

environments and is considered as candidate material for various applications in spent nuclear fuel reprocessing plants involving highly concentrated nitric acid medium. Zirconium and its alloys are thus considered as candidate materials for various applications in spent nuclear fuel reprocessing plants involving nitric acid of high concentrations at high temperatures. Also, unlike titanium and its alloys, zirconium is unaffected by vapour and condensate of boiling nitric acid.

An attempt was made to study the corrosion behaviour of Zircaloy-4 (Zr-with Sn-1.4%,

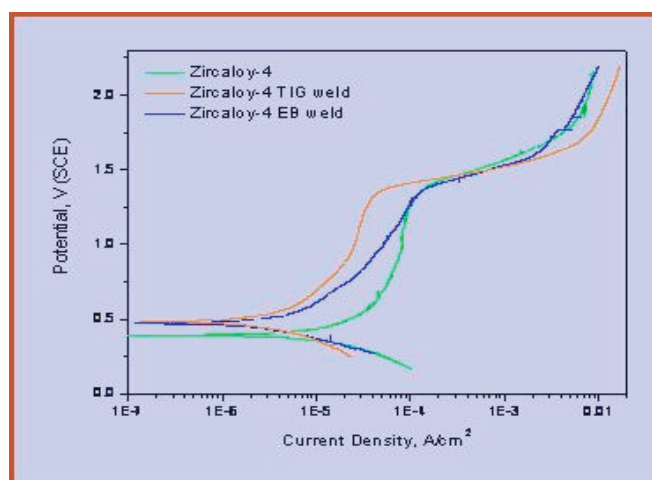
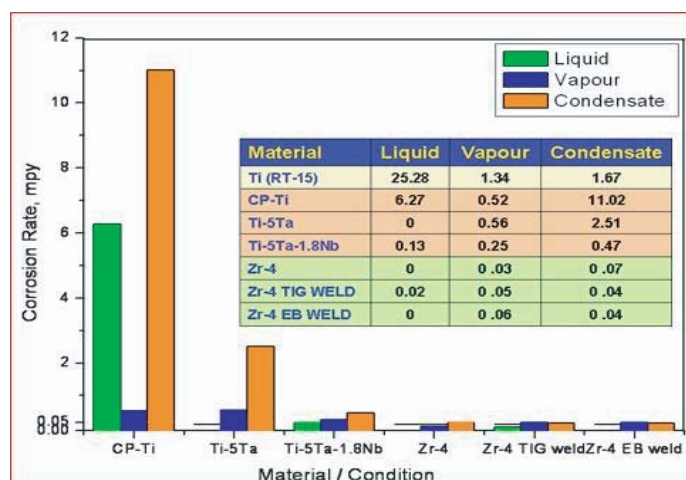


Fig.1 (a) Corrosion rate of materials in three phase corrosion test, (b) Potentiodynamic polarisation curves of wrought and welded samples, in 11.5M HNO₃ medium.

Fe-0.22%, Cr-0.1%) in wrought and welded forms in comparison with other candidate materials like CP Ti, Ti-5%Ta and Ti-5%Ta-1.8%Nb. Manual TIG welding and electron beam welding were carried out with Zircaloy-4, and radiography was made for choosing defect free regions for making samples for corrosion investigations. Three phase corrosion testing in liquid, vapour and condensate regions was conducted in boiling 11.5M nitric acid using a specially designed experimental set up. The corrosion rates were evolved based on the weight change after the test for 240 h, and the tested base samples in liquid and condensate phases were analysed for the nature of surface films by using X-ray photoelectron spectroscopy (XPS), while that exposed to liquid phase was analysed by using secondary ion mass spectroscopy (SIMS). Potentiodynamic polarization technique was used to study the polarization behaviour in both base and welded conditions in 11.5M HNO₃ solution at room temperature.

The average corrosion rate for five individual periods in liquid, vapour and condensate phases of boiling 11.5M nitric acid for CP-Ti, Ti-5%Ta, Ti-

5%Ta-1.8%Nb, Zircaloy-4, Zircaloy-4 TIG weld and EB weld samples are shown in Fig.1 (a). As the corrosion rates are in close ranges the values are also provided in Table inserted in the figure. The corrosion rates clearly indicated superior corrosion resistance of zircaloy-4 in both wrought and welded conditions as 'near-zero corrosion material' in comparison to CP-Ti, Ti-5%Ta, and, Ti-5%Ta-1.8%Nb. The electron beam welded samples did not show any deterioration and performed similar to wrought alloy. The high corrosion resistance of zirconium and its alloys in highly oxidizing nitric acid conditions is due to a stable and adherent ZrO₂ film formed on their surface. XPS and SIMS spectra indicated the formation of ZrO₂ protective film on the surface after testing. The binding energy of Zr3d_{5/2} from high resolution spectra indicated the presence of Zr in +4 valency state in condensate phase. SEM examination revealed insignificant corrosion attack of Zircaloy-4 and its welds in all three phases in comparison to CP-Ti, Ti-5%Ta, and Ti-5%Ta-1.8%Nb after testing in liquid, vapour and condensate phases. However, accelerated corrosion attack was noticed for titanium after testing in condensate phase.



Fig.2 Zircaloy-4 corrosion testing system for three phase corrosion evaluation in 11.5M HNO₃.

The polarization curves for Zircaloy-4 and its welds exhibited a wide region of stable passivation up to 1.5 V (SCE) beyond which distinct breakdown of passivity was noticed. The welded samples showed similar or better corrosion behaviour (Fig.1 (b)) compared to wrought alloy in 11.5 HNO₃ M solution.

The results of microstructure, microhardness, corrosion rate, morphology of attack and nature of surface film formed clearly established that zircaloy-4 is a candidate material for application in highly corrosion concentrated nitric acid at high temperatures in reprocessing plants. Based on the results of the investigation a zircaloy-4 testing system (Fig.2) with an option to conduct long term corrosion study in liquid, vapour and condensate region was fabricated, commissioned, and evaluated for corrosion behaviour.

IV.C.4. Glass-ceramic Waste Form for the High-level Waste from Pyrometallurgical Reprocessing of Nuclear Fuels

The high-level radioactive waste (HLW) generated from pyrometallurgical reprocessing of irradiated nuclear fuels in molten LiCl-KCl media cannot be immobilized in the conventional borosilicate glass, as chlorides have very poor solubility in glass. Immobilization of the chloride waste in a glass-ceramic such as glass-bonded sodalite, has emerged as a promising option. Sodalite is a naturally occurring mineral, and the glass-ceramic waste form based on it is considered suitable for disposal in geological repositories. The waste form fabrication involves the occlusion and/or ion exchange of the radioactive waste on to a zeolite, tailoring with a glass binder, and subsequent conversion to the glass-ceramic. The preparation and characterization of such a waste form using a simulated waste composition have been investigated.

Dehydrated Zeolite 4A was homogenized with simulated chloride HLW of a representative reference composition (2 wt% CsCl, 2 wt% BaCl₂, 9 wt% NdCl₃ and the rest LiCl - KCl eutectic) in

an inert atmosphere glove box, and the mixture was equilibrated at 848 K for 100h in static argon. The salt-loaded zeolite (SLZ) was washed with water, and the eluate analyzed by atomic absorption spectrometry in order to ascertain the extent of salt uptake in the zeolite matrix. The SLZ was then converted to glass-bonded sodalite [Na₈(AlSiO₄)₆Cl₂] by blending it with 25wt % of a specially prepared boroaluminosilicate glass, pelletizing and heating at 1188 K for 15h in flowing argon. By this procedure, several batches were prepared by varying experimental

parameters such as the zeolite-to-salt ratio. X-ray diffractograms of the final waste form showed sodalite as the major phase and nepheline as a minor phase (Fig.1). SEM micrograph of the product showed a uniform microstructure (Fig. 2).

Thermophysical properties like thermal expansion and glass transition temperature of the glass-ceramic were studied by high-temperature XRD and differential scanning calorimetry, respectively. The variation of the lattice parameter with temperature was found to be similar to that

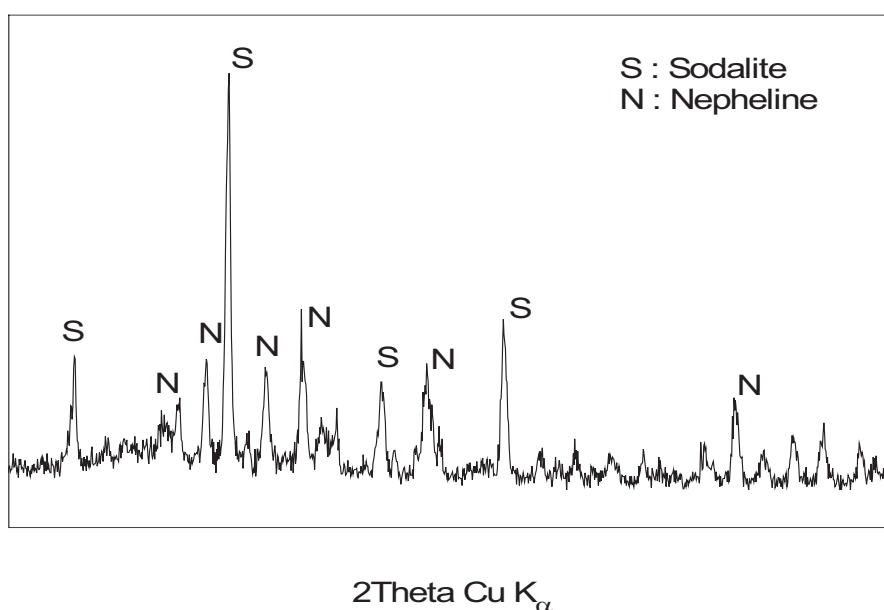


Fig.1 Powder XRD pattern of the glass-bonded sodalite

of pristine sodalite, indicating that the incorporation of fission products in the sodalite matrix

does not significantly alter its thermal expansion behaviour. The glass transition

temperature (T_g) of the glass-bonded sodalite system (808 K) was found to be significantly lower than that of the borosiluminosilicate glass (868 K) used as the binder. This appears to be the indication of some interaction between the ceramic phase and the glass, the exact nature of which is to be established. With the glass composition employed in this study, the waste loading per canister has to be such that its centre line temperature stays well below the glass transition temperature of 808 K.

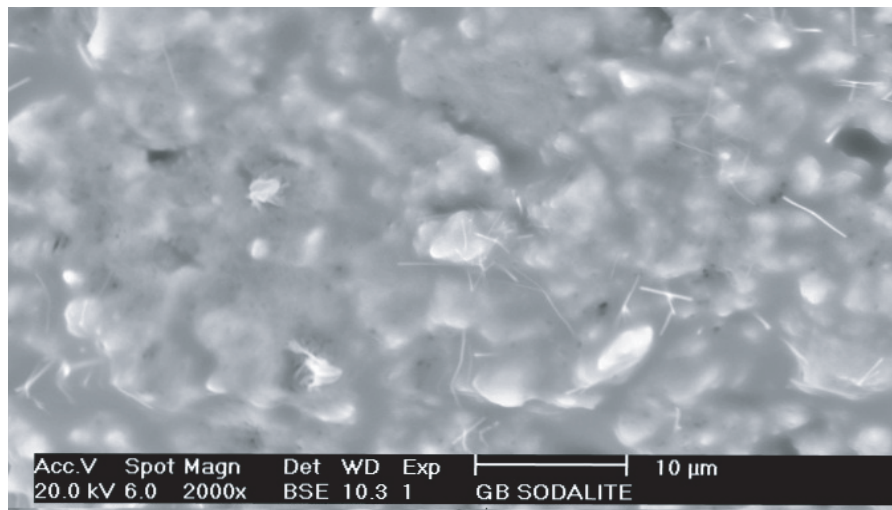


Fig.2 SEM micrograph of the glass-bonded sodalite

IV.C.5. Development of NDE Technique for Detection of Sodium Voids in Metallic Fuels - a Simulation Study

Non-destructive evaluation (NDE) plays a vital role for ensuring stringent quality assurance of nuclear fuel cladding tubes. Eddy current (EC) NDE technique is routinely employed during manufacturing stages of cladding tubes of fast reactors as it is a versatile, high-speed and high-sensitive technique.



Fig.1 Aluminum tube with machined notches simulating voids in sodium and the experimental set up for imaging voids in sodium bonding.

This technique is also used during post-irradiation examination of fuel pins in hot cells to detect and size surface and sub-surface defects in the cladding wall as well as certain anomalies in encapsulated fuel pellets. Metallic fuels are candidate fuels for fast breeder reactors for generation of nuclear power in future. The metallic fuel slugs in this type of fuels are encapsulated in cladding tubes with sodium bonding.

During fabrication stages, there exists a possibility for formation of voids filled with

inert gas due to improper sodium filling. Non-destructive detection of these voids or inert gas bubbles in sodium is important as their presence affect the heat transfer and thereby the fuel centre temperature and burn-up. From the design considerations, it is required that voids larger than $1.4 \times 2.1 \text{ mm}^2$ be detected during manufacturing stages of the fuel pins. In this direction, eddy current technique has been attempted to detect voids smaller than the specified size, using a pancake type probe, subsequent to initial studies on quartz tubes filled with sodium

and having a variety of inert gas voids. The pancake probe when used in conjunction with a scanner is expected to detect, image and locate voids in fuel pins and hence, detailed experimental studies have been carried out.

In order to simulate the voids in sodium column, a 0.3 mm thick aluminium tube having electrical conductivity nearly equal to sodium has been chosen and a variety of holes, notches and slots identical to the expected voids have been

machined. Typical simulated notch in aluminium tube inserted in a FBTR cladding tube, and the experimental set up comprising of in-house developed z- θ scanner, EC instrument and pancake probe are shown in Fig.1.

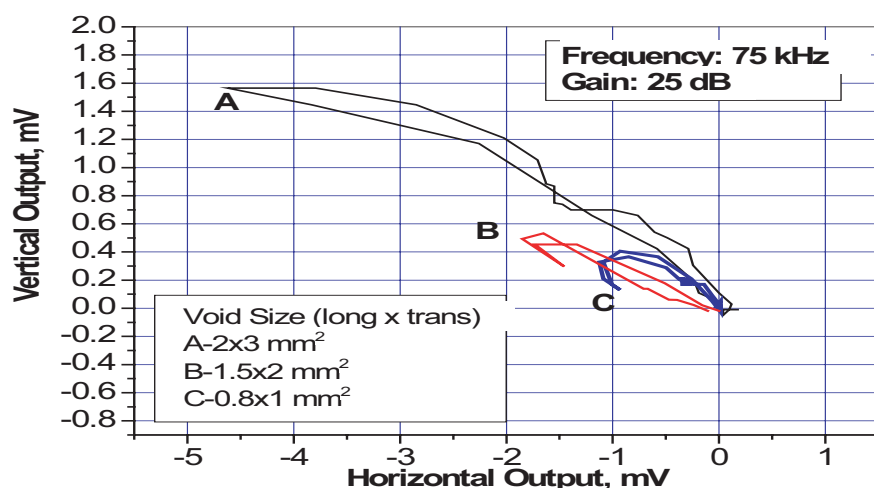


Fig.2 EC signals of simulated voids (notches in aluminium tube) at 75 kHz.

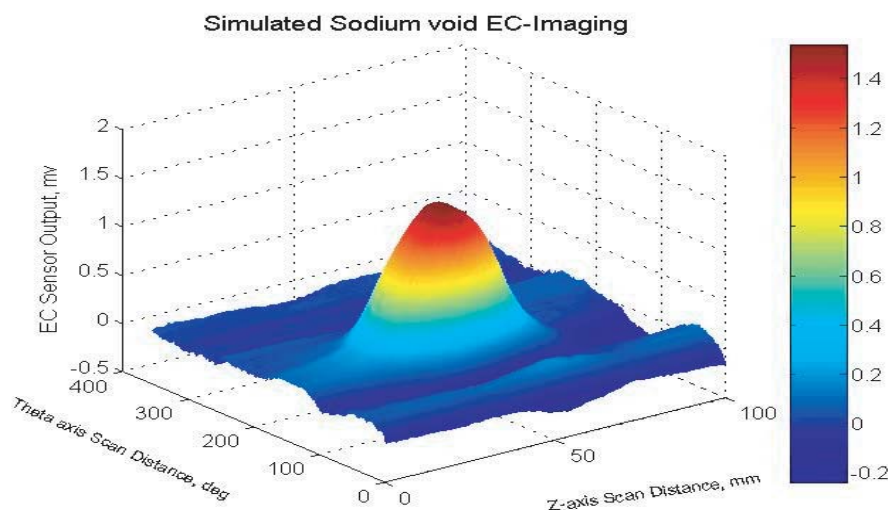


Fig.3 Eddy current image of 2x3 mm² notch simulating void in sodium.

Typical EC signals from three simulated voids of 2x3mm², 1.5x2 mm² and 0.8x1 mm² at 75 kHz using a pancake probe are shown in Fig.2. As can be observed, the 0.8x1 mm² notch, which is much smaller than the specified void size of 1.4x2.1 mm², has produced unambiguous signal even at a small gain of 25 dB.

In order to determine the circumferential location of voids, the pancake probe has been attached to the z- θ scanner and imaging of simulated notches has been carried out to develop detailed test procedure for reliable detection of voids. Typical image of 2x3 mm² notch is shown in Fig.3. Studies reveal that it is possible to identify the location of a void from the axial and the circumferential location of the signal/image feature and also to size it reliably.

IV.C.6. Temperature Evolution in Spent Fuel Subassembly during Handling in Fuel Transfer Cell

Spent fuel subassembly (FSA) is removed from the sodium filled transfer pot at the location of Ex-Vessel Transfer Post (EVTP) for handling in Fuel Transfer Cell (FTC) and subsequent storage in water pool storage bay. To prevent possible release of radioactivity due to failure of FSA clad, the temperature of clad should not exceed its permissible limit of 923 K. To achieve this, the FSA is force cooled from the top of the FSA by supplying nitrogen at 323 K filled in FTC itself in re-circulation mode (Fig. 1). In the event of loss of forced cooling, the temperatures of clad and hexcan increase, till the heat loss under natural convection and radiation equals the decay power. It is essential to determine the final steady state values of these temperatures, to assess whether natural cooling adequate. Also, knowledge of transient temperature evolution in the FSA is essential to determine the time available for the operator to take safety action. These have been evaluated by detailed conjugate computational fluid dynamics studies.

In the absence of forced cooling, the mode of heat transfer within the bundle (i.e) between the pins is only conduction and radiation as natural convection of nitrogen through the compact fuel bundle is negligible. Heat

transfer from hexcan to FTC ambient (nitrogen) is by natural convection and radiation. A 30 degree sector of FSA with the active fuel pin region of 1 m height has been considered in the analysis. For a single pin, the temperature difference

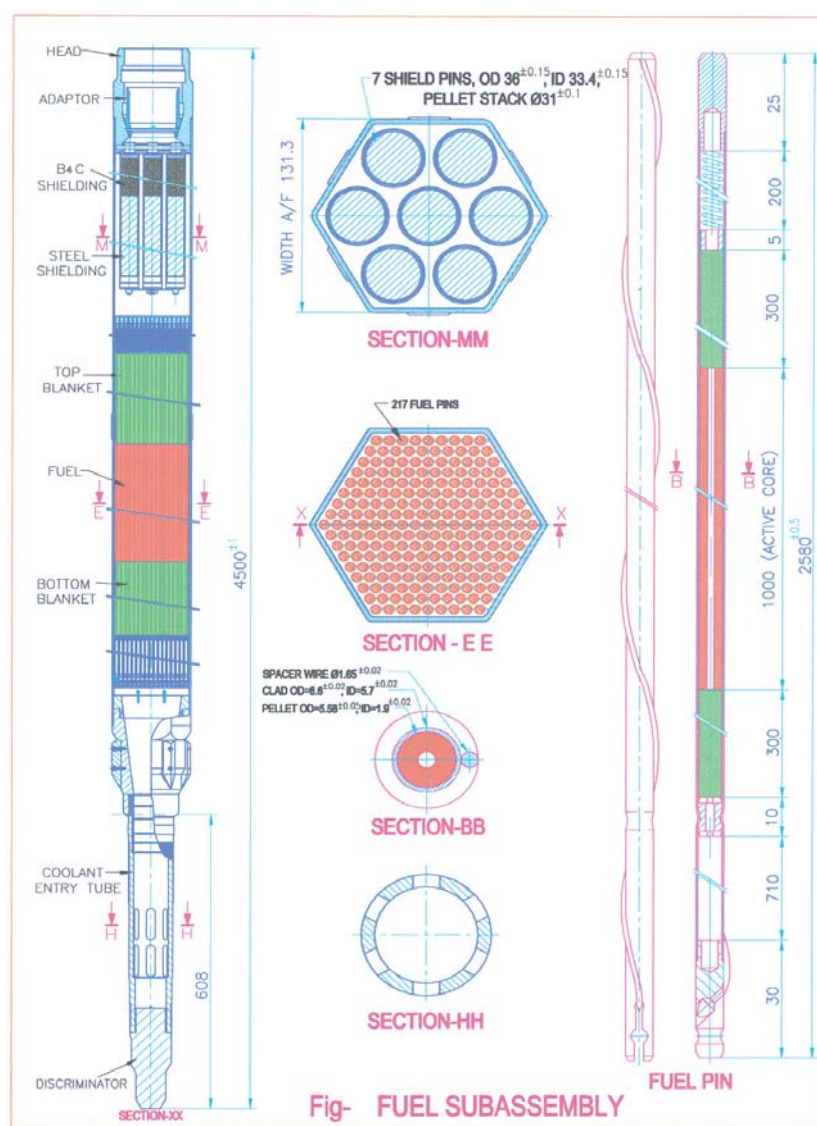


Fig.1 Spent fuel subassembly force cooled by nitrogen from top

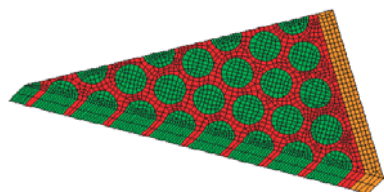


Fig.2 Computational mesh of 30° sector of FSA

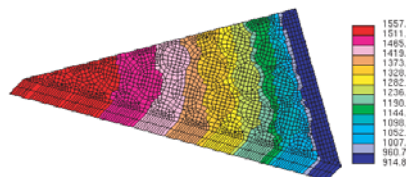


Fig.3 Steady state temperature of fuel pins and nitrogen (in K) for 5 kW decay power

between the fuel centre and clad surface is estimated as ~ 1 K only due to very low decay power of 5 kW. Hence, the fuel, clad and the gap between them are lumped into a single material having equivalent properties. The finite volume mesh of the FSA generated using STAR-CD code is presented in Fig. 2. The decay power of the FSA is given as volumetric heat source in the fuel pins. Appropriate values of

surface emissivity have been taken for clad and hexcan, considering the fact that sodium is coated on the surfaces.

Predicted steady state temperatures of the fuel pins, stagnant nitrogen within the FSA and hexcan, for 5 kW decay power, are presented in Fig. 3. As the heat transfer takes place in the radial direction and towards the heat sink which is outside the hexagonal sheath, the pin surfaces facing the sheath are at lower temperature compared to pins surfaces facing the centre of the FSA. It is seen that the temperature of central pin clad is 1557 K. Since the clad temperature is exceeding 923 K, forced cooling of the FSA is essential. Similar maximum clad temperature is estimated for various values of decay powers (from 1 to 5 kW). It is

found that for a decay power of 1 kW, the clad temperature is 883 K which is within the limit of 923 K. For 2 kW decay power (corresponding to internal storage for 2 campaigns), the clad temperature is 1118 K. Hence, FSA with decay power less than or equal to 1 kW can be handled in FTC without any forced cooling. For higher powers, forced cooling is essential.

The transient temperature evolution of spent FSA central pin clad in FTC is presented in Fig. 4, for the case of 5 kW decay power. The normal fuel handling time of spent FSA is 30 - 45 min for its travel from primary sodium pool to EVTP. When the FSA reaches EVTP after this time, the clad temperature is ~ 773 K. At EVTP location, the FSA is taken out of the sodium filled transfer pot and the clad temperature again starts to increase when forced cooling is unavailable for the FSA inside FTC. It takes 15 min for the central pin clad temperature to reach the limiting value of 923 K. After this it takes a long time (~ 4 h) to reach the steady state temperature of 1557 K. Hence, it is established that loss of cooling can be sustained for about 15 min.

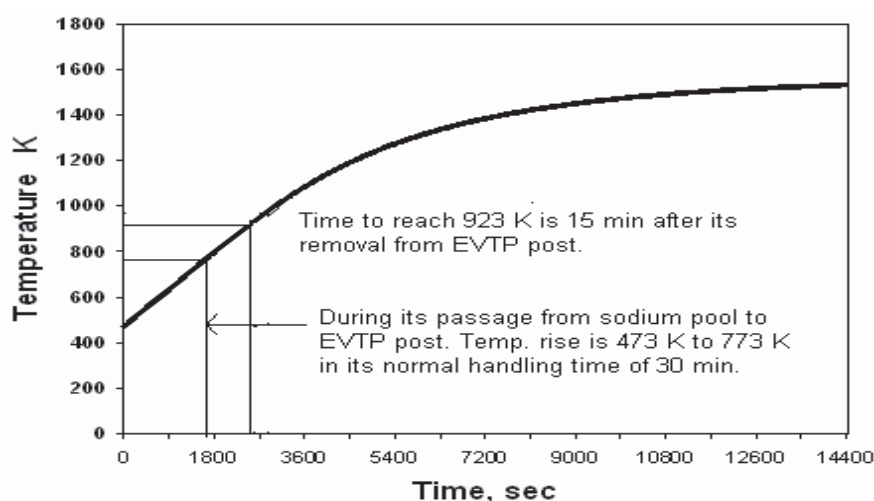


Fig.4 Evolution of central pin clad temperature during loss of cooling (5 kW decay power)

IV.D. FRFCF

IV.D.1. Status of work on Fast Reactor Fuel Cycle Facility

A Fast Reactor Fuel Cycle Facility (FRFCF), that is a first of its kind in the country, is planned to reprocess the spent fuel from PFBR to recover plutonium and uranium, and recycle them to manufacture fresh fuel and supply to PFBR for reloads. This would lead to closing of the PFBR fuel cycle and eliminate transport of plutonium required for PFBR in public domain. This large project, which is a green-field project, would require developing the complete designs of plant and machinery needed to achieve the objective. The facility will contain a reprocessing plant, a fuel fabrication plant, a

reprocessed uranium oxide plant, a core sub assembly plant, and an integrated waste management plant. The facility would be self-contained and located at Kalpakkam. The work is being piloted by IGCAR with technical support from BARC and NFC. The project will continue on to the XII Plan as well. The site selected for FRFCF has been approved by AERB after evaluation. As a preparatory step to construction of FRFCF, sanction has been obtained for development of infrastructure for FRFCF and appointment of consultants for detailed design. Basic infrastructure is being created to reduce the lead time

required to commence the construction work once the FRFCF project is sanctioned.

Design of selected infrastructure buildings has been completed. Construction activity related to Main power station (Fig.1), Stores, and workshop buildings is in progress. Work on construction power supply system has been completed. Topographic survey, and Geotechnical / hydrogeological investigations of the site have been completed and the results of geotechnical investigations are presented in the article "Integration of Geophysical and Geotechnical Investigation at FRFCF Site". AERB has constituted a Project Design Safety Committee for FRFCF and review of the preliminary safety analysis report is in progress. The committee inspected the FRFCF site during geotechnical investigation phase (Fig.2). Appointment of consultants for the detailed design is being processed. Detailed project report for FRFCF is planned to be submitted for financial sanction during the year 2008-09.



Fig.1 Work on main power station building in progress at FRFCF site



Fig.2 PDSC Members inspecting the FRFCF site. Soil load bearing capacity test set up is in the background.

IV.D.2. Integration of Geophysical and Geotechnical Investigations at FRFCF Site

Geophysical methods have been used successfully for geotechnical engineering applications which include establishing stratigraphy, depth to bed rock, and locating discontinuities and abnormalities. Appropriate inclusion of a geophysical survey into geotechnical subsurface exploration and testing programme also provides valuable information on the lateral variation of soil properties. A shallow seismic refraction survey was carried out during the initial planning stage at FRFCF site to decide the foundation level of various civil structures of this facility. Subsurface exploration of this site was carried out at this site to evaluate properties of the sub soil. Fig. 1 shows a view of the drilling work at FRFCF site. Findings of geophysical and geotechnical investigations were integrated to obtain

complete site characterization. Generalized soil profile, velocity model for site classification, rock mass classification, and dynamic properties were arrived through integration of the results.

The investigations show that bed rock is available at a depth of 15m to 20m below the ground level. The top level of weathering grade III rock established from seismic refraction and geotechnical investigation shown in Fig.2.

Dynamic properties were evaluated from the seismic cross-hole survey and are shown in Table 1. The variation of shear wave velocity with depth is shown in Fig 3. These values will be used to provide the elastic parameters for earthquake analysis and also as input in dynamic response studies.



Fig.1 Drilling work at FRFCF

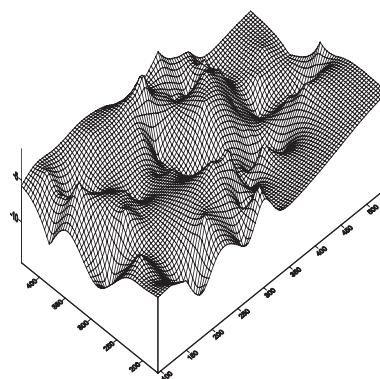


Fig.2 Top of weathering grade 3 rock

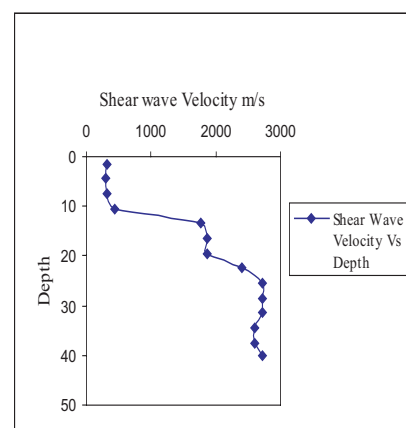


Fig.3 Variation of shear wave velocity with depth

Table 1: Range of dynamic soil properties

Strata	S-Wave Velocity (m/s)	P-Wave Velocity (m/s)	Poisson's-Ratio	Shear modulus GPa
Sand	316-429	600-769	0.27-0.36	0.17-0.34
Weathered rock	1765-1875	2857-3797	0.17-0.2	8.57-15.85
Bed rock	2400-2727	4225-4400	0.16-0.21	17.2-20.47

Chapter -5

ENABLING TECHNOLOGIES

V.A. Inspection Techniques

V.A.1. Development of Novel Combination of Immersion and Time of Flight Diffraction for Examination of Thin Weldments

Time of Flight Diffraction (TOFD) technique is an advanced ultrasonic nondestructive testing method which can be used for accurate sizing of the discontinuities. This method is based on the time difference between the diffracted signals obtained from the tips of the discontinuity. Codes of practice recommend TOFD for weldments with thickness greater than 12.5 mm. Very few studies have been undertaken internationally for specimen thickness less than 12.5mm. Internationally TOFD combined with signal processing has been applied to specimen thickness down to 6mm. As the thickness of the specimen decreases, the lateral wave, diffracted echoes from the discontinuity and the back wall echo merge together and hence defect detection and

characterization is not possible. This problem has been successfully overcome at the Quality Assurance Division using a novel combination of TOFD and immersion. The principle is illustrated as a schematic sketch in Fig.1.

For initial studies, three stainless steel plates with artificial reference defects were chosen. Plate 1 was 10 mm thick and had five side drilled holes of 2 mm diameter at different locations. Plate 2 was 5 mm thick with 5% and 10% notches and two side drilled

holes (2 mm diameter) and Plate 3 was 3 mm thick with a 5% and 10% notch. Since the plates were quite large and the region of interest was small, to maintain the required water path, a dam was constructed. Fig. 2(a) shows the experimental setup.

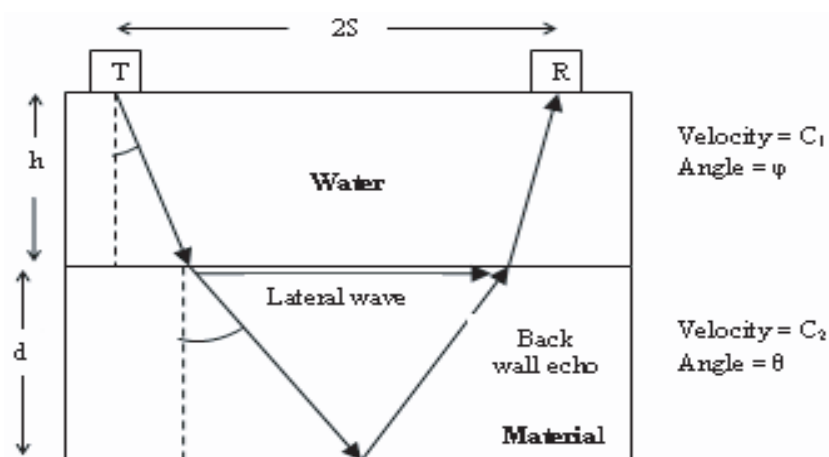


Fig.1 Beam path and angle of propagation through water and material in the immersion TOFD experiment

The parameters to be considered were thickness of the water column over the material and probe tilt (Fig.1). Based on the time of flight equations, the time difference between lateral wave and back wall echo was computed as a function of probe tilt for specimens of different thickness. It was observed that as the probe separation and the propagation angle inside the material decreases, this time difference increases which leads to better spatial resolution (Table1).

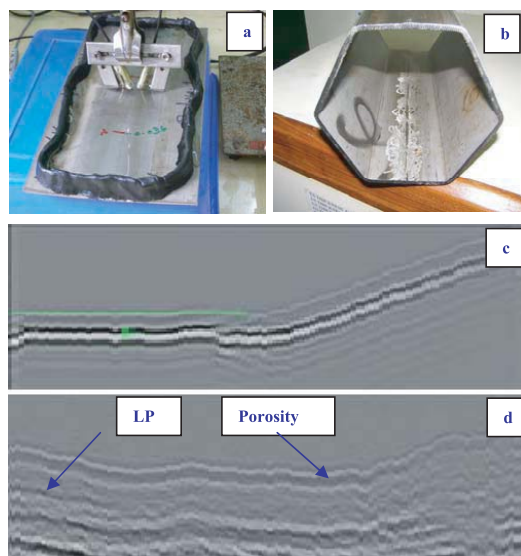


Fig.2 (a) Experimental setup (b) 3.15 mm thick welded hexagonal sheath (c) TOFD image of a welded plate having no defect (slop is due to curvature of the plate) and (d) TOFD images indicating lack of penetration and porosity.

The required lower probe separations were not possible in conventional TOFD because of the size of the probes. Based on the experiments on the reference specimens, further examinations were carried out on welded specimens of thickness 3.15mm. These specimens pertain to the hexagonal sheath of the dummy fuel sub-assembly. The weld specimens had defects such as lack of penetration and porosity

Table 1 : Different parameters to be considered for immersion TOFD

Probe tilt in water (ϕ)	Wave propagation angle inside the material (θ)	Probe Separation (2S) (mm) for plates of		Time difference between lateral wave and back wall echo (μ Sec)	
		5mm	3mm	5mm	3mm
2.5	10	1.2	0.7	1.483	0.889
3.7	15	1.8	1.1	1.396	0.837
4.9	20	2.4	1.5	1.312	0.787
6.1	25	3.1	1.9	1.228	0.737
7.2	30	3.8	2.3	1.147	0.687
10.2	45	6.6	4.0	0.894	0.536
12.5	60	11.5	6.9	0.623	0.374
13.6	70	18.2	10.9	0.427	0.255

which were earlier confirmed through radiography. The combination of TOFD and immersion could pick up these defects, which was not possible with conventional TOFD method. Typical TOFD images are shown in Fig. 2 (c) and 2(d) respectively. The welded specimens were subjected to

radiography and the radiographic images were processed with appropriate methodologies and dimensions of the defects estimated. Dimensional measurements from radiographs were compared with the dimensions from TOFD measurement. A very good correlation was

obtained with errors being less than 5%.

This experiment establishes that TOFD combined with immersion extends the limits of examination of conventional TOFD and is a novel solution for the examination of thin weldments.

V.A.2. Infra Red Thermal Imaging of Weld Pool in Real Time during GTAW of Type 316 LN Stainless Steel

In remote welding operations, on-line monitoring and control of Gas Tungsten Arc Welding (GTAW) process is very essential and a methodology is being established using IR Thermography. The infra red camera was mounted on the torch assembly to facilitate on-line monitoring of the welding process and determine surface temperature distribution surrounding the weld pool

during GTAW. The interference from the arc light and the hot tungsten electrode on the image quality is minimized by using band pass filters. The instantaneous thermal images of the weld pool that were captured by the infra red camera was transferred to a computer. The infra red camera determines the surface temperature distribution of the plate by capturing the emitted

energy within a wavelength band of 4 - 6 μ m. Each scan of the camera was transferred as a frame consisting of 320 x 240 discrete temperature measurements. Full frame analysis was carried out to determine the temperature surrounding the weld pool for the entire length of the plate being welded and is shown in Fig. 1. This data was very useful in validating the heat flow

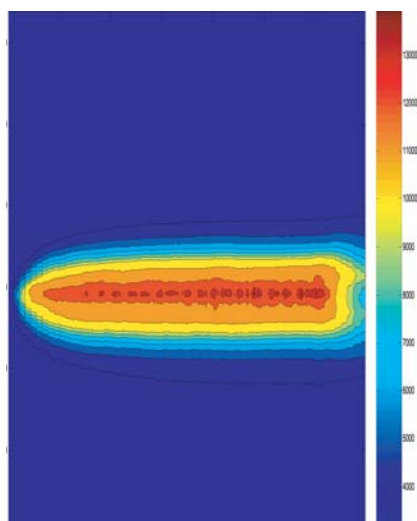


Fig. 1 Temperature distribution surrounding the weld pool

models developed using FEM and also in identifying the various microstructural zones in a weldment. Weld bead width was measured and displayed

on-line for the entire length of the weld as shown in Fig. 2. There was good correlation between thermal bead width and the actual bead width. Macroscopic temperature gradients determined using line scan technique was correlated with the variations in the depth of penetration. A fuzzy rule based control algorithm is being developed for on-line monitoring and control of GTAW in order to achieve the desired weld bead geometry.

Full frame analysis was carried out to generate thermal signature images for detecting various weld defects such as

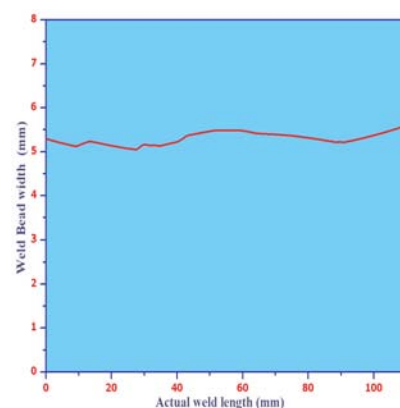


Fig.2 Weld pool width for the entire weld length

lack of penetration, lack of fusion, tungsten inclusion and porosity. These signature images are being used as reference images for on-line quality monitoring of the 316 LN stainless steel weld during GTAW.

V.A.3. Multi-NDE Techniques for Comprehensive Characterization of Microstructures in M250 Maraging Steel

M250 maraging steel, by virtue of its excellent mechanical properties i.e. ultra-high yield strength combined with good fracture toughness, is preferred as structural material for critical applications in advanced technologies. Besides, its high strength to weight ratio, good weldability and easy machinability in solution annealed (SA) condition and dimensional stability during aging make this material an

ideal choice for critical rocket motor casing applications in aerospace industries. The strength in aged condition is derived from the fine and coherent intermetallic precipitates, whereas low carbon martensitic structure provides the high fracture toughness. Over-aging results in coarsening of the intermetallic precipitates in addition to reversion of martensite to austenite which affects both tensile and fracture

properties. Characterization of the complex microstructures generated in components during aging is very important for qualification of components integrity. Non-destructive evaluation (NDE) techniques show good potential for quick and reliable characterization of microstructures. Interaction of non-destructive interrogating media with complex microstructural features is different, with each NDE techniques giving

Table 1 : Relative comparison of sensitiveness of different NDE techniques for characterization of ageing behaviour in maraging steel

NDE Parameters	Defects (Vacancy/dislocation)	Precipitates	Reverted Austenite
Ultrasonic Velocity	N	YY	Y
Positron Annihilation	YY	Y	N
Magnetic Barkhausen	Y	Y	YY
Eddy Current	Y?	Y	Y
X-Ray Diffraction	N	N	Y

N-Non sensitive Y-Sensitive

YY-More sensitive Y?-Sensitive but requires precise measurements

complimentary information or confirming the observation of other techniques, this enhances the use of multiple techniques and adopting multi-parametric approaches is very attractive and is expected to enable very effective characterization of microstructures. In this study, NDE parameters such as ultrasonic velocity, magnetic Barkhausen emission (MBE) RMS voltage, eddy current (EC)

methodology for characterization of ageing behaviour of M250 grade maraging steel aged at 755 K for different durations.

The variations in hardness, ultrasonic longitudinal wave velocity and positron annihilation life time with aging duration are shown in Fig.1. The variations in hardness, MBE rms voltage, volume % of austenite (XRD based) and impedance amplitude with aging duration are shown in Fig.2. Ultrasonic velocity showed good promise in characterizing the intermetallic precipitation process and was able to pick up the austenite information to some extent. Its drawback is with respect to obtaining any information about the defect structure and early detection of initiation of austenite reversion. Hence, this technique is found to be very sensitive to monitor only the intermetallic precipitation

behaviour. Positron annihilation studies were found to be very sensitive to changes in defect structure during initial aging and precipitation to some extent. Fig.3 shows the bright field TEM image of defects (dislocations) in solution annealed condition. The austenite reversion has insignificant effect on positron annihilation parameter. Hence, this technique can be used for high sensitive characterization of defects such as vacancies or dislocations. MBE study showed good promise in identifying the non-magnetic austenite phase compared to the intermetallic precipitation and defect structure. EC technique had shown good promise in characterizing the austenitic reversion ahead of ultrasonic and almost on par with MBE. As this technique is more amenable to shop floor, it can be used for quick and reliable determination of volume % of austenite on shop floor as well as on components. The bright field TEM image showing

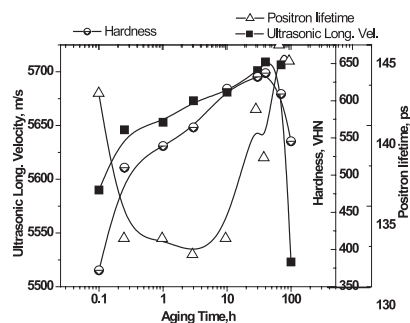


Fig.1 Variation in hardness, ultrasonic wave velocity, and positron annihilation life time parameter with aging at 755 K.

impedance magnitude, positron life-time and X-ray diffraction based austenite volume fraction have been employed to develop a comprehensive NDE

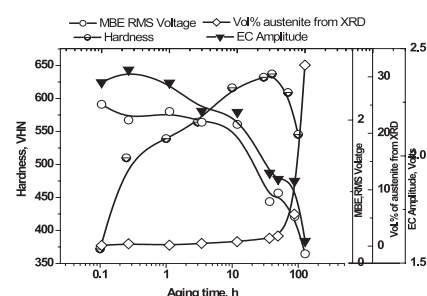


Fig.1 Variation in hardness, MBE rms voltage, EC amplitude and volume % of austenite determined by XRD with aging at 755 K.

austenite and the intermetallics could be observed in Fig.4. XRD technique was found to be good in quantifying austenite

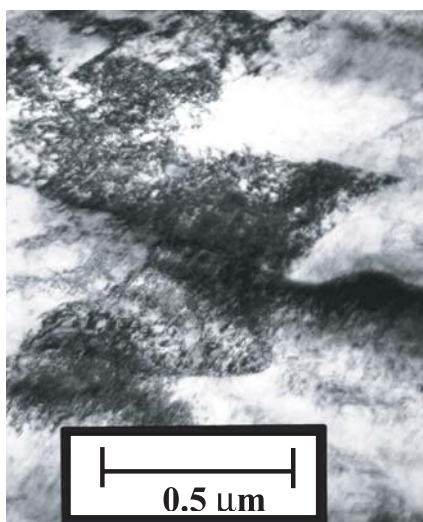


Fig.3 Bright field image (showing high dislocation density) specimen solution annealed at 1093 K for 1 h followed by air cooling.

but was unable to determine the austenitic initiation early due to low sensitiveness of the technique for austenite volume

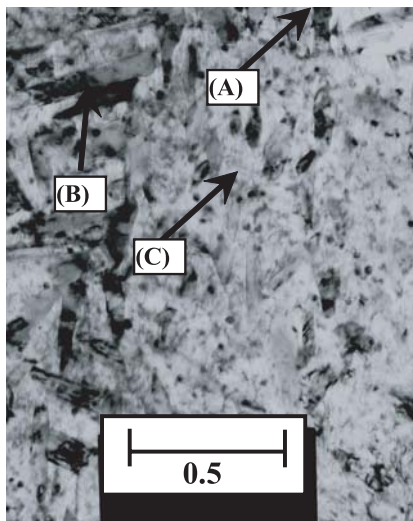


Fig.4 Bright field image of the specimen thermally aged at 755 K for 100 h followed by water quenching, showing long and patchy austenite (marked as A), patchy $\text{Ni}_3(\text{Ti, Mo})$ (marked as B) and globular Fe_2Mo (marked as C)

fraction (less than 2 %). However, XRD techniques has been used as a benchmark for quantitative estimation of volume fraction of reverted austenite using MBE and EC techniques. Table 1 brings out at a glance the relative capabilities of various NDE parameters employed for characterization of various microstructural features in M250 grade maraging steel. Thus, by adopting multi-NDE approach, it is possible to get a comprehensive picture of interaction of interrogating media with microstructural features towards developing a robust methodology for characterization of microstructures.

V.A.4. A Novel Methodology based on Ultrasonic Attenuation to Characterize the Dynamically Recrystallized Microstructure in Alloy D9

A new methodology based on ultrasonic C-scan presentation has been identified to image the microstructural evolution during dynamic recrystallization (DRX) of alloy D9. Hydraulic press forging operations were carried out on 30 mm height and 20 mm diameter compression specimens at a mean strain rate of 0.22 s^{-1} using a 250-ton triple-action hydraulic press. Four specimens

were forged at 1273 K for different strains in the range of 0.1 - 0.5. The in-house

developed ultrasonic C-scan imaging system 'ULTIMA 200' and a 6 MHz point focused

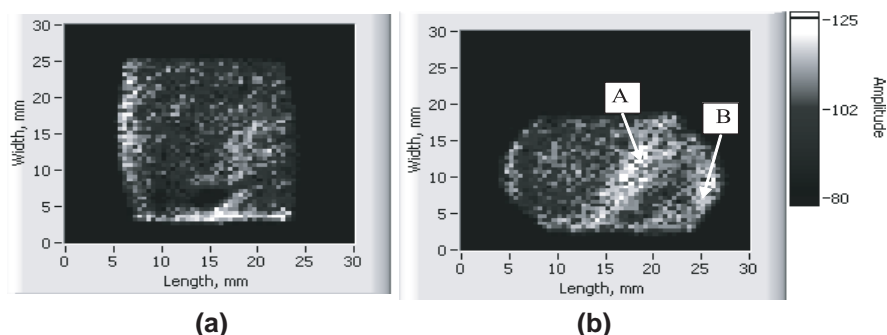


Fig. 1 C-scan image of the specimens forged at 1273 K to a strain of (a) 0.2 and (b) 0.5

immersion transducer were used to acquire the data and obtain the C-scan images. The first backwall echoes obtained were gated to obtain the C-scan image corresponding to their amplitude. Electron back scattered diffraction (EBSD)

data were collected using a TSL-OIM (orientation imaging microscopy) system on FEI Quanta 200 SEM operating at 20 kV.

From the ultrasonic study, it has been observed that the

specimens with true strains of 0.2 (Fig.1a) or lower did not show any variation in the amplitude of the ultrasonic first backwall echo. The specimen with 0.3 strain, on the other hand, showed visible variation in the C-scan image. However, this variation was not systematic. The specimen forged to 0.5 strain could clearly bring out systematic variations in the amplitude of the first backwall echo. It exhibited higher amplitude of the first backwall echoes along one of the diagonals and one of the curved sides (marked as 'A' and 'B' respectively in Fig. 1b).

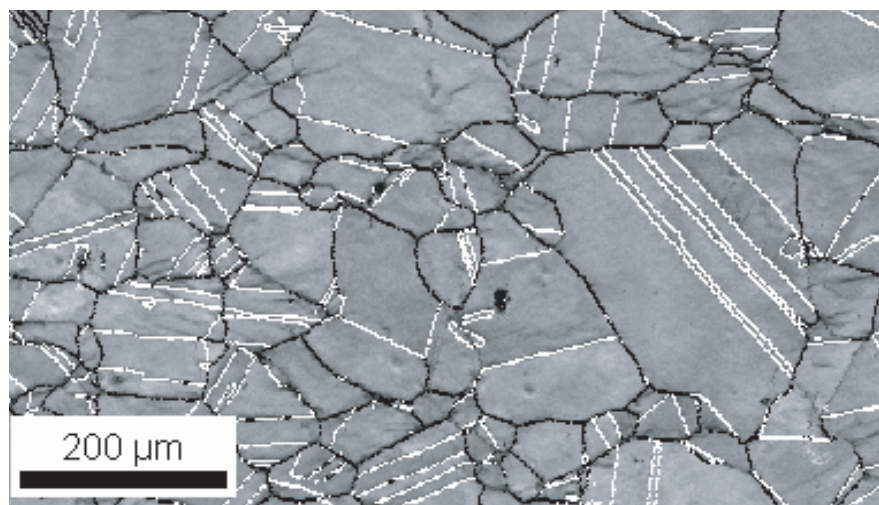


Fig.2 Image quality (IQ) maps of hot deformed specimens at 0.2 strain. Boundaries with more than 5° misorientation and the twin boundaries are respectively marked as dark and white lines

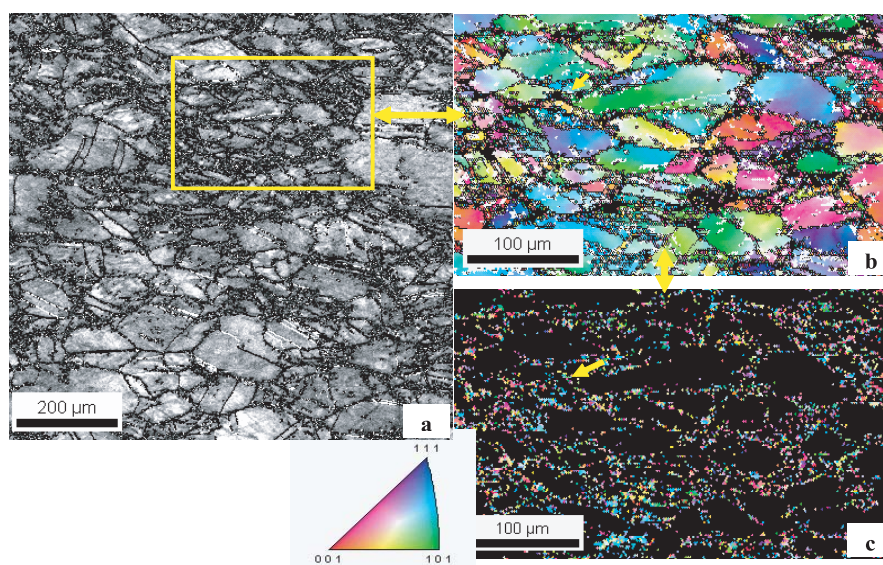


Fig.3 (a) Image quality (IQ) map of specimen forged to 0.5 strain. Graphics conventions are same as in figure 2. (b) Enclosed section of (a) is brought out (at a higher magnification) as IPF (inverse pole figure) map, with more than 5° boundaries marked as dark lines. (c) The 'necklace' grains (fine equiaxed grains around the grain boundaries) were partitioned from (b). Grains with less than 5 m size were considered as 'necklace' grains

It has been observed in our recent study that attenuation of ultrasonic waves of a particular frequency in alloy D9 is mainly governed by grain size. The specimen with larger grain size has been found to scatter more as compared to the finer one. Accordingly, larger grain size regions lead to lower amplitude of the first backwall echoes and vice versa. This observation could be employed to analyze the findings of C-scan images. Since specimen with 0.2 strain did not show any perceptible variation in the amplitude of the first backwall echo, it is likely that this specimen contains almost uniform grain size distribution. This could be

corroborated from the Image Quality (IQ) map (as obtained from EBSD imaging) of this specimen (Fig. 2). The higher amplitudes of the first backwall echoes along one of the diagonals and one of the curved sides at 0.5, on the other hand, indicate presence of finer grains. Such grains, on the other hand, can be related to deformation and/or dynamic recrystallization. It needs to be noted that intense shear zone formation is expected from strain heterogeneities along the diagonal. The formation of

intense shear zone along only one of the diagonals is attributed to the presence of a little skew in the deformation. To corroborate this, EBSD scans were performed on this deformed sample. The presence of necklace DRX grains could clearly be observed from the EBSD map (Fig. 3). The EBSD studies, thereby, substantiate that the ultrasonic C-scan system can be used for imaging the variations in microstructure, in particular grain size, in the specimens.

Imaging of microstructural features through ultrasonic measurements is advantageous as the average of the microstructural features in the thickness direction is revealed by ultrasonic measurements as compared to only surface information through metallographic techniques. Further, the C-scan image can also be converted to the image of average grain size, if a proper correlation between amplitude of the first backwall echo and grain size is established a priori for any material of investigation.

V.B. Sensors

V.B.1. Performance Evaluation of a Semiconducting Oxide Based Sensor for Measuring Trace Levels of Hydrogen in Argon Cover Gas of SOWART Facility

For continuous monitoring the hydrogen levels in the argon cover gas over liquid sodium of Sodium Water Reaction Test Facility (SOWART), a hydrogen monitoring system using a thermal conductivity detector (TCD) has been installed and is in service. A thin film based palladium doped SnO_2 semiconductor oxide sensor, shown in Fig.1 has also been installed in tandem with this TCD based system for its performance evaluation. It

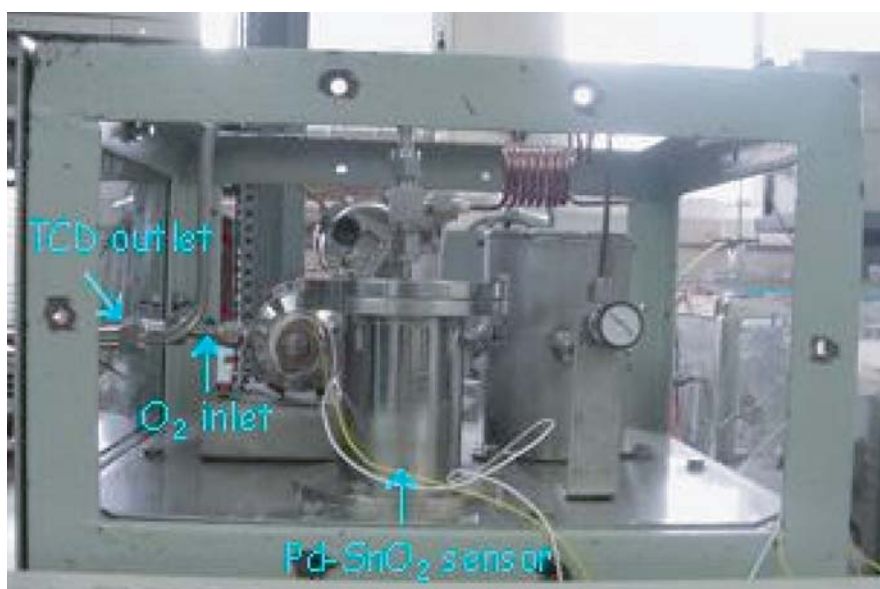


Fig.1 Photograph of SnO_2 sensor installed in SOWART

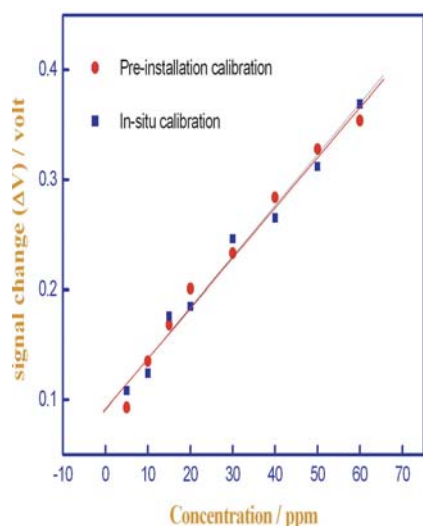


Fig.2 SnO_2 sensor output for different concentrations of hydrogen in argon

analyses hydrogen concentration of the argon carrier gas that exits from the nickel coil continuously. This sensor is operated at 623 K with a control cum signal processing unit designed and developed in-house by CIFD, CG. The output of the sensor varies linearly with hydrogen concentration in the range from 5 to 70 ppm for H_2 , as shown by the calibration plot given in Fig. 2. The performance of the sensor has been under study for nearly seven months, during which sodium in the loop had been refilled twice and dumped once. The background stability of the sensor during this seven months is ± 1 ppm.

After introducing the sensor in the loop, liquid sodium was filled in SOWART (after a shutdown duration of 46 days). The temperature of sodium was

isothermally maintained at 573 K for 70 h and was subsequently increased to 723 K. The sensor output increased from a background value of 0.03 V to 0.15 V, which, corresponds to about 14 ppm of H_2 as inferred from the calibration plot [Fig. 2]. During the next sodium dumping, the sensor output increased to 0.18 V which corresponded to about 20 ppm of H_2 . During the second filling of sodium into the loop (after a shutdown duration of 20 days), 0.5 V increase in the signal output was observed and this corresponded to > 70 ppm of H_2 . All these three observed transients are shown in Fig. 3.

The sensor was calibrated on-site after these excursions and calibration trace obtained matched with the pre-installation calibration shown in Fig. 2. This indicates that the calibration of the sensor towards different concentrations of hydrogen is stable over the duration.

When the sodium in the loop is in dumped state, the nickel diffuser coil of the TCD based hydrogen sensing system is maintained at 423K. After the sodium filling of the loop, the temperature of the nickel coil is raised gradually to 773 K within about 2 h. The heat-up

duration is ca. 2 h. Theoretical calculations showed that the equilibrium hydrogen concentration in the argon carrier gas inside the nickel coil would be at least 50% or above when its temperature increases above 573 K. When the coil temperature reaches 773 K, the argon carrier gas that exits from the nickel diffuser coil is in complete equilibrium with hydrogen in argon cover gas. Based on these considerations, the following inferences can be drawn : a) there is an increase in hydrogen concentration in the cover gas of the sodium system during sodium filling process and the increase is found to be at least in the range of 5 to > 70 ppm and b) the changes in H_2 concentration at these low levels are reliably detected by the semiconducting oxide based sensor.

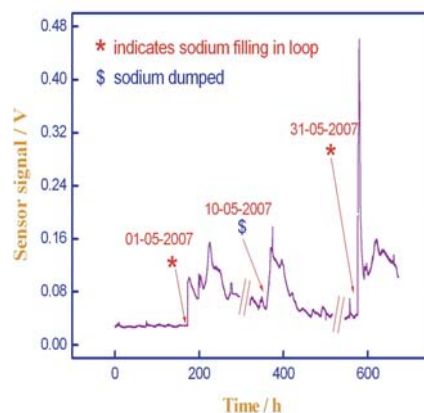


Fig.3 Response transients of SnO_2 sensor during sodium filling campaigns

V.B.2. Development of PEM Based Three Electrode Amperometric Hydrogen Sensor with Control and Measurement Electronics

Hydrogen sensors find application in many areas of fast reactor technology. Hydrogen is required to be monitored in the argon cover gas of fast reactors and also in the inert medium during sodium cleaning and sodium disposal operations. A fuel cell based amperometric hydrogen sensor in three electrode configuration has been developed and tested in chronoamperometric mode for hydrogen monitoring during the above processes. Three electrode amperometric sensors are expected to have better selectivity, stability and response behavior compared to two electrode sensors. A compact, portable, potentiostatic control and measurement electronics has



Fig.1b Experimental set-up

been developed for the three electrode sensor. This compact electronics realises in-situ industrial application of three electrode sensors and replaces the imported potentiostat which is general purpose in nature and is hence bulky and suitable only for laboratory applications. This is also an import substitution step. The circuit fixes the sensing electrode potential with respect to reference electrode. This is achieved using the feed back current between the sensing and reference electrode and by injecting the required current at the counter electrode in an analog loop. The sensor uses Nafion as proton exchange membrane (PEM) and platinum as electrodes. The sensor functions in fuel cell mode, $H_2/Pt//Nafion//Pt/O_2$. The reference electrode is a platinum wire at the counter electrode side. The supply of hydrogen at the sensing electrode is limited by a physical barrier incorporated at

the sensing electrode. The counter electrode is exposed to air and the sensor functions as a 'self breathing' device requiring no air flushing at the counter electrode. Fig. 1 shows the schematic of the sensor and the photograph of the experimental setup. Fig. 2 shows the response curve and calibration plot of the sensor. The above design opens venues to the development of multi potentiostat based electrochemical sensors with multi gas measurement capability.

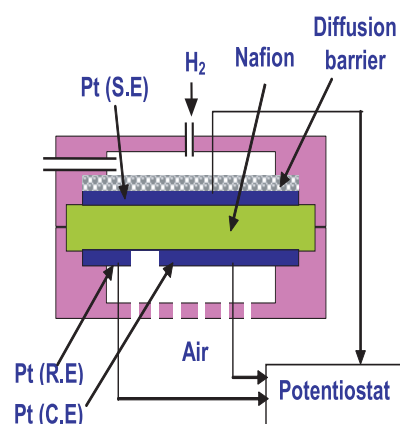


Fig.1a Schematic of the hydrogen sensor

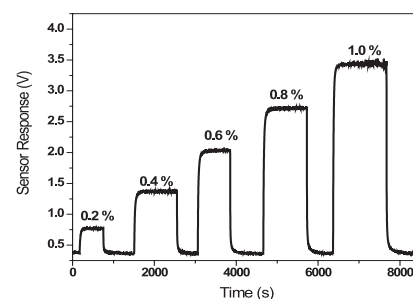


Fig.2a. The response curve of the sensor

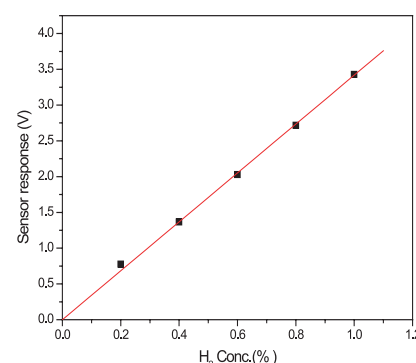


Fig.2b The calibration plot of the sensor

V.C. Electronics and Instrumentation

V.C.1. Optimum Location of Core Monitoring Thermocouples

Thermocouples housed in thermowells are provided in Control Plug (CP) for continuous monitoring of sodium temperature at the exit of all fuel-subassemblies (FSA) and first row of blanket-subassemblies (BSA) in PFBR. These thermowells for the thermocouples are supported by the Core Cover Plate (CCP) and guided by Lattice Plate (LP). Sodium jet issuing out from the core impinges on thermowells, LP and CCP and gets deflected horizontally. This horizontal deflection leads to radial bending / flowering of the streamlines. This effect demands that thermocouples of various SA are required to be lowered sufficiently such that they are submerged in their respective streams. To measure the coolant temperature issuing out from various SAs, the thermocouple tips should be located as close as possible to the SA exit. But to aid under-sodium viewing before fuel handling, the thermocouple tips are located at an axial distance of 100 mm from SA top (at operating temperature). It is very important to determine the temperature attenuation of the

coolant streams at the thermocouple tips through experiments.

An experiment has been carried out in SAMRAT model to determine the optimum location of core temperature monitoring thermocouples above core top so that the SA exit temperature can be monitored accurately. SAMRAT is a 1/4 scale model of PFBR primary circuit. De-mineralized water is used as simulant fluid in this model.

Though the hydraulic properties of water are identical to that of sodium, the thermal properties are far from similar.

It has been established that water can be used as analogous fluid to simulate the mixing phenomena of non-isothermal sodium jets if Reynolds (Re) number and Peclet (Pe) number are sufficiently large ($Re > 20,000$ and $Pe > 600$) both in prototype and model. The experiments have been carried out in model satisfying the above similarity criteria.

There is a provision to send water separately in few subassemblies at the last row of the fuel zone. The last row of fuel zone was selected for this experiment because maximum attenuation of temperature is

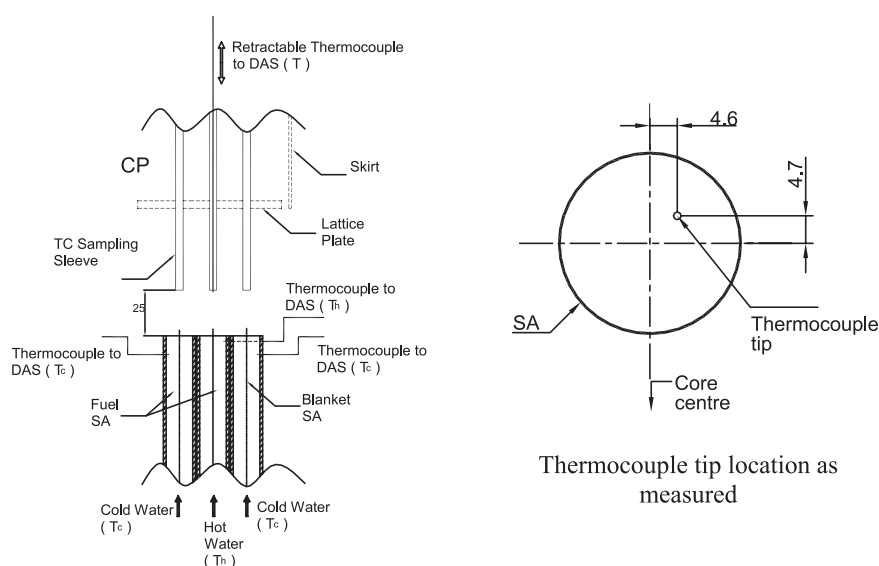


Fig.1 Schematic showing retractable thermocouple location

expected in this row. Hence the optimum position of the thermocouple tip determined for this location will be conservative for the other inner rows. Hot water (≈ 338 K) was sent through one SA, whereas in the rest of the core, cold water was circulated. The attenuation of temperature at this thermocouple tip location by the neighbouring SAs was studied. A retractable thermocouple was inserted in this location from the CP top as shown in Fig.1. The height of the thermocouple tip above core top can be varied by traversing the thermocouple from CP top. From the statistical analysis of data the mean temperature as seen by each thermocouple was estimated. These temperature data are presented in a normalized form to transpose

the result into reactor case by substituting the prototype parameters. The normalization is done in the following manner.

$$T_{mean}^* = \left(\frac{T - T_c}{T_h - T_c} \right)$$

where,

T = Mean temperature of the fluid as measured by the thermocouple mounted in CP

T_h = Mean temperature of the hot inlet fluid (Thermocouple mounted at the SA exit)

T_c = Mean temperature of the cold inlet fluid (Thermocouple mounted at the SA exit)

The normalized mean temperature (T_{mean}^*) is plotted against the elevation of the thermocouple tip above core top for various

experimental conditions. The result is presented Fig. 2. It can be seen from the above figure that normalized mean temperature is close to unity (which means the fluid temperature as measured by the thermocouple is almost equal to the SA exit temperature) at the core temperature monitoring point upto the height of 34 mm above core top in model and then it decreases gradually along the jet axis due to the increased mixing of the liquid streams. The corresponding height of the thermocouple tip in reactor is 136 mm (because the geometric scale of the model is 1:4). The normalized mean temperature is also independent of Re upto this tip elevation above core top.

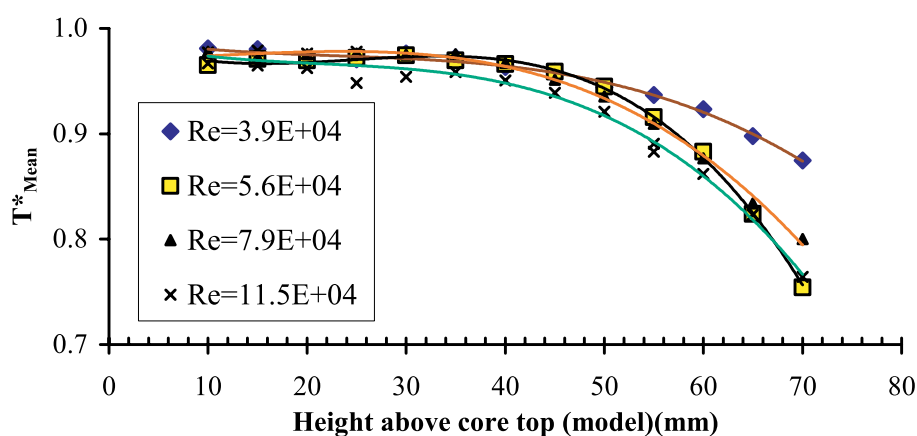


Fig.2 Variation in mean temperature along the jet axis (in model)

V.C.2. Development of Pulse Coded Safety Logic System for PFBR

Reactor safety logic is designed to initiate safety action against Design Basis Events. The reactor is shutdown by de-energizing electromagnets and dropping the absorber rods under gravity. In PFBR, shutdown is effected by two independent shutdown systems, viz., Control and Safety Rod Drive Mechanism (CSRDM) and Diverse Safety Rod Drive Mechanism (DSRDM). Two separate safety logics are developed for CSRDM and DSRDM, i.e., Safety Logic with Fine Impulse Test (SLFIT) for CSRDM, and Pulse Coded Safety Logic (PCSL) for DSRDM. The PCSL primarily utilizes the fact that the vast majority of faults in the logic circuitry result in static conditions at the output. It is arranged such that the presence of a dynamic logic signal is required to hold the shutdown actuators and any DC logic state will release them. It is a dynamic, self-testing logic and fail safe design.

PCSL system will be introduced for the first time in Indian reactor. Being a safety critical system, PCSL system was developed in three phases. To demonstrate the principle of

PCSL, a lab prototype PCSL system with 3 parameters was developed and tested successfully with actual EM coil.

After completion of lab prototype, functional prototype PCSL System having all 14 parameters required for PFBR was developed. It is implemented using hardware, not calling for software verification and validation. State-of-art technology has been used for PCSL system. To avoid clock failure, redundant clock oscillator has been used. The digital logic has been implemented in Complex Programmable Logic Devices (CPLD), achieving high reliability due to high level of integration, less number of interconnection and low power consumption. To improve further reliability, back plane arrangement was done to avoid loose interconnection. All the 10 number of Printed Circuit Boards (PCB) are accommodated in a 19" sub rack. To drive the EM coil current, Power MOSFETs are used. To vary the current through EM coils, rheostats have been used. For current indication, Indication Alarm Meter (IAM) has been used

which also processes the alarm to control room at low current. To improve reliability of the system, both the safety logic systems were linked optically. Being a digital logic, stuck at '1' and stuck at '0' fault may occur. Pulse pattern fault, latch test fault, power gate fault, trip parameter status annunciation and cross link between two safety logic faults are analyzed. To diagnoses all these types of faults, a diagnostic logic was designed and implemented. Diagnostic logic annunciates alarm locally through LEDs, to Control Room (CR) and Backup Control Room (BCR) through relays and to Distributed Digital Control System (DDCS) through opto-isolation. At the design stage, diversity between two safety logic systems is maintained using different design methodology, different components having different technology. The whole system was assembled in a 19" rack. To test the functionality of the system manual simulators were designed. The signal simulator simulates the trip signals from the reactor, control room simulator designed for displaying CR related outputs and backup control room simulator designed for



Fig.1 Industrial version of PCSL system

displaying BCR related outputs. The functional test was completed successfully.

The PCSL system is to be used in PFBR. It will be under industrial environment. Before putting the system under industrial environment, the entire qualification test has to be done. Finally an industrial version PCSL system was designed. Here all the aspects of industrial environment have been taken care from EMI/EMC to environmental qualification. In the design stage we have implemented all the required

features. For EMI/EMC qualification of sub rack, all the PCBs have qualified for signal integrity, cross talk and EMI using Hyperlinx software and for thermal qualification; thermal analysis was done using Beta-soft software. The 19" Sub rack which houses all the PCBs is also designed to qualify the above. Industrial version PCSL system (Fig.1) was implemented in a 19" rack of 48U height. General arrangement of the system has been made to qualify the whole system for EMI/EMC and environmental qualification.

V.C.3. Reliability Analysis of Safety Critical I & C Systems of PFBR

PFBR contains many Safety Critical Systems like, Safety Logic Systems (Safety Logic with Fine Impulse Test for Shutdown system 1, Pulse Coded Safety Logic System for Shutdown system 2), Core Temperature Monitoring System, etc. Atomic Energy Regulatory Board specifies target for the Safety Critical System. The probability of failure on demand of the system should be less than the target. During the design of a safety critical system, reliability target of the system will be considered among other requirements.

The Instrumentations & Control systems important for safety can be broadly classified into two categories, viz. i) Safety-Critical systems and ii) Safety-Related systems. The Safety Critical systems form the second layer of defense and are provided to assure safe shutdown of the reactor, removal of heat from the reactor core during any deviation from normal operation and containment of radioactivity during accident conditions. The Safety Critical systems, for example, Core Temperature Monitoring

system, require a very high reliability.

Various reliability analysis techniques like Failure Modes and Effects Analysis (FMEA), Fault Tree analysis (FTA), Event Tree Analysis are performed as a part of Probabilistic Risk Assessment. Relex Software, shown in Fig.1, is popularly used to perform these analyses. FMEA is a bottom up approach where the failures of each component of the system are identified along with their modes of failures. Effects of those failure modes on the

system are analyzed. Fault Tree Analysis, shown in Fig.2, is a Top down approach, where the failure of system in a particular mode is taken as top event and the causes of that failure along with the interrelation between the causes are analyzed until we reach the basic causes. Apart from these qualitative methods there are many quantitative reliability analysis methods used to compare different topologies, and evaluate the probability of failure on demand.

Calculation of Failure rate forms the basis for Quantitative reliability analysis. For electronic components, US MIL 217-F Notice-2 standard provides empirical formulae to find out the failure rate.

Reliability prediction of electronic components is done by Parts Stress Method or Parts Count Method. In case, for any component, if the failure rate is not available, failure rate data given by the manufacturer is used in the calculations. While arriving at the failure rate, the derating of the component, quality level, temperature and intended environment are taken into consideration.

IEC 61508 provides guidelines for the determination of probability of unsafe state of the system. Using these guidelines, the probability of unsafe state can be calculated at different conditions. Verification and Validation of the Software and Hardware should be done to verify

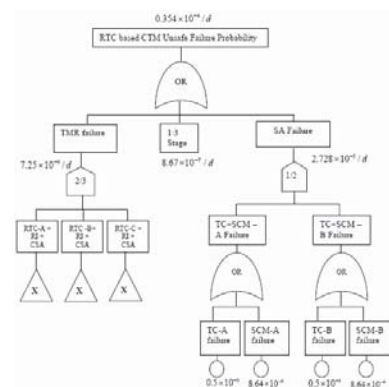


Fig.1 Example Fault Tree model

whether the system is matching the requirements or not.

The reliability analysis of Safety Logic Systems and Core Temperature Monitoring system proved the safety of the system theoretically. The results are used as inputs in the Level 1 Probabilistic Safety Assessment of PFBR.

V.C.4. Safety Logic with Fine Impulse Test System for PFBR

PFBR is provided with two independent, fast acting and diverse shutdown systems namely SDS-1 & SDS-2 to detect any abnormalities in reactor core and to initiate safety action. Each system consists of sensors, signal-processing systems, logic systems, drive mechanisms and absorber rods. The absorber rods of the first system are

Control and Safety Rods (CSR) and that of the second are called as Diverse Safety Rods (DSR). There are nine CSR and three DSR. While CSR are used for startup, control of reactor power, controlled shutdown and SCRAM, the DSR are used only for SCRAM. The respective drive mechanisms are called as CSRDM & DSRDM. For SDS-1, Safety

Logic with Fine Impulse Test (SLFIT) System is provided whereas for SDS-2, Pulse Coded Safety Logic (PCSL) System is provided.

SLFIT system receives trip parameters from neutron flux monitoring, failed fuel detection, sodium flow monitoring, reactor inlet temperature monitoring systems

and performs logical operations to drive Electro-Magnet (EM) coils of Control & Safety Rods (CSRs). SLFIT system de-energizes the EM-Coils whenever a trip parameter crosses its threshold limits or there is a demand for reactor shut down. The trip parameters are triplicated in nature i.e. Triple Modular Redundancy (TMR) concept is employed to achieve high reliability and availability. Being a safety critical system, features like Design Diversity, Independence, Isolation, High Reliability and Testability have been incorporated in the design and implementation of SLFIT System [Fig. 1 & 2].

The main building blocks for SLFIT System are Signal Conditioning Circuits, 2/3-Logic Circuits, Grouping Logic Circuits, Timer & Latching Circuit, FIT Logic Circuit, FIT Logic (Diagnostics) Circuit and EM-Coil Drive Circuit.

Due to the tremendous growth in Very Large Scale Integration (VLSI) technology, Integrated Circuits (ICs) have made digital systems more reliable by reducing the number of external interconnections from one device to another. In ICs the connections are internal to the ICs, where they are protected from poor soldering,

breaks or shorts in connecting paths on a circuit board, and other physical problems. ICs have also drastically reduced the amount of electrical power needed to perform a given function.

SLFIT system is built using VLSI technique. The digital logic circuits for the SLFIT System have been implemented using Very High Speed Integrated Circuits (VHSIC) Hardware Description

Language (VHDL) and the designs are fused in to One-Time-Programmable (OTP) Field Programmable Gate Array (FPGA) Devices, which are based on anti-fuse technology. The EM-Coil drive circuit is built using Insulated Gate Bipolar Transistors (IGBTs).

The probable faults in Digital ICs is stuck-at fault, which implies the fault effect to be a line segment stuck at logic 0 or 1 (i.e. stuck-at 0 or stuck-at 1).



Fig.1 Front view of the SLFIT system



Fig.2 Rear view of the SLFIT system

For SLFIT System, stuck-at 1 is an unsafe fault, which needs to be detected on-line in a minimum possible time. To prevent Safety Logic System failing in unsafe mode, an on-line test facility i.e. Fine Impulse Test (FIT) logic is provided. FIT Logic monitors the health of Safety Logic System on-line and detects safe and unsafe failures. FIT logic injects short

duration (1 ms) trip pulses periodically at the input of Safety Logic in required combinations and verifies the propagation of these pulses at the output of Safety Logic System. Each parameter is tested with a periodicity of 3 minutes. Whenever a fault is detected, the information is sent to the Control Room (CR) for further action.

SLFIT system shall remain functional even under stringent environmental conditions. Hence, the system will be subjected to Electro Magnetic Interference (EMI) / Electro Magnetic Compatibility (EMC), Environmental and Seismic qualifications. Industrial Prototype of SLFIT System has been fabricated and testing is under progress.

V.C.5. Development and Commissioning of Pulse Shape Discrimination Electronics for Phoswich Detector System

Phoswich detectors [Thin NaI(Tl) + Thick CsI] are generally used for measuring X-ray or low energy gamma emitting radionuclide contamination in lungs. In phoswich detectors the interference due to high energy (HE) scatter component in low energy (LE) region is reduced using different schemes of pulse

shape discrimination (PSD) electronics. The PSD electronics utilizes the difference in the decay time characteristics of two phosphors to discriminate the interactions of HE and LE photons. Previously a custom built electronics with discrete components was being used, which has suffered frequent failure of components, thereby

resulting in poor performance and timing resolution. The new PSD electronics is configured using readily available nuclear electronic modules, which makes it convenient to replace any of the modules for easy maintenance.

The phoswich is of SCIONIX make having 203 mm dia, 3

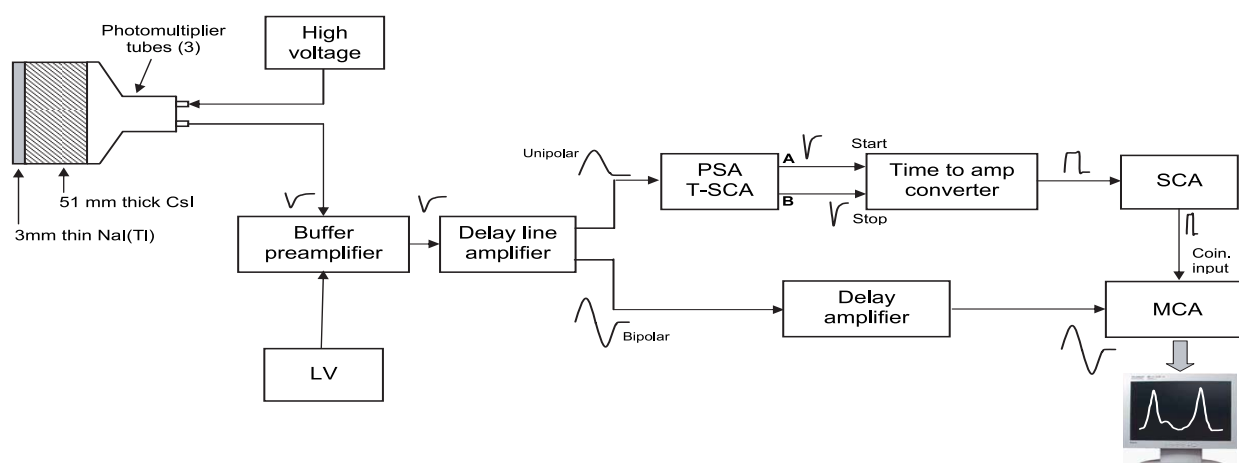


Fig.1 Phoswich system electronics with typical signal details

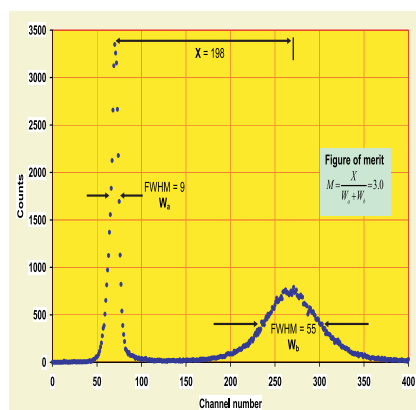


Fig.2 Timing spectrum

mm thick NaI(Tl) crystal coupled with 203 mm, 50 mm CsI(Tl) crystal and optically coupled to three matched 3" dia photomultiplier tubes (ETL 9255). The detector has an ultra low background 0.5 mm thick beryllium entrance window. The new PSD, based on scintillation time comparison, uses the rise time difference in the signals of NaI(Tl) (250 ns) and CsI(Tl) (1100 ns) to produce a gating pulse to selectively choose the pulses due to LE photon interactions in NaI(Tl) alone. The schematic of the PSD electronics with typical signals is shown in Fig.1.

The Pulse Shape Analyser (PSA), analyses the input pulses and generates two negative pulses, one at 90% peak amplitude labeled as "A" and another at selected fraction (B) of the peak amplitude labeled as "B". The outputs "A" and "B" from PSA are fed to the inputs of Time to Amplitude Converter

(TAC) as "Start" and "Stop" pulses, respectively. This results in TAC unit generating a square pulse whose amplitude is proportional to the time difference between A & B. Hence, the LE photon interaction from NaI(Tl) generates pulses with lower amplitudes compared to the pulses from CsI(Tl). Once the amplitude of TAC pulses corresponding to NaI(Tl) or CsI is known, any of them can be selected for gating by using a SCA with properly selected LLD & ULD.

Processing of pulses for risetime analysis results a time delay in generating gate pulse. Typical time delay is observed to be $3.75 \mu\text{s}$ for NaI(Tl) pulses and $5.75 \mu\text{s}$ for CsI pulses. Every bipolar pulse from delay line amplifier is precisely delayed and then presented to MCA for analysis. One of the inputs of MCA coincidence circuit is the delayed pulse from delay amplifier and the other input is the gating pulse from the SCA. The input pulses to the delay amplifier are accepted for spectrum analysis only when the gating pulses occur simultaneously. This results in rejection of most of the unwanted high energy interactions, which will have a time characteristic of CsI(Tl) detector, thereby reducing the

background considerably.

The timing spectrum obtained with ^{137}Cs source, with optimized PSD parameters, is shown in Fig.2. The figure of merit (M) for the obtained timing spectrum is estimated to be 3.0.

Comparison of the peak position and the FWHM values obtained for 17 keV, 60 keV and 122 keV with and without PSD electronics clearly shows that PSD has not affected spectrum parameters. In order to quantitatively estimate the background reduction, spectra were obtained with and without PSD (Figure-3). The inclusion of PSD electronics has reduced the background from 9.5 cps to 0.28 cps in 17 keV region and 5.8 cps to 0.3 cps in 60 keV region. This results in an improvement in the MDA values by a factor of 2.

A state of art pulse shape discriminator employing readily available nuclear electronics

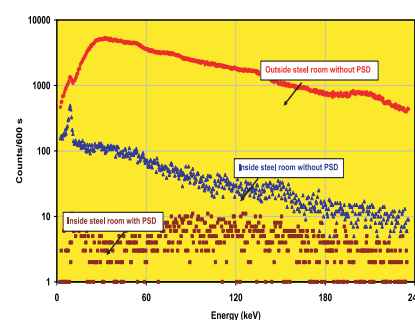


Fig.3 Background reduction with PSD electronics

modules was configured and optimized for using with phoswich based plutonium lung monitor. The PSD electronics has not altered any of the spectrum parameters like shape

of spectrum, peak position and FWHM. The figure of merit obtained for the timing spectrum is 3.0. The background reduction obtained is 97% with PSD and with a

signal loss of only 4%. This effective background reduction improves the MDA values by factor 2.

V.C.6. Digital Design Verification

For safety systems of nuclear reactors, electronic hardware systems are preferred to software systems wherever feasible. This is so because, for software, terms like reliability and quality are difficult to quantify. EID has designed and developed a number of complex digital circuits using Very Large Scale Integration (VLSI) techniques for the Safety Systems of PFBR. These designs have been implemented using Very High Speed Integrated Circuit (VHSIC) Hardware Description Language (VHDL). These circuits have been tested extensively and found to function well. But here, since the hardware design was also done using a HDL, it was thought necessary to perform extensive verification of the HDL code used in the design. Therefore, a collaboration project was undertaken with Indian Institute of Technology, Madras (IIT-M) for the development of generic tools

for the verification of VLSI designs made at centre. As part of the project, six VHDL designs were taken up for verification. The first phase included preparation of detailed design specifications, finalizing the test plans and providing other required inputs to the IIT-M team. For each design, a test plan was first prepared. After a few iterations to ensure that the test plan would really cover all the areas that need to be tested, it was approved by the IGCAR team. Following this was the design verification phase.

The verification of the designs was performed using e verification language in Specman Elite environment. The various components of the environment are shown in Fig.1. The 'e' verification Language can be used to construct components to do the following functions.

Generation: e automates the generation of stimuli based on

the constraints provided.

Driving stimulus: e provides a simulator interface and the necessary mechanism to drive the generated test vectors into the DUT.

Collecting output: After the stimulus is applied to the DUT, output is produced from the DUT. e provides a simulator interface and the necessary mechanism to receive data from the DUT

Data checking: Data value checks compare the output data values against the expected data. Temporal assertions monitor the functional protocol at important interfaces. Temporal checking constructs are used to build protocol monitors.

Coverage: Functional coverage tells the verification engineer if the test plan goals have been met.

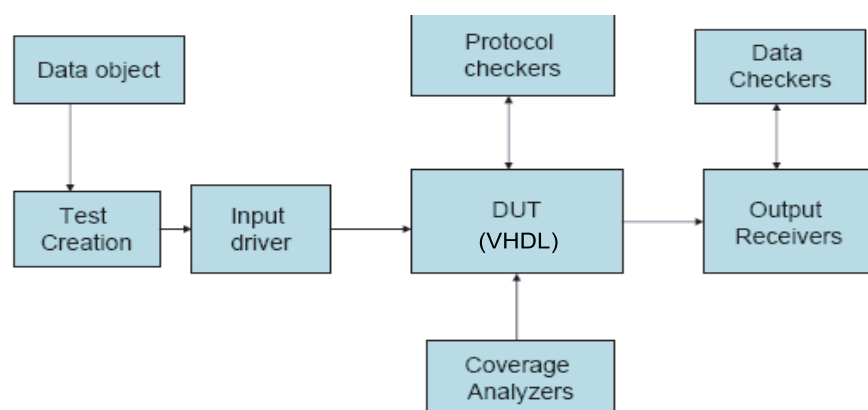


Fig.1 Components of the verification environment

Verification has been completed for all the six designs. The e verification language significantly reduces the time needed to create a verification environment and

test suite, as well as enables the most modern and powerful verification methodologies. Using a high-level verification language that is combined with the built-in engines of a testbench automation tool, a project team can be more productive much sooner in the project schedule, thus reduce the time and resources needed for the verification environment and significantly increase the quality of the final product.

V.C.7. Distributed Operator Information System for Augmented Boron Enrichment Plant

Fast Reactors require enriched 10B for control and shutdown rods and also for detectors. Hence an ABEP has been designed and commissioned at IGCAR. The enrichment is based on Ion Exchange Chromatography Technique which requires accurate monitoring of process parameters such as pH, conductivity, level, flow etc. A computer based Operator Information System (OIS) with analysis package has been implemented by EID and the salient features of the system are described here.

monitor all the plant parameters, track the progress of the process and store data for further analysis of the process.

Features of OIS

OIS scans 180 digital and 50

analog signals at the interval of 1Sec and 10 Sec respectively. Different forms of displays are provided as mimic, bar chart, trend chart, alarm overview panel, Tabular, digital and summary of all signals. These displays are regrouped

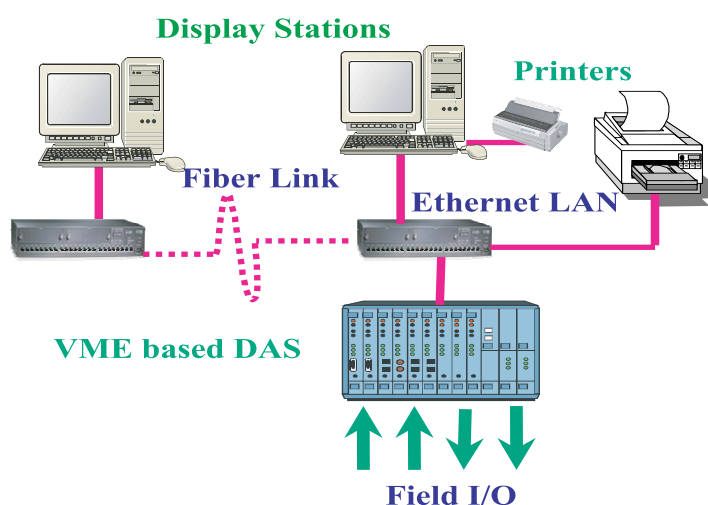


Fig.1 Architecture diagram of OIS

Operator information system (OIS)

The purpose of the OIS is to



Fig.2 Photograph of the DAS

dynamically as per the user needs. All the Input /Output cards and network are configurable. One year data and events are stored with mirroring for archival and retrieval. Hard copy of current alarm signals, events and all displays are provided. On line help is available for overall guidance.

Architecture of OIS

The architecture of the OIS is shown in Fig 1. It is a physically and logically distributed system with real time computer, based on VME bus for data acquisition and PC based systems called as Process Display Stations (PDS) for display as well as storage. Data Acquisition System (DAS) is located in local control room whereas PDS are located in the main control room and all the systems are interconnected by

fiber optic Ethernet Local Area Network (LAN) with TCP. Network printer is used for printing the alarm signals, events and displays. A dedicated printer is also provided for printing the events as and when they occur.

DAS consists of in-house designed and developed 68020 based CPU card, analog & digital input cards as in Fig. 2.

Software

The complete software of the OIS consists of four modules as follows.

- ◆ Embedded Software
- ◆ Communication Software
- ◆ Data management with storage and retrieval
- ◆ Data Presentation with

Human Machine Interface (HMI)

Embedded software which is running in DAS is written as per MISRA C guidelines and fused in EPROM. The main functions of DAS are scanning the input signals at regular intervals, packet formation, sending the packets to all PDS connected in the LAN and configuring the I.O and network cards.

Communication software provides communication between DAS and PDS by TCP.

Data management module receives and validates the data and then processes the data to engineering unit. One-year data and events are stored with mirroring for fault tolerance which is used for analysis.

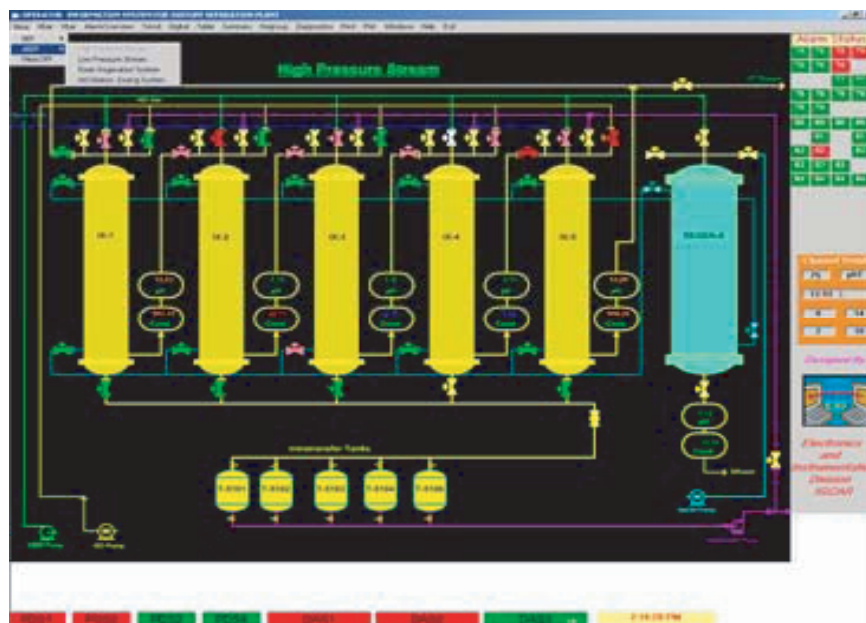


Fig.3 Mimic diagram

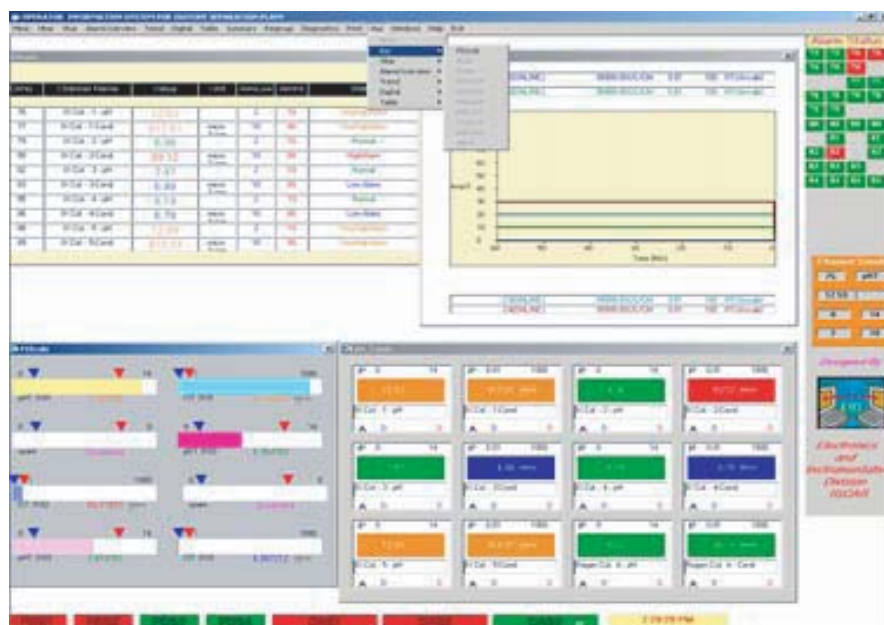


Fig.4 Different forms of displays

Data presentation module provides HMI which has the following functions

- ◆ Display data in different formats as shown in Fig. 3 and Fig. 4
- ◆ Dynamic Regrouping
- ◆ Diagnostics
- ◆ Hard copy on demand

◆ On-line Help

Fig. 3 shows the typical mimic diagram for high pressure stream. pH and Conductivity values are displayed as text for each ion exchange columns. Text color indicates the status of the signal.

Security of OIS

Only OIS application software will be running in PDS and all other applications are blocked. Password is provided for configuration, regrouping and to exit the application.

Documentation & User Training

A one day training programme on the I&C system was conducted for the benefit of the concern staff. Hardcopy and softcopy of all the documents and source code were handed over. Hands on training was given to all the users about the system in interactive manner. Hardware & software of the system were explained in detail. OIS for ABEP has been installed, commissioned, & found to be working satisfactorily.

V.C.8. An Intelligent Titrator for Quick Chemical Assay of Process Solutions

Any service or quality control laboratory attached to a chemical plant or a dedicated facility, conventional or radiochemical, has to often carry out analyses of a few chemical species routinely at frequent intervals round-the-clock following the same methodologies. Results provide

information with respect to variations in process parameters. Simplicity, reliability, speed, performance, remote adaptability and operator friendliness are the guiding factors behind choice of appropriate techniques and instruments for analytical work. An inexpensive but high

performing and intelligent titrator from the Innovative Instrumentation Section, the laboratory creation of which based on the in-house developed pulsating type sensing devices, described in this article, can be the kind of instrument of choice for a set of chemical species which are

amenable for assay either by conductometric or potentiometric or by pH titrations. Miniature rapid titration units developed earlier with pulsating sensors were based on discrete addition of titrating solutions either in the form of tiny droplets or through

addition in small volume steps. These are general purpose and are being used extensively for chemical characterisation in solutions through titrations involving acid-base, REDOX, complex forming, precipitation, or exothermic/endothermic reactions for research and

analytical work. The present development is targeted to meet repetitive analytical needs in industrial settings as mentioned above.

The set up is shown schematically in Fig.1. An immiscible hydrocarbon liquid layer of fixed volume floats over an aqueous solution of the desired titrating agent on the right arm of a U-tube. The titrating solution is dispensed continuously under gravity at a flow rate of about 50 micro liters per second into the solution to be titrated through a needle when the normally closed solenoid valve is made to open. A laboratory made pulsating level sensor follows on-line the extent of volume dispensed as a function of time in one channel. The progress of reaction is monitored in another channel by making use of an appropriate pulsating sensor for conductometric or potentiometric or pH titration. The trains of digital pulses from the level and reaction monitoring sensors are fed to a PC via a laboratory made hardware interface for power supply, signal routing and control of the solenoid valves. The in-house developed software performs the following operations: (i) solenoid valve control, (ii) pulse counting for frequency determination with

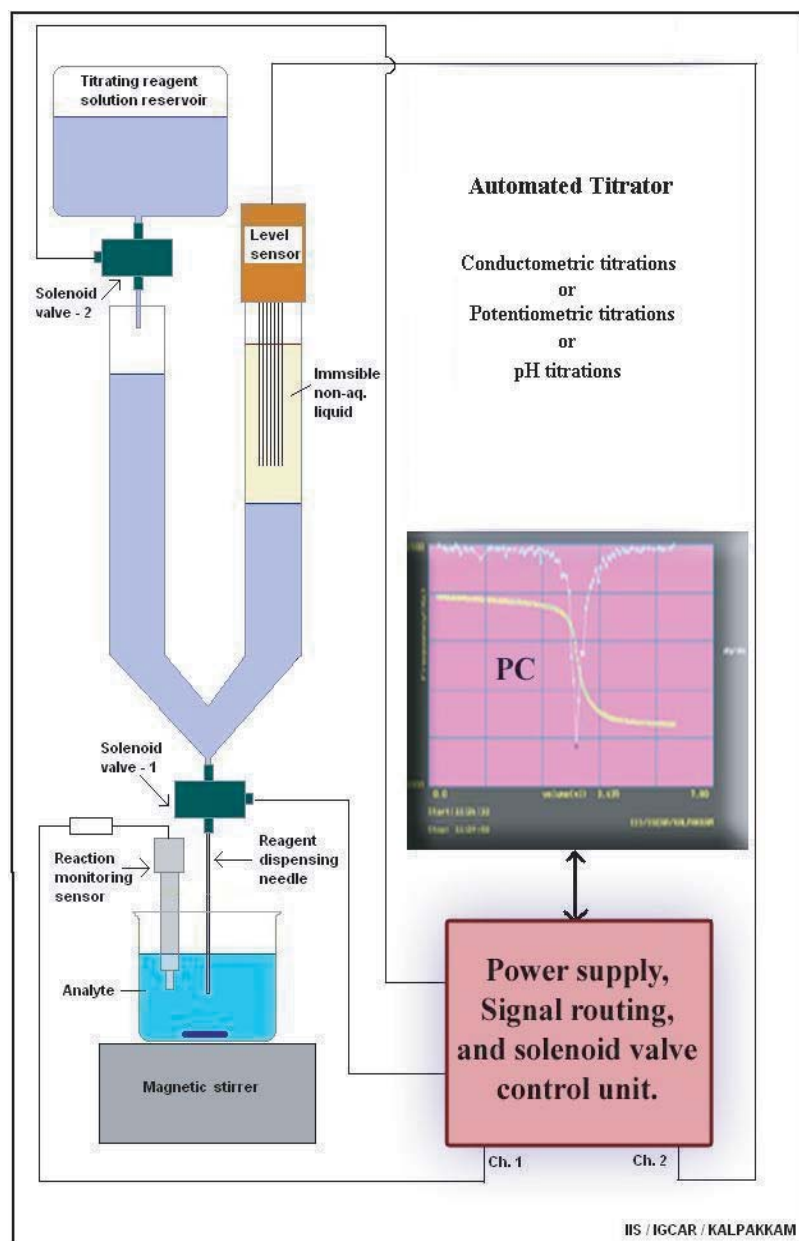


Fig.1 Schematic representation of a laboratory version of an intelligent titrator

derivation of parameter values using the pre-established calibration relationships, (iii) real time graphic display of volume dispensed and progress of reaction in time domain till termination, (iv) unfolding of data in volume domain at the close, and (v) display of the titration plot with numerically fitted regions before and after the end point which is automatically derived from the intersections for conductometric titrations, or display of titration plot with first derivative for locating the end point for potentiometric and pH titrations. A reservoir of titrating solution is placed above with another solenoid valve which automatically opens at the beginning of the next titration to fill the aqueous solution in the left arm up to a preset level before commencement of the fresh titration. The unit has also a built in feature for protection against drainage and overflow of liquid.

Partial screen views of three typical titrations carried out with this laboratory set up are shown together in Fig. 2. The first one is for determination of chloride in service water by conductometric titration following the precipitation reaction with dilute AgNO_3 solution. The second and third

screen captures are the titration plots for a typical REDOX and a pH titration respectively.

Any titration can be completed with generation of reportable data in less than five minutes with this intelligent unit, and it is ready for next titration with the same titrating solution immediately. Thus it makes the job of repetitive analysis easy with minimum strain on the operator. The unit can also be used in batch mode for assay of different chemicals when each batch is specific for

a given chemical species. It takes maximum of about half an hour for setting up the same unit for titrations requiring a different titrating agent for a different batch, permitting multiple chemical species assay with one unit only, if necessary. However, when the need for analysis is too frequent and urgent for a given chemical species, such a unit can be a dedicated one for that particular requirement.

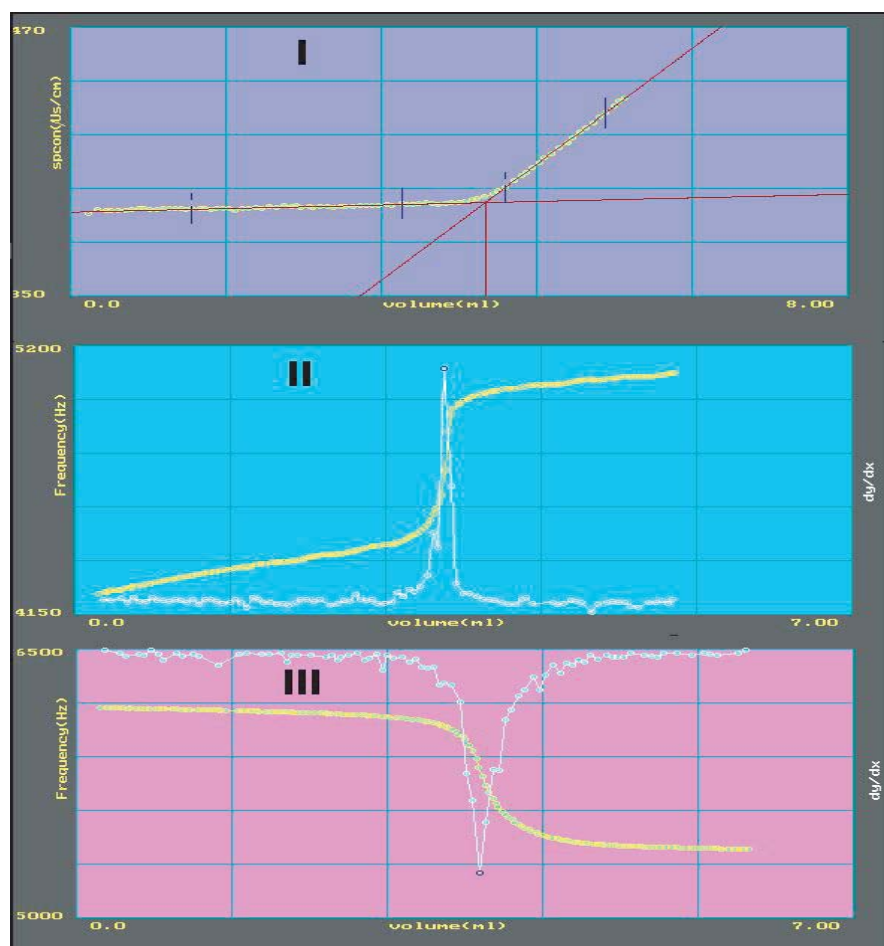


Fig.2 Typical examples of displayed titration plots for different titrations in dilute solutions: I. Cl^- Vs. AgNO_3 by conductometric titration; II. Fe^{2+} vs. Ce^{4+} by potentiometric titration; and III. An acid-base reaction by pH titration.

V.C.9. Wireless Signal Transmission from Pulsating Sensors

The pulsating sensors, have several attractive features for deployment besides their high performance. One such aspect is their adaptability in a simple way for pulse-by-pulse wireless transmission of primary signals in the form of trains of digital pulses from the sensors to data receiving stations located elsewhere in a building or in fields. In-house development of appropriate wireless transmission and reception modules in support of the pulsating sensors is described here.

The transmission and reception modules are designed in such a manner that the pulsed signal output profiles before transmission are practically reproduced during reception as if the signals were received by wired means, thereby making them indistinguishable for the subsequent signal handling and data processing systems which were earlier developed for direct use. Transmission and receiver modules make use of available low power consuming 5 V DC driven modulation and demodulation chips, enabling transmission on a carrier

frequency of about 433 MHz falling under ISM band for use in industrial, scientific and medical applications.

The developments have been made for two types of uses: (i) mains/battery operated transmitter - receiver pair for use with one sensor at a time, usable fully for field applications, and (ii) transmitter - receiver pair for simultaneous use with seven pulsating sensors by time division multiplexing, mainly for use within a building. In the second type, the tasks of pulse counting, data processing and presentation are carried out at a signal receiving location by a PC, feeding output signals from the receiver directly through the parallel port. The block diagram of the transmitter and receiver modules made in the laboratory is given in Fig.1.

Modules were made and tested with highly satisfactory results. Fig.2 shows seven different sensors which sense diverse parameters namely conductivity (in ch-2), chemical *emf* (in ch-3), pH (in ch-4), temperature (in ch-5) levels of a non-aqueous and aqueous

liquids (in ch-6 and ch-7) and differential pressure (in ch-8), are connected to the transmitter module in one room. The transmitted pulsed signals are received in another location a few rooms apart. Signals are being processed and data are displayed in real time as histograms as well as in time dependent plots for all the eight

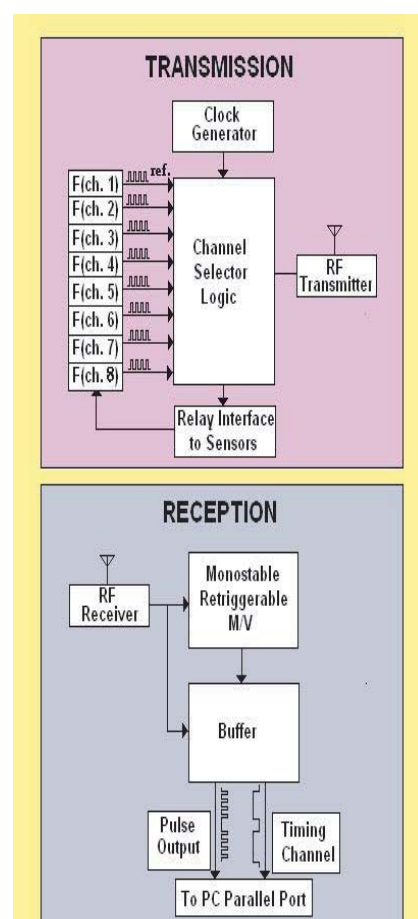


Fig.1 Block diagram of the wireless transmitter and receiver modules for simultaneous use with seven different pulsating sensors.

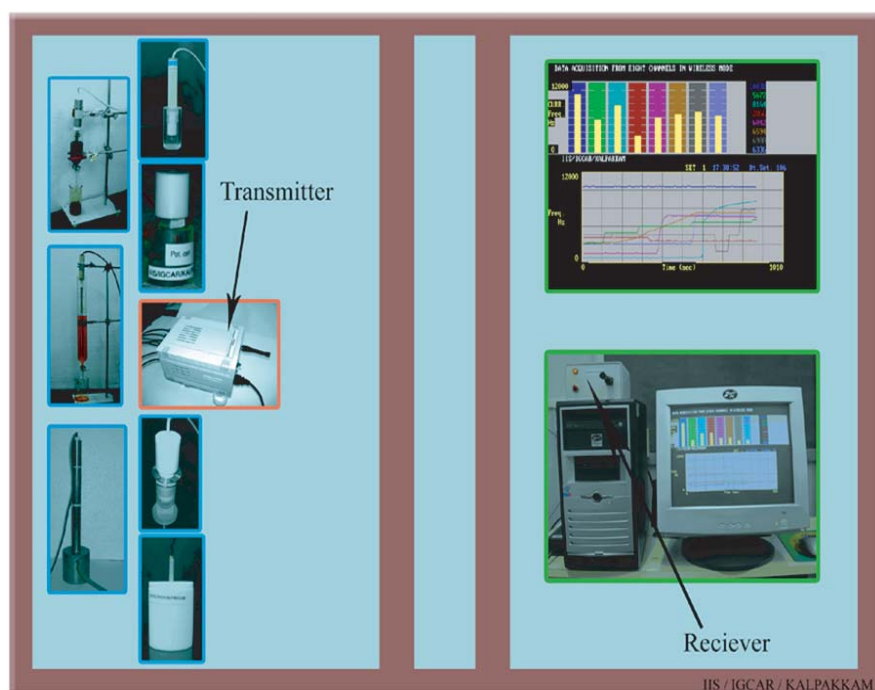


Fig.2 Wireless transmission and reception of digital pulse signals from seven pulsating sensors within a building between two rooms.

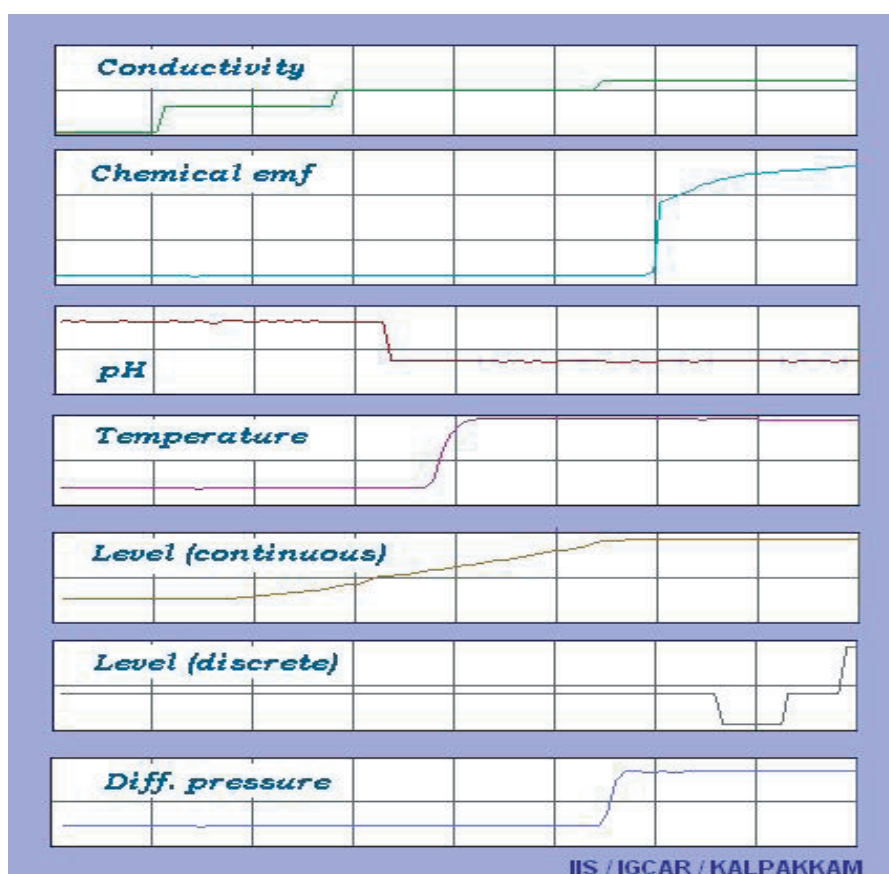


Fig.3 Profiles of different parameters as recorded in another room after wireless reception from seven pulsating sensors which were subjected to changes in respective parameters being sensed at the transmission end.

channels. Reference pulse frequency in ch-1 serves to assess the quality of transmission and also used as the marker for beginning and end of repetitive sequential transmission-reception cycles.

Sensors were subjected to changes in respective parameters being sensed. Data received by wireless transmission (Fig.3) reflected the same profiles as imposed on each sensor at the source.

A methodology for direct wireless transmission of signals from pulsating sensors has thus been demonstrated to work simultaneously with seven sensors using only one unidirectional communication. The low power transmission modules worked very well within a building and outside. The Ethernet enabled stand-alone embedded processors, already developed for the pulsating sensors, permit connectivity for on-line viewing and recording of data anywhere within the IGCAR Intranet. The wireless feature will extend the above feature of wide connectivity for sensing and measurement by pulsating sensors in locations away from LAN access points such as within fume hoods or glove boxes or outside building premises.

V.C.10. Single Chip Embedded Experimental Automation Design

An inexpensive embedded automation design for Raman spectrometer system shown in Fig.1, has built with a single Programmable System On-Chip (PSoC), a Cypress Micro System's mixed array microcontroller.

This automation system allows the on-line acquisition of spectroscopic data and the control of the experimental setup operation, using PC as a window based graphical user interface (GUI). The menu driven user-friendly software in

virtual instrument (VI) control program written in LabVIEW ver.7.1, a graphical language, interacts with the embedded single chip design for the total automation of the experiment. The user friendly menu driven virtual instrument program interacts with the embedded PSoC design through its USB-serial interface.

Fig.2 shows the front panel of the PSoC based menu driven user-friendly virtual instrument program with a acquired

Raman spectrum in zinc cyanide, $\text{Zr}(\text{CN})_2$ acquired in the range of 2200 cm^{-1} to 2240 cm^{-1} for a preset time of 5 seconds in steps of 0.5 cm^{-1} . The menu driven GUI program has the facilities like (i) storing the data in the user specified file path, (ii) loading the previous spectrum form the user file path, (iii) automatically configure the initial, final and step wave number on the graph immediately after the user entry, (iv) print spectrum, (v) clear spectrum and (vi) functioning

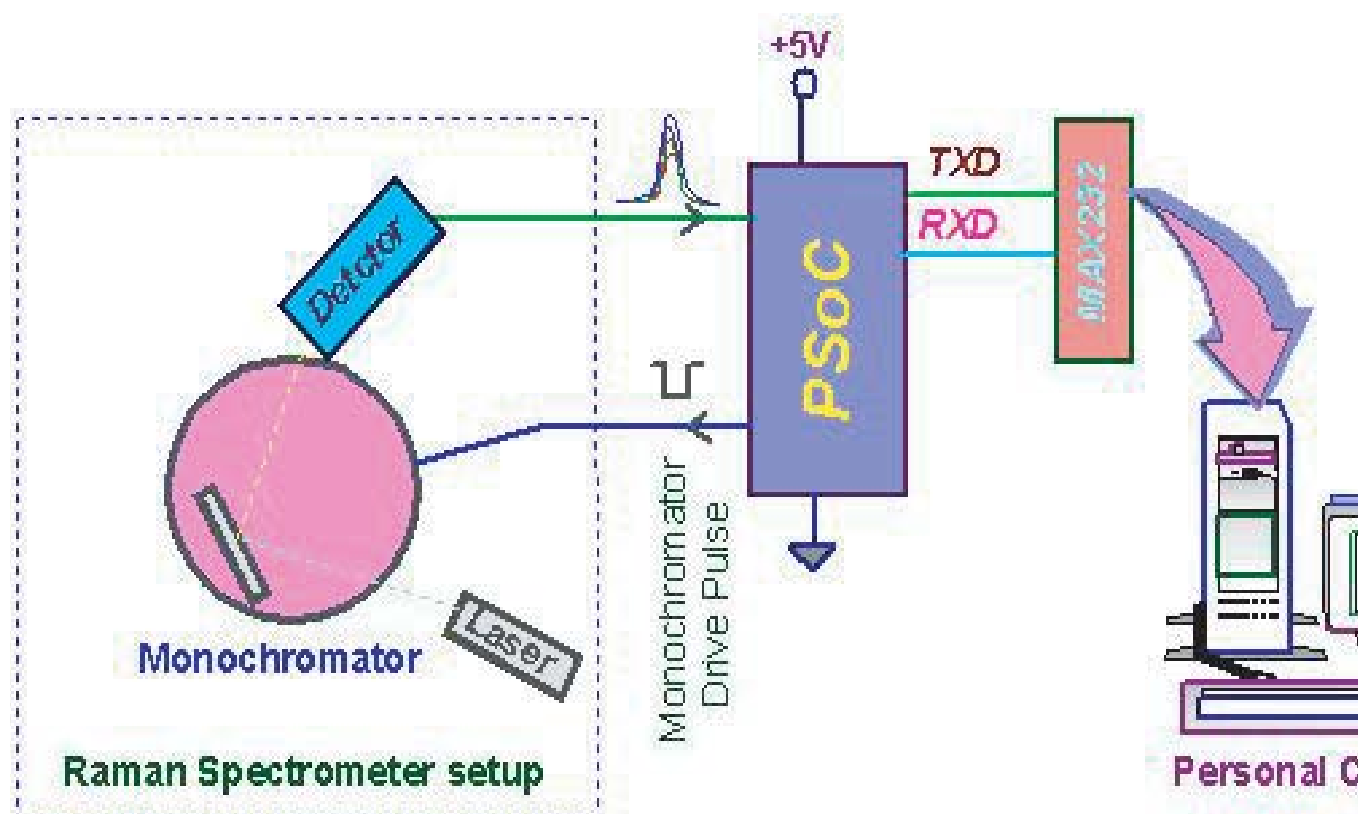


Fig.1 Block diagram of raman spectrometer experimental automation setup.

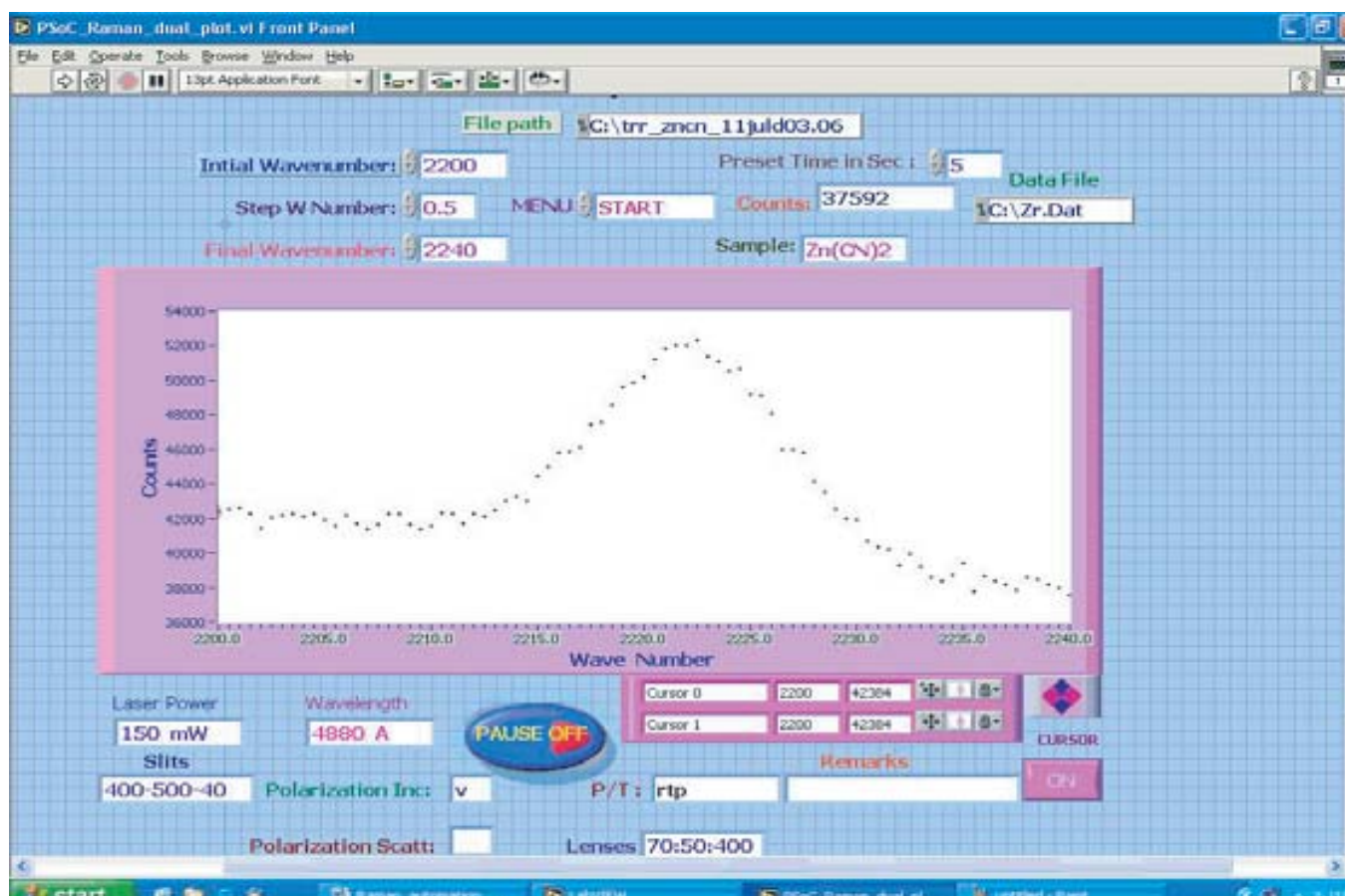


Fig.2 Virtual instrument program panel diagram for PSoC -Raman spectrometer automation design.

as a rate meter for initial setting up of the laser intensity, slit widths, etc, in the spectrometer. The panel diagram includes user variable parameters like sample name, laser power, wave length, slits information as a user file for proper documentation of the experiment.

In PSoC, the main advantage is, one can program the choice of user required function module: Using PSoC designer tool, a blank PSoC chip has been programmed to count the detector pulses for the user preset time and controls the

monochromator motor drive to move to the next user required wave number position. The count pulses have been transferred to PC memory through serial port. A 16 bit counter and a timer has been designed within the PSoC chip for counting the detector pulses from Raman setup for the user defined preset time. Interrupt handler routine in PSoC editor program, enables wider range of counting above 64k and preset time from milli-seconds to several hours, but uses only 16 bit counter/ timer functions, by using interrupts through PSoC editor program written in

'C' compiler.

This simple and cost effective embedded design automation of Raman spectrometer setup using a single Programmable System on Chip (PSoC), interfaced with PC and controlled by the virtual instrument program provides wider range of counting and preset time and works under window environment of PC. This design approach can also be extended to other automation requirements involving event counting applications.

Chapter -6

BASIC RESEARCH

VI.1. Field-Induced Extinction of Light in a Magnetic Nanofluid

A magnetically triggered extinction of light in a disordered magnetic medium, i.e., a colloidal suspension of Fe_3O_4 nanoparticles, has been observed. In this system, the size parameter and the magnetic permeability of the scatterer is tuned by changing the applied magnetic field. Both the forward and backward scattered light intensity as a function of applied magnetic field and the critical magnetic fields where both the forward and backward scattered light intensities drop to zero are measured.

A stable colloidal suspension of magnetite (Fe_3O_4) nanoparticles of average diameter 6.7nm, coated with oleic acid and dispersed in kerosene is used. The organic layer thickness around the particles is about 1.5nm. The experimental setup is shown in Fig.1. The ferrofluid

sample is taken in a quartz cuvette and kept inside a solenoid, where magnetic field is varied by changing the current passing through its coil using a DC power supply. The direction of magnetic field is parallel to the wave propagation. An amplitude and frequency stabilized polarized He-Ne laser (Spectra-physics) of wavelength 632.8 nm with an output power of 1 mW is used as the light source. The light intensity is measured by using a photomultiplier tube (Oriol). The output of the PMT is fed to readout through a current amplifier with variable gain. The analog output from the readout is connected to a 12 bit analog to digital converter (ADC) that is interfaced with a computer. For observation, the light scattered from the sample is projected on a screen and recorded using a CCD camera. The transmitted light intensity through the samples has been acquired as

a function of external magnetic field.

Fig.2 shows the transmitted intensity as a function of external field for different magnetite volume fractions. The intensity plotted was the ratio of the intensity transmitted through the sample with and without magnetic field. Here, at lower concentrations, the transmitted light intensity remains constant upto a critical magnetic field (H_{C1} , shown by the dotted arrow) and above which the intensity starts to decrease drastically. At another critical magnetic field H_{C2} , shown by the solid arrow in Fig. 2, the transmitted light intensity becomes a minimum. Above H_{C2} , the transmitted light intensity increases slowly. The forward scattering patterns from a magnetite suspension of 0.0067 volume fraction of Fe_3O_4 at various magnetic fields are shown in Figure 3. Here, the transmitted light

intensity drops to zero at a magnetic field strength of 115 Gauss, above which the forward scattered light shows a diffused ring like structure i.e. when the applied magnetic field is above H_{C2} . The ring becomes sharper as the magnetic field strength increases further.

It has been found that both H_{C1} and H_{C2} follow a power law decay with volume fraction ($H_C \propto \phi^n$) where the exponents are 0.423 and 0.283 respectively. Also, with increasing concentration, the slope of the transmitted intensity curve (between H_{C1} and H_{C2}) increases. Without any external magnetic field, the magnetic moments of the scatterers are oriented in random direction. With the increase in magnetic field, the moments of the magnetic particles start to align along the direction of the magnetic field. The lengths of the chains

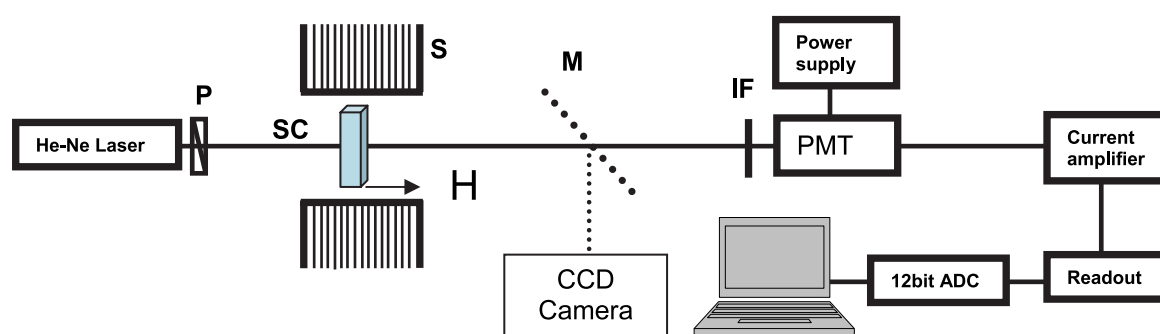


Fig.1 A schematic of the experimental set up. The direction of the applied magnetic field is along the direction of propagation of the beam. P-polarizer, SC-sample cuvette, S-solenoid, M-mirror, PMT-photomultiplier tube and IF-interference filter.

increase with increasing magnetic field till the path length of the sample cell. As the magnetic field is increased, the size of scatterers increases due to the formation of doublets, triplets or very small chains, which changes the scatterers size. At the minimum transmitted intensity, the size distribution is such that the number of scatterers that satisfy the resonance becomes maximum. Such resonances should lead to a build up of standing waves inside the magnetic scatterer and trapping of light.

The formation of the ring clearly establishes the formation of such rod like structures along the direction of propagation of the light wave above H_{C2} . The scattered wave from a long cylinder (length \gg radius) forms conic sections on a screen placed perpendicular to the incident beam. The diffused ring at lower magnetic fields indicates the distorted columns due to weak magnetic dipolar attraction. As the magnetic field increases, both the average chain length and the chain number increase. At higher fields, the ring becomes sharper indicating the formation of smooth surfaced columns as evident from the hexagonal symmetry. In

conclusion, experimental evidence has been provided for a magnetically tunable localization of light in a

disordered magnetic medium, which offer promising applications in photonic devices.

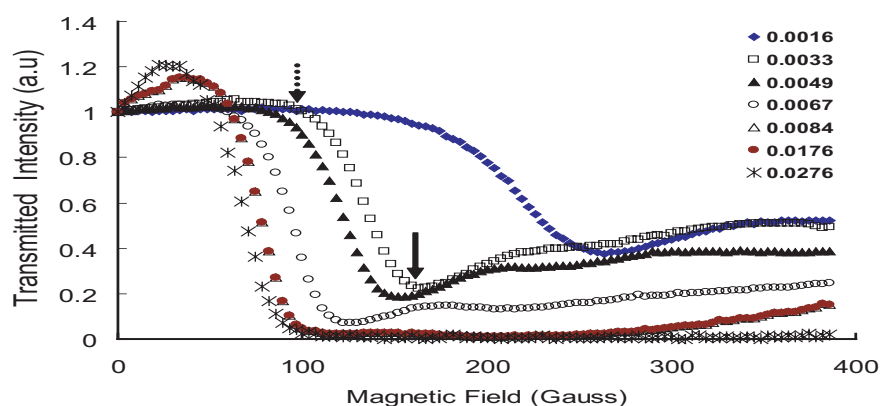


Fig.2 The forward scattered light intensity as a function of applied magnetic field for magnetite based ferrofluid of different volume fractions of magnetic nanoparticles. The average particle diameter was 6.7nm.

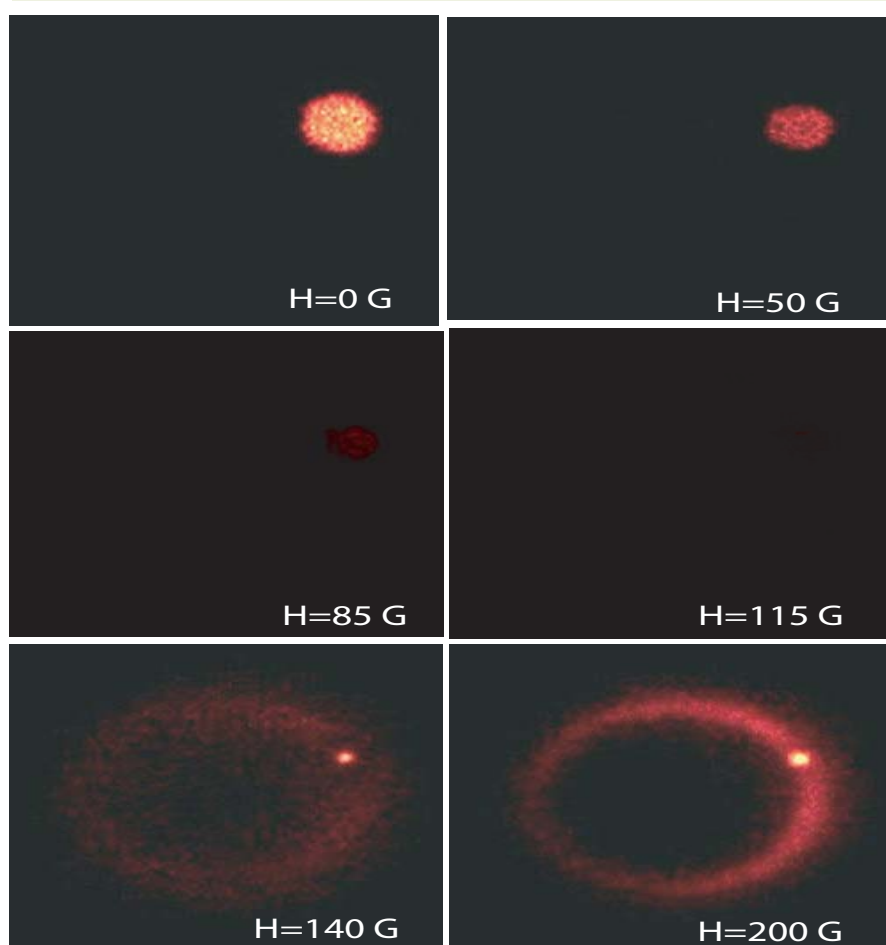


Fig.3 The forward scattering patterns from ferrofluids of 0.0067 volume fraction at various magnetic fields (a) 0, (b) 50 (c) 115 (d) 140 and (e) 200 Gauss.

VI.2. Microstructural Studies of Nanocomposite Thin Films of Ni/ CrN Prepared by Magnetron Sputtering

Synthesis of metal nitrides and metal / metal nitride composites is very challenging as they provide a good illustration how materials properties can significantly be improved. Combination of different materials creates interfaces whose properties and processing needs to be understood to apply these materials for technological applications. It is the objective of this work is to emphasize the importance of composite materials formed by metallic particles dispersed within another insulating or nanocrystalline (nc) matrix. Metal/nc-matrix interfaces play a key role in the understanding of many fundamental properties. These interfaces play a crucial role in a wide

range of technological applications such as heterogeneous catalysis, fuel cells, microelectronics and optoelectronics, as well as structural components. In addition, the metallic content and particle size effect are important issues in the design of properties, for instance, mechanical properties. Previous experimental results of hardness of nanostructured metals or metallic superlattices clearly indicate that hardness increases with decreasing grain sizes following $d^{-1/2}$ dependence known as the Hall-Petch effect. However, this trend is reversed for particle sizes less than 20nm for which the hardness decreases due to a grain sliding process along particle boundaries. The increase in

hardness is based on hindering of the movement of dislocations by the formation of sharp interfaces between several nanometers of thin layers of materials with a large difference in elastic shear moduli.

Nanocomposite coatings are deposited by a variety of techniques including high-temperature chemical vapor deposition (CVD) and low-temperature reactive sputtering, activated reactive evaporation and plasma CVD. The plasma techniques provide, besides the low deposition temperature, the possibility to control the ion bombardment of the growing film which results in a smaller grain size, a less columnar structure and a controllably

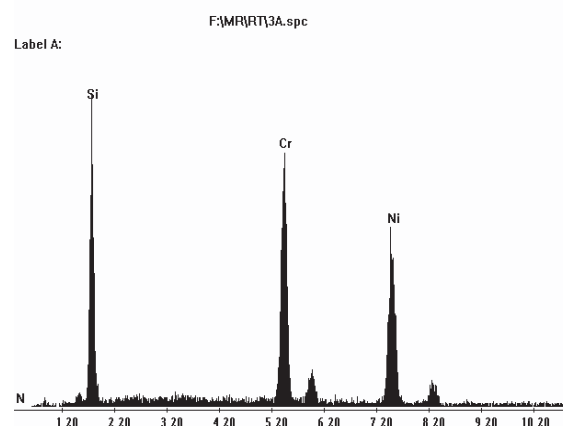
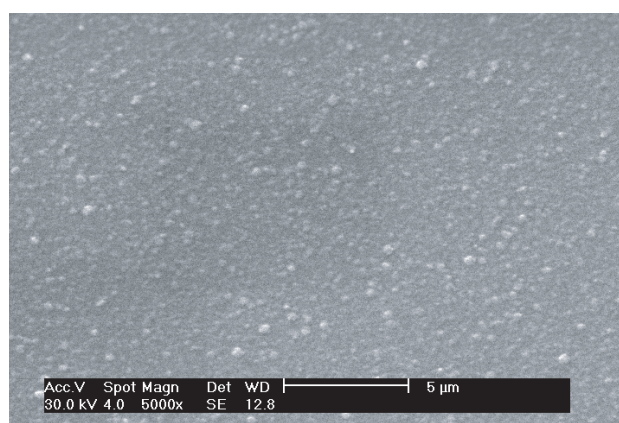


Fig.1(a) SEM micrograph of Ni/ CrN film prepared at 773 K at 10sccm, and (b) EDX analysis of the film.

adjustable compressive stress. In the present work, we demonstrate the synthesis of Ni/CrN coatings prepared by magnetron sputtering as they impart properties such as improved wear resistance, good corrosion resistance, low friction coefficients, and attractive appearance.

DC magnetron sputtering from 50Wt% Ni- 50wt%Cr target of 32.5mm diameter and 3 mm thickness was used to deposit the Ni/CrN coatings in the present study. The microstructural properties as a function of nitrogen flow rate and substrate temperatures were investigated using the

techniques of x-ray diffraction, scanning electron microscopy and microhardness measurements. SEM/EDX analysis indicated a fine distribution of particles (Fig.1a) and the composition of the films is close that of the target stoichiometry (Fig 1b). XRD analysis indicated that the films contained Ni, Cr₂N and CrN for flow rates less than 2 standard cubic centimeter per minute (sccm) and Ni and CrN for flow rates >2sccm (Fig.2). The particle size of the CrN and Ni were found to be 5 nm and 9.5-13 nm, respectively. The films deposited at 773 K showed that the particle size of the Ni was found to remain at 5 nm, while the particle size decreased from 13 nm to 9.5 nm with increasing flow rate of nitrogen. A typical TEM bright field image of Ni/CrN film deposited on NaCl and the corresponding diffraction pattern (inset of Fig.3) confirms the XRD results. Nanoindentation measurements of the films showed hardness values of about 12 GPa which is significantly lower than the hardness of pure CrN (~ 20 GPa) indicating that the composite coatings might have more ductility than that of pure intermetallic nitride phase.

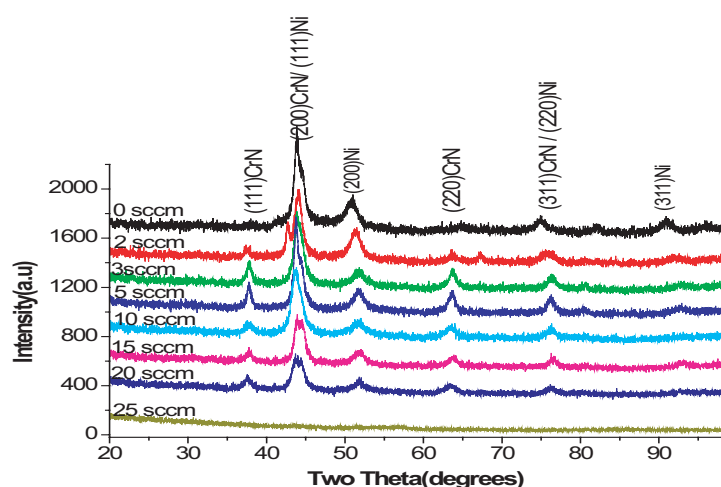


Fig.2 XRD traces of the nanocomposite films as a function of nitrogen flow rates

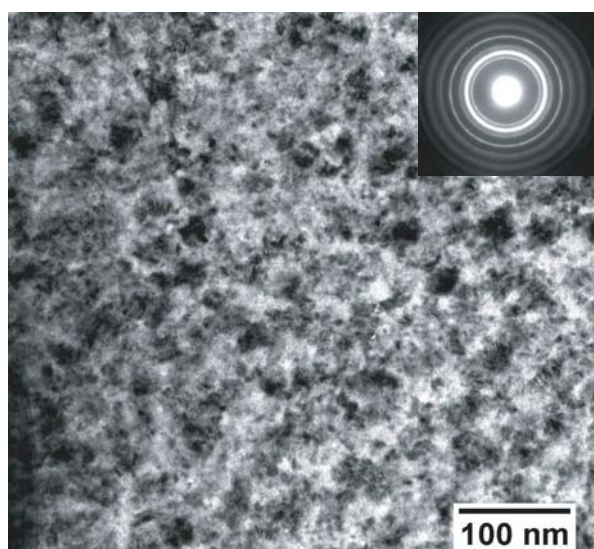


Fig.3 TEM microstructure of nanocrystalline composite film of Ni/CrN. The inset shows the diffraction pattern containing reflections of Ni and CrN.

VI.3. Synthesis and Characterisation of Nanostructured Tin Coatings By Reactive Pulsed Laser Deposition Technique

Pulsed Laser Deposition (PLD) is a versatile technique to grow high quality nanostructured coatings for several technological applications. Reactive Pulsed Laser Deposition (RPLD) offers additional advantage of synthesizing transition metal oxides, nitrides and carbides with tailored stoichiometric composition from elemental metallic target circumventing the need to prepare highly dense ceramic targets. In this technique, an ultra high pure reactive gas like nitrogen is bled into the ultra high vacuum (10^{-7} mbar) deposition chamber through a high conductance molecular leak valve. Interaction of nitrogen gas with highly energetic axisymmetric and supersonically expanding laser plume containing titanium vapour plasma produces TiN clusters ranging from 10-15 nm size. Impact of such clusters on a silicon substrate produces well adherent nanostructured TiN coatings. It is also possible to synthesize functionally gradient nitride coatings through control of partial pressure of nitrogen in the

vacuum chamber which in turn decides the N/Ti ratio.

In order to implement the above experimental philosophy, an UHV compatible RPLD setup was indigenously set up. A photograph of the facility is shown in Fig. 1. The PLD chamber was pumped by a turbomolecular pumping system to a base pressure of 10^{-7} mbar. The all metal chamber contains necessary optically transparent view ports for the transmission of laser beam. A Q-switched Nd:YAG laser with a wavelength of 1064 nm,

repetition rate of 10 Hz, pulse energy up to 900 mJ and pulse width of 7 ns was used for executing ablation of high pure metallic target in a reactive environment obtained from mass flow controlled delivery of gases. In a typical experiment aimed at optimizing synthesis conditions for nano-structured functionally gradient TiN coating, 4 layers of TiN coating were grown sequentially on a silicon substrate kept at 473 K. For each TiN layer extending to a thickness of 100 nm, a distinct partial pressure of N_2 was used. In successive advancing layers, a gradually

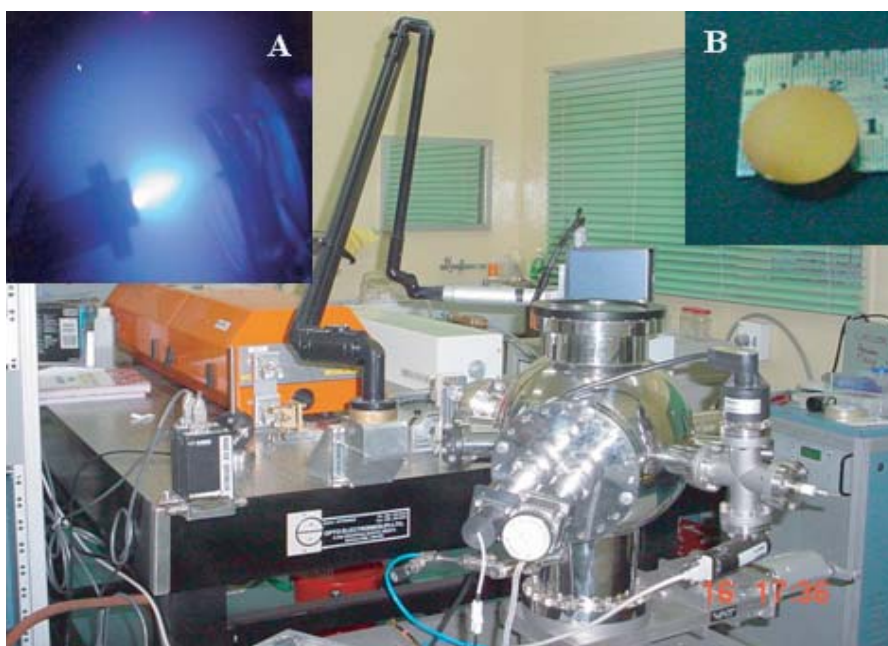


Fig.1 Reactive Pulsed Laser Deposition facility for synthesis of multilayer hard coatings (Insert) A-RPLD in progress B-RPLD grown TiN film

rising partial pressure of nitrogen gas was maintained. The compositional depth profile of this multilayer architecture was analyzed by Secondary Ion Mass Spectrometry (SIMS) using Cs^+ primary ion beam. The Cs Ti^+ and CsN_2^+ quasimolecular complexes were monitored

depth profiles for the elements Ti, Si, N and O. The N/Ti ratio increases with increase in deposition pressure from 5.0×10^{-5} mbar, reaches a maximum for films deposited at 5.0×10^{-2} mbar and then declines owing to the preponderance of O_2 at higher

stoichiometric nanostructured TiN coatings.

The high resolution TEM image of the TiN film grown on a NaCl substrate at 2×10^{-2} mbar and the corresponding Selected Area Electron Diffraction (SAED) pattern is shown in figure 3. These studies indicated the formation of films highly oriented in the $\langle 200 \rangle$ and $\langle 220 \rangle$ directions. The d-spacing calculated from the diffraction pattern matches well with the literature values reported in PCPDF data. A typical nanoindentation profile of 800 nm thick TiN film coated on silicon substrate at 2.0×10^{-2} mbar is shown as an inset in the high resolution TEM microstructure. Nanoindentation studies of thin films, are aimed at providing better interpretations of the elastic modulus, yield strength, strain hardening and hardness of the surface only. The hardness and modulus of the film at a depth of 80 nm calculated from the loading and unloading profile using Oliver-Pharr technique is 20 GPa and 231 GPa, respectively. Efforts are on to synthesize AlN, ZrN and NbN coatings in similar way with an aim to produce multilayered nanostructured films with heterolaminate architecture.

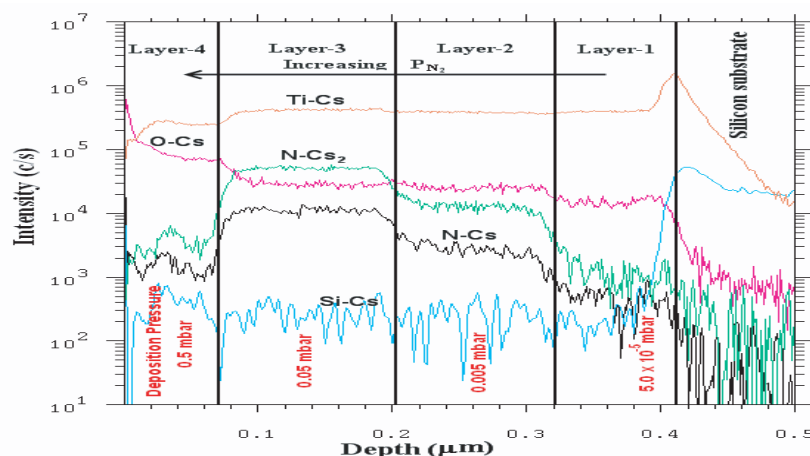


Fig.2 SIMS depth profile of TiN multilayers grown sequentially on Si substrate at various deposition pressures by RPLD

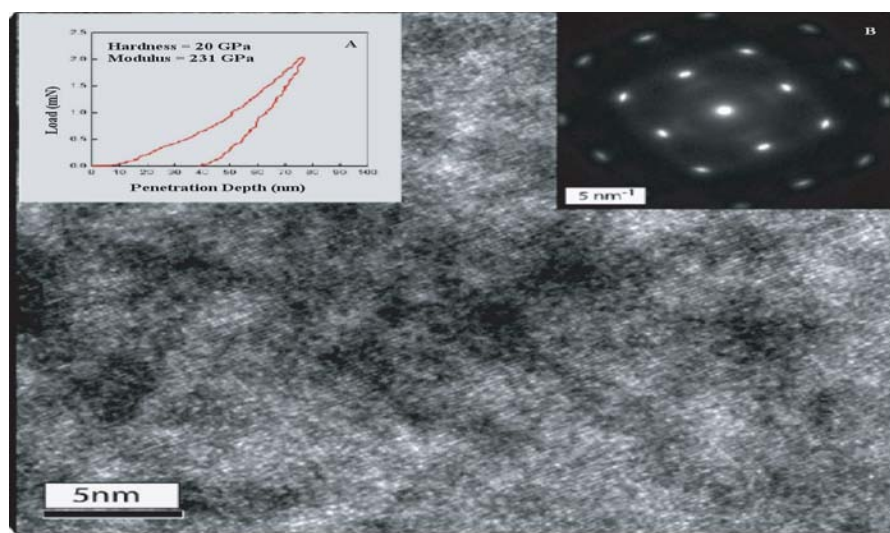


Fig.3 High Resolution TEM image of the RPLD grown TiN film (Insert A) elasto-plastic deformation profile obtained by nano-indentation (Insert B) selected area electron diffraction pattern

along with CsO^+ and CsSi^+ to get the compositional variation as a function of sputter depth. Fig. 2 shows the composition

pressures. Thus it can be concluded that the deposition pressure of $\sim 10^{-2}$ mbar is the optimal condition for growing

VI.4. Long-range Attraction between Like-charged Colloids

Among the various soft matter systems, charge-stabilized colloidal suspensions (e.g., submicron sized polystyrene latex and silica particles dispersed in water) have gained recognition as tremendously useful model condensed matter systems because of their structural ordering and rich phase behavior. Hence, these systems are of considerable interest to study fundamental questions, which are also relevant for atomic systems. Understanding of this simple model system is far from complete with respect to the effective pair-potential $U(r)$ between the charged colloids arising due to the basic

electrostatic interactions among the constituents. Using a confocal laser scanning microscope (CLSM) we probe charged latex suspensions and show that $U(r)$ between like-charged particles exhibits a long-range attractive minimum when effective charge density of the particles is quite high. We also observe stable bound pairs. These observations provide a direct and unequivocal evidence for long-range attraction between like-charged colloidal particles.

For a very dilute suspension, the pair-correlation function $g(r)$ is directly related to the effective pair-potential $U(r)$ by

$$g(r) = \exp\left(\frac{U(r)}{k_B T}\right) \quad (1)$$

Hence, $U(r)$ can be obtained by measuring $g(r)$. Digital video microscopy and optical tweezer techniques have been used in the past to measure $g(r)$ by imaging the colloidal particles. However, only the particles close to the microscope cover-glass could be imaged in these studies because of the limited depth of focus. The cover-glass has strong influence on $U(r)$. Further, the attraction observed in these experiments is attributed to imaging artifacts and projection errors. Thus, to date, there is no direct experimental evidence for existence of a long-range attractive term in the $U(r)$ of like-charged colloids in a bulk suspension with monovalent counterions.

Observation of long-range attraction in very dilute bulk suspensions requires setting-up right experimental conditions: (a) Particles of high effective charge density, are essential to increase the strength of attraction as well as to increase the counterion concentration in the medium, which mediate the attraction between like-charged particles. (b) Elimination of

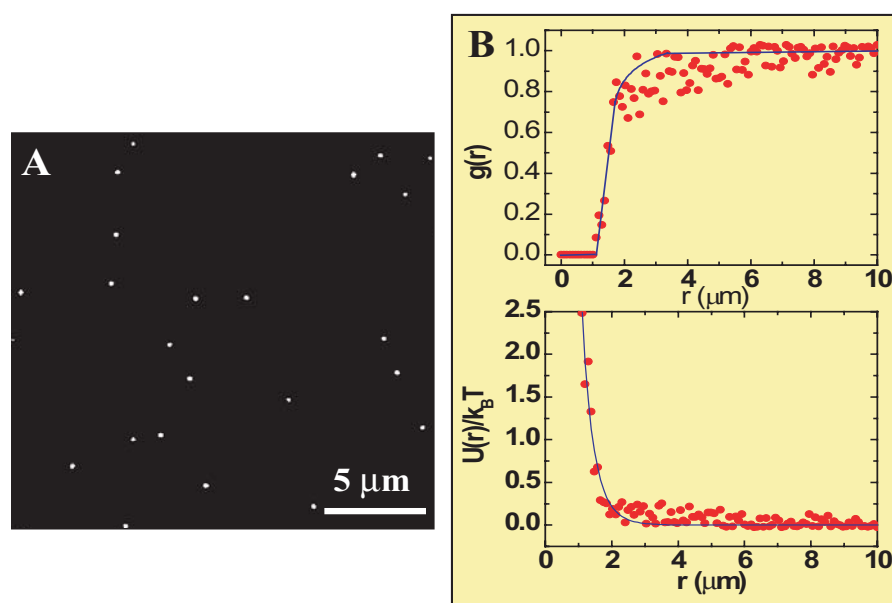


Fig.1 A. Confocal image of 780 nm polystyrene particles of low charge density. B. Pair-potential $U(r)$ obtained from measured pair-correlation function $g(r)$ shows screened Coulomb repulsion between like-charged particles

wall effects and (c) avoiding sedimentation of particles due to gravity. Highly charged polystyrene colloidal particles have been synthesized to increase the concentration of counterions and redispersed in a density-matched fluid (50:50 H₂O-D₂O mixture) to eliminate sedimentation due to gravity. The effect of charged wall is eliminated by employing a CLSM for imaging the particles far away ($> 200\mu\text{m}$) from charged cover slip. The impurity ion concentration is minimized by completely deionizing the suspension using mixed-bed ion-exchange resins.

The colloidal particles deep inside the suspensions are viewed with a fast (7.3 frames/sec) scanning CLSM to obtain two dimensional (2D)

optical slices. Several thousands of images as time series and several such series from different locations in the sample have been. In-plane $g(r)$ has been obtained by determining the positions of the particles by image analysis in each frame, and then averaging over several thousands of such frames. The $U(r)$ is obtained from the measured $g(r)$ using Eq. 1. To establish that this methodology is free from imaging artifacts we first reproduce the standard result by preparing a very dilute deionized suspension (volume fraction $\phi = 0.0001$, and diameter $d = 780\text{ nm}$) of latex particles of low surface charge density $\sigma = 0.004\text{ }\mu\text{C}/\text{cm}^2$. Only individual particles (Fig. 1A) undergoing Brownian motion are observed

and the $U(r)$ (Fig. 1B) obtained from measured $g(r)$ is found to be screened Coulomb repulsive and fits to the potential form given by Derjaguin-Landau-Verwey-Overbeek theory.

In dilute suspension of high charge density ($\sigma = 2.7\text{ }\mu\text{C}/\text{cm}^2$) latex particles we observe stable bound pairs (Fig. 2A) and higher order particle clusters. These observations provide direct evidence for existence of long-range attraction between like-charged colloids. Existence of such stable bound pairs implies an attractive minimum U_m with magnitudes of the order of thermal energy $k_B T$ or more in the pair-interaction $U(r)$ between the like-charged particles. The magnitude of U_m and the interparticle distance R_m at which this attractive minimum occurs, have been measured by obtaining $U(r)$ using Eq. (1). The $g(r)$ and $U(r)$ for two samples with charge densities $\sigma = 2.7$ and $0.3\text{ }\mu\text{C}/\text{cm}^2$ are shown in Fig. 2. The pair-potential $U(r)$ clearly shows an attractive minimum (Fig. 2B) at an interparticle distance of about $1.45\text{ }\mu\text{m}$ which is really long-ranged as it corresponds to about 2.4 times the diameter ($d = 600\text{ nm}$) of the particles. Further, the well depth (Fig. 2B) is found to be larger ($U_m \sim 1.82\text{ kBT}$) for

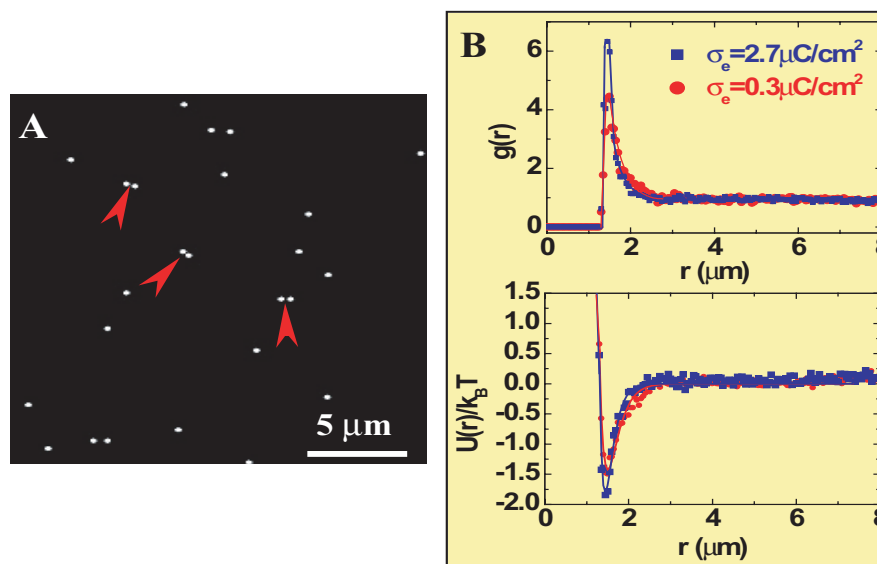


Fig.2A Pair correlation function $g(r)$ and the corresponding pair-potential $U(r)$ for particles of high charge density. **2B.** $U(r)$ shows a long-range attractive minimum $R_m \sim 1.45\mu\text{m}$

particles of $\sigma = 2.7 \mu\text{C}/\text{cm}^2$ as compared to that for particles with $\sigma = 0.3 \text{ C}/\text{cm}^2$. Measured experimental $U(r)$ data was found to fit to the following empirical expression $U(r) = A(\exp(-\kappa r)/r) - B \exp(-\kappa r)$, where the constants A , B represent the strength of repulsive and attractive

components of the interaction, respectively and κ^{-1} represents the range of interaction.

Present measurements thus confirm the existence of a long-range attractive term in the effective pair-potential between like-charged colloids. The monovalent counterion (H^+

ions) concentration is increased in the system by increasing the charge density on the particles. The attraction is believed to arise from the counterions mediation between the macroions.

VI.5. Soft Modes and NTE in $\text{Zn}(\text{CN})_2$ from Raman Spectroscopy and First Principles Calculations

Vibrational spectroscopy is an excellent tool to study the mechanism of thermal expansion, especially in materials that exhibit the anomalous behaviour of negative thermal expansion (NTE). $\text{Zn}(\text{CN})_2$ is reported to exhibit one of the largest NTE coefficient over a wide temperature range. As some vibrational modes in a material can be optically inactive, or have low Raman scattering cross section, leading to low intensity Raman lines, it is not always possible to study the complete set of vibrational modes of a material experimentally. Hence, we need to simulate the phonon dispersions at different pressures using *ab-initio* methods and calculate the mode Gruneisen parameters of all the phonons as required for

calculation of thermal expansion coefficient.

First-principles, *ab-initio* density functional calculations are performed at different pressures and phonon dispersions calculated using

frozen phonon approximation with SIESTA code. Norm conserving pseudopotentials in the generalized gradient approximation are used in calculations. A $3 \times 3 \times 3$ supercell of $\text{Zn}(\text{CN})_2$ unit cell is used for determining the

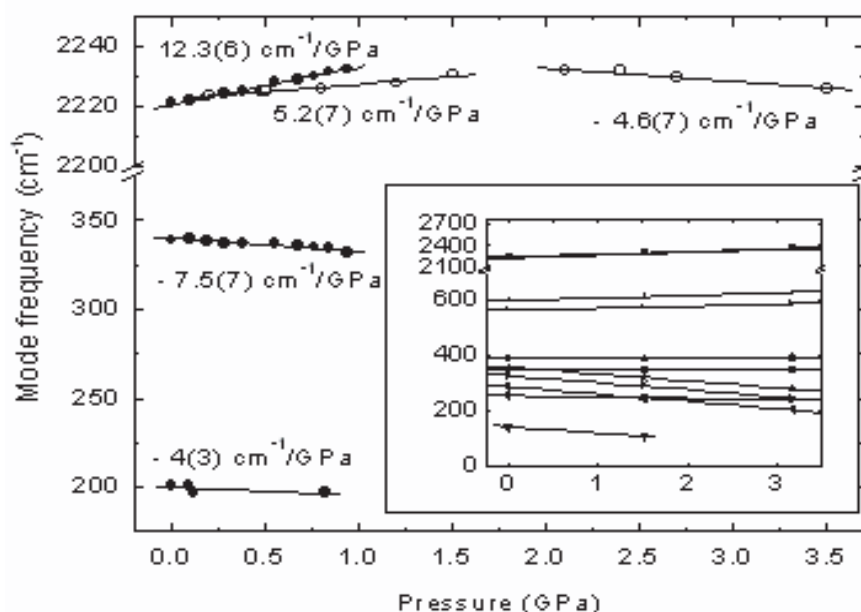


Fig.1 Behaviour of observed Raman modes at different pressures. Inset shows pressure variation for the calculated mode frequencies.

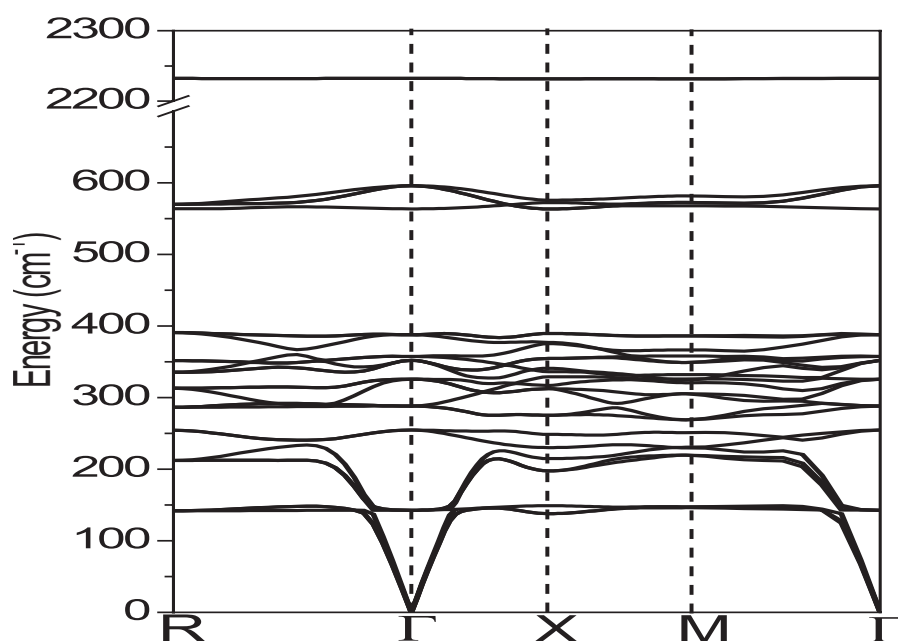


Fig.2 Calculated phonon dispersion curve for Zn(CN)_2 at ambient pressure

relaxed atomic configuration and phonon frequencies at different pressures. Calculations are performed on $8 \times 8 \times 8$ k-point grid, with 350 Rydbergs energy cutoff, using a 16-node Linux cluster. Extra care is taken to ensure that inter-atomic forces in the relaxed structure remain below 10^{-6} eV/Å, as otherwise phonon dispersion at ambient pressure shows imaginary frequencies. Thermal expansion coefficient is calculated from Gruneisen parameters of all modes. Phonon eigenvectors are used for assignment of phonon modes. Soft phonon modes contributing to NTE are identified from the high pressure experiments and simulations. Zn(CN)_2 procured

from Alfa-Aesar (purity > 99.5%), is loaded into a Mao-Bell type diamond anvil cell with methanol-ethanol (4:1) mixture as pressure transmitting medium. Ruby fluorescence is used to measure pressure. Raman spectra are recorded at different pressures in the backscattering geometry using the 488-nm line of an argon ion laser, using a double monochromator, and detected with a cooled photomultiplier tube operated in the photon counting mode. The spectral range covered is $10\text{--}2400\text{ cm}^{-1}$ that also includes the $\text{C}\equiv\text{N}$ stretch mode around 2220 cm^{-1} .

Figure1 depicts the phonon frequency (ω) vs. pressure (P)

for the three modes observed by Raman spectroscopy. Inset shows the behaviour of the calculated mode frequencies. Fig.2 shows the phonon dispersion obtained for Zn(CN)_2 from simulation at ambient pressure. Each of the mode frequencies in Fig.1 inset correspond to those at the Γ point in the phonon dispersion. It has been suggested that ZnC_4/N_4 rigid units are responsible for NTE. But our results show that only the $\text{C}\equiv\text{N}$ bond can be treated as rigid unit and the soft modes correspond to the librational and translational modes of $\text{C}\equiv\text{N}$ bond, with librational modes contributing more to thermal expansion. Out of the eleven zone-centre optical modes, six modes exhibit negative Gruneisen parameter. The value of thermal expansion coefficient, α , calculated from the Gruneisen parameters is in excellent agreement with experimental value. A rapid disordering of the lattice is found above 1.6 GPa from x-ray diffraction. The present calculations and measurements provide the first insight into the relative role of the different phonons in causing negative thermal expansion in Zn(CN)_2 .

VI.6. Atomic Scale Study of Negative Thermal Expansion in Zirconium Tungstate

Vast majority of materials have a positive coefficient of expansion and their volume increases upon heating. Zirconium tungstate (ZrW_2O_8) exhibits negative thermal expansion (NTE) isotropically over the temperature range 4 to 1000 K, whose mechanism is yet to be completely understood. It was earlier understood that a large transverse vibration of the oxygen atom in the middle of the W-O-Zr linkage, which requires corresponding rotations of the polyhedra, is the primary origin of NTE in this material due to unconstrained feature of the structure. It becomes essential to study the local structure at Zr and/or W sites for obtaining the structural variations of ZrO_6/WO_4 polyhedra towards a better understanding of NTE in this system

ZrW_2O_8 is a cubic compound consisting of a three dimensional network of corner linked ZrO_6 octahedra and WO_4 tetrahedra, with the latter having one non-bridging W-O bond. We probe at Zr sites (as WO_4 are more rigid than ZrO_6) by looking at the variation of

quadrupole parameters of probe atoms occupying Zr sites using Perturbed Angular Correlation (PAC) which is a hyperfine interaction technique. We have carried out $^{181}\text{Hf}/\text{Ta}$ based PAC spectroscopy on this system to probe local structure at ZrO_6 . Using this technique Electric Field Gradient (EFG) tensors at the site(s) of occupancy of probe atoms are deduced. Principal component of EFG tensor is proportional to the quadrupole frequency (ν_Q) and is inversely proportional to Zr-O bond length. Asymmetry parameter (ratio of relative

change of other two components of EFG and the principal component) is sensitive to orientation distortion if any associated with ZrO_6 .

A few representative time dependent anisotropy spectra $R(t)$ and their Fourier transform $P(\omega)$ are shown in Fig.1. Analysis of the spectra shows that there are four distinct Zr sites experiencing distinct quadrupole parameters such as quadrupole frequency, asymmetry parameters. The fraction which is predominant

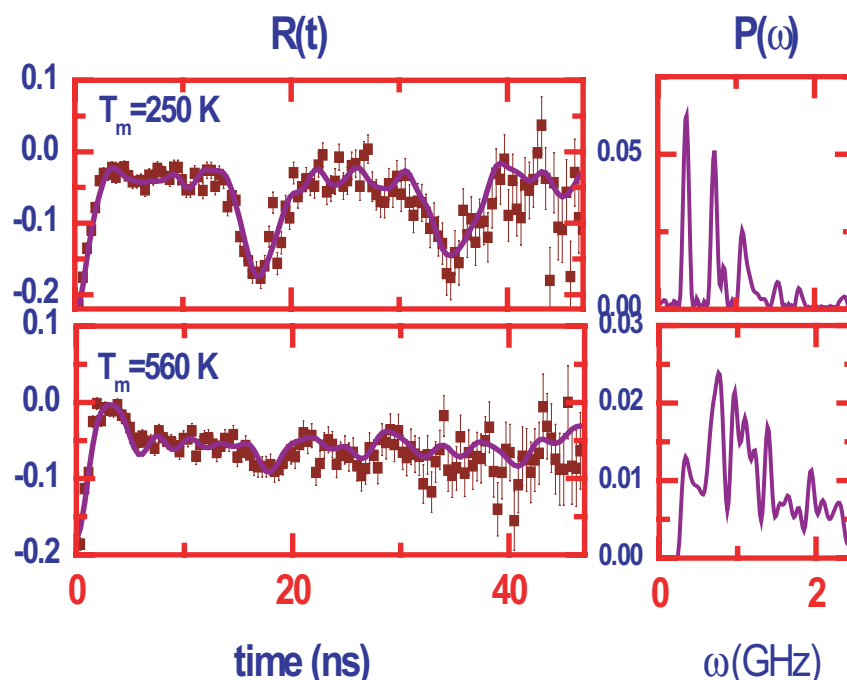


Fig.1 Representative TDPAC spectra and their fourier transforms for measurements carried out at 250 K and 560 K.

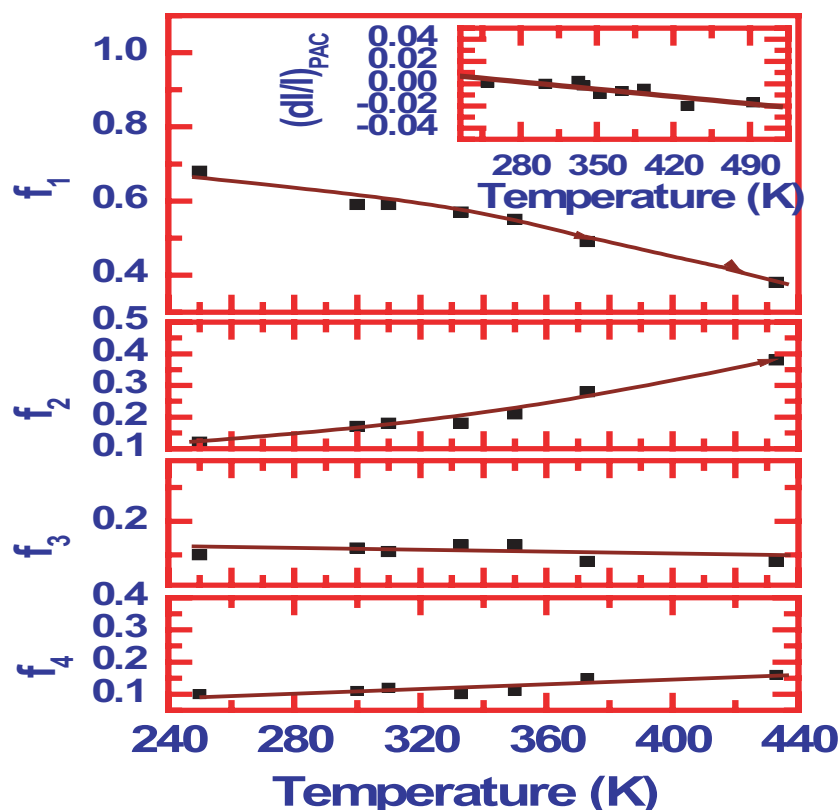


Fig.2 Variation of fractions of probe atoms associated with distinct ZrO_6 octahedra. Notice the increase in the fraction corresponding to distorted octahedra, f_2 with increase of temperature. Shown in the inset is the fractional change in the average Zr-O distance, dl/l with temperature.

at 250 K is interpreted to be due to probe atoms occupying regular ZrO_6 . This is supported by a point charge model based computation of EFG carried out by us. Based on the values of quadrupole parameters it is interpreted that the other three sites are associated with probe atoms occupying contracted and distorted ZrO_6 . An increase in the fractions experiencing higher quadrupole frequencies at higher temperature is seen in Fig 2.

Shown in Fig.2 is the variation of the fractions with the measurement temperature. f_1 representing the regular ZrO_6 octahedra decreases (Cf. Fig.2) while the other fractions increase with temperature. PAC spectra and the results in terms of variation of quadrupole parameters with temperature are repeatable at room temperature after in-situ measurements till 600 K. This means that the observed quadrupole parameters are due to different equilibrium configurations that ZrO_6 take

as a consequence of inward rotations of polyhedra. Plotted at the top inset in Fig. 2 is the variation of dl/l with temperature. The mean value of Zr-O bondlength is obtained as the average of the negative cubic root of quadrupole frequencies weighted with respect to corresponding values of the fractions. Slope of the plot represents the coefficient of thermal expansion which is found to be negative having a value of approximately $-6 \times 10^{-5} K^{-1}$.

This implies that the existence of higher frequency components and importantly an increase in the magnitudes of these fractions is essential to obtain a negative slope in the variation of mean Zr-O bondlength with temperature. This means that the existence of fractions other than f_1 which represent contracted and distorted ZrO_6 octahedra caused by the inward rotations of polyhedra is essential for understanding negative thermal expansion in zirconium tungstate. Thus this atomic scale study provides a proof that an effective contraction of distinct ZrO_6 octahedra due to inward rotations of polyhedra accompanied by distortions is a very important factor contributing for the observed NTE in these systems.

VI.7. Synthesis of sp^3 Bonded Carbon in Laser Heated Diamond Anvil Cell at 14 GPa and above 2273 K

There is intense scientific as well technological interest in hard ceramics prepared by various techniques, such as high pressure-high temperature, chemical vapour deposition etc. Diamond, diamond like carbon (DLC), cubic BN, boron carbides, TiN, etc are some such well known materials. The applications of superhard, super high thermal conductivity and super low friction of various forms of carbon are well known. Synthesis of these carbon forms starting from various precursors such as graphite, fullerenes, nanotubes etc., under the action of pressure and temperature, is a frontline research area. The DLC materials are hard, amorphous and contain a significant fraction of sp^3 bonded carbon atoms. Depending on the pressure and temperature conditions of synthesis, these can contain fully or partially amorphous and diamond crystallites. Here, the synthesis of various sp^3 bonded phases of graphite under the action of high pressure and high temperature is reported.

The experiment was carried

using a laser heated diamond anvil cell (LHDAC) facility developed in our laboratory. It consists of a Mao-Bell type diamond anvil cell (DAC) in which a tiny sample was squeezed to very high pressure in an inert pressure transmitting medium like Ar. A high power CO_2 ($\lambda=10.6\mu m$) laser beam is focused onto the pressurized sample through the diamond window to heat it very high temperatures. The pressure and temperature achievable with this set up are 100 GPa and 5000K respectively. The DAC, mounted on a nanomover translation stage, can be moved in steps as small as 10 nm with respect to the focused laser spot. By the controlled movement of the DAC stage, various regions of the sample are subjected to laser heating. During the process of heating, the sample inside the DAC and the focused laser spot can be viewed on the PC screen with the help of a CD imaging system. Temperature and pressure are the two crucial parameters that have to be measured in a LHDAC facility. Temperature measurement is done by recording the black-body radiation spectrum of the

hot microscopic sample and utilizing Planck's law. Pressure is measured using the well-known ruby fluorescence method, in which the calibrated wavelength shifts of the ruby R_1 and R_2 fluorescence peaks are employed. The black body radiation of the sample and also the ruby fluorescence spectrum are recorded by a LN_2 -cooled CCD based spectrometer (M/s Jobin-Yvon). Since graphitization of diamond takes place at $\sim 900K$, sufficient thermal insulation has to be provided to the diamonds. For this purpose, Argon gas is used as pressure transmitting media, which also acts as a good thermal insulator and IR window.

A small chip of pyrolytic graphite of size $\sim 70 \times 70 \times 30$

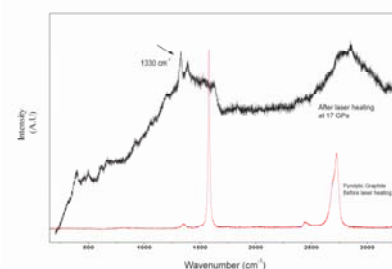


Fig.1 The micro-Raman spectrographs obtained from the granular region of the graphite sample after laser heating showing signatures of diamond (Raman peak at 1331 cm^{-1}) and DLC.

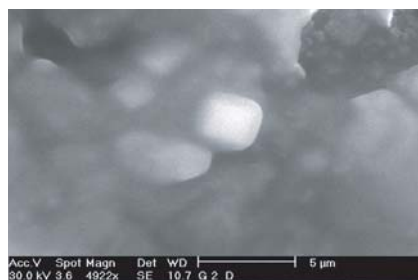


Fig.2 Secondary electron images of the laser heated graphite shows micron size diamond crystals embedded in graphite and DLC materials.

μm was mounted on a small crystal of ruby to insulate it from the diamond in a stainless steel gasket hole of diameter $\sim 150\mu\text{m}$ along with ruby crystals of size $\sim 10\text{-}15\mu\text{m}$ for pressure calibration. The

graphite sample was pressurised to $\sim 14\text{ GPa}$ and the CO_2 laser was focused on it for heating. The sample was rastered with respect to the laser beam by manipulating the nanomover system for uniform heating. After sufficient heating, pressure was released and the sample was retrieved for characterization. In order to investigate further micro-Raman was carried out by focusing the incident laser beam on various regions of the sample. The micro Raman spectrum obtained from the region of granular structure is

shown in Fig.1. It clearly shows the features of sp^3 bonded carbon that is both diamond and DLC. SEM images revealed that several microcrystal of diamond have grown in a matrix of graphite and DLC as shown in Fig.2. The observation of diamond and DLC is quite interesting as it provides further impetus to our pursuit in the exploration of superhard phases. Further experiments using C_{60} instead of graphite is being carried out to explore the predicted ultrahard phases.

VI.8. Two Detector Coincidence Doppler Broadening Studies on Bulk Nickel Silicides

Positron annihilation spectroscopy (PAS) is a unique defect characterization tool, which relies on the propensity of positrons to become localized in open-volume regions of a solid. In the conventional Doppler broadening spectroscopy, a single Ge detector records the Doppler broadened energy spectrum of the annihilation gamma rays (511 keV), but the spectrum suffers from high background contributions. The core annihilation events contributing to high momentum region (520 - 540 keV) overlap

with the background region. This region contains information pertaining to the core-electrons, using which one can deduce elemental specific information. To overcome the difficulty associated with the large background contributions in the high momentum region, the annihilation spectra are recorded using two Ge detectors in coincidence mode. In this way, the peak to the background ratio is dramatically improved in the tail region and the contribution of the core electrons can be easily extracted. This is

demonstrated in Fig. 1, where a conventional single detector spectrum for Si sample is

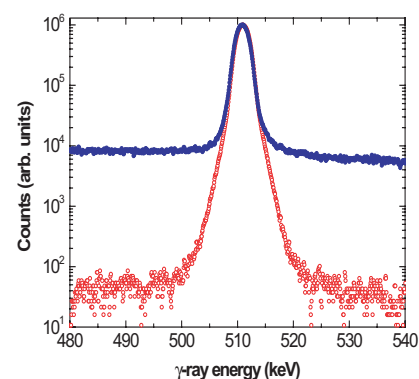


Fig.1 Comparison between a conventional doppler spectrum (blue) and a coincident doppler spectrum (red) recorded on Si. Note the large reduction in the background (520 to 540 keV) in coincidence doppler spectrum

shown along with two-detector coincidence spectrum. As can be seen, the peak (511 keV) to background (around 530 keV) ratio is about 10^2 for single detector, while it is about 10^5 for coincidence mode. Thus, the Coincidence Doppler method allows to analyze the high momentum regions with much better precision, enabling chemical sensitivity.

A two detector coincidence system has been setup consisting of a pair of HPGe detectors, spectroscopy amplifiers and ADC's and a MCA capable of acquiring the coincident spectrum. The Ge detectors are of 30 % efficiency having an energy resolution of 1.27 keV and 1.5 keV at 662 keV γ -ray. Fig. 2 shows a two-dimensional spectrum recorded on Si (100). The channel numbers (converted to annihilation energies) of the two detectors form the

horizontal and vertical axes of the figure. The horizontal and the vertical bands correspond to the intensities of the annihilation gamma rays of the individual detector. The intense peak at the center corresponds to the counts for $E_1=E_2=511$ keV. The elliptical region extending diagonally with $E_1+E_2=1022$ keV originates from the coincidence events and corresponds to the annihilations with high momentum electrons. This region is nearly background free.

Coincidence Doppler measurements have been used to investigate Nickel Silicides. The ratio of the measured Doppler curve in Ni, NiSi and NiSi₂, with respect to Si is shown in Fig. 3. The Ni curve shows a maximum around $p_L = 13 \times 10^{-3} m_0c$ which corresponds to annihilation of

positrons with 3d electrons and the broadening of the curve is due to the contribution from the more localized 3p electrons. Unlike the Ni curve, the NiSi and NiSi₂ do not exhibit a maximum around $13 \times 10^{-3} m_0c$, implying that the contributions from 3d electrons have decreased. It may be noted that there is a distinct maxima arising around $27 \times 10^{-3} m_0c$ for NiSi and NiSi₂. This may be attributed to positron annihilation with 3p electrons thus bringing out the potential of coincidence Doppler measurements in distinguishing annihilations from both NiSi and NiSi₂. These experiments illustrate the efficacy of coincidence Doppler broadening technique, that facilitates measurement of Doppler broadening spectrum with a high peak-to-background ratio to probe the high momentum regions.

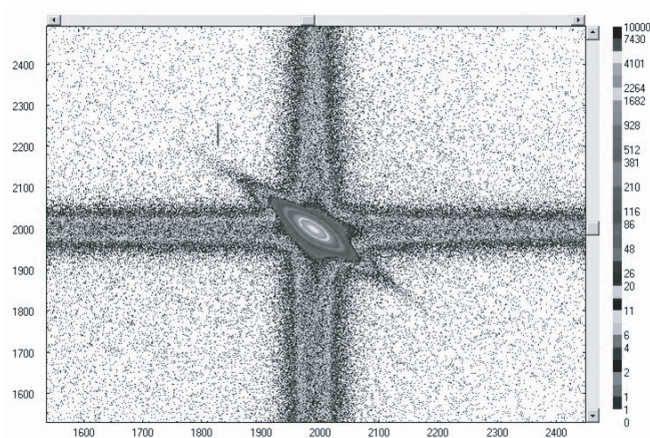


Fig.2 A two dimensional display of the coincident events collected on Si (100). A total of 3×10^7 counts are accumulated in the spectrum.

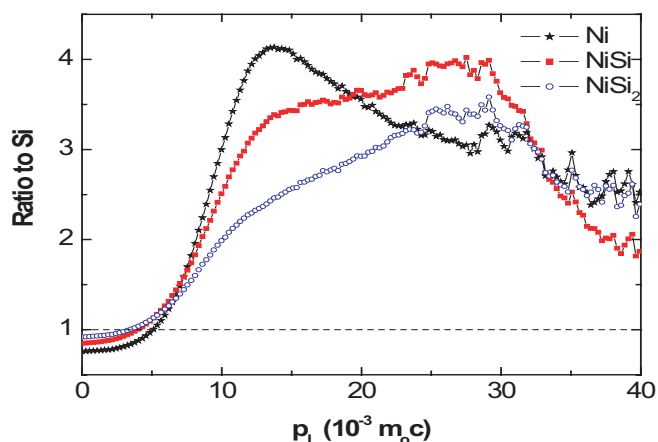


Fig.3 Ratio of the experimental curves with respect to Si.

VI.9. Eigen Vector Based Approach for Enhancement of NDE Images of Defects

Non-destructive evaluation (NDE) is used for detection and imaging of defects in materials. In ferromagnetic materials such as carbon steel, impedance change in eddy current (EC) probe due to defects and permeability variations are usually of same phase angle and this makes even the multi-frequency methods inadequate to suppress the noise due to permeability variations. The impedance changes due to the permeability variations are incoherent whereas the impedance changes due to defects extend spatially depending on the foot-print of the eddy current probe used. Similarly, the magnetic leakage flux (MFL) from deep-surface defects is feeble and contains undesirable and incoherent noise from variations in

magnetic permeability, surface roughness and stress. Utilising the incoherent nature of noise, an innovative approach based on Eigen value and Eigen vector (Eigen pair) has been developed and has been successfully applied to EC and MFL images of defects in carbon steel.

In this approach, the energy packing property of the Eigen values is effectively utilized to suppress incoherent noise and to reconstruct images. This approach involves determination of Eigen pairs of image covariance matrix and reconstruction of images after considering the significant Eigen pairs having the maximum information of the defects. The insignificant Eigen pairs representing mostly the

incoherent noise due to permeability variations are ignored in the reconstruction during the inverse transform. The performance of the approach is assessed on eddy current images of surface defects in 25 mm thick carbon steel plate and on MFL images of deep-surface defects in 12 mm thick carbon steel plates.

A carbon steel plate (thickness 25 mm) consisting of a hole and a notch is used in the studies. Using a 3.5 mm diameter surface absolute eddy current probe, images of 2.5 mm diameter hole (depth 0.25 mm) and a notch (length 10 mm, width 0.5 mm, and depth 0.5 mm) are obtained at an excitation frequency of 50 kHz. Using a C-core electromagnet (4A current) and high-sensitive

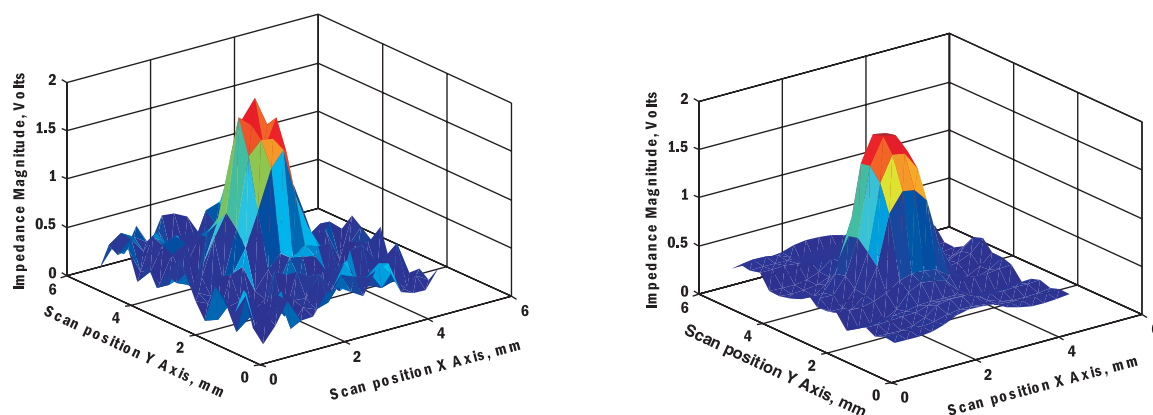


Fig.1 Raw eddy current image of a 0.25 mm deep hole in carbon steel plate (left) and the image after reconstruction after taking the most significant Eigen value (right).

GMR sensor, MFL images of notches (length 15 mm, width 0.5 mm) located at 3.1 mm, 6.3 mm and 8.6 mm below the surface of 12 mm thick carbon steel plates are obtained. The EC and MFL images are used for validation of the Eigen vector approach.

Typical EC raw image of 0.25 mm deep hole and the reconstructed image are shown in Fig.1. The MFL images of deep-surface notch located at 8.6 mm below surface and that of 1.1 mm deep surface-breaking notch are shown in Fig.2 along with the

reconstructed images by the Eigen vector approach. As can be observed, there is a significant enhancement in the quality of EC and MFL images after processing.

The quality of reconstruction has been assessed by determining an empirical parameter called, noise reduction factor (NRF) which is the ratio of average noise amplitude in a defect-free region in a raw image to that of the same region in reconstructed image. The NRF is found to be high when the most significant Eigen pair is

used for reconstruction. However, when more Eigen pairs are included in the reconstruction, NRF is found to decrease. This is due to the fact that the smaller Eigen pairs which contain the incoherent noise information of magnetic permeability variations contribute to the reconstruction process resulting in image degradation.

This approach has enabled reliable detection of deep-surface notch located at 8.6 mm below surface. More than 1.6 times improvement in signal-to-noise ratio has been

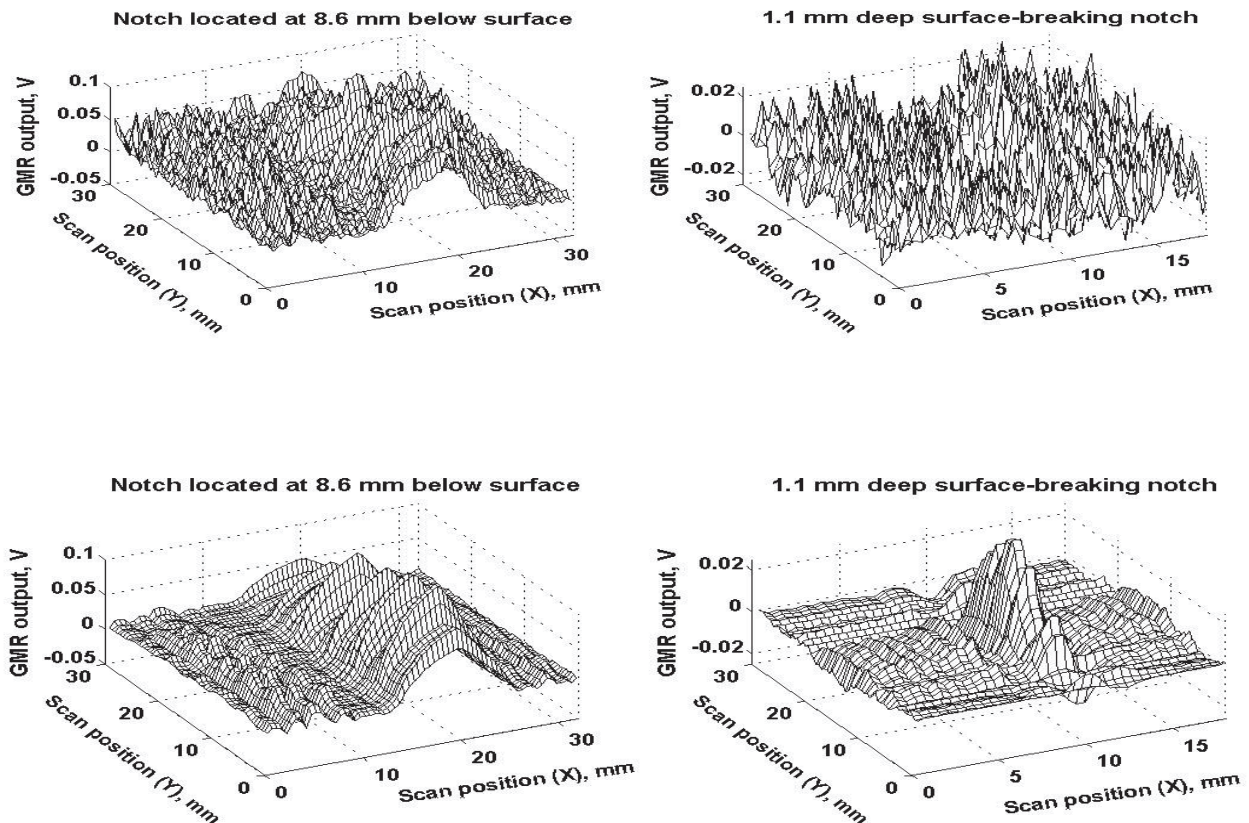


Fig.2 Raw (top) and processed (bottom) MFL images of a notch located 8.6 mm below surface and a 1.1 mm deep surface-breaking notch in carbon steel plates.

observed after processing. This approach is very attractive for processing NDE images affected by incoherent noise due to local variations in material properties, coupling etc. and particularly useful for processing images from regions

in operating components for detection of very shallow and incipient fatigue cracks that disturb structural integrity. This approach can also be applied to other types of NDE images for enhancing the sensitivity for detection and improving the

accuracy for sizing the defects. Further, the reconstructed images can be used as input images for artificial intelligent schemes for quantitative characterization of defects.

VI.10. Indigenous Development of Thermoluminescence and Long Afterglow Phosphors

Synthesis of highly sensitive CaSO_4 : Dy TLD phosphor by a novel co-precipitation technique

Thermo luminescence (TL), is a luminescence phenomenon observed when a crystalline solid exposed to ionising radiation is thermally stimulated, liberates some of the charge carriers (electrons or holes) that are trapped at lattice imperfections in the crystal. TL materials are widely used for personnel monitoring of radiation workers due to its reliability, sensitivity and cost effective availability. In India, about one lakh radiation workers use the TL badge based on CaSO_4 :Dy Teflon discs for personnel monitoring and about 100 kg of this phosphor is being made annually for this purpose. Presently, this phosphor is synthesised by re crystallization technique in which Gypsum

($\text{CaSO}_4 \cdot 2\text{H}_2\text{O}$) with activator (Dysprosium oxide) is dissolved in concentrated sulphuric acid completely and then totally evaporated to dryness using a distillation unit in a fume hood. This technique requires the evaporation of one litre of H_2SO_4 to get 100 g of CaSO_4 :Dy phosphor.

For the first time, a simplified co-precipitation technique has been developed for the CaSO_4 :Dy phosphor synthesis which circumvents the cumbersome procedure used so far. In the new co-precipitation technique, radiation dosimetry grade CaSO_4 :Dy crystals are precipitated from the solution containing dissolved CaSO_4 and Dy_2O_3 using a liquid at room temperature. New recipe

of CaSO_4 :Dy based on co-precipitation technique is not only economical but also compatible for large scale production. The TL glow curves of the phosphor prepared by co-precipitation and conventional method are compared in the Fig. 1. The main advantages of this co-precipitation technique over the conventional re-crystallization technique of phosphor preparation are (i) preparation time is very less. (ii) quantity of concentrated H_2SO_4 evaporated is insignificant (iii) higher TL sensitivity - 20% more than that of presently used material (iv) better glow curve structure (v) lesser glow peak shift and better linearity to gamma dose and (vi) uniform crystal morphology and lower grain size - all grains are mostly

cuboidal in shape, quite uniform and small (average size about 25 micron), suitable for manufacturing teflon discs in as-prepared form whereas the presently used conventional phosphors are mostly (90%) above 75 micron and has to be ground for dosimetric applications.

Long afterglow phosphors

Phosphorescence (or afterglow) refers to the light emission at room temperature from a phosphor that persists

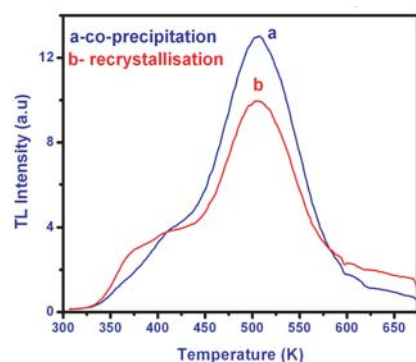


Fig.1 Comparison of TL glow curves of $\text{CaSO}_4\text{:Dy}$ phosphor

after removal of the excitation source. Presently oxide based phosphors like aluminates and

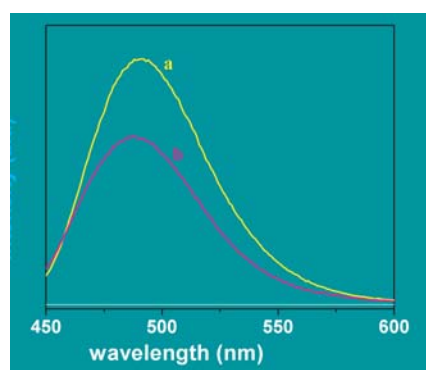


Fig.2 Afterglow spectra of (a) combustion (b) solid-state synthesis

silicates are widely used as afterglow materials. Rare earth doped long glow aluminate phosphors find application in various fields due to their high quantum efficiency and long persistence time. This Centre has developed one such long-afterglow phosphor, $\text{Sr}_4\text{Al}_{14}\text{O}_{25}\text{:Eu}^{2+},\text{Dy}^{3+}$.

This phosphor was synthesized through both solid state reaction and combustion synthesis routes. In case of solid state reaction, boric acid flux was added to facilitate the product synthesis at low temperature. To improve the afterglow (AG) characteristics of the phosphor, the stoichiometry was varied by taking different Sr/Al molar ratios. The luminescence properties of Eu^{2+} in $\text{Sr}_4\text{Al}_{14}\text{O}_{25}\text{:Eu}^{2+},\text{Dy}^{3+}$ was also studied by substituting Sr with other divalent cations like Ca, Ba and Zn. Photoluminescence (PL) intensity of both the strontium deficit and rich phosphors were enhanced in non-stoichiometric (NS) host whereas no definite correlation was observed between the AG intensity and non-stoichiometry. NS compositions led to the formation of different phases / compounds of strontium aluminates which resulted in either blue or green shift of the

PL emission. However, the afterglow emission was not affected by the NS. Similarly the divalent ion substitutions also led to the formation of different aluminate compounds which could change the PL and afterglow characteristics significantly. Interestingly at higher concentration of Ca in the aluminate, the host exhibits emission peaks at 440 and 530 nm. The blend of these lights produces the white afterglow emission. Silver doping in this host enhanced the afterglow intensity by nearly 10 times by decreasing the trap depth and increasing the trap density but no significant change in the PL or AG intensity was observed in the presence of sodium. The afterglow and PL emission of the phosphor synthesized through combustion route was better than that prepared through solid-state method (Fig.2). The greenish-blue AG from $\text{Sr}_4\text{Al}_{14}\text{O}_{25}\text{:Eu}^{2+},\text{Dy}^{3+}$ as shown in Fig. 3 persists for more than 7 h. The indigenous phosphor developed by us gives an equivalent intense emission and its afterglow persistence time is comparable to that of the commercial ones.

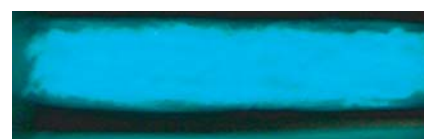


Fig.3 Visually observed afterglow from $\text{Sr}_4\text{Al}_{14}\text{O}_{25}\text{:Eu}^{2+},\text{Dy}^{3+}$

VI.11. Indigenous Development of X-ray Imaging Plate Based on Photostimulated Luminescence Phosphor

For over 100 years, X-ray radiography has relied on film as the image detection and display medium. Recently, photographic films are being gradually replaced by imaging plates (IP) based on photo stimulated luminescence (PSL) storage phosphors, mainly, BaFBr:Eu^{2+} . These are superior to conventional X-ray film due to high detective quantum efficiency, wide dynamic range and reusability. IPs made of BaFBr:Eu^{2+} are used worldwide in hospitals and in several other applications such as X-ray diffraction, auto radiography, transmission electron microscopy etc. Computed Radiography (CR) using PSL technique allows the radiological community to go

digital. By image processing of the actually acquired data, superior image quality can be obtained. Hence multiple exposures are not needed. Comparatively, the non-linear film response implies that X-ray exposures must be chosen quite carefully to avoid over or under exposures. Further benefit of CR is that the digital data can be easily transmitted to other places to seek specialist's opinion.

With the aim of indigenously developing an X-ray imaging plate, high sensitive BaFBr:Eu^{2+} storage phosphor has been successfully synthesized recently using high temperature solid state diffusion route in a reducing atmosphere. The PSL

spectra of the BaFBr:Eu^{2+} synthesised are comparable to that of commercial IP (Fuji) after irradiation. A broad stimulation spectrum in 480 - 650 nm region corresponding to the depopulation of the electrons trapped at $\text{F}(\text{Br})$ centers is observed. Fluorine-excess non-stoichiometric, $\text{BaF}_{1.015}\text{Br}_{0.985}:\text{Eu}^{2+}$ showed maximum PSL with 590 nm light stimulation. The stimulated luminescence process in this phosphor can be explained on the basis of the presence of interstitial fluorine ions (F_i^-) and bromine ion vacancies prior to X-irradiation (during crystal growth) in non-stoichiometric materials as shown in Fig. 1a. On X-irradiation, electrons dislodged

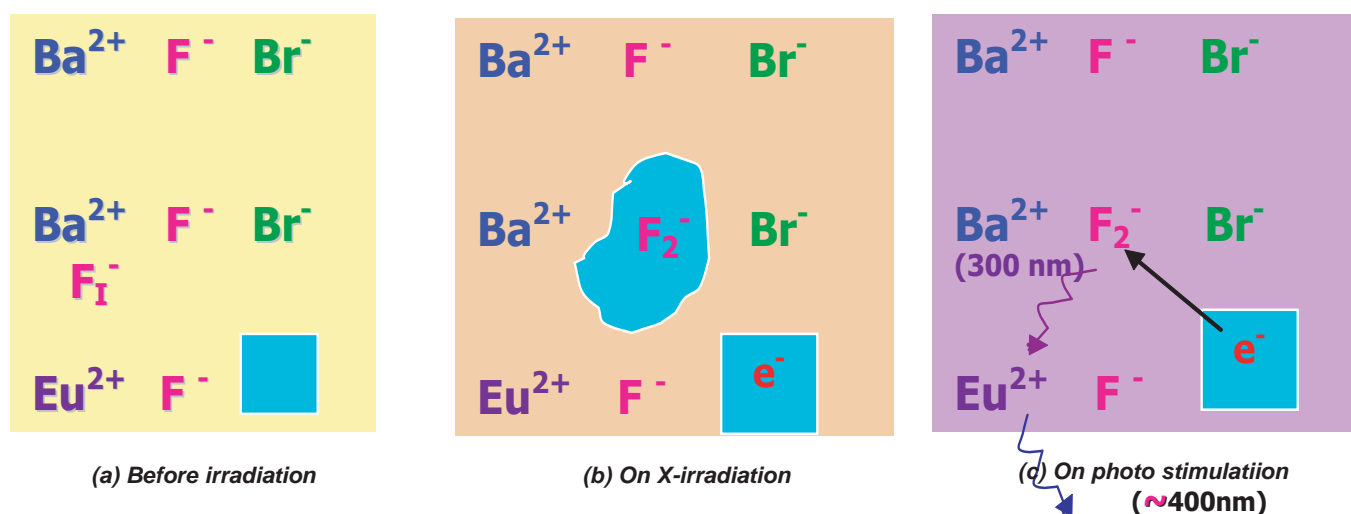


Fig.1 Proposed model of PSL process in $\text{BaF}_{1.015}\text{Br}_{0.985}:\text{Eu}^{2+}$

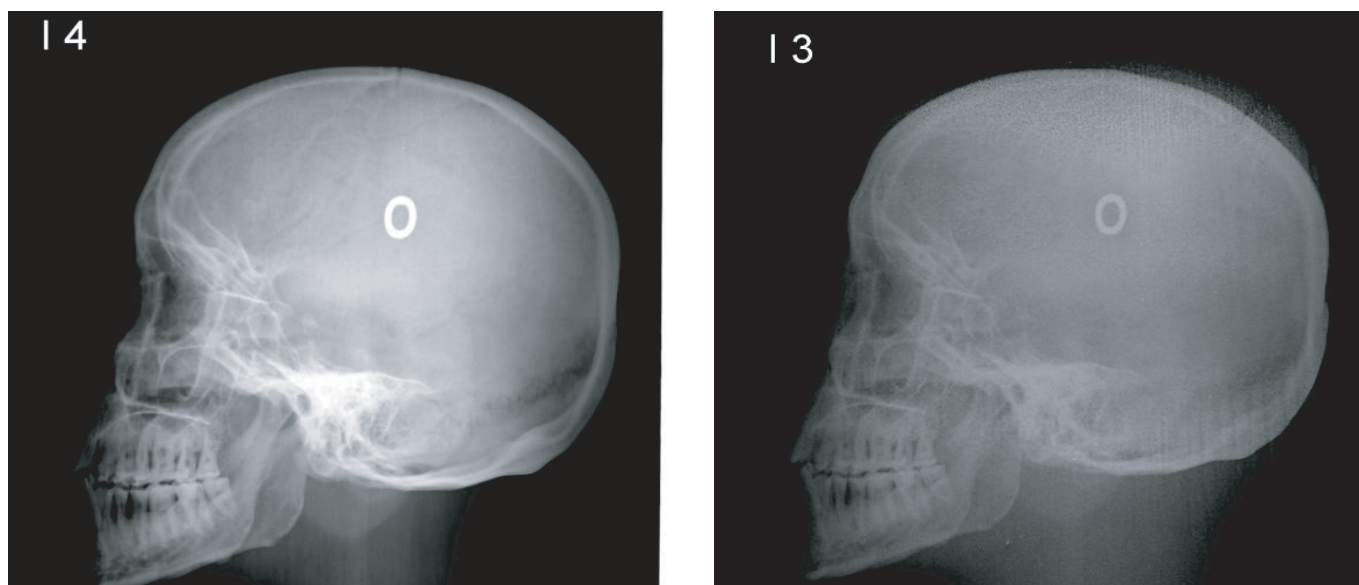


Fig.2 Skull phantom image using Kodak IP (14) and IGCAR IP (13)

from F_i^- get trapped at bromine ion vacancies thereby forming $F(Br^-)$ centers. The interstitial fluorine atoms thus formed combine with the lattice fluorine ions to form molecular ions, F_2^- (H type center), whose presence on x-irradiation was detected by ESR (Fig. 1b). In the proposed model, F_i^- ions act as hole traps and bromine vacancies act as electron centers. On photo stimulation, the electrons released from $F(Br^-)$ centers recombine with holes trapped at F_2^- centers, which results in intrinsic (self-trapped exciton) emission (~ 300 nm) which is characteristic of the BaFBr host (Fig. 1c). This radiatively excites the Eu^{2+} ions thereby causing PSL emission around 400 nm. The merits of the proposed mechanism are: it explains why only fluorine excess compounds

cause intense PSL, it provides a charge compensation mechanism arising out of the presence of bromine vacancies, it supports the experimentally observed F_2^- centers on X-irradiation in fluorine excess BaFBr, and above all it brings the material back to its initial state on photo stimulation.

An imaging plate has been made with the help of M/s Kiran X-ray screens Ltd, Mumbai using the indigenously synthesized storage phosphor. A comparative skull phantom image was recorded using a commercial scanner and a commercial Kodak IP as well as the IP made from the storage phosphor synthesized at IGCAR at the same X-ray exposure parameters (Fig. 2). All the salient features of the image

are seen in the IP made from our phosphor. The sensitivity is comparatively good but the contrast needs improvement. The grain morphology is uneven and higher than the desired value, which causes uneven light scattering that reduces the image contrast.

Modified synthesis techniques and grinding procedure of the phosphor developed recently have improved the grain morphology (grain size ~ 20 μm). Recent efforts in preparing the phosphor in large scale with a simple and cost effective technique using the local make chemicals have been successful. Manufacturing more number of test IPs and comparative studies with commercial IPs are in progress.

VI.12. X-ray Diffraction Studies using Imaging Plate as an Area Detector

Imaging plate based X-ray area detectors were initially used for protein crystallography in the 1980s and more recently, their use has extended to small-molecule structural analyses and powder diffractometry. The usage of imaging plate is particularly advantageous for the characterization of polycrystalline materials since it permits simultaneous collection of many orders of Bragg reflections. There is also a significant size advantage compared to CCD based area detector. In addition to the enormous reduction of data acquisition time for analyses, two-dimensional diffraction patterns contain much more

information than conventional linear scans (i.e. - 2 scans) collected using standard powder diffractometers. Two dimensional diffraction patterns of polycrystalline samples typically consist of concentric (Debye-Scherrer) rings produced by the superposition of reflections from many crystals illuminated by the X-ray beam, which are oriented with a set of (hkl) crystallographic planes oriented to fulfill the Bragg condition. Depending on sample characteristics, these rings might be continuous or spotty and display specific variation in the intensities along them. These features contain important information about

the microstructure of the sample: grain size, preferential orientation, mosaicity, stress etc. Additionally, two-dimensional patterns can be converted into conventional linear scans by radial or azimuthal integration of pixel intensities. The generated linear scans can be processed as usual for mineral phase identification, crystallinity or Rietveld refinement studies. Nevertheless, during this data reduction procedure, most of the information regarding the microstructure of the material is lost. Hence to get the full advantage of two-dimensional diffraction for polycrystalline materials we have to extract the information contained in the two dimensional diffraction patterns. Here we are reporting the diffraction experiment results obtained using the imaging plate as an area detector for both single crystal and powder experiments. The imaging plate reader has 5 mega pixel resolution for 250 mm X 200 mm size plate with each pixel size of 100 the data file size is 10 Mbytes.

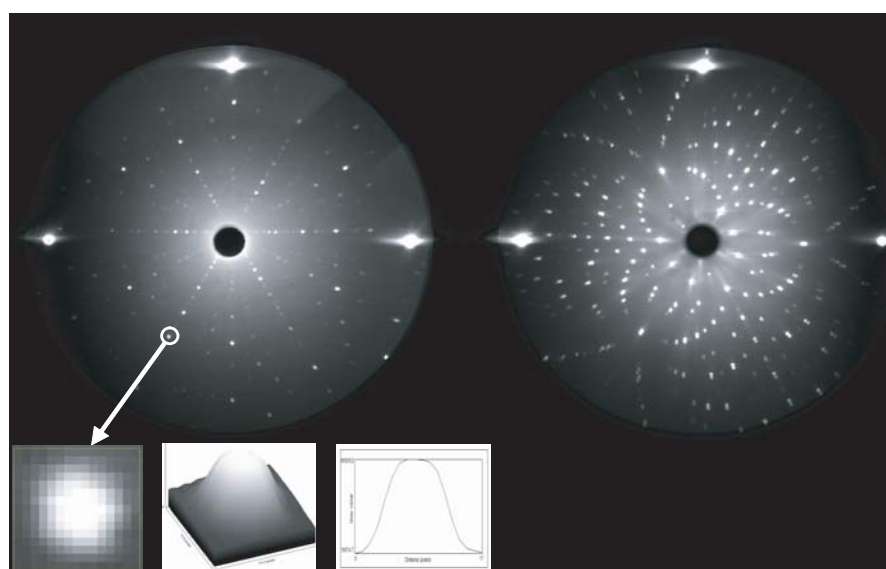


Fig.1 Laue diffraction pattern of a Si single crystal obtained using the Imaging plate as an area detector (the plate read using reader developed at MSD IGCAR). The inset shows the maximum zoom of a diffraction point and its intensity profile in surface and line plot.

Laue X-ray diffraction is historically the first diffraction method for structural

characterization of the crystals and even today it is the first step in assessing the crystal quality. In the Laue camera, instead of the photographic X-ray film an imaging plate cut in a circular shape is loaded and covered with an opaque paper. The exposed plates are scanned to obtain the image. The Laue diffraction pattern for Si crystal in both transmitted and back reflected geometries are given in Fig.1. The inset in Fig. 1 shows the enlarged view of a particular Laue spot which depends on the nature of the crystal.

The powder XRD experiment was carried out using the imaging plate for a BaF_2 standard sample. The sample was kept in front of the collimator in Debye Scherrer geometry and the imaging plate kept at a distance of 77.6 mm from the sample. Mo K X-ray with a wavelength of 0.709 \AA is used for this experiment. The

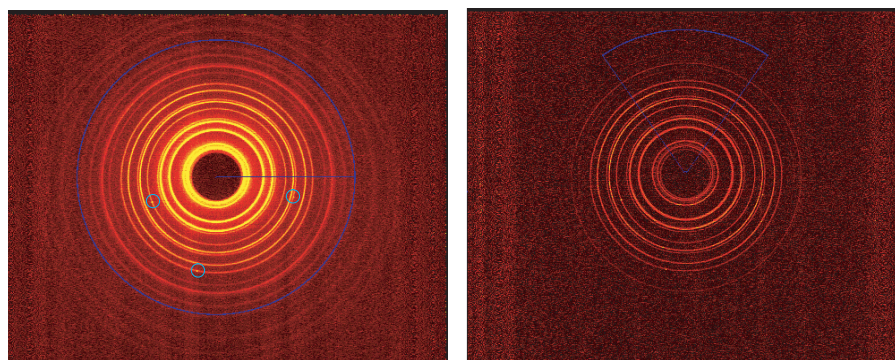


Fig.2 Powder diffraction pattern of BaF_2 sample; with some isolated diffraction spots along the Debye rings indicated using the small circles in the images. The blue circle and the arc shows the psi angle

XRD image obtained is shown in figure 2. The sample was well powdered before carrying out the diffraction experiment. In spite of this there are a few isolated diffraction spots (shown by the circles in the image) in the powder pattern indicating the coarse grained nature of the sample. This 2D pattern is converted into a 1D pattern by azimuthal integration of pixel intensities from 0 to 360° and by increasing the radius value from the centre of the concentric rings to the edge of the plate (2000 units). The center point of the rings is identified by triangulation of

three points of any one of the rings. This centre is a crucial factor in the 1D data quality hence its accurate location is essential. In order to compare the integrated data with that collected using a standard powder diffractometer (with a point detector), the intensity of every 2 step is normalized by the number of pixels contributing to it. Also in the converted data there is high background hence it is removed from the image using an algorithm. The as acquired XRD image and the background subtracted image are shown in Fig. 2 and the inset (intensity plot along the circumference of the ring) shows the coarse grained nature in the sample. The converted 1D pattern before and after removing the background is shown in figure 3. The conclusion is that if there is a single crystal diffractometer with area detector like imaging plate the same could be used for powder diffraction experiments.

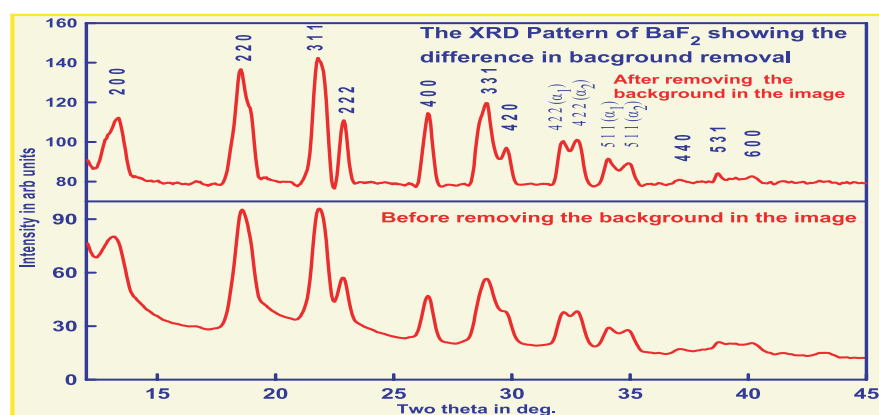


Fig.2 Powder diffraction pattern of BaF_2 sample; with some isolated diffraction spots along the Debye rings indicated using the small circles in the images. The blue circle and the arc shows the psi angle

VI.13. Identification and Localization of Dipoles for Magnetoencephalography

Magnetoencephalography (MEG) is a technique for non-invasive functional imaging of the brain using Superconducting Quantum Interference Devices (SQUIDs). In MEG, the neural current sources have to be determined based on the magnetic field distribution measured outside the brain. To obtain an approximate solution to this inverse problem, the brain is typically modeled as a set of concentric spheres and the neural currents that cause the magnetic field are represented as current dipoles which are either rotating or stationary. The identification of the locations of dipoles and their temporal characteristics (rotating and non-rotating) in the presence of noise has been done using the Multiple Signal Classification (MUSIC) approach. With the

development of SQUID sensors at IGCAR and setting up of MEG facility, these results will be of practical importance for the analysis of MEG signals.

The radial component of the magnetic field b_r produced outside the skull at $\vec{r}'(x_n', y_n', z_n')$ by a set of equivalent current dipoles of strength q_i 's situated inside the cortex at $\vec{r}(x_i, y_i, z_i)$ can be written as a product of a gain matrix M and the column vector Q representing their strength (Fig.1).

$$b_r(x_n', y_n', z_n') = M(x_i, y_i, z_i, x_n', y_n', z_n') \cdot Q$$

For four dipoles, 118 measurement locations and 100 time slices, b_r is a 118x100 matrix, M is a 118x12 matrix and Q is a 12x100 matrix. To simulate a

realistic measurement, we add to b_r a Gaussian noise term with mean zero and variance 10% of the maximum magnetic field due to the source to obtain the noisy data matrix b_{rn} .

An approximate solution to the problem of deducing the locations and the strengths of the equivalent current dipoles can be obtained by minimizing the residual error between the simulated magnetic field b_{rn} and the calculated field. If b_{rn} is decomposed into $[U\Sigma V^T]$ by singular value decomposition (SVD) and is seen to have a rank r , then the noise subspace can be approximated by $U_{m-r}U_{m-r}^T$ (U_{m-r} is the matrix containing of $m-r$ columns at the extreme right of the decomposed matrix U). To find the dipole locations by MUSIC approach, G_i , the single dipole

Table 1 : Results of inversion calculation for four dipoles with 10% noise.

	Non-rotating dipoles						Rotating Dipoles					
	First Dipole			Second Dipole			Third Dipole			Fourth Dipole		
	X	Y	Z	X	Y	Z	X	Y	Z	X	Y	Z
Actual (cm)	-3.75	-2.03	8.26	-2.02	3.71	8.28	3.43	2.59	8.25	3.50	-2.54	8.23
Calculated (cm)	-3.6	-1.9	8.3	-2.0	3.7	8.3	3.3	2.5	8.3	3.5	-2.4	8.3
Deviation	0.15	0.13	0.04	0.02	0.01	0.02	0.13	0.09	0.05	0.0	0.14	0.07

gain vector is decomposed into $[U_i \Sigma_i V_i^T]$ and the matrix comprising of first three column vectors of U_i is represented as

U_{iq} which is the signal subspace. In MUSIC, the anti-correlation cost function matrix J is the product of signal

subspace and noise subspace.

To identify the positions of the dipoles, the minimum eigenvalue of the cost function. $J_{ls} = \lambda_{\min} (U_{iq}^T U_{m-r} U_{m-r}^T U_{iq})$ Matrix J is evaluated in the region of interest and peaks in the inverse of this function J_{ls} are identified to indicate the position of the dipoles, thus avoiding any apriori assumption of number of dipoles. If the dipole is rotating then all the eigenvalues of the cost function matrix J are zero which imply that trace of J is zero. Thus identification of rotating and non rotating dipoles can be done just by evaluation of J alone.

Results of numerical simulations

Human head is modeled as a sphere of radius 12 cm with the cortex as a shell having a radius 8 cm and thickness 2 cm (Fig 1). Four current dipoles are positioned within the cortex in the upper hemisphere. The strengths of first two dipoles are assumed to evolve in time with the functional dependence of the form $t \cdot \exp(\gamma - t)$ with different time constants γ . The other two dipoles are assumed to rotate with different frequencies. The magnetic field due to these four dipoles were calculated at 118 measurement locations on the surface of a concentric upper

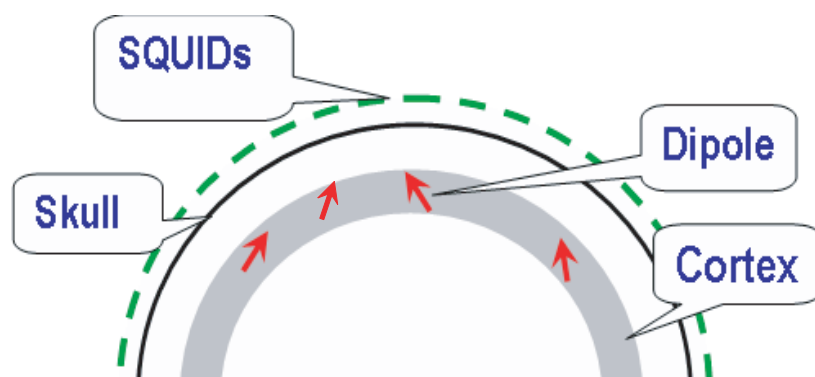


Fig.1 Spherical model of head with cortex as an annular shell. The magnetic field is measured on the surface of a concentric hemisphere using SQUID sensor.

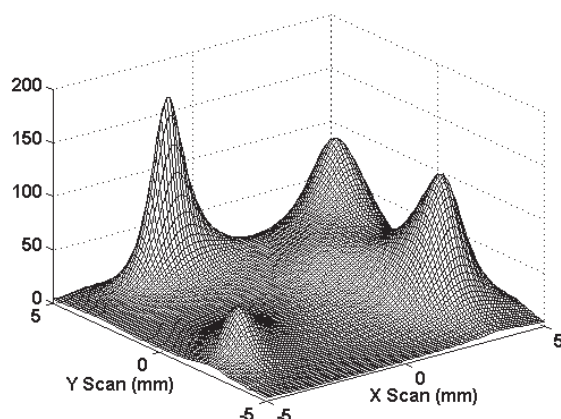


Fig.2 Inverse of cost function (J_{ls}) plot w.r.t the scan coordinates showing the presence of all the four dipoles both rotating and non-rotating and their locations

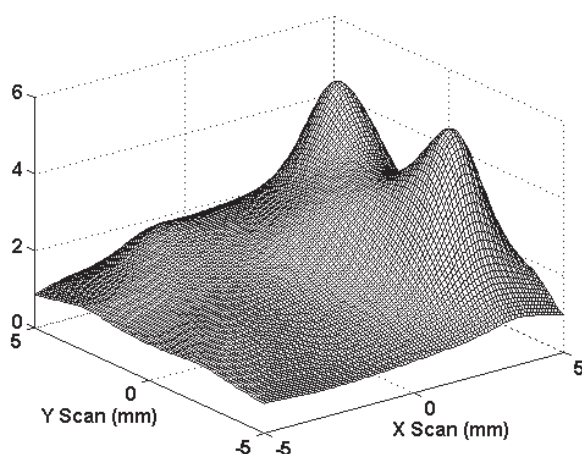


Fig.3 Inverse of trace of the cost function matrix J w.r.t scan coordinates showing presence of only two rotating dipoles and their respective locations

hemisphere of radius 13 cm in 100 time slices. 10% Gaussian noise with mean zero is added to the computed data to obtain the b_m matrix. By using the MUSIC approach described above locations of all the dipoles are identified as shown

in Fig.2. with characteristic rotating dipoles being identified after plotting the inverse of trace of the cost function matrix J as shown in Fig.3. It is seen from the results presented in Table -1 that the locations of the dipoles identified by this

inversion algorithm are accurate to within 2 mm within the cortex even in the presence of 10% noise.

VI.14. A Novel Technique to Irradiate Blood Cells in vitro with Alpha Radiation for Cytogenetic Analysis

The need for determining a reliable Radiobiological Effectiveness (RBE) value for alpha exposures has become important as reported literature values vary widely. Moreover, increasing nuclear reprocessing facilities the world-over calls for measures to estimate alpha radiation doses during a criticality accident such as the one that occurred at Tokaimura, Japan, in 1999. In order to construct dose-response curves and calculate RBE factors for risk estimation

required for purposes of radiation protection, human blood cells need to be irradiated in vitro. However, unlike gamma radiation, due to the low penetrating power of alpha rays, it has always been a challenge for radiation biologists to handle alpha sources. A simple technique to irradiate human blood lymphocytes *in vitro* using radon gas emanating from a solid radium source has been designed and developed. The difficulties in delivering and

estimating exact activity concentrations have been handled in a unique and safe way. Such a method was used to score chromosome aberrations induced by radon and progeny.

Radon exposure

The radon source used in the present study was procured from Pylon (Canada). The assembly used for irradiation is shown in Fig 1. Activity was determined using a custom designed Lucas cell (Fig.2).

The radon concentration and doses were calculated using the equations:

$$\text{Activity (Bq/m}^3\text{)} = 0.06967 \times \frac{\text{NC}}{\text{Eff} \times 0.14} e^{(-0.00012584 \times \text{DT})} \times 1 - e^{(-0.00012584 \times \text{CT})}$$

Metaphases prepared by standard culturing methods were captured using a Metaphase finder (Metasystems, Zeiss) available at RSD. (Fig.3).

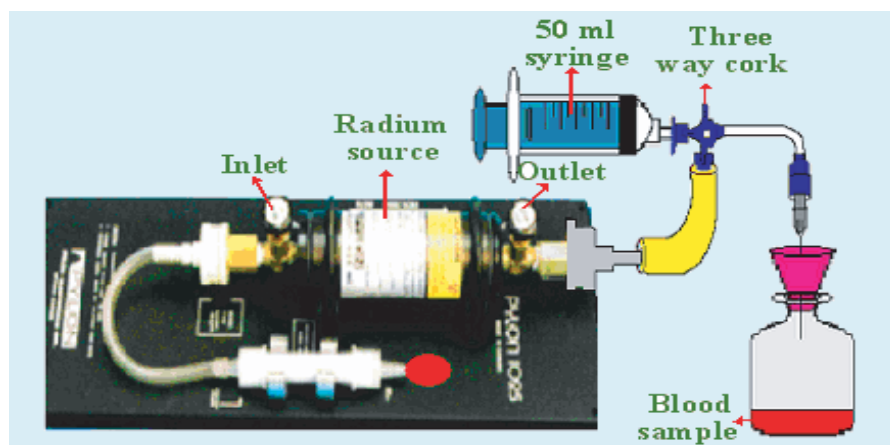
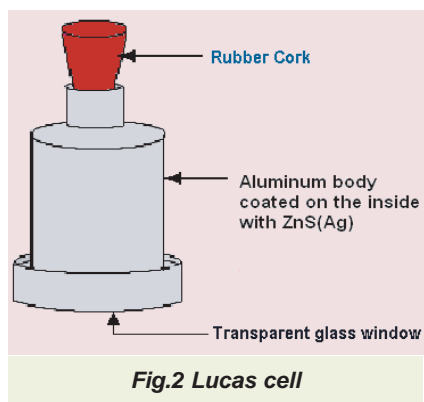


Fig.1 Blood irradiation using the radon source

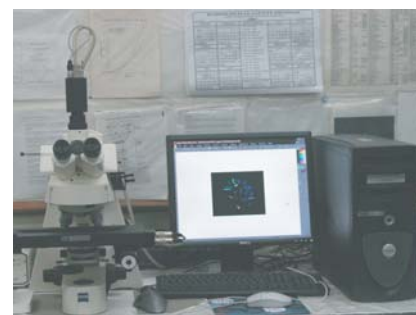
Highlights of the new technique

The new technique designed to irradiate blood, medium and other cells has features such as: (a) portable alpha irradiation



facility, unlike those designed earlier, (b) safe to handle as it does not involve liquid alpha source, (c) can be easily set up and dismantled, (d) samples can be irradiated under sterile conditions and (e) the irradiation procedure gives a 4π geometry making it easier to apply Marinelli formula for dose calculations.

The irradiation facility also serves as an excellent *in vitro* method to characterize the



DNA damaging effects of radon and its progeny, which is known to be a major cause of lung cancer among miners and people living in areas with high natural background radiation.

VI.15. Vaporization Study of Ru-Te Binary System by Knudsen Effusion Mass Spectrometry

Continuing the high temperature chemistry research on systems involving the fission product tellurium and the SS clad components or other fission products, a vaporization thermodynamic study of the Ru-Te binary system has been conducted at IGCAR by using Knudsen effusion mass spectrometry. The only condensed phase known to exist in this system is RuTe_2 and no report of mass spectrometric investigation exists for this system. Four samples were employed for this study, two having compositions 40.0 and 50.5 at.% Te and corresponding to the two-phase field ($\text{Ru} + \text{RuTe}_2$) and the other

two having compositions 69.5 and 71.5 at. %Te and corresponding to the two-phase field ($\text{RuTe}_2 + \text{Te}$).

The experiments can be broadly classified into three series: 1) many runs of temperature dependence measurements on ($\text{Ru} + \text{RuTe}_2$) two-phase field samples (860-1030 K), interposed between pressure calibration measurements on elemental tellurium and occasionally on silver; 2) continuous measurements on ($\text{RuTe}_2 + \text{Te}$) two-phase field samples at various isothermal sections as the shift in the composition (towards Ru-rich values) and

consequently the phase fields, too, were occurring; and 3) temperature dependence measurements on the end products of series-2 experiments - to examine or rather confirm whether the results are in accord with results of series-1 experiments. Te_2 (g) being the sole identifiable vapor species, measurements in all three series were performed for most part on the ionic species Te_2^+ , and sometimes on the fragmentation product Te^+ also. Fig.1 shows the results of a temperature dependence run (series-1) for Te^+ and Te_2^+ at an electron impact energy of ~ 30 eV. Fig. 2 shows the results of a homogeneity range experiment

(series-2). A temperature cycle imposed on the sample after it exited the RuTe_2 single phase region revealed that $I(\text{Te}_2^+)$ at 980 K was consistent in both decreasing and increasing temperature directions.

The results of series-1 experiments yielded a $p(\text{Te}_2)$ - T relation for $\text{Te}_2(\text{g})$ and $\Delta_r H_m^\circ(T)$ for the incongruent vaporization reaction: $\text{RuTe}_2(\text{s}) = \text{Ru}(\text{s}) + \text{Te}_2(\text{g})$. The series-2 experiments, mainly performed to be able to determine the Te- and Ru-rich boundary compositions of RuTe_2 phase, gave somewhat disconcerting results, the Te-rich boundary values showing some dependence on the starting composition or the amount. The Ru-rich boundary values are relatively consistent (i.e. within the uncertainties associated with such experiments) and close to stoichiometric value, which we assumed while evaluating the series-1 data. It is now proposed to conduct a few more experiments on at least two newer compositions (one, only slightly Te-rich relative to the hitherto reported Te-rich boundary composition, and the other 73.5 at.% Te) to examine the reason for dependence of Te-rich boundary values on the starting composition.

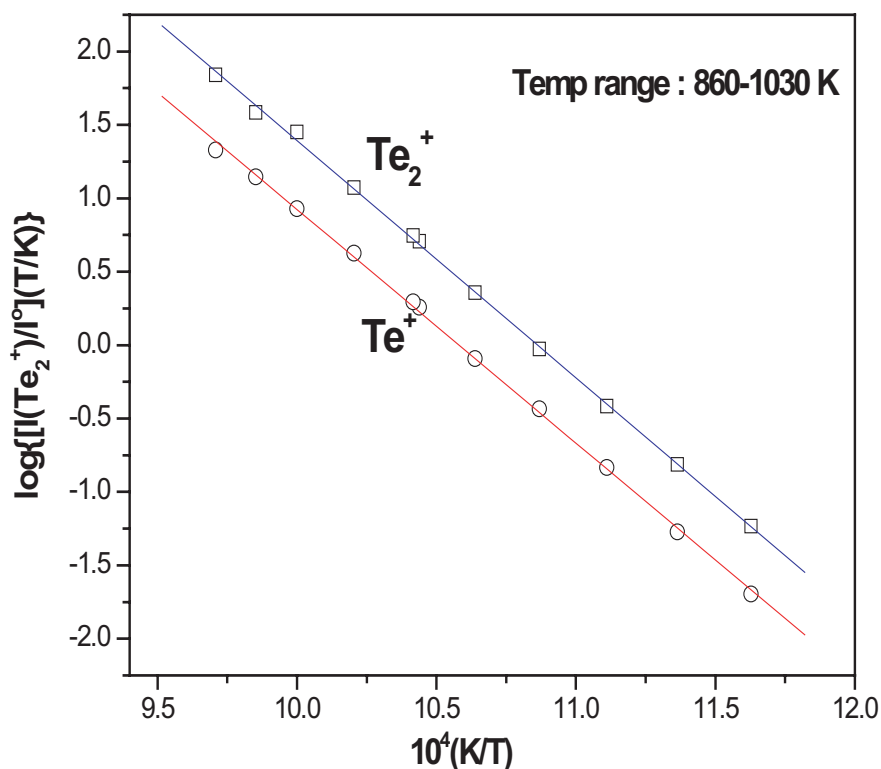


Fig.1 Temperature dependence of ion intensities of Te^+ and Te_2^+ at $\sim 30_{\text{eV}}$

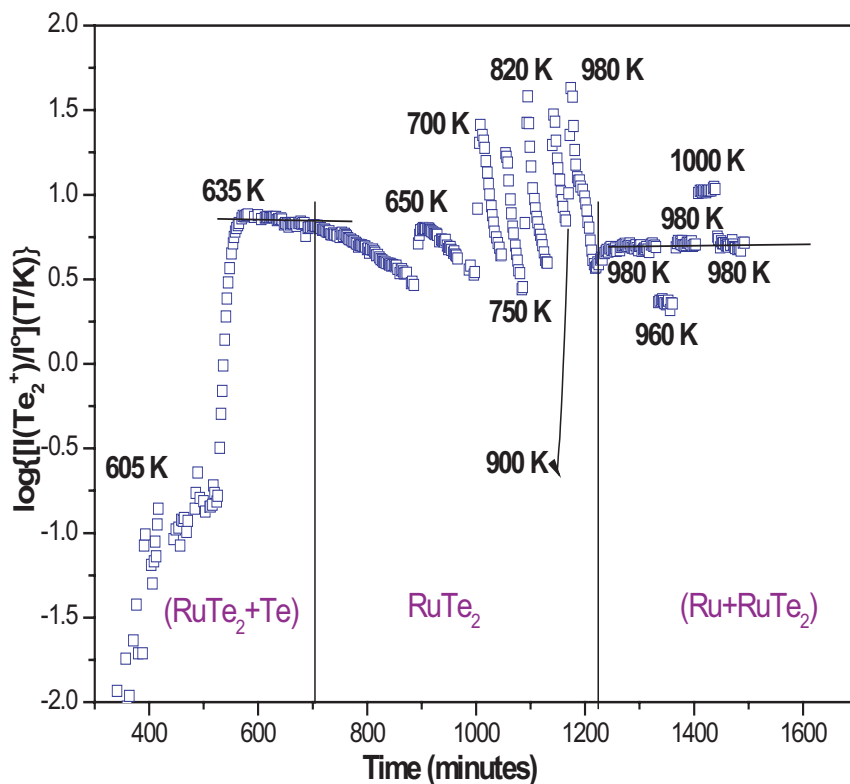


Fig.2 variation of $1/(\text{Te}_2^+)$ as a function of time at different temperatures; composition of the sample 69.5 at.% Te

Chapter -7

INFRASTRUCTURE FACILITIES

VII.1 . Fabrication of Beam Chamber and Cryostat Vacuum Plumbing Lines for VECC, Kolkata

Three numbers of Beam chamber plumbing lines and one number of Cryostat vacuum plumbing line (Fig.1) were fabricated meticulously for VECC, Kolkata, for the large super conducting cyclotron facility K500, which is planned to provide accelerated particle energies for frontline experiments at par with their international counterparts to our nuclear physicists.

These Beam chamber and Vacuum plumbing lines are designed to connect with Turbo pump & Pumping modules to operate in the pressures $< 1 \times 10^{-6}$ mbar and 5.0×10^{-8} mbar respectively.

Each plumbing line consists of 12 components made of SS316 material, The Overall size of the assembly is 2232 x 1155 mm. The critical requirement is leak tightness of the assemblies in the order of 1×10^{-10} mbar * l /s and 100 % radiography on all welds.

To achieve this task, meticulous process planning, selection of the optimum parameters for machining the components precisely in different machines to meet the stringent dimensional tolerances were selected.



Fig.1 Beam chamber and cryostat vacuum plumbing lines

Unique layout was prepared for each assembly, stage inspection , fit up of components, assembly and welding by GTAW process was used to minimize distortion. All the weld joints were subjected

to Liquid Penetrant Inspection, 100% Radiography and Final Assembly was subjected to Helium leak test to 1×10^{-10} mbar * l /s and found satisfactory.

VII.2. Machining of Iron Thimbles for Fabrication of Electrochemical Carbon Meters

Thirty numbers of Amco Iron thimbles were machined precisely for fabrication of electro chemical carbon meters (Fig.1). The thimbles are made up of soft Armco Iron material of size OD 19mm, ID 16mm and 90mm length. The critical dimension of 0.5mm wall thickness was standardized for rapid diffusion of carbon through iron thimbles. Mock-ups were carried out to establish process sequence and machining parameters to achieve the critical requirement of 0.5 mm uniform wall thickness, close dimensional,



Fig.1 Machined iron thimbles

geometrical tolerances and surface finish. The critical machining of ID $16 \text{ mm} \pm 0.01 \text{ mm}$ was achieved by progressive machining using drilling, hole mill cutter and boring tool. A mandrel was designed to suit ID and used to

machine the OD of soft iron thimble to achieve 0.5 mm uniform wall thickness and to prevent possible damage during machining and achieved the dimensions within the tolerance of 0.01 mm.

VII.3. Manufacture of In-core Neutron Detector Assembly for PFBR

PFBR in-core neutron detector assembly (Fig.1) was precisely manufactured meeting the stringent specifications for testing High Temperature Fission Chambers (HTFC) and neutronic channels of PFBR and to compare the results with the output from FBTR neutronic channels to assess its performance characteristics.

This test set up consists of two major sub assemblies, namely inner rod assembly and outer sheath assembly comprising 22 numbers of precisely machined components made of AISI 316 material. The overall length and diameter of assembly are 5950.0 mm and 101.0 mm respectively. Manufacturing of this assembly requires precision machining of components to comply with the stringent dimensional, geometrical tolerances, surface finish and also the best methodology to assemble the machined components. Machining of outer sheath of length 5950.0 mm and OD 101.0 mm was a critical job due to its slenderness, very low wall thickness and bends in the raw material 100NB Sch.80 SS316 pipe. Before machining, the pipe was straightened using a

specially designed set up and hydraulic press. To machine the slender pipe in lathe machine, considering the low wall thickness and length, the machining parameters were optimized and the machining carried out in six steps to prevent buckling, puncturing and possible damage during machining. Ultrasonic thickness gauge was used in-situ to measure the uniform thickness along the length of pipe.

Machining of shielding shell top of dia 85mm and length 1821 mm with 7mm O-ring groove on the circumference at 3 places were critical feature of machining and it was successfully machined and achieved the dimensions with in the tolerance of 0.01mm. The assembly was carried out in nuclear clean hall. Segmental and sequential GTA welding techniques with controlled heat input was adopted for all the weld joints to minimize distortion and achieved the concentricity of 0.50mm for inner rod assembly and 1.22 mm for Outer sheath assembly. All the components were inspected at stages and at the final stage. Weld joints were subjected to liquid penetrant

inspection and 100% radiography inspection. Helium leak test was conducted and achieved the overall leak rate of 10^{-10} std.atm-cc/sec against the design requirement of 10^{-7} std.atm-cc/sec.



Fig.1 Neutron detector holder assembly

VII.4. Revamping and Upgradation of Cooling Towers

Central Water Chilling Plant (CWCP) is responsible for air conditioning and ventilation of various laboratories of IGCAR. The CWCP operates continuously in round the clock shifts to ensure uninterrupted and reliable chilled water supply for air conditioning of various labs and buildings at IGCAR. The CWCP comprises of six no. centrifugal chillers and allied accessories like condenser water pump, chilled water pump, cooling towers etc. There are two cooling towers of eight cells each at CWCP, IGCAR to cool the condenser water of centrifugal chillers. The performance of cooling towers had deteriorated resulting in frequent maintenance and high energy consumption. It has been observed that during summer all the 16 cells are put into service to remove the heat load of just three chillers and to maintain the condenser water inlet temperature within permissible limit of 305 K. The performance of the cooling towers was evaluated and it was found that the effectiveness of the cooling tower is below 40%. Poor performance of the cooling towers has resulted in

Table1 : Cooling tower specification

Description	Specification	
	Old	Revamped
Type	Induced draft cross flow	Induced draft cross flow
Flow of water	600 USGPM/cell	700 USGPM/cell
Rated Capacity	187.5 TR per cell	240 TR per cell
Inlet water temperature	310 K	310 K
Outlet water temperature	305 K	305 K
Design wet bulb temperature	301.3 K	301.3 K
Range	5 K at 301.3 K	5 K at 301.3 K
Fan assembly	72 inches, H 3-6	72 inches, H 3-8
Fill/Splash bar	Wood	PVC perforated C-bar
End wall casing and louvers	Asbestos	FRP

high condenser water inlet temperature, which eventually caused surging in the chillers and high-energy consumption. Also, the wooden fills and structures got aged resulting in frequent maintenance. Hence, it was decided to upgrade and revamp the cooling towers as per the following specification in Table 1.

After revamping it was found that 10-12 cells are sufficient to

run 3-4 chillers and the current taken by each fan is 13 A (8 kW) against 16 A (9.8 kW) resulting in substantial savings in energy.

VII.5. Variable Refrigerant Flow Air-conditioning System

Variable Refrigerant Flow (VRF) air-conditioning system has been introduced for the first time in IGCAR at Boron Enrichment Plant and HASL. The capacity of the systems is 26TR in each building (Fig.1).

The VRF AC systems are the next generation in intelligent and energy efficient air-conditioning. A VRF system typically consists of an outdoor unit (Fig.1) with multiple compressors and different types of indoor units for different zones or areas (Fig.2). It also comes with a highly sophisticated electronic control centre to enable zone wise climatic control. The VRF systems offer a wide range of indoor units wall mounted

splits, ceiling mounted splits, ductable units, cassettes, concealed units, etc. The VRF systems offer immense benefits such as optimal control of

individual spaces, energy efficiency, compatibility with Building Management System (BMS) compatibility, and ample choice and flexibility in designing the air-conditioning system to suit space and interiors. The VRF systems can operate at ambient temperature as high as 325 K



Fig.1 12.8 TR (16 HP) Outdoor unit



Fig.2 Typical indoor units - Ceiling & Wall mounted

VII.6. Unique Experience in Installing, Testing and Commissioning Aerial Bunched Cables

The power supply to Anupuram Township is being fed from Central Switching Station and the present peak load demand is about 1 MVA. It is proposed to have further house construction at Anupuram cater to the requirement of BARCF, BHAVINI and IGCAR. The load growth

during 11th and 12th plan is expected to be about 3 MVA. There are two independent 11 kV feeders to Anupuram, which feeds the total power requirement of Anupuram Township. At a time only one of the feeders will be in service and the other feeder will be kept in hot standby mode. Prior



Fig.1 Cross section of the ABC cable



Fig.2 ABC cable suspended from spun pole

to 1990 both the feeders were of Overhead line (OH). One of the feeders was changed from OH line to Under Ground (UG) cable in 1995 except the region in which it crosses the Buckingham canal. The other feeder remained as OH line till 2005. The main problem faced with the OH line is the frequent tripping during cyclonic and rainy season either due to flash over or mechanical damage to the insulators. The mechanical breakdown of the porcelain insulators also contributed to the trips. In order to improve the reliability of power supply to Anupuram, it was decided to convert the existing OH line to UG Cable including the partial OH line in the other feeder.

It was not possible to convert the entire stretch of the OH line to UG cable due to site constraints especially cross over across the Buckingham canal. The existing state government rule restricts the use of UG cable across the BC. They

specify that the minimum clearance between the conductor/cable and water surface during high tide should not be less than 6 meters. As the possibility of widening and deepening of the canal is not ruled out, it is not advisable to provide UG cable. Since the UG cable is not designed to take self weight and wind load, the usage of Aerial Bunched Cables (ABC) was only option for the application.

ABC is a very novel concept for over head, power distribution. Compared to conventional OH line, ABC provides higher safety and reliability, lower power losses and ultimate system economy by reducing installation, maintenance and operational cost. ABC is the best choice for power distribution in congested urban areas with narrow lanes and by lanes. It is also used in terrains and bushy area where excavation is difficult. There are three or four cores for the cable and the cores are bunched around a bare messenger conductor. The messenger conductor provides the mechanical strength and takes care of the wind load. The typical cross section of the conductor including the method of suspension is shown in the Fig.1. The resistivity of the messenger conductor also shall

be very low so as to provide low resistance path for the current flow during unbalanced loading and during fault conditions.

After the choice of ABC is finalized, interaction with the manufacturers was pursued and a detailed specification and estimation was prepared. The usage of the ABC cable was limited for a size 70 sq. mm cable. Since we are planning to design the system for a peak load of 5 MVA by considering the future growth, the minimum conductor size needed is 185 sq. mm. An estimate showed that the cost of using ABC cable is very high compared to UG cable for the entire length. Based on further review, it was decided to use ABC cable for a stretch of 500 m across the canal and for about 300 m in the village where it is not possible to lay UG cable (Typical Cross section of the ABC cable is shown in Fig.1).

Design of ABC cable and pole supports

By considering the load growth, the minimum conductor size was fixed as 185 sq. mm. The messenger size depends on the maximum span length and the sag permissible for the above span. The span length is 70 m and

the permissible sag is 6 m above the water surface. By considering a wind velocity of 150 km/h and a safety factor of 2 the messenger size is fixed as 150 Sq. mm. Each core of the cable is constructed similar to an XLPE cable and is screened with thin copper flat and having extruded outer sheath. The outer sheath along with the black tape protects the cable against UV radiation while exposed to sunlight.

Special type suspension clamps and end clamps required to support it from the poles are available in India. Reinforced Cement Concrete

(RCC) poles are being used for suspending transmission lines and its designed load is only up to 500 kg. Due to its limited load bearing capacity, the usage of RCC pole is not found to be feasible. Further enquiry resulted in the selection of Spun poles for this special application. These poles are manufactured by a special process and the load bearing capacity is up to 1000 kg. The poles were load tested at factory site and found suitable for our application. In order to improve the safety margin extra stay sets were provided (the Fig.2 shows the details of ABC Suspension from Spun pole).

Supply, installation testing and commissioning of the cable

The cable was manufactured by M/s Torrent cables according to our specification and was tested at factory to ensure that it meets the required specifications. The spun poles were manufactured by M/s CPC & Co, Madras and were erected at site by means of special tackles and tools. The ABC cable was joined with UG cable using special straight through joints. The entire system is commissioned and is in service for more than six months.

VII.7. Biometric Attendance Recording System

A Biometric Attendance Recording system consisting of 37 RFID (Radio Frequency IDentification) cum hand geometry readers located at various buildings of IGCAR and 2 servers, all connected over the campus back bone network was installed and commissioned dispensing with the old manual system of registers & punching machines. The main advantages of the new system are accurate attendance logging for the complete spectrum of employees, elimination of proxy

punching and finally security. RFID cards issued to the employees store employee's

ICNo., Name, Division, Section, reference hand template along with two 48 bit

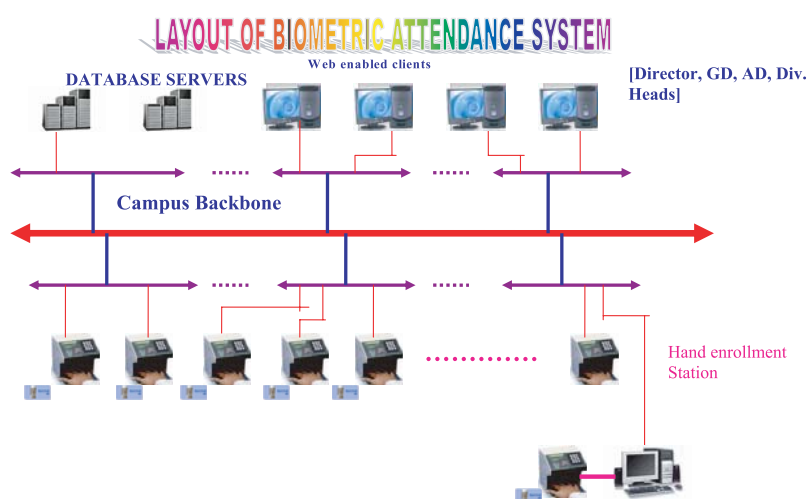


Fig.1 Architecture of biometric recording system



Fig.2 Employee registering attendance through biometric system

secure keys. These two keys ensure the security of data stored in the card and make the card tamper proof. The system architecture is shown in Fig.1.

The servers acquire transaction data from all the 37 readers and store them in the ORACLE database. The server also contains a web server which can be accessed via the standard web browser of

individual PCs connected on the IGCAR intranet. The web server provides various reports related to the entire centre or a particular section / Division / Group depending the official accessing the reports. Thus all the senior officials are provided with Username and a password for monitoring the attendance of staff reporting to them. Apart from this, all the employees also can access their individual

reports by means of employee login facility.

Readers are having the facility to store 10,000 transactions even in the case of failure of communication for a long time. Also all the readers are provided with redundant power supply (battery which can operate for a period of 8 hours incase failure of mains supply) and the servers are provided with UPS which shall provide backup for a period of 4 hours incase of power failure. All the RFID cum biometric reader's clocks are updated by the server every 10 seconds, thus the time stamping of all the transactions from the readers shall have the same Real Time Clock (RTC). Figure 2 shows an employee registering attendance using new biometric system.

VII.8. Monitoring of Coastal Waters: Occurrence of *Trichodesmium erythraeum* (Ehr.) Bloom in the Coastal Waters of Kalpakkam

Trichodesmium erythraeum, a marine cyanobacterium, is an important nitrogen-fixer in the sea. It is one of the common bloom-forming species found in tropical and sub-tropical waters, particularly in the eastern tropical Pacific and

Arabian Sea, contributing > 30% of the algal blooms. Estimated global nitrogen fixation by *Trichodesmium* bloom (~ 42 Tg N yr⁻¹) and during nonbloom conditions (~ 20 Tg N yr⁻¹) suggests that it is likely to be the dominant

organism in the global ocean nitrogen budget. In the east coast of India, phytoplankton blooms are common during February to May when the prevailing hydrobiological conditions are relatively stable. During this period, due to the



Fig. 1 Yellowish-green streaks of trichodesmium observed in the coastal waters of Kalpakkam

western Bay of Bengal current (WBC) a phenomenon called upwelling occurs bringing highly nutrient enriched bottom water to the surface and thus found to enhance phytoplankton growth. During a regular coastal water monitoring program, a prominent discolouration of the surface water was noticed in the coastal waters of Kalpakkam on 16th March 2007. The bloom was very dense and created yellowish-green coloured streaks (Fig.1) of about 5 m width and extended to a few hundred metres. The phytoplankton responsible for discolouration was identified as *Trichodesmium erythraeum* (Fig.2). Although, bloom of *Noctiluca scintillans* and *Asterionella glacialis* has been reported in the coastal waters of the Kalpakkam, there has been no report of 'green tide' formation by *Trichodesmium erythraeum*. One of the interesting features of this

bloom was that it was sighted only for one day and drastically declined on the next day with negligible *Trichodesmium* cell density. Such a sudden appearance and decline in bloom forming organisms in general and *Trichodesmium* in particular is very peculiar and interesting. The three different phases of a typical phytoplankton bloom such as, the exponential phase (log phase), peak & senescent phase (lag phase) could not be seen during this observation as usually observed for any bloom. Its appearance if continued for a relatively longer period, could have significantly affected not only the

commercially important marine species but also the lives of people who consume fishes. As this species has been identified as toxic and reported to contain neurotoxin commonly associated with paralytic shellfish poisoning. Interestingly, the bloom was sighted just after the southwest to northeast monsoon transition during which the current direction changes from equator-ward to pole-ward in Bay of Bengal. Close monitoring of the coastal waters during this period with respect to chemical and biological characteristics revealed significant changes in its quality. An abrupt increase in ammonia and phosphate content was noticed on the day of bloom. Phosphate values reached a maximum of $2.56 \mu\text{mol l}^{-1}$ with the peak coinciding with the day of highest cell density. This appears to be about 10 times higher than the normal phosphate values encountered

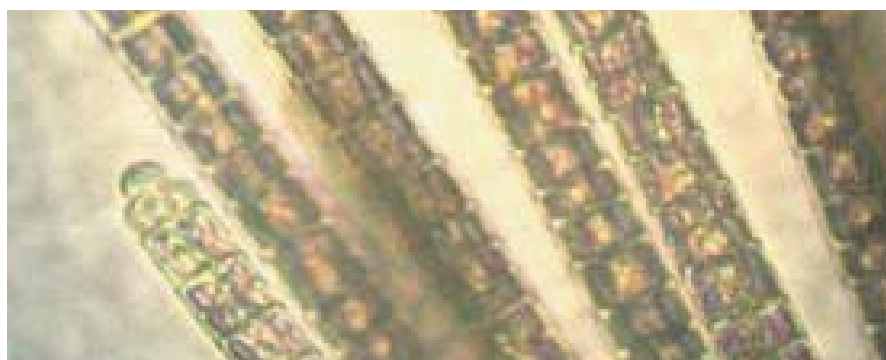


Fig.2 A bunch of trichodesmium erythraeum diatoms

in the coastal waters. Concentration of ammonia was unexpectedly high ($126.72 \mu\text{mol l}^{-1}$) on the day of bloom, which could be ascribed to the diazotrophic nature of *Trichodesmium*, which depicts

its ability to produce ammonia from dinitrogen through the process of nitrogen fixation. This level of ammonia if sustained for a longer period could seriously affect the fish population. Therefore it is

imperative to monitor coastal waters at a regular and close frequency to observe any subtle change in its physico-chemical and biological characteristics due to such natural events as above.

VII.9. Development of Medicinal Plants at IGCAR

Herbal remedies have become increasingly popular as more and more people are health conscious and seek natural and safer products. This statement holds greater significance when it comes to a society dedicated to science and technology. In our fast track life searching for new horizons and venues of nuclear energy; keeping in mind the prime health of our community cultivation of medicinal herbs have been initiated in the IGCAR project site.

With the natural green habitats shrinking day-by-day it is most appropriate that cultivation and conservation of medicinal plants for the benefit of human beings has been thought of at this site.

India is bestowed with a treasure of medicinal plants. The Indian system of medicine has identified around 15000 medicinal plants of which 500 species are commonly used in the preparation of medicinal drugs.

Scoparia Dulsis (Fig.1)	2 or 3 leaves consumed daily in the morning hours will control diabetes.
Asparagus Racemosus (Fig.2)	The root of the plant is useful for controlling urinary problems
Andragraphis Paniculata (Fig.3)	Consuming the leaves of this plant will decrease the affect of the poison due to snake bite
Talinam Trangularare (Fig.4)	These leaves when cooked and consumed along with our food remove blood clot.
Centella Sessibis	The powder of the dried leaves when consumed, after mixing it with water increases the memory power and reduces ulcer.
Bacopa Monnieri	The powder of the dried leaves when consumed, after mixing it with water increases the memory power. Also relieves stress.
Gymnema Sylvestre	Diabetes can be controlled when the powder of these dried leaves are mixed with water and consumed before taking food.
Ormocarpum Spennoides	The leaves of these plants have to be grinded. The resulting paste when applied over the fractured area heals the fracture over some period of time. Also increases the blood circulation in the affected area.
Casia Auriculata	The powder of the dried leaves when mixed with medium hot water and consumed, helps in curing heart ailments. Also keeps the body cool.
Orthosiphon Spiralis	The powder of the dried leaves when consumed, after mixing it with water removes kidney blockage.
Solanum Trilobatum	These leaves when cooked and consumed along with our food reduce cough and fever.



**Fig.1 Scoparia Dulsis
(curing diabetes)**



**Fig.2 Asparagus Racemosus
(for urinary problem)**



**Fig.3 Andragraphics Paniculata
(snake bite)**



**Fig.4 Talinum Triangularare (remote
blood clot)**

Nearly 7000 medicinal plants are being used in Ayurveda medicines, 700 in Unani medicine, 600 in Sidha medicine, 450 in homeopathy and 30 in modern medicines.

Some of the important herbal plants in the project site and its uses have been described below.

The idea of cultivating mainly is to create awareness not only among the scientists, personnel but also among the children in the vicinity. Plants mentioned above are cultivated as part of Phase-I program which is already completed. A separate area of 8000sqm is identified for the purpose of medicinal garden consisting of varieties

of herbal plants. Besides medicinal drugs, these plants are also used in various industries for producing other herbal products.

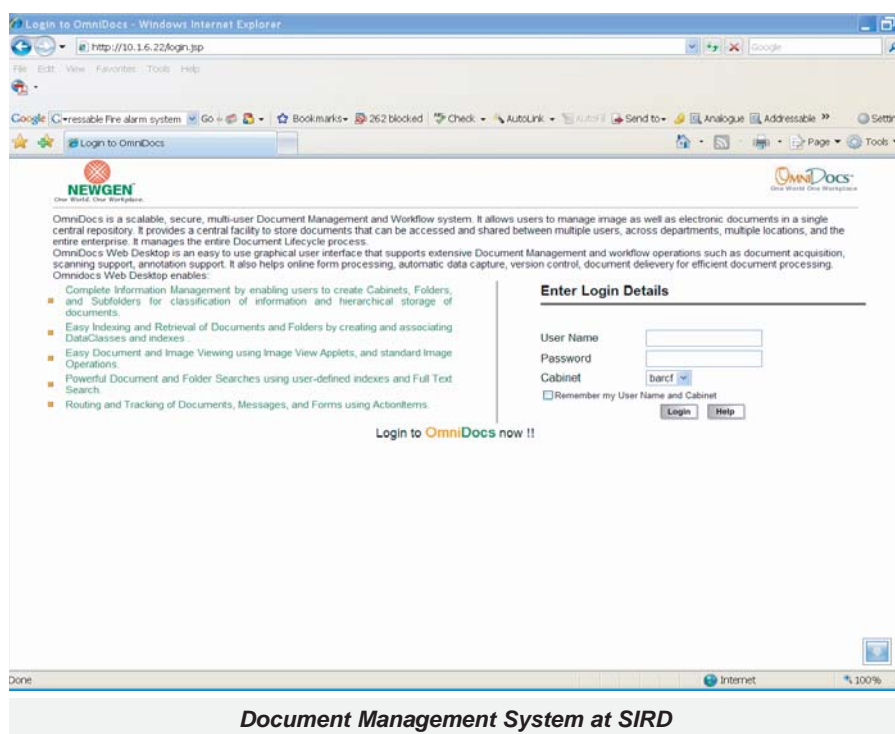
VII.10. Library Document Management System

During the 10th plan period, Scientific Information Resource Division (SIRD) has procured around 4500 reports and digitized more than 5500 documents on Fast Reactor Technology.

Digitization and subsequent management documents need a specified software system which can manage and provide access to the relevant documents to multiple users. OmniDocs is a scalable, secure, multi-user Document Management and Workflow

system. It allows users to manage image as well as electronic documents in a single central repository. It provides a central facility to store documents that can be accessed and shared between multiple users, across departments, multiple locations, and the entire enterprise. It manages the entire Document Lifecycle process.

SIRD has made the document management systems web accessible with graphical user interface that supports extensive Document Management and workflow operations such as document acquisition, scanning support, and annotation support. It also helps online form processing, automatic data capture, version control, and document delivery for efficient document processing.



AWARDS & HONOURS

Dr. Anish Kumar, Metallurgy & Materials Group has been selected for the prestigious **INSA Young Scientist Award** for the year 2007

Dr. Baldev Raj has been honored with the prestigious **Padmashri Award** by Government of India. He has received the **Meritorious Contribution Award** for 2006 from NACE International India Section. He has been awarded the prestigious the **National Metallurgist Award-2007 (Research-Academy)** by Ministry of Steel, Govt. of India and Indian Institute of Metals. He has been awarded the prestigious **Life Time Achievement Award** of Indian Institute of Welding. He has also received **Stanley Ehrlich Gold Medal** during the National Symposium on Acoustics (NSA-2007),

Dr. P. Chellapandi, Reactor Engineering Group has been awarded **"Mechanical Engineering Design Award - 2006"** by The Institution of Engineers, India.

Shri. S.C. Chetal, Reactor Engineering Group has been conferred **National Design Award** by The Institution of Engineers, India.

Shri. Chittaranjan Das, Metallurgy & Materials Group has been selected for the **ASM young metallurgist award**, Chennai chapter

Dr. U. Kamachi Mudali, Corrosion Science & Technology Division has been elected as a **Fellow of the Indian Institute of Metals for 2006**.

Dr. C.K.Mukhopadhyay, Non-Destructive Examination Division has been selected to receive the **ISNT National NDT Award** under the category excellence in contribution to research & development, jointly sponsored by ISNT & M/s. Electronic & Engineering Co., Mumbai, for the year 2007.

Shri. R. Natarajan, Reprocessing Group has been awarded **INS - Award - 2006** by Indian Nuclear Society.

Dr. S. Ningshen has been awarded the **NACE International India Section (NIIS) Best Ph.D award** in the field of Corrosion Science for the Year 2007.

Mrs. B. Sasi, Non-destructive Evaluation Division has been awarded **R.Chandrasekhar Memorial Prize** for Best Industry-oriented research work during National Seminar on Physics & Technology of Sensors (NSPTS-12) held during March 2007 at Mumbai.

Shri. Sumantra Mandal from Materials Development and Characterisation Group has been selected for **INAE Young Engineer Award** for the year 2007.

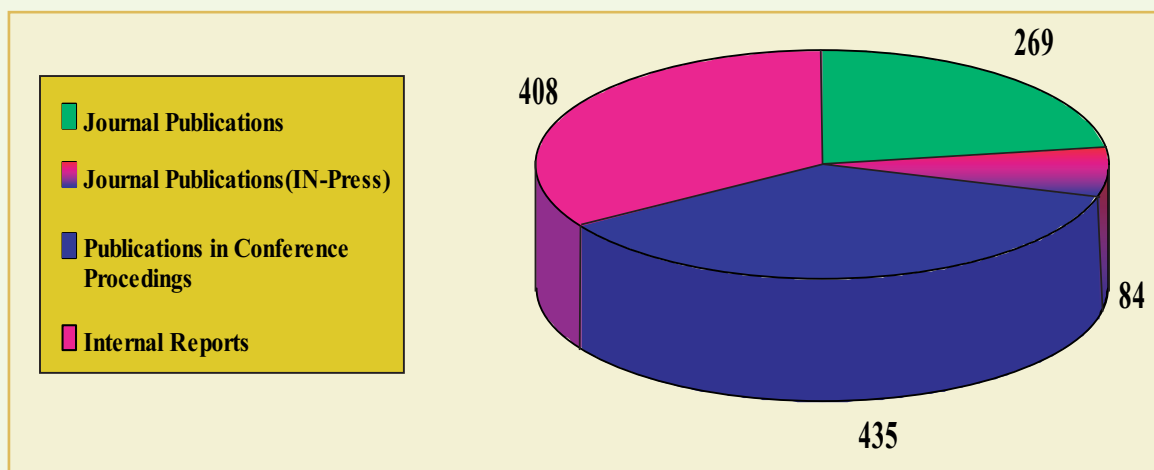
Dr. A. K. Tyagi, Materials Science Division has been awarded the **MRSI Medal** for the year 2008 by Materials Research Society of India (MRSI).

Dr. Vidhya Sundararajan, Strategic & Human Resources Planning Section has received the **Tamil Nadu Young Women Scientist Award** for the year 2006.

Dr. M. Vijayalakshmi, Physical Metallurgy Division has been awarded the **Metallurgist of the Year Award** for the year 2007 by Ministry of steels and Indian Institute of Metals.

IGCAR has won the **First Prize** for the category **"Mass Awareness Campaign"** for the year 2006-07. The apex national PR body, **Public Relations Society of India (PRSI)** has honoured the Centre for its team efforts in the mass campaign for the role of Fast Breeder Reactors in ensuring the energy security for India.

PUBLICATIONS - 2007



BOOKS

1. B.P.C. Rao, **"Practical Eddy Current Testing"**, Series editors: BaldevRaj and B. Venkatraman, Narosa publishing house, New Delhi, 2007.
2. **Frontiers in Design of Materials**, Baldev Raj, S.Ranganathan, S.L.Mannan, K. Bhanu Sankara Rao, M.D.Mathew and P.Shankar (Eds.), (2007), Series in Metallurgy and Materials Science, University Press, Hyderabad.
3. P. Kalyanasundaram, C.K. Mukhopadhyay and S.V. Subba Rao, **"Practical Acoustic Emission"**, Series editors: Baldev Raj and B. Venkatraman, Narosa publishing house, New Delhi, 2007.
4. **Nuclear Fuel Cycle Technologies: Closing the Fuel Cycle**, Ed. Baldev Raj and P.R. Vasudeva Rao, BRNS, Mumbai (2006).
5. **Advances in Materials Characterization**, G. Amarendra, Baldev Raj and M. H. Manghnani (Eds.) (2007), University Press, Hyderabad.

PATENTS

1. C. Ramesh, N. Murugesan, S.Velmurugan, A. A.M. prince, V. Ganesan, S. V. Narasimhan, **A Measuring system for on-line measurement of corrosion rate of metals in an aqueous medium**, Patent No. 204092, Date of Grant: 26-12-2006.
2. Title of the Invention: **High Strength and Highly Precipitated Austenitic Stainless Steels**, Inventors : Kinkar Laha, Junro Kyono and Norio Shinya Japanese Patent No: 3975275

Colloquia, Seminars and Conferences - 2007

IGC Colloquia

1. Nuclear Fusion as a Future Energy Resource by Dr. D.D.Sood, Former Director, RC &IG, BARC on 2, Jan 2007.
2. India's Nuclear Power Programme-Yesterday, Today and Tomorrow by Shri S. K. Jain, Chairman & Managing Director, NPCIL on 31, Jan 2007.
3. Vignettes of Indian Armed Forces by Lt.Gen. B.J.Gupta, Commandant, Defence Services Staff College, Wellington, Tamil Nadu on 19, Feb 2007.
4. Recent Advances in Computational Science and Engineering by Shri. H.S. Kushwaha, Director, HS&EG, BARC- 16, Mar 2007.
5. Role of Satish Dhawan Space Centre - Space Port of India in the Indian Space Program & Space Capsule Recovery Experiment by Dr.K.Viswanathan -SHAR,ISRO on 19, Mar2007.
6. In principle predictability of earthquakes by Prof. G.Ananthakrishna, IISc,Bangalore on 4, Jul 2007.
7. Plant Life Management of Nuclear Power Plants by Dr. Philip Tipping, Senior Scientific Officer, Swiss Federal Nuclear Safety Inspectorate, SWITZERLAND on 11, Oct 2007.
8. Nuclear and Non-Nuclear Safety Basis by Dr. J.C.Laul, Los Alamos National Laboratory, Los Aalmos, New Mexico, USA on 31, Oct 2007.
9. A Historical Review of Reactor Safety by Prof. Bal Raj Sehgal, Nuclear Power Safety Royal Institute of Technology, Alba Nova University Center, Stockholm, Sweden on 7, Nov 2007.
10. Structure of the Atomic Nucleus and Origin of the Universe by Dr. Dominique Goutte, Director, Dept. of Energy in the French Ministry of Research (former Director of GANIL) at Caen on 26, Nov 2007.
11. Photonic Band Gap Materials: Semiconductors of Light by Prof. Sajeev John, Department of Physics, University of Toronto, Ontario, CANADA, on 24, Dec 2007.

Special Lectures

12. Personality Development and Stress Management by Dr.Sambanthan on 10, Feb 2007.
13. Remote Sensing from Orbital Platforms for Evaluation of Natural Resources by Dr.P.Manavalan, ISRO, Bangalore organised by Indian Association for Radiation Protection on 15, Feb 2007.
14. Complexation of Actinides in Solution : Thermodynamic Measurements and Structural Characterisation - **Seaborg Memorial Lecture** by Dr. Linfeng Rao, Senior Scientist LBNL, Berkeley, USA 21-22, Feb 2007.
15. Special Lecture by Dr. Kamala Selvaraj, **Modern Developments in Treatment of infertility** on the Occasion of International Women's Day on 8, Mar 2007.
16. Engineering Village-2, **Elsevier Talk** on 17, Apr 2007.
17. Science and Spirituality: A Modern Look at Ancient Indian View Point by Prof. T.R. Anantharaman on 28, Jun 2007.
18. Enrichment of Boron for Fast Reactor Control Rod Application, IE Colloquium by Dr. C. Anand Babu, Head, ST&HD, FRTG on 29, Jun 2007.
19. Global Warming by Dr.Shankar, IMSc., Chennai organized by Tamil Nadu Science Forum on 2, Oct 2007.
20. Resuscitation of Sudden Cardiac Arrest, **World Anesthesia Day - Lecture** by Dr. K.Mathiyalagan organized by AARCO on 16, Oct 2007.
21. Measuring and Assessing Science, **Vikram Sarabhai Memorial Lecture** by Prof. P. Balaram, Director, IISc. on 18, Dec 2007.

Seminars, Workshops and Meetings

22. Technical Meeting (Third Research Co-ordination Meeting) of the CRP on Studies of Advanced Reactor Technology Options for Effective Incineration of Radioactive Waste Hosted by IGCAR at Chennai, 15-19, Jan 2007.
23. Industrial Training Course on Intelligent Instrumentation System 22-26, Jan 2007.
24. CEA-IGCAR Technical Seminar on LMFBR Safety Aspects Related to Severe Accidents, Kalpakkam, 12-16, Feb 2007.
25. DAE Anu Week Celebrations - 2007 at VIT University, Vellore, 13-17, Feb 2007.
26. Quality Circle Case Study by Star and Samurai QCs on 8, Mar 2007.
27. Seminar on Emerging Trends in Electron Microscopy, IIM and IGCAR on 22, Mar 2007.
28. Workshop on Synthesis and Characterisation of Advanced Functional Materials, 26-28, Mar 2007.
29. Seminar on "Technological Developments in $\text{CaSO}_4\text{:Dy}$ TLD Phosphor and BaFBr:Eu Image Storage Phosphor" by Dr. A.R. Lakshmanan, President, IARP, Kalpakkam Chapter and Former Head, Radiation Dosimetry Section, RSD, IGCAR on 11, Apr 2007.
30. International Workshop on Imaging NDE-2007, 25 - 28, Apr 2007.
31. ASTM Standards Workshop organised by IGCAR and Anna University on 6 Jun 2007.
32. Training Programme on "Disaster Management", 22-23, Jun 2007.
33. Management of Water Resource and Nuclear Waste Repository, on 27, Jun 2007.
34. Quality Circle Case Study by M.S. Ashok Leyland, Chennai on 6 Jul 2007.
35. "Web Tools and IT Enabled Services" - Pre-conference Tutorial, READIT-2007 on 11, Jul 2007.
36. READIT-2007 - Conference on Information to Knowledge: Technology and Professionals, Kalpakkam, 12-13, Jul 2007.
37. DAE Workshop on "Nuclear Energy for National Development and Environmental Sustainability" (WONDER - 2007) at Chennai, 19-21, Jul 2007.
38. Information Security from Obscurity to Knowledgeable Practice by Shri Sekhar Sethuraman, Head, IT Security - Greater Asia, LexisNexis on 31, Jul 2007.
39. Colloquium on Evaluation of Quality Circles on 27, Sep 2007.
40. Quality Circles Annual Meet (QCAM-2007) 6 - 7, Sep 2007.
41. Discussion Meeting on Fusion Reactor Materials and Manufacturing Technologies, Kalpakkam on 14, Sep 2007.
42. Hindi Fortnight - 2007, 14-24, Sep 2007.
43. Training Program on "Web Design for Knowledge Exchange" organised by AARCO & IGCAR, 17 - 22, Sep 2007.
44. Convergence of Technologies for Rapid Development: Institution of Engineer's Day Celebrations on 8, Oct 2007.
45. AIM -IGCAR Academia Meet on 12, Oct 2007.
46. 14th National Convention of Electro Chemists, 6 - 7, Dec 2007.
47. Workshop on Industrial Safety, 28-29, Nov 2007.
48. CEA-IGCAR Technical Seminar on Liquid Metal Fast Reactor Safety Functions Strategy - Experience and Strategy for Future Plants. Kalpakkam, 19-21, Dec 2007.

Nurturing Activities

49. Summer Training in Physics and Chemistry (STIPAC 07), a six weeks summer training programme in Physics and Chemistry for final year M.Sc., (Physics/Chemistry) students from 28, May 2007 to 6, Jul 2007.
50. Graduation Day Celebration of Training School at IGCAR on 4, Sep 2007.
51. Professor Brahm Prakash Memorial Materials Quiz-2007, an annual event of Materials Quiz organized for students of Class XI and XII, An International Event, on 13, Oct 2007.
52. SIRD - Quiz on 5, Dec 2007.

NEWS & EVENTS

Memorandum of Understanding between IGCAR and UGC-DAE-CSR - January 16, 2007



Dr. Baldev Raj, Director, IGCAR and Dr. Praveen Chaddah, Director, UGC- DAE-CSR following the signing of MoU between IGCAR and UGC-DAE CSR.

A Memorandum of Understanding between IGCAR and UGC-DAE CSR was signed on January 16, 2007, at Kalpakkam. Under this agreement, IGCAR will open its medium sized, but high technology facilities for University researchers to promote collaborative research in the area of Physical, Chemical and Engineering Sciences. This MoU envisages the creation of a UGC-DAE CSR Node at Kalpakkam, that will house high-end research facilities that would be open to University researchers. The Node would help to foster an active collaboration between DAE and the academic institutions through the involvement of young research scholars.

Joint Meeting of the Indian Nuclear Society and American Nuclear Society - January 19-20, 2007

A Delegation of the American Nuclear Society (ANS) visited Kalpakkam during January 19-20, 2007. The ANS delegation was led by Dr. Harold McFarlane, President, ANS and the INS delegation was led by Dr. Placid Rodriguez, President, INS. The ANS delegation consisted of Dr. Harold Finley McFarlane, President, American Nuclear Society; D-ALD, INL, Dr. James Lake, Past President, ANS; Battelle Executive, Dr. Alireza Haghighat, Chairman, NEDHO; Chair NE Dept. University of Florida, Dr. Arvind Kumar, Chair NE Dept. University of Missouri, Mr. Arthur DiGiovine, Vice-President, Studsvik ScandPower, Inc., Dr. Atambhir Singh Rao, Int'l Committee, ANS; Nuclear Energy Directorate, IAEA, Dr. Samit Bhattacharyya, President, RENMAR and Dr. Dennis Berry, Director, Nuclear Programs, Sandia. The INS delegation consisted of Dr. Placid Rodriguez, President, Indian Nuclear Society, Mumbai, Shri S.C. Chetal, Director, Reactor Engineering Group, IGCAR, Shri P. Swaminathan, Shri G.D. Mittal, Secretary, Indian Nuclear Society, Mumbai, Dr. V. Ganesan, Treasurer, Indian Nuclear Society, Kalpakkam Branch, Dr. M.L. Jhoshi, Head, Health Physics Division, BARC, Dr. R.R. Puri, Head, Human Resources Development Division, BARC and Dr. M. Sai Baba, Head, Strategic & Human Resources Planning Section, IGCAR. The ANS delegates visited some of the facilities at IGCAR, MAPS, BHAVINI, BARCF and SRI at Kalpakkam on January 19, 2007. On January 20, 2007, a joint workshop of the two societies on the theme "Preparing for the Nuclear Renaissance: Strategies for Human Resources Development and Nuclear Knowledge Management" was held with opening remarks by Dr. Placid Rodriguez, President, INS. A number of presentations were made by members of INS and ANS delegations on the theme.

DAE Anu Week Celebrations-2007, VIT University, Vellore - February 13-17, 2007

Public Relations Activities Implementation Committee (PRAIC) of IGCAR organized the DAE's prestigious 'Anu Week Celebrations 2007' on the theme "Unleashing the energy of nuclei for a sustainable future" in collaboration with the VIT University, Vellore during February 13-17, 2007 in the University campus. The programme included a 5-day DAE Exhibition, a two-day Workshop for secondary school science educators and target specific Essay, Quiz, Elocution & Cartoon Contests in English and Tamil for students of various classes from schools and colleges situated in and around Vellore district.

Dr. Baldev Raj, Distinguished Scientist and Director, IGCAR inaugurated the Celebrations, and Shri. Prabhat Kumar, Project Director, BHAVINI declared the exhibition open. Theme address was delivered by Dr. S.K. Malhotra, Head, Public Awareness Division, DAE, Mumbai. Shri G Viswanathan,

Hon'ble Chancellor, VIT University presided over the inaugural ceremony, along with other dignitaries of VIT. Shri. P.V.Ramalingam, Director, ROMG, IGCAR proposed the vote of thanks. Resource persons from IGCAR, MAPS, BARC & DAE covered the multifaceted applications of radiation and radioisotopes for the benefit of mankind, during the teachers' workshop. Informal contests were conducted for the participants. Field visits were organized on the third day for the teachers to the Christian Medical College (CMC), Vellore and BHEL, Ranipet and the use of radioisotopes in the healthcare and industry were demonstrated to them. During the valedictory function on February 17, 2007, the Chief Guest Shri S.Krishnamurthy, Station Director, MAPS distributed certificates and prizes in the form of gift exchange vouchers for books for a total value of Rs.60,000/- to the winners and runners of various contests.

The academia and the general public in this semi-urban part of Tamil Nadu were excited and benefited by participating in the Celebrations, which had helped to spread the awareness about the activities of the Department of Atomic Energy.

Visit of delegates from the Japan Energy Safety Organisation, Japan - March 1, 2007



Dr. Hirofumi Haghihara and Dr. Masaki Nakagawa from Japan Energy Safety Organisation, Japan with Dr. P.R. Vasudeva Rao, Director, CMMG and Dr. M. Sai Baba Head, S&HRP IGCAR

Dr.Hirofumi Haghihara, Associate Vice-president and In-charge of International Cooperation and Dr.Masaki Nakagawa, Senior Officer, International Affairs Group, Safety Information Research Division from the Japan Energy Safety Organisation visited the Centre on March 1, 2007 and held discussions with the Director, and senior scientists at IGCAR on safety related issues of Fast Reactors. Presentations on behalf of IGCAR were made by scientists of the Centre and the visitors also gave a presentation of their mission. The delegates visited various laboratories of the Centre.

Visit of IBSA delegation on Nanotechnology - April 6, 2007



Prof. J.A. Brum, Brazil, Dr. Baldev Raj and Dr. T. Hille, South Africa during the meeting at IGCAR on April 6, 2007

A twelve member overseas delegation, comprising six scientists from Brazil and six from South Africa led by Prof. J.A. Brum and Dr. T. Hillie respectively, visited IGCAR on April 6, 2007 under India-Brazil- South Africa (IBSA) initiative on Nanotechnology. Dr. Baldev Raj, Director, IGCAR, is the co-ordinator of IBSA nanotechnology initiative from India. The delegation also visited Indian Institute of Technology (IIT), Delhi and Inter University Accelerator Centre (IUAC), Delhi on April 2nd 2007, Bhabha Atomic Research Centre (BARC) and Tata Institute of fundamental Research (TIFR) at Mumbai on April 3 and 4 2007 and Indian Institute of Science (IISc),Bangalore on April 5th 2006. The visits were coordinated by Indira Gandhi Centre for Atomic Research (IGCAR), Kalpakkam on behalf of DST, India. It was ensured that experts in nanotechnology from all parts of India participate in the discussions in at least one of the above mentioned destinations, to present and evolve their ideas for collaborative projects under this initiative.

The IBSA nanotechnology initiative is a trilateral collaborative program between the Departments of Science and Technology of three participating countries, namely, India, Brazil and South Africa. The objective of this initiative is to formulate tri- and bilateral mega collaborative programs in the area of nanotechnology, of mutual interests to the participating nations. The accepted priority areas of common national interest to all three countries under this initiative include, advanced materials, energy systems, sensors, catalysis, health (TB and Malaria), water treatment, agriculture and environment.

Summer Training in Physics and Chemistry (STIPAC 07) - May 28 to July 6, 2007



Students, Faculty Members and Organizers of STIPAC - 07

Like in the past, this year too a six week summer training program in physics and chemistry (STIPAC-07) was organized by Indira Gandhi Centre for Atomic Research -Kalpakkam for students entering their final year of regular or integrated M.Sc (Physics/Chemistry) during May, 28 - July 6, 2007. This six week long programme comprised of both theoretical lecture courses and hands-on laboratory experience through projects. This programme was aimed at motivating the students to pursue a career in research. The theme for this year's course was Physics and Chemistry of Nanomaterials.

Forty students (Twenty from Physics and twenty from Chemistry) were selected from about 500 applicants in physics and chemistry. The selection was done based on their academic track record and the write-up on "why you think size matters in the physical & chemical properties of matter". Care has been taken to select students from as many states as possible and as many universities/colleges as possible. This resulted in selecting 20 students from within Tamilnadu and 20 students from outside representing 10 states for both the disciplines. The selected students are provided a stipend of Rs. 3000/- per month, and their travel expenses are reimbursed.

The six week technical program of STIPAC course consisted of 90 hours of lectures and 90 hours of project work for both physics and chemistry students. The guest lectures were 15 and 8 for physics and chemistry respectively. The lectures were delivered by senior scientists and the guest lectures were delivered by eminent speakers drawn from reputed institutes and universities from all over India. The topics that have been covered during the lectures in physics include synthesis and characterization of nanomaterials, nanoparticle dispersions and gels and the influence of size on optical, magnetic, mechanical, electronic and transport properties. The topics that have been covered in chemistry were classified in three broad categories namely, core subjects in chemistry, application in nuclear energy programme and nanoscience & technology. The special lectures covered a variety of topics in biotechnology, nanotechnology, fluorescence of novel organic compounds, ab-initio quantum mechanical approach in understanding spectroscopy, sensors and storage devices. Students have gained hands on experience through their project works. They also got the opportunity to listen to the special lectures on "Random walk" and "Status of sodium cooled fast reactors with closed fuel cycle" by Dr. Baldev Raj, Director, IGCAR; "Opportunities for scientists in Fast Breeder Reactor Technology" by Shri. Prabhat Kumar, Project Director, BHAVINI and "Key elements of Periodic Table - Relevance to DAE" by Dr. P.R. Vaudeva Rao, Director, CG& MMG.

WONDER-2007

DAE Workshop on 'Nuclear Energy for National Development and Environmental Sustainability' July 19-21, 2007 - Loyola College, Chennai



Dr. S.K. Sharma, Chairman, AERB, addressing the crowd

For the first time in this region, a 3-day workshop exclusively for the University and College Professors of Physical and Life Sciences and allied disciplines was jointly organized by DAE at Loyola (Autonomous) College, Chennai during July 19-21, 2007. The response was over-whelming and 250 teaching faculty were short-listed and registered. Preference was given to those belonging to Institutions situated in and around Chennai city. The Workshop was inaugurated by Dr.S.K.Sharma, Chairman, AERB. He highlighted the stringent

safety standards and regulations being adhered to in Indian nuclear installations. Dr.P.R.Vasudeva Rao, Director of Chemistry, Materials and Metallurgy Groups of IGCAR in his key-note address drew the attention of the audience to the world of challenges and opportunities prevailing in the nuclear science and technology. Dr.S.K.Malhotra, Head of Public Awareness Division of DAE, Mumbai spoke on the theme of the Workshop. Shri.PV.Ramalingam, Director, Reactor Operations and Maintenance Group, IGCAR and the Chairman of the IGCAR Public Relations Implementation Committee proposed the vote of thanks.

The Workshop comprised of 12 invited technical lectures, practical demonstrations, informal contest, feed-back / panel discussion session and field visits to leading hospitals like Apollo Specialty Hospital, Cancer Institute (WIA - Adyar), Institute of Cardiovascular Diseases (Madras Medical Mission), Vijaya Health Centre, Dr.Kamakshi Memorial Hospital (Pallikaranai), Sri Ramachandra Medical Centre (SRMC - Porur), Advanced Nuclear Medicine Research Centre, Dr.Rai Memorial Medical Centre, Dr.Mohan's M.V. Diabetes Research Centre and Madras Isotope Laboratory, where radioisotopes are being used for diagnostic and therapeutic purposes.

The Chief Guest of valedictory function Dr.R.Krishna Kumar, Head, Dept of Nuclear Medicine, Cancer Institute (WIA - Adyar) gave away the Certificates and Prizes to the 20 winners of the informal contest. He underlined the importance of radioisotopes in cancer management. Dr.K.Raghuraman captivated the participants by his informative address and made them feel proud of the contributions of Indian scientists and engineers to the UN body, IAEA. Shri.Frederick.J. Kaplan, Consul for Public Affairs, US Consulate General for South India was the Guest of Honour at the function. Shri.J.Daniel Chellappa, Head, Technical Co-ordination & Public Awareness, IGCAR, Chennai summed-up the proceedings of the Workshop. Authorities of Loyola College including the Principal, Rector, Secretary and Dean of Sciences participated in the inauguration and valediction.

The participants were extremely impressed and felt greatly benefited by their participation. Many of them desired to have repeat programmes in their institutions. They admired and appreciated the DAE programmes, and most of them vowed to be our ambassadors! The Workshop facilitated closer interactions with the academia, and also further strengthened the research-academia linkage. Thus, the event has successfully fulfilled its objectives!

Graduation Function of the first batch of trainees from Training School at IGCAR - September 4, 2007



First Batch of Graduates of Training school with the Chief Guest, Chairman, AEC along with senior colleagues

The first twenty graduates from the BARC Training School at IGCAR have successfully completed their training and were graduated in a glittering ceremony that took place on 4 September, 2007 in the Sarabhai Auditorium, Homi Bhabha Building, IGCAR. Distinguished Academician, Prof. J.B. Joshi, Director, University Institute of Chemical Technology, Mumbai was the Chief Guest and Dr. Anil Kakodkar, Chairman, AEC & Secretary, DAE presided over the occasion. Dr. M. Sai Baba, Head, Strategic and Human Resources Planning Section and Head, IGCAR Training School welcomed the gathering. Dr. Baldev Raj, Distinguished Scientist and Director, IGCAR gave the Director's address. A souvenir featuring the first year of the training programme at IGCAR was released by Prof. Joshi on this historic occasion. Dr. Anil Kakodkar then delivered the Presidential address. A few of the Trainee Scientific Officers from 1st batch voiced their feedback about the courses and their stay at the hostel. Prof. Joshi gave away the prestigious 'Homi Bhabha Prize' comprising of a medallion and books worth Rs.5000 to the meritorious topper from the Mechanical Engineering discipline, Shri. Ankur Kaushik and Shri. Sukant Kothari from the Electronics and Instrumentation discipline. He also gave away the course completion certificates to all the graduates passing out. Prof. Joshi addressed the gathering with a very inspiring and thought provoking lecture. Finally, Dr. G. Venugopal Rao, S&HRPS proposed the vote of thanks.

CEA-DAE Collaborative meeting on "Nanoscience: nanomaterials - production and characterization; interfaces - self-assembled monolayers" - October 4, 2007



Shri. S.C. Chetal, Director, Reactor Engineering Group, IGCAR with the CEA Delegation of CEA-DAE Collaborative meeting on "Nanoscience: nanomaterials - production and characterization; interfaces - self-assembled monolayers"

A meet on the CEA-DAE collaboration on the theme, "Nanoscience: nanomaterials - production and characterization; interfaces - self-assembled monolayers" was held at IGCAR Kalpakkam on October, 4, 2007. A six member CEA Delegation comprising of Dr. Pascal Boulanger, Dr. Nathalie Herlin-Boime, Dr. Arianna Filoramo, Dr. Roberto, Calemczuk Doris Neumann-Maazi and Hughes de Longevialle along with Dr. J.V. Yakhmi, Associate Director (P), BARC, participated in the one day meet at Kalpakkam. The technical programme comprised of presentations by CEA and IGCAR scientists and visits to the laboratories. Topics for collaboration in the area of Chemical Sensors and participation in Synchrotron experiments were discussed.

Academia-IGCAR Meet (AIM-2007) - October 12, 2007



Chief Guest Prof. Dr. Tmt. Nalini Ravindran, Director of Collegiate Education, Govt of TN listening to Director IGCAR's address

Guided by the success of the Centre's major initiative launched on October 2nd last year, IGCAR organized a 1-Day Academia-IGCAR Meet (AIM-2007) at Kalpakkam on Friday, October 12, 2007 for the Academia in science and engineering disciplines. A team of 250 resolute researchers, from various colleges and universities in Tamilnadu, with excellent track of research and promising problems for exploration were short-listed for participation. The Meet focused on reinforcing the existing collaborations, and also on identifying new enabling partners in India's march towards its cherished vision of becoming a global leader in Sodium Cooled Fast Breeder Reactor (FBR) and associated fuel cycle technologies by 2020 AD. Academia from various others districts of the State, who have a strong desire to collaborate, also joined their Chennai colleagues in large numbers.

AIM-2007 provided an excellent platform for showcasing their expertise and the infrastructure of their institutions. They presented relevant project proposals for joint ventures and shared their excitements in pursuing science and engineering R & D with IGCAR scientists. They were keyed-up at the Centre's top-notch research culture and the commitment of our scientists. The day's programme included brain-storming session with Dr. Baldev Raj Distinguished Scientist and Director IGCAR, visits to laboratories of their interest, technical presentations by the Heads of the respective facilities, one-on-one interactions with their chosen scientists, business networking, feed-back session and panel discussion for formulating the roadmap to take the initiatives ahead. The progress of the collaborative ventures and the offshoots of AIM-2007 will be documented for periodic monitoring and further directions by the Centre.

Visit of CEA, France delegation - October 17-18, 2007



Shri. S.C. Chetal, Director, Reactor Engineering Group, IGCAR presenting a memento to Dr. P. Chaix (DEN/DSOE) along with Dr. A. Alamo and Dr. C. Robertson

A three member CEA delegation comprising of Dr. A. Alamo, Dr. P. Chaix and Dr. C. Robertson visited IGCAR during October 17 and 18, 2007. Presentations on "CEA Basic Research Programs for Nuclear Energy Applications", "Advanced Steels and ODS Alloys for Nuclear Applications", and "Strain Localization in Irradiated Austenitic Stainless Steels, were made by the visiting CEA Scientists, followed by in-depth discussions. The main objective of the discussion session was to put into action the Implementing Agreement "Investigation of irradiation-induced microstructure in ODS materials using JANNUS facilities and multi-scale modelling" that was signed in Cadarache on 24th September 2007. The scientific and technical aspects of the collaborative programme that deals with investigation of the stability of nano-sized yttria particles in iron matrix, under various irradiation conditions and mechanical loading was discussed in detail to evolve the various steps of experimentation and simulation.

India-Japan Specialists' Meeting on Safety in Nuclear Energy - November 12-13, 2007



Dr. Baldev Raj, Director, IGCAR and Prof.Y.Fuji-ie, former Chairman, Atomic Energy Commission of Japan, with the participants of the "India-Japan Specialists' Meeting on Safety in Nuclear Energy".

The India-Japan Specialists' meeting on Safety in Nuclear Energy was held at IGCAR, Kalpakkam during 12-13 November, 2007. A thirteen-member Japanese delegation led by Prof.Y.Fuji-ie, Former Chairman, Atomic Energy Commission of Japan participated in the specialist meeting. From Indian side twenty members from IGCAR and BHAVINI attended the meeting. The meeting started with introductory remarks by Dr. Baldev Raj, Director, IGCAR and Prof. Fuji-ie, leader of the Japanese delegation. In his introductory remarks Dr. Baldev Raj, gave an overview of the current status of

fast reactor development in India. In his talk Prof. Fuji-ie, touched upon "Nuclear Development in Japan" and "Basic idea of securing nuclear system safety". In all there were eight presentations, four from Japanese delegation and four from Indian participants. Mr. A. Yoshida from O-arai Research and Development Center, JAEA, talked on "The Operating experience of Japanese fast experimental reactor Joyo" and Dr. Y. Kani, Leader of the Fast Reactor Programme in Japan and the Deputy Director General, Fast Breeder Reactor Research and Development Center, JAEA gave a talk on "Safety approach and safety evaluation of Japanese prototype fast reactor Monju". Mr. N. Suda from the Nuclear Safety Technology Centre, Japan, in his talk gave the details of the "System for prediction of environmental emergency dose information (SPEEDI)". Shri S.C. Chetal, Director, Reactor Engineering Group, discussed the "Safety criteria & design provisions of Prototype Fast Breeder Reactor in India" and Shri. P.V. Ramalingam, Director, Reactor Operation & Maintenance Group, in his talk covered the "Operating experience of Fast Breeder Test Reactor". Shri. M. Rajan, Director, Safety Group touched upon the "R&D studies concerning sodium fire at Indira Gandhi Centre for Atomic Research" and Dr. P. Chellapandi, Associate Director, Nuclear Engineering Group, REG discussed in his talk "Beyond design basis events and containment related aspects of Prototype Fast Breeder Reactor in India".

Possible areas for further cooperation were discussed in the concluding session. The members of the Japanese delegation visited Fast Breeder Test Reactor and Prototype Fast Breeder Reactor, under construction by BHAVINI.

Visit of Parliamentary Standing Committee on Science & Technology, Environment & Forests - December 21, 2007

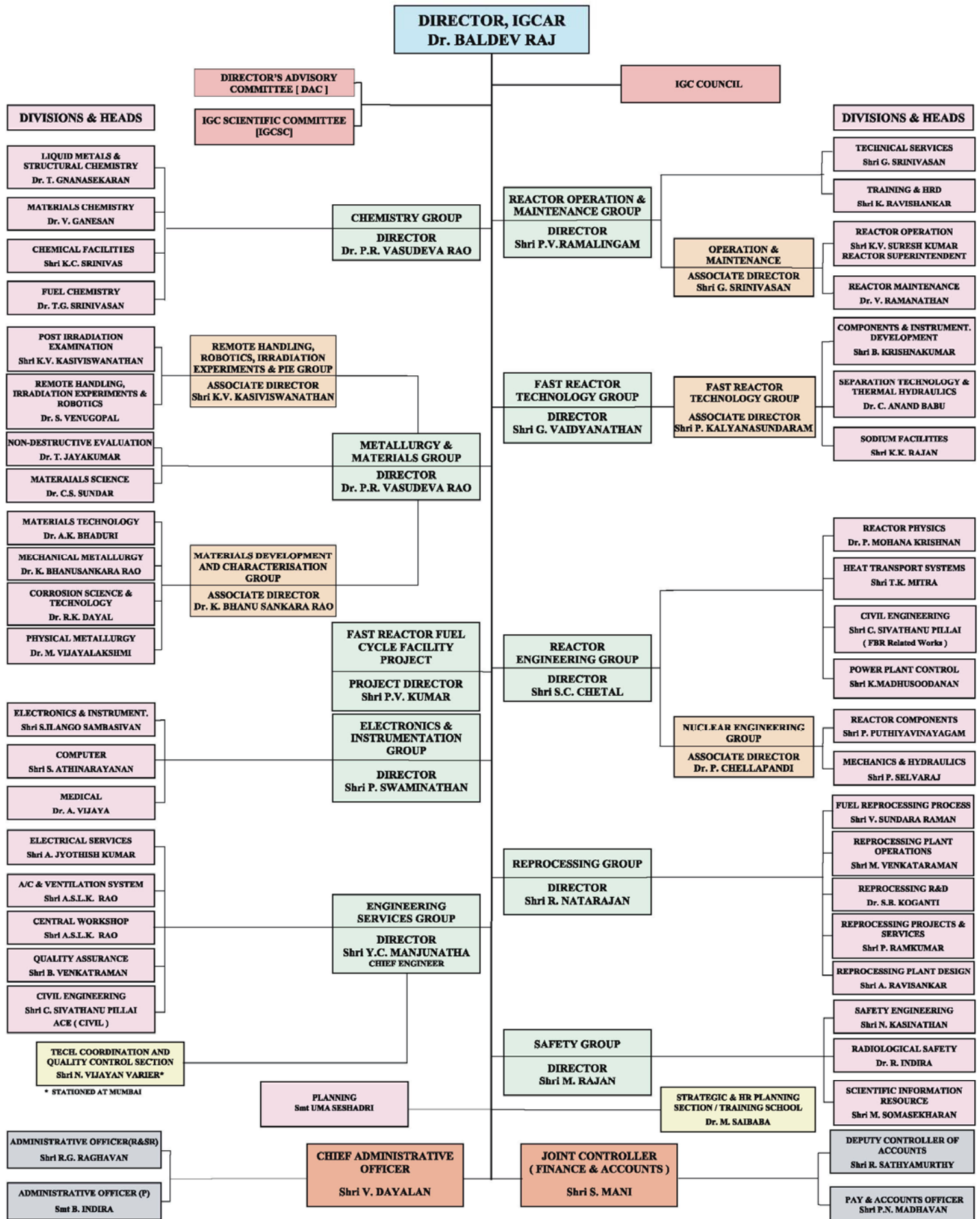


Dr. V. Maitreyan, Chairman and Members of the "Parliamentary Standing Committee on Science & Technology, Environment & Forests" with Dr. Baldev Raj, Director, IGCAR and senior members of IGCAR during their visit to IGCAR.

A delegation of members of the "Parliamentary Standing Committee on Science & Technology, Environment and Forests" under the Chairmanship of Honourable Member of Parliament, Dr. V. Maitreyan visited the Centre on 21 December, 2007. The delegation was received by Dr. Baldev Raj, Director, IGCAR and Heads of other DAE units at Kalpakkam and senior colleagues of the Centre. Dr. Baldev Raj, Director, IGCAR in his talk presented a status report on the Fast Breeder Test Reactor and the R&D activities of the Centre and gave a perspective of the future growth of fast breeder reactor program. An

interesting and thought provoking discussion followed the presentation. The members of the standing committee expressed their appreciation for the progress made by the Centre in the development of fast breeder reactor technology and associated fuel cycle technologies

The members of the delegation visited; Fast Breeder Test Reactor, Radiometallurgy Laboratory and Engineering development and testing facilities of Fast Reactor Technology Group. They also visited the Prototype Fast Breeder Reactor, under construction by BHAVINI.



IGC COUNCIL MEMBERS

Chairman



Dr. Baldev Raj, Fellow, Third World Academy of Sciences, Indian National Science Academy, Indian National Academy of Engineering, Indian Academy of Sciences, Bangalore, The National Academy of Sciences, Allahabad, Tamil Nadu Academy of Sciences, BE from Ravishankar University and Ph.D. from IISc, Bangalore, D.Sc. (h.c.) from Sathyabama University, Chennai, is a Distinguished Scientist & Director, Indira Gandhi Centre for Atomic Research.

His specializations include materials characterization linked to performance, NDE and Quality Management, testing and evaluation using non-destructive evaluation methodologies, materials development and performance assessment and technology management. He has steered and participated in many national programmes of great significance such as Intelligent Processing of Materials, Characterization of Cultural Heritage, IAF programmes of ageing management. He has 36 years of experience, which has led to many first of its kind observations and discoveries in the field of materials characterization and applications. He has more than 650 publications in journals. He has co-authored 12 books and co-edited 28 books and special journal volumes. He has 5 Indian Standards and 18 patents to his credit. He is Editor-in-Chief of two series of books: one related to NDE Science & Technology and another related to Metallurgy & Material Science. He has contributed 9 articles in Encyclopaedia and a large number of reviews.

He has won major awards such as NDT Man of the Year, G.D. Birla Gold Medal, Sir C.V. Raman Award, Keith Hartely Award, International Committee on NDT Researcher Award, VASVIK Award, Lifetime Achievement Award of Indian Society for Nondestructive Testing, Lifetime Achievement Award of Indian Welding Society, Raman-Chandrasekhar Award of Acoustical Foundation for Research & Education, V.S. Jain Memorial Lecture of Indian Society for Nondestructive Testing, MRSI-ICSC Superconductivity & Materials Science Annual Prize, Jaeger Award of International Institute of Welding, Indian Nuclear Society Award, NOCIL Award of Indian Institute of Chemical Engineers, Dr. S. Bhagavantam Award of Acoustical Society of India, Indian Science Monitor Award and Padma Shri from Govt. of India.

He is on many Commissions, Committees and Councils, Editorial Boards nationally and internationally such as Standing Advisory Group on Nuclear Energy, International Atomic Energy Agency; Scientific Advisory Council to Prime Minister; Nano Science & Technology Initiatives of Department of Science & Technology, Member, Board of Directors, Bharatiya Naabhikiya Vidyut Nigam Ltd. (BHAVINI), Nuclear Fuel Complex, Member, National Committee of Centre for Co-operation in Science & Technology in Developing Societies under the auspices of Indian National Science Academy, Board of Director, International Institute of Welding, etc. He is Senior Professor of Homi Bhabha National Institute (a University of the Department of Atomic Energy). His interests include technology management, heritage, philosophy, theosophy and education. He is an acclaimed specialist in the area of archeometallurgy and education.

Members



Dr. C.V. Ananda Bose, IAS, is presently Joint Secretary (Research and Development), Department of Atomic Energy. Coming from the Kerala Cadre, he has held several positions in Kerala including the Principal Secretary to Chief Minister of Kerala. He is a visiting Professor of Birla Institute of Technology and Science, Pilani and has authored eight books and about a hundred papers and articles in the fields of Habitat, Architecture, Environment and Land Reforms. He is a recipient of several National and International Awards that include Jawaharlal Nehru Fellowship, Bremen Partnership Award and Rajiv Gandhi National Award for Excellence in Management. He has received more than a hundred prizes and medals and is a member of several International and National Expert Groups. In 2006, Shri Ananda Bose has been appointed as Chairman of Atomic Energy Education Society, Mumbai.



Shri S.C. Chetal, B.E.(Mech), is a Distinguished Scientist & Director, Reactor Engineering Group at IGCAR. Since 1971, he has been engaged in the field of fast reactor engineering. He has made significant contributions towards design of FBTR sodium systems and components. He has also contributed to the material selection, manufacturing technology, R&D, design and manufacturing of 500 MWe Prototype Fast Breeder Reactor. He is a member of many professional institutions and a Fellow of the Indian National Academy of Engineering. He has received National Technology Award 2000 from DRDO for significant contributions in the field of high purity titanium sponge production, Indian Nuclear

Society Award 2003 for contributions towards nuclear related high technology and National Design Award-2007 by Institution of Engineers (India). His interests apart from Fast Reactor Engineering include pressure vessel and materials technology. He has to his credit 300 publications in Journals/Symposia/Conferences.



Shri R.N. Jayaraj is presently the Chief Executive of Nuclear Fuel Complex (NFC), Hyderabad. He is a Mechanical Engineer, graduated from Osmania University. After successful completion of one-year orientation course in Nuclear Engineering from the 17th batch of BARC Training School, he joined Atomic Fuels Division of BARC and contributed in the production of metallic uranium fuel assemblies for CIRUS reactor and development of fuel assemblies for DHRUVA reactor. After his transfer to NFC, he played a key role in establishing the assembly plant and successfully fabricated all the core sub-assemblies, for the first time in India, required for FBTR. He was instrumental in scaling up of production of

fuel bundles required for all the PHWRs, thus consistently meeting the requirements of Nuclear Power Corporation of India Limited (NPCIL). He has to his credit the indigenous development of various equipment for critical processes involving welding, machining centers and assembly stations, thus creating a strong base for establishing self-reliance in PHWR fuel manufacturing. He played pioneering role in standardizing the manufacturing processes for the fuel bundles required for 540 Mwe PHWRs. He served the Department for the last 32 years in various capacities in different Units and gained rich experience in developmental and production of fuel for Thermal Research Reactors, PHWRs and BWRs. Shri Jayaraj, besides being a Member of IGC Council, is also on the Boards of UCIL and IREL.



Shri H.S. Kamath, B.E (Metallurgy), is a Distinguished Scientist and Director of the Nuclear Fuels Group in BARC. He has been associated with the development of plutonium bearing nuclear fuels for the last 35 years, which started with the fabrication of fuel for 'PURNIMA' in 1970-1972. His main area of work is in the development of uranium-plutonium mixed oxide (MOX) fuels for nuclear power programme. He has made important contributions in this field both in laboratory scale as well as industrial scale activities. His most important contribution has been the setting up of the industrial scale MOX fuel fabrication plant at Tarapur. Shri Kamath is the recipient of Indian Nuclear Society Award for the year 2003 in recognition of his outstanding contributions in the field of nuclear fuel fabrication.



Prof P.K. Kaw, Ph.D (Physics) from IIT Delhi, is the Director of Institute for Plasma Research, Gandhinagar since 1986. The Institute has pioneered plasma physics research in India which includes design, development and fabrication of two tokamaks, ADITYA and SST 1, research work on a large number of fundamental plasma physics experiments and work on industrial applications of plasma physics. ADITYA was the first tokamak to discover intermittency in edge and SOL turbulence. The Institute also spearheaded India's case for participation in ITER and is now the nodal domestic agency for ITER. Prof. Kaw's personal research work in this period includes physics of intermittency, drift waves and

anomalous transport, MARFES, solitons, laser fusion, anomalous stopping effects, dusty plasmas, nonneutral plasmas, quark gluon plasmas, etc. Earlier he had held positions like Princeton University Plasma Physics Laboratory Research Staff, Professor at Physical Research Laboratory, Ahmedabad and at Princeton Plasma Physics Laboratory before taking over as Director, Plasma Physics Program at Physical Research Ahmedabad in 1982. He played a key role in initiating tokamak physics program in India. He has more than 284 research papers to his credit in international journals. He has several honours and delivered important lectures. Artsimovitch Memorial lecture at the IAEA Fusion Energy Conference in 1992, Invited talk on International Energy Research at the APS Centennial celebrations (1999) in Atlanta, Georgia and a presentation on the International impact of USDOE Fusion Theory Program to the NSF-NRC Panel Chaired by C F Kennel, San Diego are just a few of them to name. Prof Kaw was also the Chairman of the International Fusion Research Council (IFRC) of IAEA from 2000 to 2007.



Shri H.S. Kushwaha, B.Sc., M.Tech.(IIT, Kanpur), is presently the Director of Health, Safety and Environment Group at BARC. He has made significant and important contributions in the design and analysis of nuclear structures, components and piping of Indian Pressurised Heavy Water Reactors (PHWR). He has done pioneering work in the area of seismic design and analysis of 500 MWe PHWR being built at Tarapur, Maharashtra. He has developed several finite element computer programmes in the field of structural mechanics, heat transfer and fluid mechanics. He has developed an improved finite element method using upwinding schemes to solve three dimensional advection-diffusion equation. He

is an active member of Project Design Safety Committee of PHWRs/FBR, Civil Engineering Safety Committee and Safety Review Committee for Operating Plants (SARCOP) constituted by AERB, Mumbai. He has published around 400 papers/reports in national and international journals.



Shri R. Natarajan, a Chemical Engineer from the Annamalai University, joined the Department of Atomic Energy in 1975. He is presently the Director, Reprocessing Group in IGCAR. Under his leadership, the CORAL facility, for establishing the process technology for the reprocessing of fast reactor fuels, was designed, erected and commissioned. He led the team which has successfully completed the reprocessing of fast reactor spent fuel, with a burnup of as high as 155 GWd/t with Plutonium rich fuels, for the first time in the world. As Director of Reprocessing Group, he is responsible for the R&D activities of fast reactor fuel reprocessing and setting up of Demonstration as well as the commercial PFBR

fuel reprocessing plants. His specialization is in the design process flowsheets and plant design. He has also experiences in the design and operation of Thorium-Uranium cycles. He has participated in the irradiated thorium fuel reprocessing campaigns at the Reprocessing Development Laboratory and the Uranium - 233 recovered is used as fuel for the reactor KAMINI. He has interests in solvent extraction process modeling, extraction equipment design, design of feed clarification systems of high active solutions, acid recovery systems, system designs of radioactive offgas circuits and ventilation design of radiochemical plants. He has over ninety five technical presentations and publications to his credit. He has won prestigious NOCIL Award for Excellence in Design and Development of Process Plant and Equipment for the year 2005 for his contribution in the development of fast reactor fuel reprocessing. He is also the recipient of Indian Nuclear Society's INS award for the year 2006 for his contributions in Nuclear Fuel Cycle technologies.



Shri Y.C. Manjunatha, Director, Engineering Services Group of Indira Gandhi Centre for Atomic Research, Kalpakkam, is a M. Tech. in Electrical Engineering from IIT, Madras and belongs to the 16th batch of BARC Training School, Department of Atomic Energy. He steers one of the largest multidisciplinary groups in the Centre which focuses on providing reliable and robust services through cutting edge technologies and methodologies. Some of his major contributions are development and sustenance of infrastructural works of IGCAR & GSO involving civil, electrical, air conditioning and ventilation, communication, workshop and QA activities. He has published more than 10 papers.



Shri S.D. Misra, B.E (Electrical & Mechanical Engineering) is presently the Director of Nuclear Recycle Group at BARC. He is from 13th Batch of BARC Training School and has been involved in the Back End activities of Nuclear Fuel Cycle. He was a member of the team that pioneered setting up of the first Vitrification Plant in the country. Shri Misra was responsible for design and construction of vitrification plants at Trombay & Kalpakkam. He was also instrumental in solving all the problems faced in the first resin fixation facility at Narora Atomic Power Project and made it operational. Shri Misra has participated in a number of symposia and seminars on radioactive waste management and

has also worked as an expert on various technical committees of International Atomic Energy Agency. Presently he is a Member of International Radioactive Waste Technical Committee (WATEC) of IAEA.

He has also served as Director, Purchase & Stores, DPS. In this capacity, he has successfully overcome the problems of technology control regime and made available some of the critical stores for the programmes of the Department. Presently, as Director, Nuclear Recycle Group, he is holding the responsibility of setting up and operation of Reprocessing and Waste Management Plants at various sites in the country.



Shri M. Rajan steered the Safety Group at IGCAR till 31st December 2007, the day on which he superannuated. He obtained his B.E. (Hons) in Chemical Engineering at Annamalai University in 1972. He underwent one year advanced course in Nuclear Technology at Bhabha Atomic Research Centre, Mumbai during 1972-73. His main contributions in the past 30 years are on development works related to the use of sodium as a coolant in Fast Breeder Nuclear Reactors and Engineering Safety. He has designed and constructed many high temperature sodium systems and developed many components & methods for the Fast Breeder Reactors. He is a fellow of Indian National Academy of Engineering,

Indian Institute of Chemical Engineers and Institution of Engineers.



Shri P.V. Ramalingam is an Outstanding Scientist and presently Director of Reactor Operation and Maintenance Group in IGCAR. He graduated in Electrical Engineering with Honours from Madras University in 1969. He worked in CIRUS reactor, BARC from 1969 to 1975. He was transferred to IGCAR in 1975. He was actively involved in preparing the FBTR station documents and training the operation staff. He was responsible for commissioning the primary sodium system and its auxiliary circuits of FBTR and he had the privilege of making the first criticality of FBTR on October 18, 1985. He was closely associated in taking the reactor power in stages to the power level of 17.4 MWt. He was responsible for

implementing many improvements in FBTR for increasing the availability factor of the reactor and in the recently concluded 13th irradiation campaign the availability factor was 94 %. He has to his credit 51 publications in journals/symposia/conferences.



Shri A.L.N. Rao, B.E.(Electrical), is presently the Chairman & Chief Executive of the Heavy Water Board. He joined Bhabha Atomic Research Centre as 15th batch trainee in the year 1971. He was awarded Junior License Certificate in 1974 and took independent charge of the unit consisting reactor, turbine, generator and associated utilities and control systems of TAPS. As unit control engineer he operated the unit safely and without any accidents. He has handled emergency situations and took immediate action to bring the reactors under safe conditions. Shri A.L.N. Rao participated in the first refuelling operations which consisted of transferring the irradiated fuel bundles from the reactor core to fuel storage pool

and loaded the fresh fuel bundles from storage pool into the reactor under 60 ft. of water. He had also replaced the core components which was a challenging task. In the year 1978, he obtained Senior License Certificate and took independent charge of the complete plant in shifts. Shri A.L.N. Rao moved from Nuclear Power Board to Heavy Water Board in the year 1984. He closely followed up the project activities of the Captive Power Plant of Heavy Water Plant (Manuguru) being set up at Aswapuram in Khammam district of Andhra Pradesh. In the year 1987 he took over as Operation Manager of Captive Power Plant. He has successfully monitored the erection of equipments and carried out precommissioning and commis-

sioning activities of the Captive Power Plant having capacity to generate 265 x 3 T/hr of superheated steam and 3 x 30 MWe of electricity generation. He assumed charge as General Manager of the complete Heavy Water Plant (Manuguru), which is the largest heavy water producing plant in India, in the year 1998. He became Associate Director (Projects/Energy & Services) in the year 2003 at the Central Office and took charge as Director (Energy & Services/Operation) in the year 2004. In 2005 he was designated as Executive Director (Projects/Energy & Services) and monitored the physical and fiscal progress of the Projects at Board level. He discharged the duties as the Secretary of the Heavy Water Board. He coordinated all activities related to export of Heavy Water to South Korea and the Republic of China. As Management Representative for Quality Management Systems as per ISO 9001, he followed up all the activities and obtained ISO 9001 Certificate for Board Office.



Shri R.K. Sinha, B.E (Mechanical Engineering), is presently a Distinguished Scientist, Director of Reactor Design and Development Group, and Director of Design Manufacturing and Automation Group at BARC. He is a nationally and internationally recognised expert in the area of nuclear reactor technology. He has handled several major assignments relating to the Indian research and power reactors. In particular, he has specialised in design, development and safety related activities relating to coolant channels of heavy water reactors. He is currently guiding the design and development of the innovative Advanced Heavy Water Reactor and Compact High Temperature Reactor. Shri Sinha has received several awards and honours including the Homi Bhabha Science and Technology Award, VASVIK Award and Indian Nuclear Society Award. He is a Fellow of the Indian National Academy of Engineering.



Shri P Swaminathan graduated with honours degree in Electronics & Communication Engineering from Regional Engineering College, Tiruchirappalli in 1971. He is the Gold medalist of University of Madras. After undergoing one year course in Nuclear Science & Engineering from BARC Training School. Shri P Swaminathan joined Indira Gandhi Centre for Atomic Research in 1972. He further underwent one year course in Main frame system from International Honeywell Bull Training Institute, Paris. Shri P Swaminathan is the main architect for the design, development, installation and commissioning of Fault Tolerant Safety Critical Real Time Computer System for Fast Breeder Test

Reactor. As Director of Electronics & Instrumentation Group, Shri Swaminathan is actively engaged in the development of Safety Instrumentation, Full scope Training Simulator and Knowledge Management System for Fast Breeder Reactor Programme. Shri P Swaminathan is a Fellow of Institution of Engineers and also holds Master Degree in Management Science. He actively interacts with project students and is also Distinguished visiting professor of INAE. He has over 40 publications in International journals/seminars. Also as Chairman, Hospital Management Committee, Shri P Swaminathan ensures the smooth functioning of Health Care System.



Shri Umesh Chandra, Distinguished Scientist, is a graduate in Electrical Engineering from IIT, Kanpur. He is currently Senior Executive Director (R&D and KM) in Nuclear Power Corporation of India. He has been responsible for establishment of R&D activities in NPCIL. The R&D facilities are located at R&D Centre, Tarapur for Nuclear Systems and R&D Lab., NUB, Mumbai for Electronic Systems. He is also directing development and deployment of Computer Based Systems in nuclear power plants for Control and Instrumentation Systems, Main Control Rooms and Training Simulators for PHWR and LWR. He is also managing the IT infrastructure and applications in the organisation. He has guided

design of reactor control mechanisms, various types of remote inspection tools, manipulators and instruments for monitoring radiation. He is also directing the Knowledge Management activities in NPCIL. He was responsible for Control and Instrumentation of the first 540MWe nuclear power plant TAPS-4, which achieved criticality within 5 years of start of construction. Earlier at Reactor Control Division, BARC, he has been engaged in the development of computer based control and operator information systems for nuclear power plants. He was responsible for computerized control system for on-power refuelling machines of PHWRs from NAPS onwards and Dual Processor Hot Standby (DPHS) based - Process Control System and Reactor Regulating System for Kaiga-1,2 and RAPS-3,4 reactors. He participated in activities

of AERB as a member of several safety committees and Advisory Committee for Code, Guides and manuals for safety in design for nuclear power plants. He was Head, Reactor Control Division and Associate Director, Automation and Manufacturing Group, BARC before joining NPCIL.



Shri. G. Vaidyanathan, graduated in Engineering from Delhi University in 1971 and joined IGCAR in 1972 after completion of one year orientation course in BARC Training School. Later he acquired a Post Graduate Degree in Operation Management. Presently he is an Outstanding Scientist and Heads the Fast Reactor Technology Group at IGCAR as Group Director. Since 1972, he has been actively involved in the field of Fast reactor design, analysis and experiments. He has made significant contributions to numerical simulation of heat transfer and fluid flow processes in sodium cooled fast reactors. He has meticulously planned and carried out R&D for the thermal hydraulics of Fast Reactors. He has also contributed significantly as member of the IGCAR safety committee. He was instrumental in setting up the Steam Generator Test Facility at IGCAR with minimal cost and time overrun. He has to his credit about 175 publications in journals/conferences and has co-authored one book.



Dr. P.R. Vasudeva Rao, is a Distinguished Scientist and presently Director of Chemistry Group as well as Metallurgy and Materials Group in IGCAR. He obtained his Doctorate degree in Inorganic Chemistry from Bombay University in 1979. He has played an active role in shaping the Radiochemistry Programme of IGCAR to its current status. His research interests cover a wide range of areas such as development of alternate extractants and resins for actinide recovery solvent extraction, third phase formation, thermodynamics, applications of photochemistry in actinide separations, development of pyrochemical and other non-aqueous processes for recovery of actinides and rare earths, thermochemical studies on nuclear materials, application of microwaves in synthesis of nuclear fuels and other ceramic materials, nuclear fuel cycle, fuel behaviour in reactors, burn-up measurements, and non-destructive assay. He has published more than 150 papers in reputed international journals apart from guiding several research scholars for their doctorate degrees. He is a life member of Indian Nuclear Society, Materials Research Society of India, Society for Advancement of Electrochemical Science and Technology, Indian Association of Nuclear Chemists and Allied Scientists (IANCAS), and President of the Southern Regional Chapter - IANCAS. He has been awarded the MRSI Medal in 1998 and is also a Fellow of Tamil Nadu Academy of Sciences. He is a member of the International Advisory Board of the Journal of Nuclear Materials



Dr. V. Venugopal, M.Sc., Ph.D, is presently an Outstanding Scientist and the Director of Radiochemistry and Isotope Group at BARC, Mumbai, and Officer-in-charge, Nuclear Material Accounting and Control (NUMAC) cell of DAE. He is currently a member of Standing Advisory Group for Safeguard Implementation (SAGSI) to advise Director General IAEA on Safeguards Matters. He is a specialist in the field of thermal/ thermodynamics of plutonium based fuels at high temperature, chemical quality control of fuel, X-ray and solid state chemistry and oversees Radioisotope and Radiation Technology Programs at BARC. He is the chairman of Radiation Technology and Applications Committee (RTAC) of BRNS and a member of BRIT board. He is a member of safety committees such as OPSRC and CFSRC under BSC at BARC. He has to his credit more than 300 publications out of which 165 are published in reputed international journals. Widely acclaimed as an expert in the area of thermodynamics, Dr. Venugopal is the President of Indian Thermal Analysis Society (ITAS) and vice president and editor, INS news of Indian Nuclear Society (INS). He is also a member of several professional bodies IANCAS, NAARRI, ISAS, ISEAS, ISMAS, MRSI and Hindi Vigyan Parishad. He has received many awards including the Netzsch-ITAS award in 2001, ISCAS silver medal in 2002 and MRSI medal for 2003-04 and INS award for 2005.

Indira Gandhi Centre Scientific Committee (IGCSC) and Activities of Various Groups

Chairman



Dr. Baldev Raj
Director, IGCAR

Reactor Engineering Group



Shri S. C. Chetal
Director



Dr. P. Chellapandi
Associate Director, NEG



Dr. P. Mohanakrishnan
Head, RPD



Shri T.K. Mitra
Head, HTSD



Shri P. Puthiyavinayagam
Head, RCD



Shri K. Madhusoodanan
Head, PPCD



Shri C. Sivathanu Pillai
ACE, Civil



Shri P. Selvaraj
Head, MHD

Reactor Engineering Group (REG) is responsible for the design of 500 MWe Prototype Fast Breeder Reactor. Design of Nuclear Steam Supply System is carried out in-house. For Balance of Plant, design coordination is carried out by REG while the consultants are assigned the design work. REG is responsible for getting the design clearance of 500 MWe FBR from AERB. R&D coordination towards FBR and execution of R&D for structural mechanics is the responsibility of the Group. As FBR is primarily based on indigenous technology, the manufacturing technology development of important nuclear components was undertaken by REG with the active participation of Indian Industries and has been successfully completed. The components include main vessel, inner vessel, grid plate, roof slab, shutdown mechanisms, steam generator and largest size sodium service valve. REG provides the design support to FBTR. REG has acquired expertise in design of fast reactor. As a spin-off, structural mechanics expertise is being provided for non-reactor activities. REG is presently engaged in preparation of the blueprint for the future FBRs to provide enhanced safety and improved economics.

Metallurgy and Materials Group



Dr. P.R. Vasudeva Rao
Director



Dr. K. Bhanu Sankara Rao
Associate Director, MDCG



Shri K.V. Kasiviswanathan
Associate Director, GRIP



Dr. C. S. Sundar
Head, MSD



Dr. R.K. Dayal
Head, CSTD



Dr. T. Jayakumar
Head, NDED



Dr. S. Venugopal
Head, RIRD



Dr. M. Vijayalakshmi
Head, PMD



Dr. A.K. Bhaduri
Head, MTD

The Metallurgy and Materials Group has the mandate for comprehensive materials R & D programme focussed towards FBR technology. This requires multifaceted and multidisciplinary approaches that include development of special alloys, welding consumables, optimisation of fabrication schedules, characterisation of mechanical properties under sustained as well as varying loads at elevated temperatures over a wide ranges of strain rates, comprehensive characterisation of corrosion and bio-fouling, development and application of specialised NDE techniques, innovative designs, and robotics for remote handling. This has been backed by fundamental studies in basic science that includes studies on microstructure dependence of the various properties, radiation damage, positron annihilation, thermo-physical properties and mathematical modelling. Some significant contributions of the group include PIE of FBTR fuel pins that has led to enhancement of target burn up, and development of indigenous structural steels and welding consumables for PFBR applications. At the same time, the outstanding research contributions have brought international recognition in fields as diverse as life prediction under creep and creep-fatigue conditions, characterisation of microstructures by NDE techniques, welding science and technology, and materials science.

Fast Reactor Technology Group



Shri G. Vaidyanathan
Director



Shri. P. Kalyanasundaram
Associate Director, FRTG



Dr. C. Ananda Babu
Head, ST & HD



Shri K. K. Rajan
Head, SFD



Shri B. Krishna Kumar
Head, CIDD

The Fast Reactor Technology Group is actively involved in development and testing of models and prototype components for Prototype Fast Breeder Reactor (PFBR), development and testing of sodium instrumentation, and sodium pumps and flow meters. The group has both water and sodium test facilities and carries out a wide range of tests/studies such as heat and mass transfer studies in cover gas above sodium free levels, development of sodium components like cold trap, plugging indicator, filters, heaters, valves etc., development and testing of sodium sensors for level and flow and leak detection sensors for sodium leak, testing of control rod mechanisms, testing of inflatable seals, testing of fuel and other sub-assemblies for pressure drop and cavitation, reactor assembly flow patterns, testing of full scale fuel handling machines in air and sodium. A 5.5 MW_t steam generator test facility for carrying out detailed temperature measurements and study of transient response and thermohydraulic instability is also a part of the group. The group is also responsible for vibration testing of steam generator and intermediate heat exchanger. In short the group is working on all engineering aspects of FBRs.

Reactor Operation and Maintenance Group



Shri P. V. Ramalingam
Director



Shri G. Srinivasan
Associate Director, O&M



Shri K. Ravishankar
Head, THRDD



Shri V. Ramanathan
Head, RMD



Shri K.V. Suresh Kumar
Head, ROD

ROMG is responsible for safe operation of Fast Breeder Test Reactor (FBTR) and KAMINI reactor with in the limits given in technical specification documents. The group takes part in the operational safety review of 500 MWe Fast Breeder Reactor (FBR) Project documents. The Training and Human Resources Development Division of the group besides training O&M staff of FBTR and KAMINI is also responsible for training the O&M staff of FBR. Introducing innovations and new features in FBTR to increase its availability, enhancing safety, and gaining newer experience for incorporation of inferred ideas in FBR construction and operation, govern a part of ROMG's activities.

Reprocessing group



Shri R. Natarajan
Director



Dr. S. B. Koganti
Head, RRDD



Shri P. Ramkumar
Head, RPSD



Shri A. Ravisankar
Head, RPDD



Shri M. Venkataraman
Head, RPOD



Shri V. Sundararaman
Head, FRPD

The Reprocessing Group (Rp G) of IGCAR is responsible for the development of Fast reactor fuel reprocessing technology and construction of the reprocessing plants. RDL has two hot cell facilities: In one of them, U-233 was recovered from irradiated thorium rods on campaign basis and used as fuel in KAMINI reactor and in FBTR (as PFBR test fuel). The other hot cell facility, called, CORAL (COmpact facility for Reprocessing Advanced fuels in Lead cells) commissioned in 2003, is a test bed for validating the process flow sheet and scaling up of equipment designs for fast reactor fuel reprocessing, by processing the FBTR fuel itself. CORAL has already processed in several campaigns mixed carbide fuels irradiated in FBTR with 25, 50, 100 and 155 GWd/t burnups. This has provided valuable experience to the design of Demonstration Fast Reactor Fuel Reprocessing Plant, DFRP, in which the FBTR fuels will be reprocessed on a regular basis. DFRP, which will also demonstrate the reprocessing of PFBR fuel subassemblies, is slated for commissioning by 2009. RpG is also carrying out the design of the reprocessing plant, FRP, for reprocessing spent fuels of PFBR on commercial basis. Various R&D activities are being carried in the Reprocessing Development Laboratory. Engineering scale testing of equipment and systems are done here before installing in for hot cell. Chopper, dissolver, feed clarification equipment, centrifugal extractors are few of the important equipment developed at RDL. Apart from equipment development, research is undertaken for understanding and solving various process and chemistry problems of fast reactor fuel reprocessing such as, mathematical modeling of solvent extraction of the complex U-Pu system, efficient solvent management, development of online monitoring of Pu for process control, liquid flow metering in high radio active fields etc.,

Chemistry Group



Dr. P. R. Vasudeva Rao
Director



Dr. T. Gnanasekaran
Head, LMSCD



Dr. T. G. Srinivasan
Head, FChD



Dr. V. Ganesan
Head, MCD



Shri K.C. Srinivas
Head, CFD

The Chemistry Group is responsible for carrying out R & D to provide inputs with respect to all the chemistry aspects of the fast reactor and its fuel cycle. In addition, it also takes up R&D programmes which would have a long term impact on the reactor programmes. Besides the R&D activities, the Chemistry Group also provides extensive analytical support using a wide range of analytical techniques to all the programmes in the Centre. The Chemistry Group has also specialized in setting up of facilities for experiments with radioactive or air-sensitive materials, and in indigenous development of chemical instrumentation. The areas of R & D in Chemistry Group include sodium chemistry, chemistry of un-irradiated as well as irradiated fuel materials, development of fuel cycle, analytical chemistry, spectroscopy and more recently, boron chemistry. Development of sensors for PFBR and sensors for environmental applications, cover gas

purification system for PFBR, development of Laser Induced Breakdown Spectroscopy and X-ray absorption based techniques for on-line monitoring of Pu streams in reprocessing plants, development of technology for production of Pu rich fuels and minor actinide containing fuels through sol-gel route and development of sodium bonding for metallic fuels are some of the R & D programmes on the anvil.

Safety Group



Shri M. Rajan
Director



Shri N. Kasinathan
Head, SED



Dr R. Indira
Head, RSD



Shri M. Somasekaran
Head, SIRD

Safety Group consists of Safety Engineering Division, Radiological Safety Division and Scientific Information Resource Division.

Safety Engineering Division is engaged in the simulated experimental studies and development of mathematical models for FBR accident scenarios such as core subassembly flow blockage, molten fuel relocation, core debris cooling in core catcher, mitigation of consequences of sodium fires and radioactivity transport and deposition in sodium circuits.

Radiological Safety Division is mainly responsible for the research and development activities in radiation safety. The division provides health physics services for all the radioactive facilities in IGCAR. Studies on criticality safety, radiological safety analysis of BDBA in PFBR, radiation detector development, biodosimetry with reference to low level radiation exposure effects, development of a neutron generator for actinide assay in wastes, studies on thermo-luminescence and radioactivity transport in media are some of the major research work being carried out presently.

The group organizes public awareness programmes on radiation safety and nuclear energy. It also carries out industrial training programme to increase safety awareness.

The Scientific Information Resource Division is taking care of the Library and Information Services at the Centre. Work is in progress towards creation of a digital library for the FBR literature and making it available for campus wide access using the IGC Network. All the IGC publications are made available in full text electronic form.

Electronics and Instrumentation Group



Shri P. Swaminathan
Director



Shri S. Athinarayanan
Head, CD



Shri S. Ilango Sambasivan
Head, EID



Shri B. Saha
Head, IIS



Dr. A. Vijaya, Medical
Superindent, DAE Hospital



Shri S.A.V. Satyamurty
Head, NS

The Electronics and Instrumentation Group is actively engaged in the development of Strategic Safety Instrumentation Systems for Fast Breeder Reactor Programme such as Real Time Computer Systems , Safety Logic Systems, Expert systems Distributed Digital Control Systems etc. Unique Instrumentation systems such as Electro magnetic Time Domain Survey System is also being developed to detect deeply buried uranium ore. Highly reliable Instrumentation systems are being developed using modern VLSI design tools, thermal design tools ,EMI/EMC design tools etc. Application software packages are being developed using powerfull CASE TOOL. Development process is ISO certified. A Full scope Replica Type Training Simulator is being developed for training the operators of Prototype Fast Breeder Reactor. Walk-through of different areas of the reactor is being developed using PDMS package. State-of-the art Visualisation center with stereoscopic projection is being set up. Intranet based Knowledge Management System is being managed. Simplicity in instrumentation is being realised through the innovative programme on creation of pulsating sensors for diverse parameters, enabling development of completely indigenous plant monitoring and surveillance systems, rapid analytical and diagnostic tools. Security electronics systems are constantly being updated for Kalpakkam site. Biometric hand geometry based attendance system is recently commissioned. The group is also responsible to ensure satisfactory health services to the residents of Kalpakkam and Anupuram Townships.

Engineering Services Group



Shri Y. C. Manjunatha
Director



Shri A.S.L.K. Rao
Head, CWD



Shri A.Jyotish Kumar
Head, ESD



Shri B. Venkatraman
Head, QAD



Shri N. Vijayan Varier
Head, QC & CS

Engineering Services Group is responsible for providing quality services pertaining to Civil Engineering, Electrical Engineering, Voice Communication Systems, Air-conditioning & Ventilation Systems, Material Handling Equipments, Central Workshop activities, Quality Control & Quality Assurance and Testing. The Group also coordinates the telecommunication requirements of the centre. The Group has a mandate to establish additional infrastructure requirements so as to meet Design, R&D and operational objectives of IGCAR. The Group has expert teams with capability to design, engineer and execute systems under their jurisdiction. Electricity, water, quality-air and other services are being extended to other units of DAE located at Kalpakkam. The nature of work involves interaction with several State-Government and Central Government - organizations.

Fast Reactor Fuel Cycle Facility (FRFCF) Project Group



Shri P.V. Kumar
Project Director, FRFCF

Fast Reactor Fuel Cycle Facility (FRFCF) is being set up to close the fuel cycle of Prototype fast Breeder Reactor (PFBR). The work is being piloted by IGCAR with technical support from BARC and NFC. Towards setting up FRFCF, the preliminary project work is in progress. The site selected for FRFCF has been approved by AERB. Basic infrastructure is being created to reduce the lead time required to commence the construction work once the FRFCF project is sanctioned. AERB has constituted a Project Design Safety Committee for FRFCF and review of the preliminary safety analysis report is in progress. Geotechnical and hydrogeological investigations of the site have been completed. Main power station building and stores buildings are under construction and construction power supply system has been commissioned. Appointment of consultants for the detailed design is being processed. Detailed project report for FRFCF is planned to be submitted for financial sanction during the year 2008-09.

Planning Division



Smt. Uma Seshadri
Head, PD

Planning Division is the nerve centre, for coordination between Project Coordinators, Accounts, Purchase and Stores for planning, budgeting and continuous monitoring of expenditure of capital projects, to meet the technological challenges of the Centre. It generates various reports which are vital in decision making process. The activities briefly are: Capital project planning (under all sectors namely R & D, industries and power); Preparation of budget for all the projects; Monitoring and controlling expenditure under capital project heads. Conducting Budget Review Meetings (BRM) every month to expedite and sort out pending issues; Automation and Integration of activities as well as coordination between indentors at IGCAR, MRPU, Accounts and Stores regarding procurements and expenditure bookings.

Madras Regional Purchase Unit



Shri K. Balachander
Regional Director, MRPU

Material management activities for IGCAR are planned and executed systematically and meticulously by Directorate of Purchase & Stores (Madras Regional Purchase Units at Chennai and Central Stores Unit at Kalpakkam). Extensive use of Office automation and computers have helped in speeding up the procurement functions, thus achieving the financial targets namely Rs.91Crores, under R&D. Some of the important, high value Research Equipments procured are Laser Raman Microprobe, Plasma Processing System, Scanning Electron Microscopes and Thermal Ionisation Mass Spectrometer.

Strategic and Human Resources Planning Section



Dr. M. Sai Baba
Head, SHRPS

The section has the mandate of planning for the Strategic and Human Resource needs of the Centre which involve: Planning and running the training school programs at Training School; Collaborative projects with various R & D Organizations and Academic Institutes; Compilation of technical reports on important activities of the Centre; interacting and coordinating with National and International delegations; Assessing and projecting the human resource needs of the Centre for effective deployment and utilization; Interacting with the research scholars at the Centre; Planning and organizing meetings related to human resource and personality development.

Administration & Accounts



Shri V. Dayalan
Chief Administrative Officer



Shri S. Mani
*Joint Controller
(Finance & Accounts)*



Shri R.G. Raghavan
AO, Secretary, IGCSC

LIST OF IMPORTANT ABBREVIATIONS

AERB	Atomic Energy Regulatory Board
BARC	Bhabha Atomic Research Centre
BARCF	BARC Facilities
BHAVINI	Bharatiya Nabhikiya Vidyut Nigam Limited
BHEL	Bharat Heavy Electricals Limited
CD	Computer Division
CDO	Central Design office
CDPS	Central Data Processing System
CERMON	Continuous Environmental Radiation Monitoring Network
CG	Chemistry Group
CORAL	COmpact facility for Reprocessing Advanced fuels in Lead cell
CSTD	Corrosion Science and Technology Division
CWD	Central Workshop Division
ED	Electronics Division
EIG	Electronics and Instrumentation Group
ESG	Engineering Services Group
FBR	Fast Breeder Reactor
FBTR	Fast Breeder Test Reactor
FChD	Fuel Chemistry Division
FRFCF	Fast Reactor Fuel Cycle Facility
FRTG	Fast Reactor Technology Group
IDEAS	Innovative Design, Engineering and Synthesis
IIS	Innovative Instrumentation Section
IIT	Indian Institute of Technology
IMSc	Institute of mathematical Sciences
ITG	Inspection Technology Group
LMFBR	Liquid Metal Cooled Fast Breeder Reactor
MAPS	Madras Atomic Power Station
MCD	Materials Chemistry Division
MMD	Mechanical and Metallurgy Division
MMG	Metallurgy and Materials Group
MSD	Materials Science Division
MTD	Materials Technology Division
NFC	Nuclear Fuel Complex
NICB	Nuclear Island Connected Buildings
NPC	Nuclear Power Corporation
NSSS	Nuclear Steam Supply System
PFBR	Prototype Fast Breeder Reactor
PHWR	Pressurized Heavy Water Reactor
REG	Reactor Engineering Group
RHS	Remote Handling Section
ROMG	Reactor Operation and Maintenance Group
RPD	Reactor Physics Division
RpG	Reprocessing Group
RRDD	Reprocessing Research and Development Division
RSD	Radiological Safety Division
SED	Safety Engineering Division
SG	Safety Group
SGTF	Steam Generator Test Facility
SIRD	Scientific Information and Resources Division

